

Characterization of Silicon Photomultiplier and Design of Front-End Electronics for ALOFT

A thesis by

Linn Amalie Kvaale Ramdal

for the degree of

Master of Science in Physics



Department of Physics and Technology

University of Bergen

June 2022

Abstract

ALOFT is an aircraft campaign led by Birkeland Centre for Space Science at University of Bergen. The primary goal of the campaign is to look for Terrestrial Gamma Ray Flashes and gamma-ray glows, both high-energetic phenomena associated with thunderstorms. Among the several instruments to be used in the campaign is the UIB-BGO instrument, which will be upgraded with two new gamma-ray detectors.

The new gamma-ray detectors will consist of two LYSO-scintillators of different sizes coupled to Silicon Photomultipliers. This thesis contributes to these detectors by characterizing the Silicon Photomultipliers and designing front-end electronics for the Silicon Photomultiplier, appropriate for the application.

The signal shape, height, and length from the Silicon Photomultiplier are verified through measurement. Additionally, they are used to conclude with the best configuration of the Silicon Photomultiplier, with timing in mind. Other important characteristics are calculated, such as temperature sensitivity and linearity. The signal shape of Silicon Photomultiplier coupled to the LYSO-scintillator is also verified.

A design of front-end electronics for the Silicon Photomultiplier is made; the challenge here was the large and fast signal from the Silicon Photomultiplier and its large detector capacitance. A solution of preamplifiers has been designed to resolve this. And a design of the shaping circuit is made; this reduces noise but still retains the fast signal. The needed parameters of the front-end electronics are calculated and verified through simulation. The specific components to be used are verified in simulations; additionally, the preamplifier is physically tested with Silicon Photomultiplier input.

Acknowledgements

First and foremost, I would like to thank my supervisor *Professor Kjetil Ullaland*. For invaluable guidance and encouragement, for having an adequate answer to every question I asked, and for always finding the time for me (even when you were super-busy being institute leader). I would like to express my gratitude to *Senior Engineer Shiming Yang* for so much help at the lab, for making the test boards, and for your valuable input on what we saw. I could not have done all those tests of the sensors without your help.

Thanks to *Professor Martino Marisaldi* for all the help with space physics, the ALOFT campaign, and understanding the detectors. Thanks to *Head Engineer Bilal Hasan Qureshi* for adding my design on the PCB you are working on, and for being friendly and helpful. Further, I want to thank *Professor Johan Alme*, *Senior Engineer Georgi Genov*, *Head Engineer Thomas Pouljanitis*, and others that helped (and offered to help) with things that enhanced my work.

A huge thanks must go to my peer students, especially *Bendik*, *Birger*, *Håvard* and *Thomas*, for an exceptional work and social environment, and for making this year memorable.

Thanks to friends and family for their support and for never giving me any career advice, which led me into this path in life.

Finally, I want to thank my dear *Richard* for always brightening my day, and for being who you are.

Contents

Abstract	i
Acknowledgments	iii
Contents	vii
List of Figures	xiv
List of Tables	xvi
Acronyms	xvii
1 Introduction	1
2 Energetic Radiation from Thunderstorms and the ALOFT Mission	7
2.1 Origin of TGFs and Glows	7
2.1.1 Relativistic Runaway Electron	7
2.1.2 Bremsstrahlung	9
2.2 About the ALOFT Mission	10
2.2.1 The UIB-BGO Instrument	11
2.3 Expected Observations	12
2.3.1 Expected Observations from TGFs	12
2.3.2 Expected Observations from Glows	13
3 Silicon Photomultipliers	15
3.1 Working Principle of SiPM	15
3.2 Characteristics of SiPM	18
3.3 Electrical Equivalent Model and Signal Shape of SiPM	21
3.3.1 Equivalent Model	21
3.3.2 Signal Shape	23
3.4 SiPMs as Scintillation Light Detectors	26
3.4.1 Working Principles of Scintillators	26
3.4.2 Signal from Scintillator	29
3.4.3 Signal from SiPM Coupled to Scintillator	30
3.5 Linearity of SiPM	32

3.6	Temperature Sensitivity of SiPM	34
3.7	Measurements of SiPM	37
3.7.1	Single Unit SiPM Measurements	38
3.7.2	Calculating Time Constant from Measurements	41
3.7.3	Time Constant in Single Unit SiPM	43
3.7.4	SiPM with Scintillator	43
3.7.5	Measurements from Array	47
3.7.6	Measurements from Array with Amplifier Readout	52
3.7.7	Comparison of Measurements and Biasing and REadout Circuits	54
4	Front-End Electronics	57
4.1	Theory of CSA and CR-RC Shapers	57
4.1.1	Charge Sensitive Amplifier	57
4.1.2	CR-RC Shaper	58
4.1.3	Noise in CSA and CR-RC ⁿ	61
4.1.4	CSA with Finite Feedback Resistor	63
4.2	Shaping of Signal from SiPM	66
4.2.1	Filtering of Measurements	69
4.2.2	Noise Compared to Signal from Front-End Electronics	71
4.3	Schematic and Choice of Components	74
4.3.1	Preamplifier	74
4.3.2	Filter	77
4.3.3	ADC Driver	79
4.3.4	Diode Clippers	81
4.3.5	Analog to Digital Converters	84
4.3.6	Other Schematic Options	88
4.4	Simulation of Complete Circuit	88
4.4.1	AC-Response of Summing Configuration	88
4.4.2	Time Domain Simulation with Realistic Input (Summing Con- figuration)	92
5	Discussion and Conclusion	95
5.1	Discussion and Conclusion	95
5.2	Further Work	97
A	Summary of Design	99
B	Schematics	105
B.1	Schematic Used in Simulation of Individual Stages	105
B.1.1	AC-Response	105
B.1.2	Impulse-Response	110
B.2	Schematic Used in Simulation of Complete Circuit	115
B.2.1	AC-Response of Summing Configuration	115
B.2.2	Time Domain Simulation with Realistic Input (Summing Con- figuration)	121
B.3	Schematics of Test Boards	127
B.3.1	Single SiPM Test Board	127

B.3.2	SiPM Array Test Board for Varying Series Resistor and Number of Pixels	129
B.3.3	SiPM Array Test Board with Amplifier Readout	131
B.4	Schematic for High-Speed ADC Board	133
C	Shared Files	157
D	Intermediate Noise Calculations	159
E	More Simulation Results	163
E.1	Simulation of Complete Circuit	163
E.1.1	AC-Response of Summing Configuration	163
	Bibliography	174

List of Figures

1.1	Top level block diagram, showing the different components and stages, relevant to this thesis, in the detector.	4
2.1	Effective frictional forces acting on a electron (or positron), from [6]. .	8
2.2	The three mechanisms that generates the energetic electrons in the atmosphere, from [6]	9
2.3	TGFs detected by the Fermi satellite, the left plot shows the location of these (from june to september) and the right plot shows the TGF occurrence in time (month of the year is shown on the x-axis). From [8].	10
2.4	One way flight range of the NASA-ER2 aircraft flying out of Key West. From [8].	11
2.5	Fluence of photons for one TGF observed at 20 km altitude. For photons above 300 keV and 10^{17} initial number of photons. From [11].	12
2.6	Observations of glows marked with a black horizontal line from the aircraft campaign in 2017. The glow is at around 3.5×10^3 counts/s and the background radiation is around 2×10^3 counts/s. From [10]. .	13
3.1	Common configuration of photodiode. Adopted from [14].	16
3.2	Operating modes of a pn-junction depending on the reverse bias voltage. The different modes are photodiode-mode, APD-mode, and Geiger-avalanche mode. Adopted from [12].	16
3.3	The cycle of the SPAD in SiPM when triggered, starting with breakdown where current increases rapidly, then the current is quenched be the quenching resistor and voltage drops, finally the voltage resets. Adopted from [15].	17
3.4	Equivalent circuit of the SiPM showing the microcells connected in parallel, each microcell consists of a SPAD (shown as a diode) and a quenching resistor, some SiPM also has a capacitors in each microcell to form a fast output. [12, 17, 15, 16]	18
3.5	Symbol for one unit of SiPM (consisting of the whole circuit in figure 3.4) consisting of several microcells. One of these is referred to as one pixel in this thesis. Adopted from [16].	18
3.6	Electrical equivalent model of SiPM [19, 20, 21]	21

3.7	Schematic for the SiPM model that was simulated.	22
3.8	Schematic used in simulation where several pixels (from figure 3.7) are connected together to model a SiPM array.	22
3.9	Results from the SiPM equivalent model simulations with the schematic in figure 3.7 and 3.8.	23
3.10	Calculated signal from one triggered cell in the SiPM for three variants and different bias voltages.	26
3.11	Discrete energy bands in insulators or semiconductors. Adopted from [14].	27
3.12	Diagram of photoelectric absorption, showing how the gamma-ray interacts with the electron in the atom. Adopted from [14].	27
3.13	Diagram of compton scattering interaction between gamma-ray and electron. Adopted from [14].	27
3.14	Energy spectrum for different sized scintillator detectors, for high energy photons. The left plot is for a small detector, the right is for a very large detector, and the middle is for intermediate sized detector. Adopted from [14].	28
3.15	Expected signal from LYSO scintillator (100 keV γ -photon), calculated with equation (3.20) and (3.22).	30
3.16	Calculated signal (using equation (3.24)) from 8×8 SiPM array coupled til $50 \text{ mm} \times 50 \text{ mm} \times 50 \text{ mm}$ LYSO-scintillator.	31
3.17	Calculated signal (using equation (3.24)) from single SiPM unit coupled til $3 \text{ mm} \times 3 \text{ mm} \times 10 \text{ mm}$ LYSO-scintillator.	32
3.18	Linearity for small scintillator and SiPM depending on absorbed gamma-photon energy in the scintillator.	33
3.19	Linearity for large scintillator and SiPM depending on absorbed gamma-photon energy in the scintillator.	33
3.20	Linearity for large scintillator and SiPM, shown for all 64 pixels and 1 of the 64 pixels. The solid line is the number of fired cells, and the dashed line is the linear approximation.	34
3.21	Change in overvoltage for temperature change, when bias voltage is kept constant	35
3.22	Calculated percentage deviation from total output charge at mean temperature (here $21 \text{ }^\circ\text{C}$), for different constant bias voltages, using two different gamma-ray energies: 100 keV (solid line) and 60 MeV (dashed line).	36
3.23	Graphs showing how the temperature affects the signal height of the SiPM depending on the incoming gamma-photon energy, and for two different mean overvoltages.	37
3.24	Setup for measuring signal from a single unit SiPM.	38
3.25	Picture of the test board used in measurements of single SiPM.	38
3.26	Signal from a single SiPM using different pulse width on LED light source.	39
3.27	Signal from SiPM for different bias voltages, with LED as light source.	40
3.28	Signal from SiPM using different voltage over LED light source.	41

3.29	General exponential decay (as in equation (3.30)), showing the different values found in measurement and used to calculate the decay time constant.	42
3.30	Picture of the test board used in measurements of single SiPM with small scintillator attached.	44
3.31	A few measured pulses from SiPM with LYSO-scintillator.	44
3.32	A few measured pulses from SiPM with LYSO-scintillator	45
3.33	Pulses in figure 3.32a normalized and plotted with expected pulse shape	45
3.34	Measured energy spectrum, for LYSO self-counts.	46
3.35	Measured energy spectrum from radioactive sources (LYSO self-counts are not subtracted).	47
3.36	Picture of breakout board from onsemi, ARRAYJ-BOB3-64P, with the ARRAYJ-30035-64P-PCB SiPM array.	48
3.37	Setup for measuring signal from SiPM array	48
3.38	Measurements from SiPM array using the breakout board from onsemi.	49
3.39	Pictures of test board used for characterizing the signal with different number of pixels connected and different series resistor values.	49
3.40	Selection of pulses from a constant number of pixels in the SiPM array using different series resistors.	50
3.41	Selection of pulses from SiPM array using constant series resistor, and varying number of pixels.	50
3.42	Selection of pulses from SiPM array using increasing number of pixels and decreasing series resistance	51
3.43	Plot of decay time constant for varying number of pixels and resistor values, measured as described in section 3.7.2 from measurements with different number of pixels and resistor values, plotted with error bars for the standard deviation of 10 measurements.	51
3.44	Picture of test board used for characterizing the signal from the SiPM, with a amplifier used for read-out.	52
3.45	Setup for measuring signal from SiPM array using preamplifier for readout. A LED was used as the light source (but is not shown in this diagram).	53
3.46	Pulse from 16 pixel of the SiPM array connected amplifier, and LED as light source.	53
3.47	Filtered output from 16 pixel of the SiPM array connected amplifier, and LED as light source.	54
3.48	Comparison of pulses from the different biasing and readout methods used.	55
4.1	Charge Sensitive Amplifier (CSA), adopted from [30].	57
4.2	Practical implementation of CSA with CR-RC, adopted from [30].	58
4.3	Output of CR-RC ⁿ filter, with constant time constant $\tau = 100$ ns, adopted from [30].	59
4.4	Normalized output of CR-RC ⁿ filter, with constant peak time $T_p = 100$ ns, adopted from [30].	60
4.5	Output of CR ² -RC ⁿ filter, with constant time constant $\tau = 100$ ns.	61

4.6	Noise sources in CSA, adopted from [30].	61
4.7	General plot of Equivalent Noise Charge, showing the contribution of series, flicker and parallel noise, adopted from [30].	63
4.8	General plot of Equivalent Noise Charge for different order shapers	63
4.9	Impulse response of CR-RC shaper with finite feedback resistance, adopted from [30].	64
4.10	Output CR-RC shaper with finite feedback resistance, when multiple pulses hit, showing each pulse is lower than the previous, adopted from [30].	65
4.11	Shaper with CSA working in transimpedance mode, when R_f is small, adopted from [30].	66
4.12	Calculated output of shaping circuit with SiPM and LYSO input	67
4.13	Calculated signal height and peak time for different shaper time constants and input signal with real length.	68
4.14	How shaping time constant affects a input signal with real length. Using a CR^2 - RC^n shaper, since this has a more complex shape the first peak (solid line), the second peak (dash-dotted line) and where the signal crosses the baseline between the peaks (dashed line) were plotted.	68
4.15	Pulse measurements from figure 3.31a (standard output of SiPM coupled with LYSO-scintillator) filtered with digital equivalent of the shaper.	69
4.16	Pulse measurements from figure 3.31a (standard output of SiPM coupled with LYSO-scintillator) filtered with digital equivalent of the shaper and normalized, the black solid line is the expected signal shape calculated with the inverse Laplace transform of equation (4.24) and (4.25).	70
4.17	Pulse measurements from figure 3.31b (fast output of SiPM coupled with LYSO-scintillator) filtered with digital equivalent of the shaper.	71
4.18	Calculated RMS noise from preamplifier compared to signal peak value as a function of signal peak time and shaping time constant, for CR - RC^n shaper.	73
4.19	Calculated RMS noise from preamplifier compared to signal peak value as a function of signal peak time and shaping time constant, for CR^2 - RC^n shaper.	74
4.20	Circuit diagram of preamplifier stage with current shown.	75
4.21	Results from simulation of preamplifier stage alone.	76
4.22	Simplified circuit showing how several amplifiers will be connected the filer and ADC driver stages.	77
4.23	Circuit diagram of general summing amplifier.	77
4.24	Results from simulation of low pass filter stage alone.	78
4.25	Results from simulation of high pass filter stage alone.	79
4.26	Circuit for ADC driver stage, using a second order low pass multiple-feedback filter, as in [1].	79
4.27	Extended ADC driver (in figure 4.26) to be used as a summing amplifier.	80
4.28	Results from ADC driver simulation alone.	81

4.29	Common connection for diode clippers, if the signal is above VDD or below ground the signal will be clipped.	83
4.30	Diode capacitance and forward voltage for different diodes	83
4.31	Diode capacitance and forward voltage for a selection of diodes	84
4.32	Normalized frequency content of signal from SiPM, LYSO-scintillator and CR-RC ⁿ filter.	85
4.33	Normalized frequency content of signal from SiPM, LYSO-scintillator and CR ² -RC ⁿ filter, this will also be similar to using the fast output of the SiPM and CR-RC ⁿ filter.	86
4.34	Option added to board, where the fast and the standard output can be used, or two of either can be used, for example for applying different gain of different filter types.	88
4.35	Gain of frequency response using time constant $\tau_{shaper} = 10$ ns, feedback resistor in preamplifier $R_f = 10 \Omega$, other resistors around $1 \text{ k}\Omega$, and gain of the summing amplifier equal to 1.	89
4.36	Phase of frequency response using time constant $\tau_{shaper} = 10$ ns, feedback resistor in preamplifier $R_f = 10 \Omega$, other resistors around $1 \text{ k}\Omega$, and gain of the summing amplifier equal to 1.	89
4.37	Output noise spectral density on the different outputs when using time constant $\tau_{shaper} = 10$ ns, feedback resistor in preamplifier $R_f = 10 \Omega$, other resistors around $1 \text{ k}\Omega$, and gain of the summing amplifier equal to 1.	90
4.38	Time domain simulation of complete circuit with summing configuration using realistic input.	92
A.1	Simplified diagram of preamplifier of filter stage, showing a voltage divider for adjusting the common-mode, as well as the supply voltage.	99
E.1	Gain of frequency response using time constant $\tau_{shaper} = 20$ ns, feedback resistor in preamplifier $R_f = 10 \Omega$, other resistors around $1 \text{ k}\Omega$, and gain of the summing amplifier equal to 1.	165
E.2	Phase of frequency response using time constant $\tau_{shaper} = 20$ ns, feedback resistor in preamplifier $R_f = 10 \Omega$, other resistors around $1 \text{ k}\Omega$, and gain of the summing amplifier equal to 1.	165
E.3	Output noise spectral density on the different outputs when using time constant $\tau_{shaper} = 20$ ns, feedback resistor in preamplifier $R_f = 10 \Omega$, other resistors around $1 \text{ k}\Omega$, and gain of the summing amplifier equal to 1.	166
E.4	Gain of frequency response using time constant $\tau_{shaper} = 10$ ns, feedback resistor in preamplifier $R_f = 10 \Omega$, other resistors around 100Ω , and gain of the summing amplifier equal to 1.	166
E.5	Phase of frequency response using time constant $\tau_{shaper} = 10$ ns, feedback resistor in preamplifier $R_f = 10 \Omega$, other resistors around 100Ω , and gain of the summing amplifier equal to 1.	167

E.6	Output noise spectral density on the different outputs when using time constant $\tau_{shaper} = 10$ ns, feedback resistor in preamplifier $R_f = 10 \Omega$, other resistors around 100Ω , and gain of the summing amplifier equal to 1.	167
E.7	Gain of frequency response using time constant $\tau_{shaper} = 10$ ns, feedback resistor in preamplifier $R_f = 20 \Omega$, other resistors around $1 \text{ k}\Omega$, and gain of the summing amplifier equal to 1.	168
E.8	Phase of frequency response using time constant $\tau_{shaper} = 10$ ns, feedback resistor in preamplifier $R_f = 20 \Omega$, other resistors around $1 \text{ k}\Omega$, and gain of the summing amplifier equal to 1.	168
E.9	Output noise spectral density on the different outputs when using time constant $\tau_{shaper} = 10$ ns, feedback resistor in preamplifier $R_f = 20 \Omega$, other resistors around $1 \text{ k}\Omega$, and gain of the summing amplifier equal to 1.	169
E.10	Gain of frequency response using time constant $\tau_{shaper} = 10$ ns, feedback resistor in preamplifier $R_f = 10 \Omega$, other resistors around $1 \text{ k}\Omega$, and gain of the summing amplifier equal to 0.25.	169
E.11	Phase of frequency response using time constant $\tau_{shaper} = 10$ ns, feedback resistor in preamplifier $R_f = 10 \Omega$, other resistors around $1 \text{ k}\Omega$, and gain of the summing amplifier equal to 0.25.	170
E.12	Output noise spectral density on the different outputs when using time constant $\tau_{shaper} = 10$ ns, feedback resistor in preamplifier $R_f = 10 \Omega$, other resistors around $1 \text{ k}\Omega$, and gain of the summing amplifier equal to 0.25.	170

List of Tables

3.1	Parameters for SiPM used (onsemi J-Series SiPM Sensors), from data sheet [23].	24
3.2	Parameters for SiPM used (onsemi J-Series SiPM Sensors), from data sheet [23]. 30020 is the 3.07 mm × 3.07 mm SiPM with 20 μm microcell size, 30035 is the 3.07 mm × 3.07 mm SiPM with 35 μm microcell size, and 60035 is the 6.07 mm × 6.07 mm SiPM with 35 μm microcell size.	25
3.3	Parameters for LYSO scintillator used.	30
3.4	SiPM breakdown voltage parameters.	35
3.5	Comparison of different decay time constants measured for different Silicon Photomultipliers (SiPMs) and measurement setups.	55
4.1	Example values used to demonstrate what the SiPM signal can look like after shaping.	67
4.2	Comparison of different amplifiers from [33].	75
4.3	Analog input and output range for amplifiers.	82
4.4	Absolute minimum and maximum input voltage to the analog inputs on the Analog to Digital Converters (ADCs).	82
4.5	ADC parameters.	84
4.6	Quantization error from the ADC, for different error distributions. Also assuming the adc input is proportional to the gamma-photon energy, and not looking at any other noise sources.	87
4.7	Output RMS noise from simulated amplifying and shaping circuit in μV_{rms} (square root of integral of figure 4.37 and equivalent plots, when some of the values are changed).	90
A.1	Component values for front-end electronics for SiPM array.	101
A.2	Preamplifier component values that deviates from table A.1 for different inputs.	102
A.3	Component values for simple ADC driver with unit gain and only one input signal.	103
D.1	α and m values for the beta function in the noise integrals for CR-RC ⁿ shaper.	161

D.2 α and m values for the beta function in the noise integrals for CR ² -RC ⁿ shaper.	162
---	-----

Acronyms

AC	Alternating Current
ADC	Analog to Digital Converter
ALOFT	Airborne Lightning Observatory for FECS & TGFs
APD	Avalanche PhotoDiode
ASIM	Atmosphere-Space Interactions Monitor
BCSS	Birkeland Centre for Space Science
BGO	Bismuth Germanium Oxide
CSA	Charge Sensitive Amplifier
DC	Direct Current
DEEP	Distribution of Energetic Electrons and Protons
ENC	Equivalent Noise Charge
FECS	Fly's Eye GLM Simulator
FPGA	Field Programmable Gate Array
FWHM	Full Width at Half Maximum
GBW	Gain-Bandwidth Product
GLM	Geostationary Lightning Mapper
GOES-R	Geostationary Operational Environmental Satellites—R Series
iSTORM	in-Situ Thunderstorm Observer for Radiation Mechanisms
LED	Light Emitting Diode
LIP	Lightning Instrument Package
LYSO	Lutetium-Yttrium Oxyorthosilicate
NASA	National Aeronautics and Space Administration
PCB	Printed Circuit Board
PDE	Photon Detection Efficiency
PDF	Probability Density Function
PMT	Photomultiplier Tube

RMS	Root Mean Square
RREA	Relativistic Runaway Electron Avalanches
SiPM	Silicon Photomultiplier
SNR	Signal to Noise Ratio
SoC	System on Chip
SPAD	Single-Photon Avalanche Diode
TGF	Terrestrial Gamma Ray Flash
UiB	University of Bergen

Introduction

One of the main questions the Birkeland Centre for Space Science (BCSS) has set to understand is how energetic radiation is related to thunderstorms. The Airborne Lightning Observatory for FEES & TGFs (ALOFT) campaign will advance this science by closely observing two energetic phenomena related to thunderstorms, Terrestrial Gamma Ray Flash (TGF)es and gamma-ray glows hereafter glows.

TGFs are intense and short (sub-millisecond) bursts of gamma-rays from thunderclouds. While glows are less intense and last several minutes (possibly more) and stretch over several square kilometers.

Understanding TGFs and glows is a piece of the puzzle of how thunderstorms and lightning work and even how the atmosphere works. Glows may also impact the local climate from the energy deposition and ionization produced by the radiation over a long extent in space and time.

TGFs have mainly been observed by spacecraft, and getting closer to the source is desired; what ALOFT will do is chase these phenomena by aircraft. ALOFT is a follow-on study from a similar campaign completed in 2017, the Geostationary Operational Environmental Satellites—R Series (GOES-R) validation campaign. But TGFs and glows was not the main objective of that aircraft campaign, and only one glow was seen, no TGFs. ALOFT will be in an area with high TGF occurrence and seek out these; if a glow is detected, the aircraft will fly back over it to observe its extent in space.

Several instruments will be used in ALOFT; one of these is the UIB-BGO instrument which can detect gamma-rays. The instrument will be upgraded with two new scintillators, which will increase the range of photon fluxes, energy resolution, and timing resolution. More about ALOFT and the UIB-BGO instrument is in section 2.2. To convert the light pulse from the scintillators to an electrical signal Silicon Photomultipliers (SiPMs) will be used.

The main work of this thesis is centered around the SiPM. The first main objective is acquiring detailed knowledge about the SiPM and characterizing this sensor alone and coupled to a Lutetium-Yttrium Oxyorthosilicate (LYSO)-scintillator. This involves exploring theory from papers and technical documents, simulations, and measurements.

The other main objective is designing the front-end electronics for the SiPM. The

front-end electronics should be suitable for acquiring energy and timing information from the fast and large signal from the SiPM. This includes finding a suitable readout and biasing method that preserves the fast signal of the SiPM and designing a shaping circuit that filters out enough noise to get good energy resolution of the gamma-photons.

Requirements

The main objective of the project is to upgrade the UIB-BGO instrument that will be used in the ALOFT campaign; the motivation to upgrade will be to fulfill these requirements:

- A large range of fluences in TGF duration ($\sim 100 \mu\text{s}$), from 10^3 counts/cm right above the TGF to 10^{-2} counts/cm with a 20 km radius from the TGF.
- A large dynamic range of 100 keV to several 10 MeV.
- Energy resolution of less than 25 % (ideally at 10 %) Full Width at Half Maximum (FWHM) at 661 keV for the complete system for the large scintillator.

To increase the range of fluences two new detectors will be added, based on LYSO-scintillators. One between the two detectors in the UIB-BGO instrument, and one smaller. To achieve this, some requirements are set:

- Design a readout for a large $5 \text{ cm} \times 5 \text{ cm} \times 5 \text{ cm}$ LYSO-scintillator, that will be used for energy and timing resolution. And a small $3 \text{ mm} \times 3 \text{ mm} \times 10 \text{ mm}$ LYSO-scintillator for extreme count rates.
- Average count rate up to 10 Mcounts/s during TGF duration (less than 1 ms); this is so the smallest detector can keep up with the fluence from a TGF strait below it.

For the new scintillators some requirements are set to achieve the dynamic range:

- Dynamic range up to 60 MeV (where the muon peak will be) for the large $5 \text{ cm} \times 5 \text{ cm} \times 5 \text{ cm}$ LYSO-scintillator.
- For the small $3 \text{ mm} \times 3 \text{ mm} \times 10 \text{ mm}$ LYSO-scintillator, the dynamic range will be up to where the SiPM will be saturated. Because of linearity of SiPM and properties of small scintillators.

Lastly, based on the requirements above, some requirements were set more specifically for this thesis:

- Acquire detailed knowledge about SiPMs in general and as a scintillation light detector.
- Verify calculated signal length, shape, and height for the SiPM alone.
- Verify calculated signal shape of the SiPM coupled to LYSO-scintillator.

- Design front-end electronics for the SiPM sensor.
- Find a suitable way to bias and readout the SiPM that fulfills the timing and energy resolution requirements above.
- Design a shaping circuit for the SiPM signal that fulfills the timing and energy resolution requirements above.
- The shaping circuit should have low noise.
- The shaping circuit should fulfill the Nyquist theorem.
- The shaping circuit should have a peak time being lower than 100 ns to fulfill the 10 Mcount/s requirement.
- Find a preamplifier or a solution with several preamplifiers that can handle the large and fast signal from the SiPM.

Scope of This Work

Figure 1.1 a block diagram of the stages in the detector. Most of the work of this thesis is centered around the SiPM and the front-end electronics. Although, some work is related to the scintillator: To understand how it works with the SiPM and the requirement for the SiPM and front-end electronics. Additionally, the Analog to Digital Converter (ADC) were considered when designing the front-end electronics.

The work with SiPM involved exploring theory, such as working principles: The difference between SiPM and other diode-based sensors, the cycle of breakdown, quenching and reset, and the building blocks of the SiPM. Characteristics such as gain, number of fired microcells and noise sources. An equivalent model and signal shape of SiPM alone and with a scintillator.

Other important properties considered for the design were linearity and temperature sensitivity. Further, measurements were taken of the SiPM to verify the most important/controversial properties. These were the signal shape, height and length, and what readout method would give the best signal quality and shortest signal length.

A design of front-end electronics was made, based on the measurements and calculations of SiPM properties and theory about amplifying and shaping circuits. Theory about Charge Sensitive Amplifier (CSA) and CR-RC shaper is first considered to lay the groundwork for how the signal will be shaped. Further, it is considered what the signal from SiPM will look like and how much noise there is compared to this signal. Choice of components and other design choices is then discussed. Finally, the circuit is simulated to see if it works and to find a better estimate of the noise.

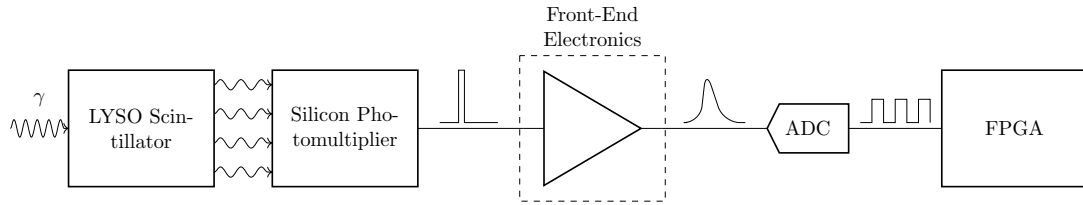


Figure 1.1: Top level block diagram, showing the different components and stages, relevant to this thesis, in the detector.

Chapter overview

This thesis starts with **Chapter 2 - Energetic Radiation from Thunderstorms and the ALOFT Mission** which is about theory about TGFs and glows, some background and information about the ALOFT campaign and the instruments that will be used, expected observations.

Since there are two big themes in the thesis; SiPM, and front-end electronics, the thesis is then divided into two large chapters about these themes.

Chapter 3 - Silicon Photomultipliers This chapter contains the basic theory, simulations and measurements of SiPM. It also contains related theory about scintillators and how this detector and SiPM work together. Further, some conclusions about temperature sensitivity and linearity are made, followed by measurements that verify the theory about the SiPM and conclusions about how the SiPM should be biased and read out. This is key to the design of front-end electronics.

Chapter 4 - Front-End Electronics This chapter starts with theory about front-end electronic (for amplifying and shaping the signal) and why it will be beneficial to connect the SiPM in such a way, based on theory and measurements of the SiPM. It continues on with a design of amplification and shaping of the SiPM signal, considering noise, sampling rate, and choice of components, and concludes on how well this will work. Lastly, the circuit is simulated to test if it works and to find a more realistic noise estimate.

Finally, there is **Chapter 5 - Discussion and Conclusion**. Which includes conclusion and discussion of what was done in this thesis, and further work towards the ALOFT mission.

At the end is the **Appendices** which includes additional information such as a summary of design choices, schematics, shared files, and additional calculation steps and simulation results.

Contributions of Others

It is worth mentioning that several others at the University of Bergen (UiB) have contributed to the project: The SiPMs was chosen and procured by Professor Martino Marisaldi in the early stages of this thesis. Senior Engineer Shiming Yang has made several test boards for the SiPM and the setup for taking measurements of the SiPM at the lab. Head Engineer Bilal Hasan Qureshi is currently making a Printed Circuit Board (PCB) (called The High-Speed ADC Board) to be used in

the ALOFT and implemented the front-end electronic design made in this thesis on that PCB.

More specifically Yang has made the test boards shown in figure 3.25, 3.30, 3.39 and 3.44, and in appendix B.3. Making the preamplifier stable was a considerable amount of Yang's work on the latter test board, and several iterations of this board was made before the one shown in this thesis.

As mentioned, Qureshi is working on the PCB to be used in ALOFT. The starting point for this PCB was a design made by Aleksander Waage and Sindre Jacobsen Færø in their bachelor thesis [1]. Waage and Færø managed to make the PCB design to the schematic stage, but the layout was not made, and the PCB was not produced.

After Qureshi took over the project, several changes were made. Among other things, a second ADC has been added; specifically, AD9257 that was proposed to be used for the Distribution of Energetic Electrons and Protons (DEEP) project in Aleksander Kårstad Nes' master thesis [2]. Moreover, several peripherals and related component (to interface with the Field Programmable Gate Array (FPGA)) has been added, these are mainly from the schematics of the Zybo Z7 development board [3] and the ZedBoard development board [4]. Other parts of Qureshi's work on this board are placement of components and layout, including length matching of signals, placement of termination resistors, and decoupling capacitors.

At the time of writing this, two other master students, Trond Eirik Knutsen and Viljar Dahle are working on the firmware/software for data acquisition, digital signal processing, data storage, and monitoring. Some groundwork for the data storage and monitoring was laid in the bachelor thesis of Asbjørn Magnus Midtbø and Harald Træet Lægneid [5].

Energetic Radiation from Thunderstorms and the ALOFT Mission

In order to understand the requirements for the electronics, knowledge about the physics that will be measured is key. This chapter starts with a brief introduction to high-energy radiation from thunderstorms. Further, there will be some background on the campaign and the sensors to be designed. Lastly, there are some expected observations to further understand what will be measured.

2.1 Origin of TGFs and Glows

X-rays and gamma-rays are emitted by thunderclouds and lightning, TGFs and glows are two of these phenomena emitting this radiation. There are different definitions of what is usually called X-rays and gamma-rays. In this thesis, the same radiation from thunderclouds will be referred to as both X-rays or gamma-rays. TGFs are intense bursts of X-rays and gamma-rays that last sub-millisecond, glows are less intense and last for minutes, or possibly more. This section will consider the theory behind these and is mainly based on [6].

The X-rays and gamma-rays are produced from energetic electrons that have gained energy from the high electric field inside thunderclouds. Which again comes from the charge structure inside the thunderclouds.

2.1.1 Relativistic Runaway Electron

Only free electrons can be accelerated in the electric field. The free electrons may come from cosmic rays, thermal kinetic energy, or other energetic electrons interacting with them. The initial energy of the electron, as well as the strength of the electric field, determines if the electron will be able to overcome the frictional forces and accelerate through the electric field.

The effective frictional forces that affect the free electrons (or positrons) depending on the kinetic energy are shown in figure 2.1 (in air at standard temperature and pressure). Figure 2.1 shows the threshold kinetic energy ϵ_{th} for an electron (or

positron) to be able to accelerate in some electric field E . E_b is the break-even field and is the lowest theoretical field that may cause electrons to run away. That an electron “runs away” means that it can acquire kinetic energies up to relativistic energies. E_c is the critical field; if the electrical field is above this, all free electrons may be able to run away.

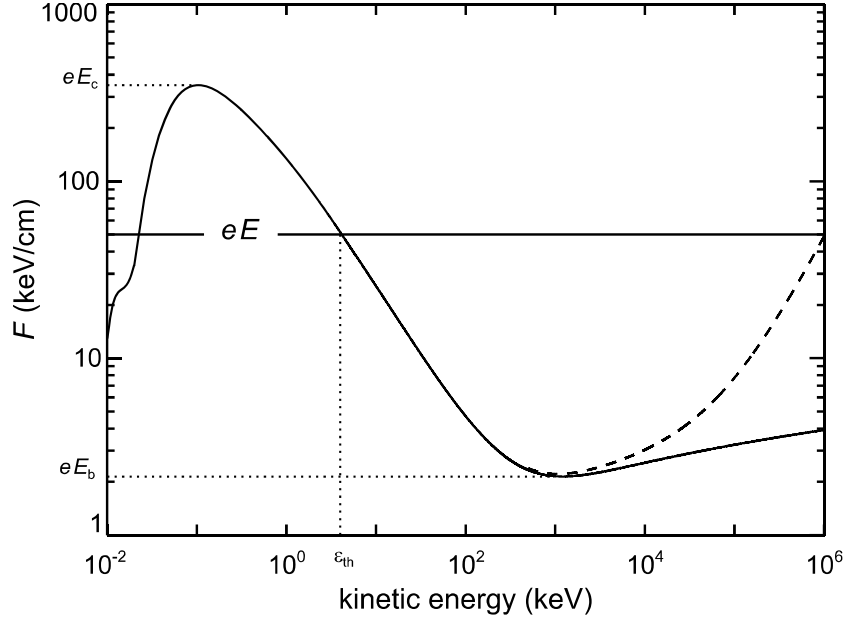


Figure 2.1: Effective frictional forces acting on a electron (or positron), from [6].

As mentioned, there are several ways to free electrons; some electrons may be free due to thermal energy, but their kinetic energy is not that high, and a strong electric field is required for them to run away. Other free electrons can come from cosmic rays, and these may have higher energies than the thermal electrons. Both the cosmic and thermal electrons are considered seed electrons and explain how a TGF or glows may be able to start, but it is not enough to explain the quantities of radiation that have been observed. Demonstrated in figure 2.2 are the mechanisms that generate energetic electrons from the seed electrons.

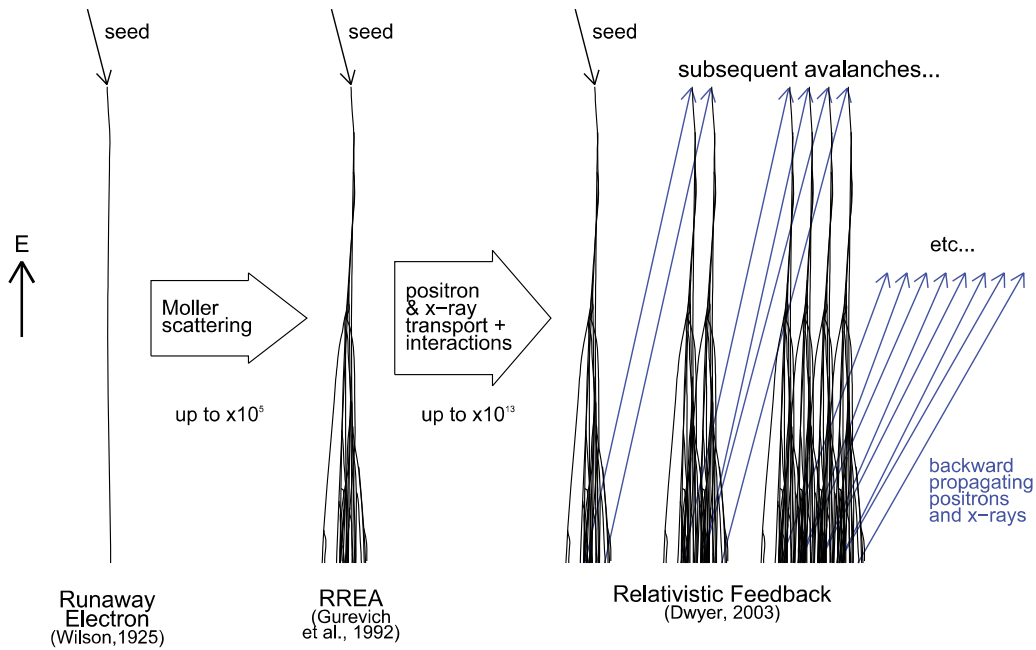


Figure 2.2: The three mechanisms that generates the energetic electrons in the atmosphere, from [6]

Møller scattering explains the difference between just the seed electron (also called Runaway Electron) and Relativistic Runaway Electron Avalanches (RREA). The seed electron will free other electrons through electron-electron elastic scattering, and the freed electrons will free other electrons, and so on. This will result in an avalanche multiplication and a large number of relativistic runaway electrons.

In addition, relativistic feedback is needed to explain the total number of high-energy photons that are observed. Positrons and X-rays are emitted from interactions with the energetic electrons. The positrons gain energy from the electric field region and release additional seed electrons by interacting with the air molecules, primarily by ionizing. The X-rays may be emitted toward the source region and also cause new seed electrons. The additional seed electrons will then cause new avalanches.

Under some conditions, the production of energetic electrons and gamma-rays may have an exponential increase, then a sudden stop, which all will happen within a few hundred microseconds; this is a TGF. With other circumstances, the propagation of electrons and X-rays may go into a metastable situation that can last several minutes, and where the gamma-ray flux is much lower; this is a glow.

2.1.2 Bremsstrahlung

X-rays and gamma-rays travel further than electrons (and positrons); therefore, they are mostly what is seen by the detector. These can be created by several mechanisms but are mostly created through bremsstrahlung in this case.

Bremsstrahlung is X-rays that are produced from rapid acceleration of high-velocity charged particles. This happens when an electron swings by a nucleus and changes direction. See for example [7].

2.2 About the ALOFT Mission

ALOFT is led by BCSS at UiB, in collaboration with several institutions in the USA: The University of Alabama in Huntsville, National Aeronautics and Space Administration (NASA)'s Marshall Space Flight Center, and Naval Research Laboratory. If not otherwise noted, this section is based on [8].

The main objective of ALOFT is to take measurements of TGFs and glows. ALOFT will also contribute to improving existing and future lightning mappers, such as Geostationary Lightning Mapper (GLM), and advance Aerosol and Cloud, Convection, and Precipitation science.

TGFs and glows have mostly been observed from spacecraft; in order to create a better understanding of these phenomena, it will be useful to observe these closer. One way to do that is to place instruments on the ground and hope to be lucky. What ALOFT will do is to try to seek out the location of TGFs and glows and follow them with an aircraft, specifically the NASA ER-2 aircraft. This is a specialized aircraft that can operate in altitudes from 20 000 feet to 70 000 feet [9] (≈ 6 km to 21 km). For ALOFT it will fly at 20 km altitude, well above the tropopause, in order to fly undisturbed over thunderstorm regions.

A similar campaign (the GOES-R validation flight campaign) with this aircraft was completed in 2017. One glow was detected during this campaign, but no TGFs. This is because the continental United States was the target region, and the TGF occurrence rate is low there.

In 2023, the aircraft will be loaded with the ALOFT instrument package and fly over one of the most TGF intense areas in the world: Central America and the Caribbean. As seen in figure 2.3 the TGF occurrence in this area is high. The campaign will also occur during the most intense season for TGFs which is July through September, as shown in figure 2.3.

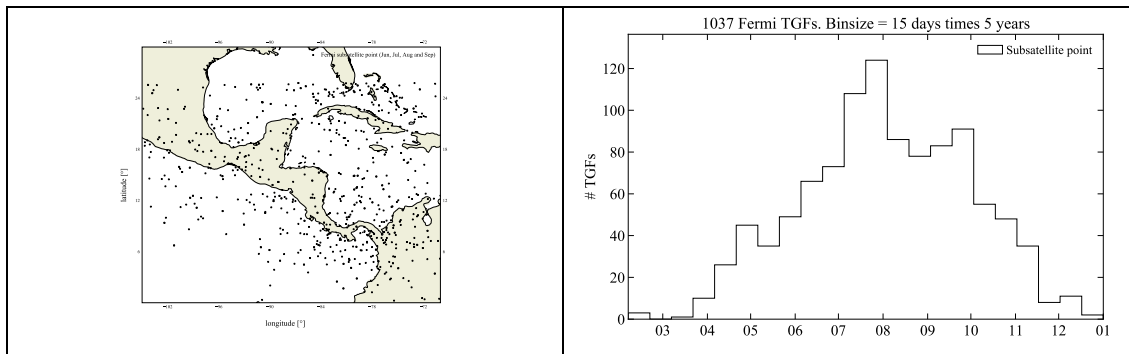


Figure 2.3: TGFs detected by the Fermi satellite, the left plot shows the location of these (from June to September) and the right plot shows the TGF occurrence in time (month of the year is shown on the x-axis). From [8].

To reach the region in figure 2.3, Key West is a good station to fly out of. Figure 2.4 shows that the entire region can be reached from this spot.

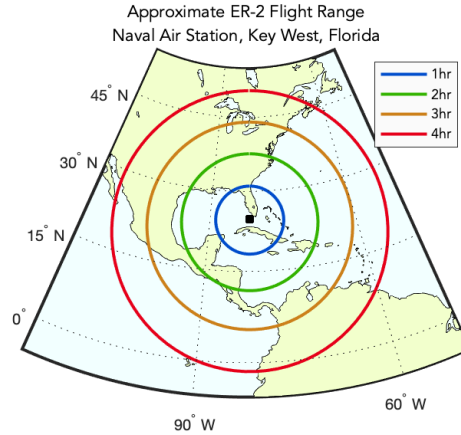


Figure 2.4: One way flight range of the NASA-ER2 aircraft flying out of Key West. From [8].

ALOFT will use the same basic instruments as the GOES-R validation campaign in 2017, with some upgrades. These instruments were Fly’s Eye GLM Simulator (FEGS), Lightning Instrument Package (LIP), UIB-BGO, and in-Situ Thunderstorm Observer for Radiation Mechanisms (iSTORM). ALOFT may also take advantage of instruments used in other campaigns, due to extra space in the aircraft.

2.2.1 The UIB-BGO Instrument

UIB-BGO is the instrument package provided by the UiB. This consisted of three Bismuth Germanium Oxide (BGO) scintillators coupled to Photomultiplier Tubes (PMTs), for a total geometrical area of $15\text{ cm} \times 15\text{ cm}$. For the campaign in 2017 a $1\text{ cm} \times 1\text{ cm}$ LYSO-scintillator coupled to PMT was added. For the ALOFT campaign, the UIB-BGO will be upgraded with two new sensors to improve energy and timing resolution and increase the range of fluxes the instrument can see; this will make a total of four gamma-ray detectors. [10]

The two new sensors will both consist of LYSO-scintillators coupled to SiPM. One will be $5\text{ cm} \times 5\text{ cm}$ scintillator with a large SiPM. This will be useful both for energy resolution (because of the large and heavy scintillator) and timing resolution (because of the fast signal from both LYSO and SiPM). The other will be a $3\text{ mm} \times 3\text{ mm}$ scintillator with a small SiPM. This will only be useful for counting (timing resolution) because photons rarely deposit all their energy in small scintillators. Most will interact by Compton scattering, and the scattered photon will leave the crystal without depositing its energy, resulting in incomplete energy measurement.

The focus of this thesis will be characterizing the SiPMs alone and together with the LYSO. And designing the front-end electronics for the analog readout of the SiPM.

Other upgrades to the UIB-BGO instrument will, among other things, be faster ADCs, System on Chip (SoC) FPGA for the digital part of the readout (for the

2017-campaign an Automotive Windows computer was used for this) and real-time monitoring of data. The real-time monitoring will provide data every 1 s with count rate from the BGO; the data will be investigated on the ground to identify possible glows. If a glow is identified, feedback will be given to the pilot such that the plane can fly over the same region to characterize it better.

2.3 Expected Observations

The photon energy from both TGFs and glows is expected to be in the range 100 keV to several 10 MeV. Additionally, energetic electrons will likely be detected directly or as secondaries following electron interaction in the aircraft and surrounding material.

2.3.1 Expected Observations from TGFs

Figure 2.5 shows the fluence (the total number of counts per area) of photons for one TGF, this plot is from [11] and is simulated data.

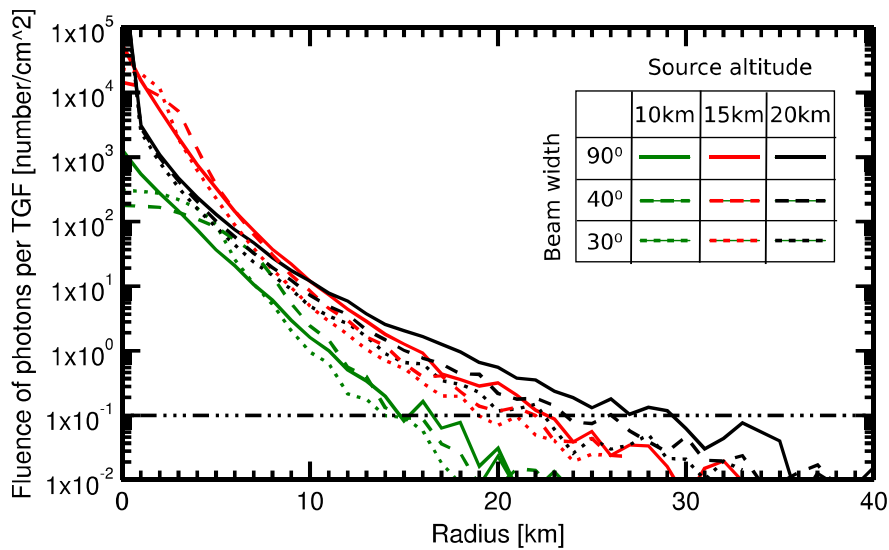


Figure 2.5: Fluence of photons for one TGF observed at 20 km altitude. For photons above 300 keV and 10^{17} initial number of photons. From [11].

From figure 2.5 the expected count rate can be estimated. Assuming the source altitude of 10 km, looking at the green line, the maximum fluence will be 1×10^3 counts/cm². Since the TGF lasts sub millisecond; 100 μ s is a good estimate, and the average flux (count per time per area) will be 10 Mcounts/cm²/s. Assuming at the smallest scintillator, with a size of 3 mm \times 3 mm \approx 1 cm², this gives an upper limit of the average count rate of 10 Mcounts/s (of course the larger detectors will be saturated at this point, but it doesn't matter because this smallest one can be used).

The fluence drops rapidly as the radius from the source increases (as seen in figure 2.5) and spans over several orders of magnitude; this motivates the use of

multiple detectors with different geometrical areas, each tailored to a specific flux range.

2.3.2 Expected Observations from Glows

The expected observations from background radiation and glows will also be useful to know; figure 2.6 shows observations of gamma rays from the flight campaign in 2017. The instrument used was a $15\text{ cm} \times 15\text{ cm} \times 3.2\text{ cm}$ BGOs coupled to PMTs, which will also be used in ALOFT and will be the largest scintillator, meaning the count rate of background and glows will be lower for the other detectors. Since glows have much lower fluxes than TGFs the BGO will be the most important for this case.

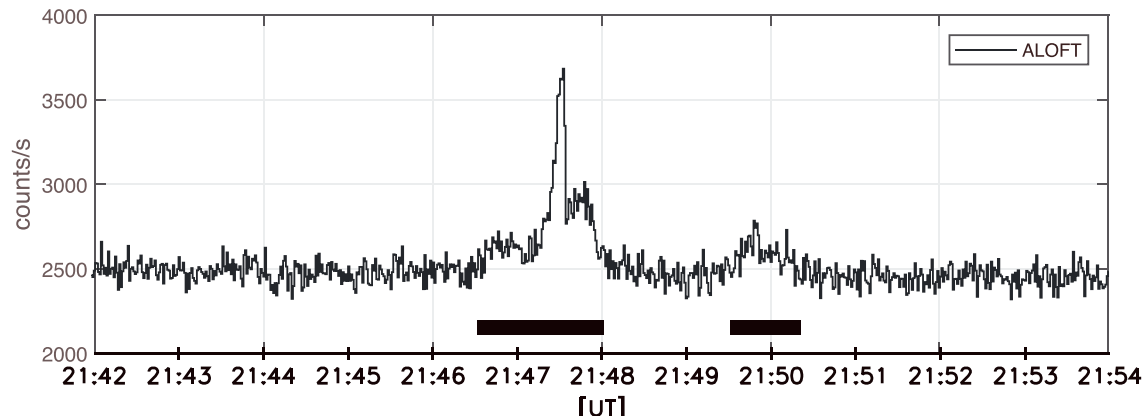


Figure 2.6: Observations of glows marked with a black horizontal line from the aircraft campaign in 2017. The glow is at around 3.5×10^3 counts/s and the background radiation is around 2×10^3 counts/s. From [10].

Silicon Photomultipliers

The SiPM is a well-established device that is, for example, used in time of flight positron emission tomography, distance measurement as LIDAR, and high-energy physics [12]. In this project related to this thesis, the SiPM will be used as a scintillation light sensor. PMTs are commonly used for this purpose, but some drawbacks to the PMT are its large size and sensitivity to magnetic fields.

Briefly explained the SiPM is an array of many Single-Photon Avalanche Diodes (SPADs) (a type of photodiode), and each SPAD has a size in the order of μm . The SPADs are also referred to as microcells and cells, or sometimes pixels. The latter will not be used for the SPAD in this thesis but will be used for one SiPM unit (consisting of thousands of microcells) that sits on a SiPM array with several of these. It is possible to read each SPAD individually in a digital fashion or as one analog signal where the amplitude corresponds to the sum of fired SPADs [13]. The latter is useful when only the number of fired SPADs is desirable to know, and exactly which SPADs that fired is not important.

3.1 Working Principle of SiPM

Figure 3.1 shows a basic photodiode, where a reverse bias voltage is applied and the signal is read out through an amplifier. An increasing reverse bias increases the size of the depletion region. In this region a scintillation photon (or a visible photon from a different source) can produce an electron-hole pair, these will drift towards the edges of the depletion region and induce a charge in the preamplifier that will give a pulse on the output. [14]

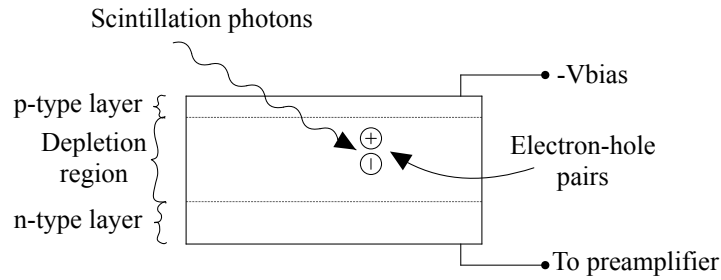


Figure 3.1: Common configuration of photodiode. Adopted from [14].

Electron-hole pairs are created similarly in an Avalanche PhotoDiode (APD), but the charge carriers accelerate and collide to create additional electron-hole pair, creating a larger signal than a photodiode [14]. In a Geiger-mode avalanche photodiode, also called as SPAD, one electron-hole pair will create a self-sustaining avalanche that has to be stopped externally.

Figure 3.2 shows the different working regimes of a pn-junction. At a lower operating voltage, it is a photodiode. At a bit higher voltage is the APD region, where the current in the pn-junction is amplified. At the highest voltage is the Geiger-mode avalanche region, where a self-sustaining avalanche will occur and continue forever if not stopped. The latter is the working mode of the SPAD in SiPMs.

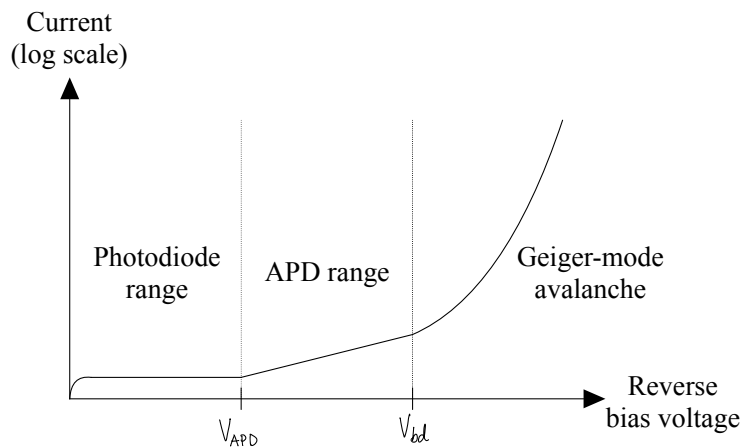


Figure 3.2: Operating modes of a pn-junction depending on the reverse bias voltage. The different modes are photodiode-mode, APD-mode, and Geiger-avalanche mode. Adopted from [12].

Figure 3.3 shows the cycle of the SPAD when triggered. It starts with the breakdown where the current increases rapidly, the SPAD is quenched where the current through the quenching resistor results in a dropped voltage over the pn-junction. Finally, the voltage resets when the current is lowered, and the SPAD is ready to be triggered again.

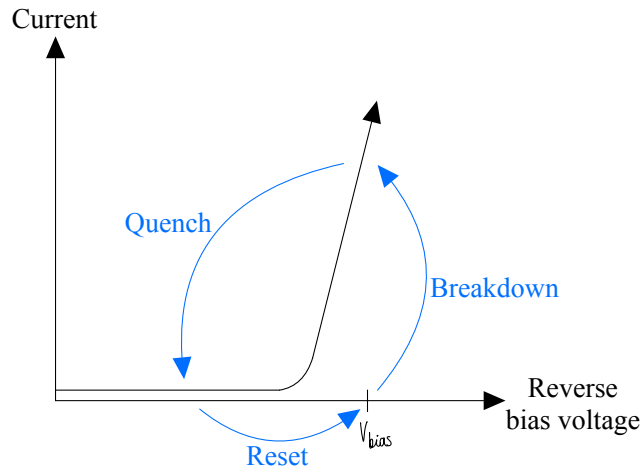


Figure 3.3: The cycle of the SPAD in SiPM when triggered, starting with breakdown where current increases rapidly, then the current is quenched by the quenching resistor and voltage drops, finally the voltage resets. Adopted from [15].

The SPADs can be laid out in an array so that if multiple photons are coming in, they are likely to hit different SPADs. If the SPADs are connected in parallel, each with a quenching resistor, they form an analog SiPM, shown in figure 3.4. The output will then be the sum of the current (or charge, to be precise) from each SPAD; this means that the amplitude of the output corresponds to the number of SPADs fired in the SiPM. Integrating the amplitude will give the total charge given by the SiPM, which is proportional to the number of SPADs fired. [12]

Figure 3.4 shows how each SPAD (shown with a photo diode symbol) is connected in the microcell, and how each microcell are connected inside the SiPM unit. Here the quenching resistors are connected to the anode of the SPAD, making a N-on-P structure, the SiPM can also have a P-on-N structure (if the quenching resistor is connected to the cathode of the SPAD). These two variants give the SiPM different properties. In the case for the SiPMs from onsemi the P-on-N structure SiPMs are sensitive to blue light, and the N-on-P structure SiPMs are sensitive to red light. Some SiPMs also has a fast output, the capacitively coupled output in figure 3.4, this output gives the derivative of the internal signal of the microcell. [15, 16]

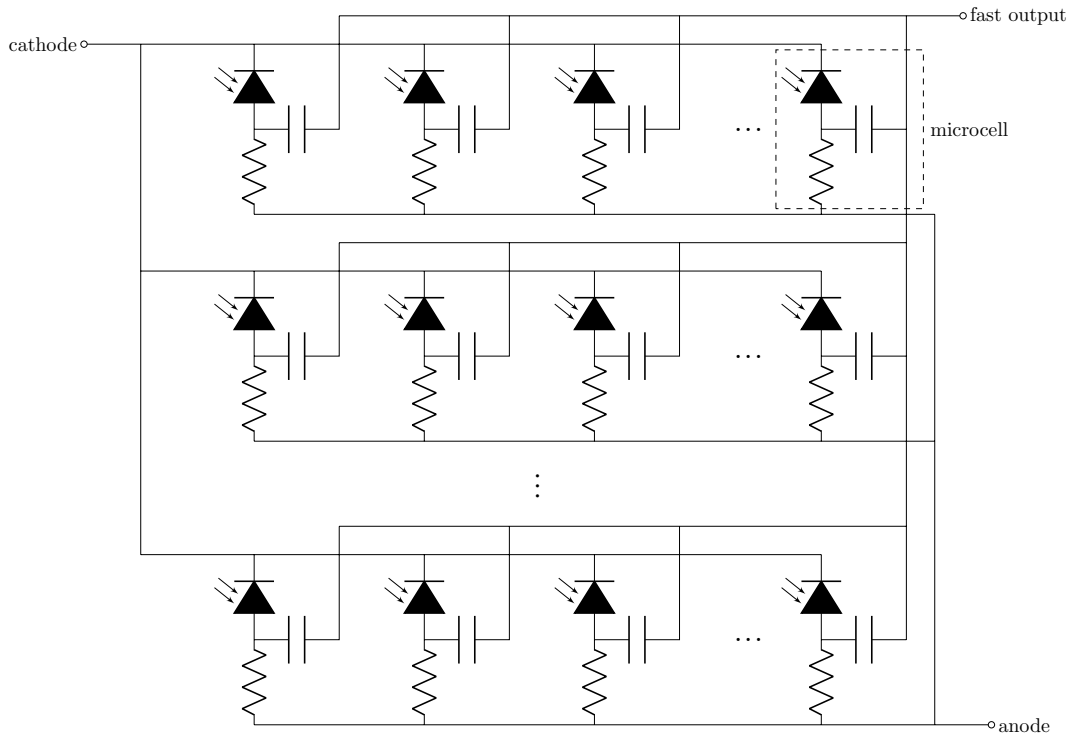


Figure 3.4: Equivalent circuit of the SiPM showing the microcells connected in parallel, each microcell consists of a SPAD (shown as a diode) and a quenching resistor, some SiPM also has a capacitors in each microcell to form a fast output. [12, 17, 15, 16]

Figure 3.5 shows a simpler symbol for the SiPM, and represents the entire SiPM unit, hence the same as figure 3.4.

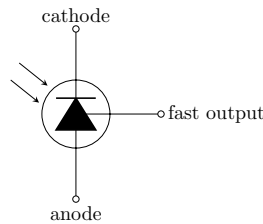


Figure 3.5: Symbol for one unit of SiPM (consisting of the whole circuit in figure 3.4) consisting of several microcells. One of these is referred to as one pixel in this thesis. Adopted from [16].

Larger SiPMs commonly consists of arrays of smaller SiPMs; these can have independent connections or have some common connections. In the case of the onsemi SiPMs the cathodes are shorted together to form a common cathode.

3.2 Characteristics of SiPM

The most important characteristics of the SiPM are gain, Photon Detection Efficiency (PDE), the number of microcells, microcell size, and the signal length. The

latter will be considered in section 3.3.2.

Gain is the number of charge carriers per fired microcell and is dependent on the overvoltage V_{ov} , as shown in equation (3.2). The overvoltage is the difference between the bias voltage V_{bias} and the breakdown voltage V_{bd} (equation (3.1)). C_d and C_q are capacitance in the SPAD and the quenching resistor. The charge of the signal (from one fired microcell) Q can be found by multiplying the gain with the elementary charge $q = 1.602 \times 10^{-19}$ C; this will give the area (time integral) of the pulse from the SiPM because . [13, 12]

$$V_{ov} = V_{bias} - V_{bd} \quad (3.1)$$

$$G = \frac{Q}{q} = \frac{V_{ov} \cdot (C_q + C_d)}{q} \Rightarrow Q = G \cdot q \quad (3.2)$$

PDE is the ratio of photoelectrons created in the detector to the number of photons arriving at the detector. The PDE is given in equation (3.3), where λ is the wavelength of the photon, QE is the quantum efficiency, P_T is the avalanche triggering probability and FF_{eff} is the effective geometrical probability. [13]

$$PDE(V_{ov}, \lambda) = QE(\lambda) \cdot P_T(V_{ov}, \lambda) \cdot FF_{eff}(V_{ov}, \lambda) \quad (3.3)$$

The number of fired cells N_{fired} is proportional to the number of photons hitting the SiPM $N_{ph,sipm}$ as long as the number of fired cells are small compared to the total number of microcells N_{total} . When this is not the case the number of fired cells are given by equation (3.4), PDE is the photon detection efficiency. [13]

$$N_{fired} = N_{total} \cdot \left(1 - \exp \left[-\frac{N_{ph,sipm} \cdot PDE}{N_{total}} \right] \right) \quad (3.4)$$

Then the total charge given by the SiPM will be given by equation (3.5).

$$Q_{total} = N_f Q \quad (3.5)$$

Equation (3.4) assumes that all photons arrive at the detector at the same time. If the light source has a larger decay time than the SiPM some cells may be able to trigger more than once during the light pulse, this makes the situation more complex, but may also increase the linear range [12].

The number of photons arriving at the SiPM $N_{ph,sipm}$ is dependent on the number of photons from the scintillator $N_{ph,scin}$ the area of the scintillator A_{scin} and the SiPM A_{sipm} , and how good the optical coupling is, where $c_{optical}$ is the optical coupling coefficient. The number of photons arriving at the SiPM is given in equation (3.6) depends on the optical coupling coefficient $c_{optical}$ and the relationship between the area of the scintillator A_{scin} and the area of the SiPM A_{sipm} . In the case where the scintillator is smaller than the SiPM, some microcells will never see the light from the scintillator and the effective number of microcells $N_{total,eff}$ is given in equation (3.7), in this case $N_{total,eff}$ should be used in equation (3.4) instead of N_{total} .

$$N_{ph,sipm} = \begin{cases} c_{optical} \frac{A_{sipm}}{A_{scin}} N_{ph,scin}, & \text{if } A_{sipm} < A_{scin} \\ c_{optical} N_{ph,scin}, & \text{if } A_{sipm} \geq A_{scin} \end{cases} \quad (3.6)$$

$$N_{total,eff} = \begin{cases} N_{total}, & \text{if } A_{sipm} \leq A_{scin} \\ \frac{A_{scin}}{A_{sipm}} N_{total}, & \text{if } A_{sipm} > A_{scin} \end{cases} \quad (3.7)$$

It is worth noting that the PDE for the peak wavelength will be an upper limit of the PDE even if the peak wavelength of the SiPM and the scintillator is the same. This is because the scintillator will also send photons outside the peak wavelength, which will have a slightly lower PDE in the SiPM.

The microcell size affects several of the SiPM properties. Smaller microcells give a larger density of microcells and a larger total number of microcells. The fill-factor is usually smaller for smaller microcell sizes because the wires between the microcells are the same width. The smaller size of the microcell also gives a lower diode capacitance, which again lowers the time constants associated with the microcell. When it comes to linearity, it really depends on the fluence of photons versus the density of microcells. This can be related to equation (3.4) by multiplying the fluence and microcell density with the area of the SiPM.

The primary noise sources in SiPM are dark current, crosstalk, and afterpulsing, the large detector capacitance may introduce noise in the front-end electronics, and the temperature dependence and non-linearity might give deviations in the signal.

Like any pn-junction, the SiPM has a leakage current, known as the **dark current**. The dark current is usually in the order of μA . Figure 4 in [18] shows that the dark current increases with bias voltage and temperature.

The **dark count rate** is the rate of SPADs/microcells spontaneously firing from a thermal electron. Because the signal is the same no matter what triggers the microcell, it is impossible to distinguish a dark count from a photon triggering the microcell. Figure 9 in [18] shows that also the dark count rate increases with temperature and bias voltage. The dark count rate is commonly given per area with units kHz/mm^2 , or for the whole device in MHz.

Crosstalk is when a microcell is triggered by a photon produced in an avalanche in the neighboring microcell and travels directly towards the triggered microcell. This happens very close to the primary event and is known as prompt or direct crosstalk. Delayed crosstalk is when a photon produced in the avalanche creates a free electron (or hole) outside the depletion region of the neighboring cell, this can slowly drift towards the multiplication region of the SPAD and trigger an avalanche. External cross talk may also happen; this is when a photon produced in an avalanche travels out of the SiPM and reflects the scintillator or protective layer, and the triggers the neighboring microcell. [12].

Afterpulsing is when the same microcell triggers after it has fired before it is fully recharged; consequently, this gives a lower pulse. This comes from charge carriers being trapped and released in the high-field region. [12]

SiPMs has large **detector capacitance**, this is not a noise source itself, but as discussed in chapter 4 the output noise from the preamplifier is very dependent on the terminal capacitance which includes the detector capacitance.

The breakdown voltage of the SiPM is **temperature dependent** [12, 18]. Consequently, the overvoltage, gain, and PDE vary with temperature for a constant bias voltage. If SiPM is used in an environment with large temperature variations, it may be necessary to adjust the bias voltage accordingly. A different approach is

keeping the temperature constant and optionally monitoring the temperature. This will be further discussed in section 3.6.

The SiPM has a non-linear output when the fluence of photons is high; this is because two photons may trigger the same microcell, but it is impossible to measure how many photons triggered the microcell. This is quantized in equation (3.4), and will be investigated further in section 3.5.

3.3 Electrical Equivalent Model and Signal Shape of SiPM

3.3.1 Equivalent Model

An electrical equivalent model for the SiPM is obtained from [19, 20, 21], and is shown in figure 3.6. In this model, R_q is the quenching resistor, with a parasitic capacitance C_q , C_d is the diode capacitance, and C_g is the capacitance from the metal grid used for routing. N is the total number of microcells, and R_s is the load resistance. The components on the left side represent the firing microcell where I_{av} can be represented by a Dirac delta pulse with total charge Q_{total} ($I_{av} = Q\delta(t)$), Q_{total} is the total charge given by one microcell. If more than one microcell is firing, I_{av} can be modeled as several Dirac delta pulses distributed over time. The components in the middle represent the microcells that are not firing. [19]

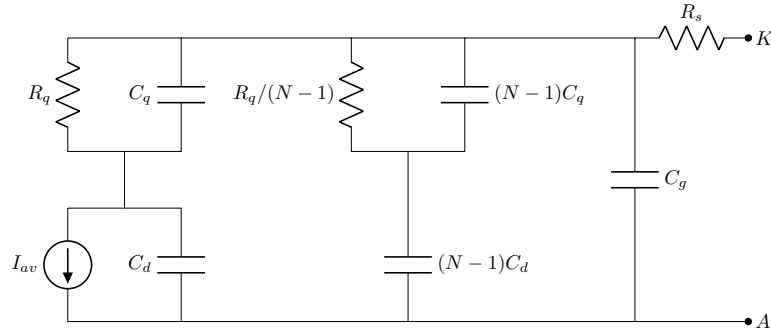


Figure 3.6: Electrical equivalent model of SiPM [19, 20, 21]

The model in figure 3.6 was simulated using and the same values used in [19] for the SiPM ITC-irst ([19] also explains how these parameters can be extracted). The schematic from this simulation is shown in figure 3.7 and 3.8. This simulation results were plotted in figure 3.9.

Simulation was performed to determine how one unit of SiPM works and how several pixels in a SiPM array work when connected together. To the left in figure 3.8 is the model of one unit. In the middle are four units read out through a common series resistor, and to the right are four units read out by separate resistors, and the current is summed at the end. The total current out of each configuration is plotted in figure 3.9.

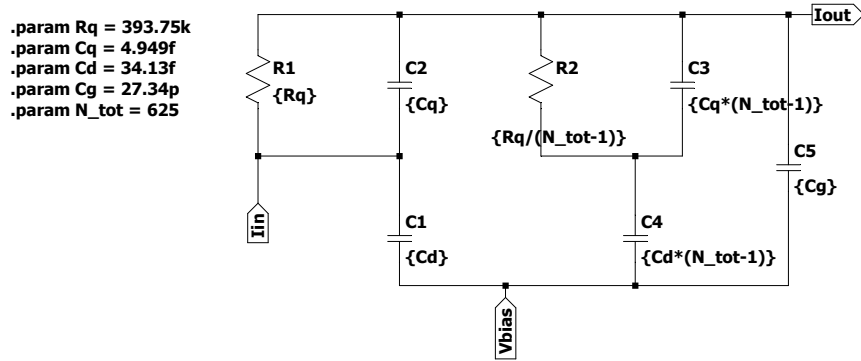


Figure 3.7: Schematic for the SiPM model that was simulated.

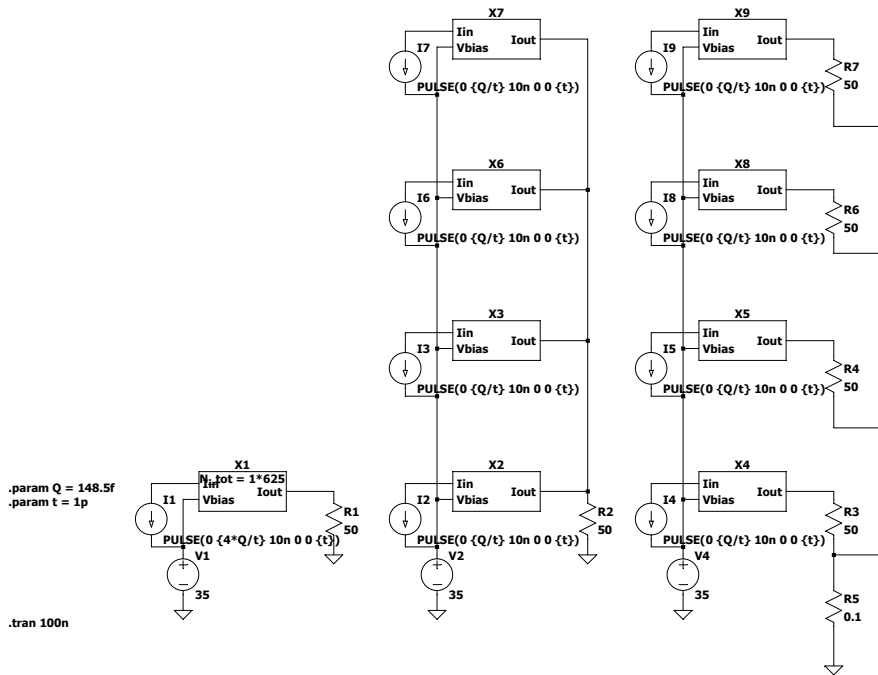


Figure 3.8: Schematic used in simulation where several pixels (from figure 3.7) are connected together to model a SiPM array.

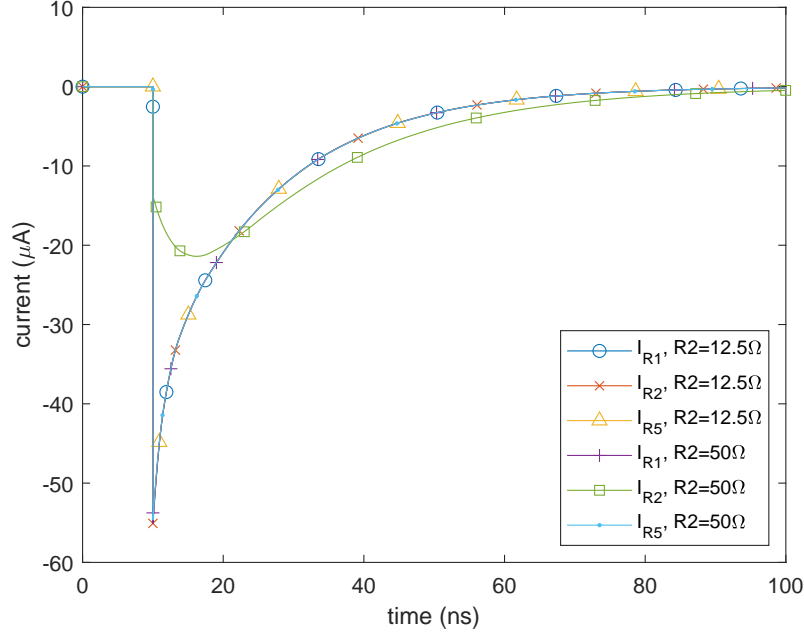


Figure 3.9: Results from the SiPM equivalent model simulations with the schematic in figure 3.7 and 3.8.

What can be concluded from figure 3.9 is that the signal is the same for the single unit with $50\ \Omega$ resistor, the four pixels with separate $50\ \Omega$ resistors, and the four pixels with a common $12.5\ \Omega$ (equal to $50/4\ \Omega$) resistor. But longer for the four pixels with a common $50\ \Omega$ resistor. This result fits well with the time constant given in equation (3.9) or equation (3.12).

3.3.2 Signal Shape

The pulse shape of SiPM is usually given by a quench time and two decay constants, a fast time constant, and a recovery time constant [22, 19]. The quench time constant, the fast decay time constant and the recovery time constant are given by equations (3.8), (3.9) and (3.10) (found in [19], where it was based on a simplified version of the model in figure 3.6). C_{eq} represents the series connection of C_q and C_d in the cells that are not firing, which gives equation (3.11).

$$\tau_{quench} = R_q \cdot C_q \quad (3.8)$$

$$\tau_{input} = R_s \cdot (C_{eq} + C_g) \quad (3.9)$$

$$\tau_{recovery} = R_q \cdot (C_d + C_q) \quad (3.10)$$

$$C_{eq} = (N_{total} - 1) \cdot \left(\frac{1}{C_d} + \frac{1}{C_q} \right)^{-1} \quad (3.11)$$

onsemi [15] combines these into one recovery time constant, given in equation (3.12).

$$\tau_{recovery} = C_d (R_q + R_s \cdot N_{total}) \quad (3.12)$$

[19] also gives an approximation of the voltage across the load resistor R_s given in equation (3.13).

$$V_{in}(t) \cong \frac{Q_{total}R_s}{\tau_{recovery} - \tau_{input}} \left(\frac{\tau_{quench} - \tau_{input}}{\tau_{input}} \exp\left(-\frac{t}{\tau_{input}}\right) + \frac{\tau_{recovery} - \tau_{quench}}{\tau_{recovery}} \exp\left(-\frac{t}{\tau_{recovery}}\right) \right) \quad (3.13)$$

$$V_{in}(t) \cong Q_{total}R_s \frac{(1 + s\tau_{quench})}{(1 + s\tau_{input})(1 + s\tau_{recovery})} \quad (3.14)$$

Equation (3.13) and (3.14) do not include rise time. However, a rise time is usually given in the data sheet, and the recovery time is also usually given, but not the other time constants.

Assuming that τ_{quench} and τ_{input} is much smaller than $\tau_{recovery}$ and looking at the current I_{in} through the load resistor gives equation (3.15). Taking the Laplace transform of this gives the frequency content of the signal, given in equation (3.16). Here $\tau_{recovery}$ is replaced with the more general τ_{sipm} that will make it easier to distinguish the time constants in the different parts of the system from each other.

$$I_{in}(t) = \frac{Q_{total}}{\tau_{sipm}} e^{-t/\tau_{sipm}} \quad (3.15)$$

$$I_{in}(s) = \frac{Q_{total}}{1 + s\tau_{sipm}} \quad (3.16)$$

	onsemi J-series SiPM		
	Minimum	Typical	Maximum
Breakdown voltage (V)	24.2		24.7
Temperature dependence of breakdown voltage (mV/°C)		21.5	
Overvoltage (V)	1		6
Operating voltage (V)	25.2		30.7
Peak PDE wavelength (nm)		420	

Table 3.1: Parameters for SiPM used (onsemi J-Series SiPM Sensors), from data sheet [23].

	onsemi J-series SiPM					
	30020		30035		60035	
Active area (mm ²)	3.07 × 3.07		3.07 × 3.07		6.07 × 6.07	
Microcell size (μm)	20		35		35	
Number of microcells	14410		5676		22292	
Overvoltage (V)	+2.5	+5	+2.5	+6	+2.5	+6
PDE (%)	30	38	38	50	38	50
Gain (×10 ⁶)	1.0	1.9	2.9	6.3	2.9	6.3
Dark count rate (kHz/mm ²)	50	125	50	150	50	150
Dark current - typical (μA)	0.1	0.45	0.23	1.9	0.9	7.5
Dark current - maximum (μA)	0.2	0.72	0.31	3.00	1.25	12.0
Crosstalk (%)	2.5	7.5	8	25	8	25
Afterpulsing (%)	0.75	5.0	0.75	5.0	0.75	5.0
Rise time (from 10% to 90%) (ps)	130	160	90	110	180	250
Microcell recharge time constant (ns)	15		45		50	
Fast output pulse width (FWHM) (ns)	15		45		50	
Capacitance (anode output) (pF)	1040		1070		4140	
Capacitance (fast output) (pF)	50		40		160	

Table 3.2: Parameters for SiPM used (onsemi J-Series SiPM Sensors), from data sheet [23]. 30020 is the 3.07 mm × 3.07 mm SiPM with 20 μm microcell size, 30035 is the 3.07 mm × 3.07 mm SiPM with 35 μm microcell size, and 60035 is the 6.07 mm × 6.07 mm SiPM with 35 μm microcell size.

Figure 3.10 shows expected signals from one triggered microcell in the SiPM, for various versions of the J-series SiPMs from onsemi. This is calculated using equation (3.15), values from table 3.1 and 3.2 and equation 3.2 to calculate the charge Q from the gain G .

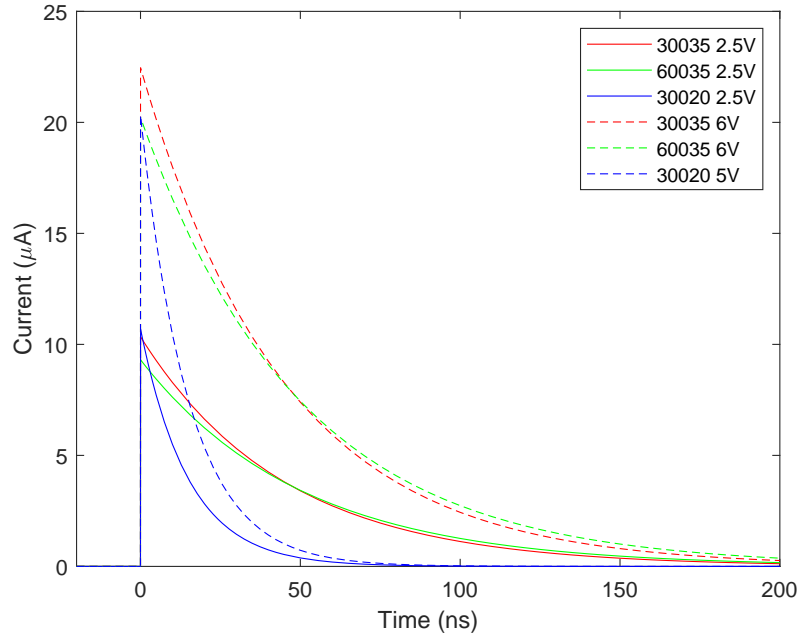


Figure 3.10: Calculated signal from one triggered cell in the SiPM for three variants and different bias voltages.

3.4 SiPMs as Scintillation Light Detectors

3.4.1 Working Principles of Scintillators

This section is based on [14].

Figure 3.11 shows the discrete energy bands in an insulator or a semiconductor. In the valence band, electrons are bound to the lattice sites, and in the conduction band, electrons are free to move around in the crystal because of their higher energy. An electron can move from the valence band to the conduction band if it absorbs energy, energies between the bands are considered forbidden. A photon is emitted when an electron moves from a higher to a lower energy state. In a pure crystal, the electron must return to the valence band from the conduction band, this results in photons way past the visible range.

Small impurities are added to the inorganic scintillator to increase the probability of photons in the visible range; this results in the activator states inside the band gap, shown in figure 3.11. This gives more energy states and less energy between each state, resulting in more photons in the visible range. Therefore, the peak wavelength will be somewhere in the visible range with a spectrum around (depending on the scintillator's material).

A charged particle moving through the detector will result in electron-hole pairs and excited electrons, and emitted photons when de-excited.

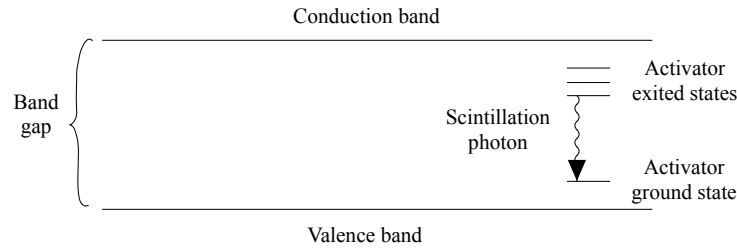


Figure 3.11: Discrete energy bands in insulators or semiconductors. Adopted from [14].

The three significant ways photons interact with matter in gamma-ray spectroscopy are photoelectric absorption, Compton scattering, and pair production. Knowing what they are is key to understanding the scintillator detector's energy spectrum.

A diagram of **photoelectric absorption** is shown in figure 3.12. All the energy of the gamma-ray $h\nu$ is absorbed by an electron, the electron will then get a kinetic energy $E_{e^-} = h\nu - E_b$, where E_b is the binding energy of the electron in the atom.

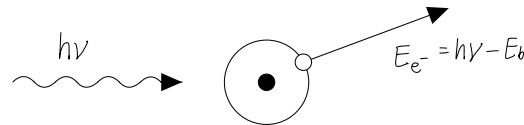


Figure 3.12: Diagram of photoelectric absorption, showing how the gamma-ray interacts with the electron in the atom. Adopted from [14].

Compton scattering is when a gamma-ray collides with an electron and both are present after the collision. As shown in figure 3.13 the electron gets kinetic energy from the gamma-ray, and the gamma-ray gets a lower energy $h\nu'$ and changes direction.



Figure 3.13: Diagram of compton scattering interaction between gamma-ray and electron. Adopted from [14].

The energy of the electron and gamma-ray after the collision is dependent on the scattering angle θ shown in figure 3.13b, and will give a continuous energy spectrum between $\theta = 0$ and π

Pair production is when a gamma-ray turns into one electron and one positron; this may happen in the strong electric field near the nuclei in the detector material. For this to happen, the energy of the gamma-ray $h\nu$ must be larger than the rest mass energy of both the electron and positron $2m_0c^2$; if there is energy left, this will go to kinetic energy of the electron E_{e^-} and positron E_{p^+} , which gives $E_{e^-} + E_{p^+} = h\nu - 2m_0c^2$. The positron is not stable and will eventually meet an electron and annihilate into two gamma-rays.

Figure 3.14 shows the energy spectrum for different sized scintillator detectors for high energies ($h\nu \gg 2m_0c^2$ where $h\nu$ is the energy of the photon and $2m_0c^2$ is the rest mass energy of one electron and one positron). The energy spectrum looks similar for small energies ($h\nu < 2m_0c^2$), but without the single and double escape peaks and, of course, the full-energy peak and Compton edge at lower energy. To the left is the extreme case of a small detector, to the right is the extreme case of a large detector, and in the middle is an intermediate-size detector.

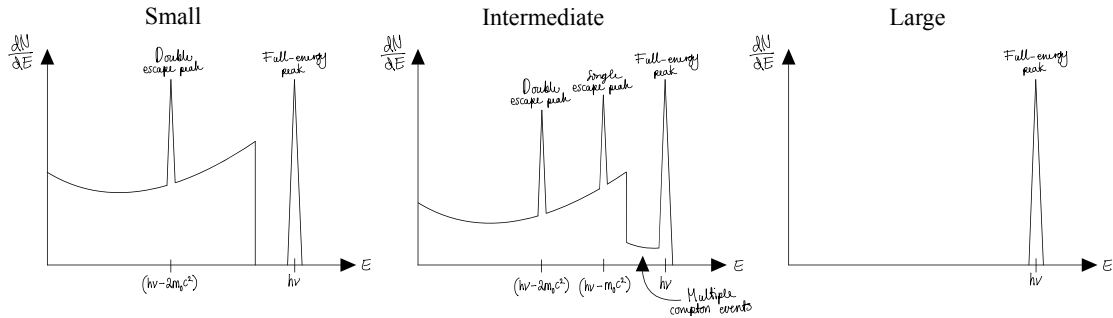


Figure 3.14: Energy spectrum for different sized scintillator detectors, for high energy photons. The left plot is for a small detector, the right is for a very large detector, and the middle is for intermediate sized detector. Adopted from [14].

For a very large detector (shown to the right in figure 3.14), the total energy of the incoming photon will be absorbed. It can be absorbed through photoelectric absorption, pair production, Compton scattering, or a sequence of the mentioned interactions; the point is that the detector is large, and none of the photon's energy manages to escape before it is absorbed again.

For the small detector (shown to the left in figure 3.14), the energy may be absorbed through one photoelectric absorption, Compton scattering, or pair production. The scattered gamma-ray from Compton scattering or both the annihilated photons from pair production will escape the detector, resulting in a sharp Compton edge and a distinct double escape peak at $h\nu - 2m_0c^2$. Note that the double escape peak is only for high-energy gamma rays.

In the intermediate sized detector (shown in the middle of figure 3.14), the gamma-ray can interact in the same ways as in the small and large detector. However, it may interact several times before all the energy is absorbed-or some of the energy escapes after Compton scattering or pair production. Since there may be several Compton events, there will be some absorbed energies between the Compton edge and the full-energy peak. Also, one of the annihilated photons from pair production may escape, resulting in a single escape peak in addition to the double

escape peak. Note that the single and double escape peak is only for high-energy gamma rays.

3.4.2 Signal from Scintillator

The Probability Density Function (PDF) $p_{t_e}(t|\Theta)$ for photons being emitted by a scintillator after some time t after the arrival of a γ -photon at time Θ is given by equation (3.17). $\tau_{tran,i}$ and $\tau_{emis,i}$ are time constant for energy transfer and emission, this occurs with a probability $P_{ec,i}$. The pulse shape from the scintillator equals the PDF, except for a normalization factor. [24]

$$p_{t_e}(t|\Theta) = \begin{cases} 0 & \forall t : (t < \Theta) \\ \sum_i P_{ec,i} \frac{1}{\tau_{emis,i} - \tau_{tran,i}} \times \left[e^{-\frac{t-\Theta}{\tau_{emis,i}}} - e^{-\frac{t-\Theta}{\tau_{tran,i}}} \right] & \forall t : (t \geq \Theta) \end{cases} \quad (3.17)$$

Now the pulse shape of a single photon in a scintillator arriving at time $\Theta = 0$ can be expressed by equation (3.18), here τ_{tran} is the rise time constant of the pulse, and τ_{emis} is the decay time constant. The area of the pulse must be equal to the total number of photons given by the scintillator $N_{ph,scin}$, and since the area of a PDF is 1 the value can just be multiplied in. This signal can be written in the frequency domain by taking the Laplace transform of equation (3.18), this gives equation (3.19)

$$I_{scin}(t) = \frac{N_{ph,scin}}{\tau_{emis} - \tau_{tran}} \left[e^{-t/\tau_{emis}} - e^{-t/\tau_{tran}} \right] \quad (3.18)$$

$$I_{scin}(s) = \frac{N_{ph,scin}}{(1 + s\tau_{emis})(1 + s\tau_{tran})} \quad (3.19)$$

By assuming that one of the time constants τ_{emis} or τ_{tran} is much larger than the other, equation (3.18) and (3.19) can be approximated to a first order system, this gives equation (3.20) and equation (3.21). Here τ_{scin} is equal to the largest of τ_{emis} and τ_{tran} , and will be the decay time constant.

$$I_{scin}(t) = \frac{N_{ph,scin}}{\tau_{scin}} e^{-t/\tau_{emis}} \quad (3.20)$$

$$I_{scin}(s) = \frac{N_{ph,scin}}{(1 + s\tau_{scin})} \quad (3.21)$$

The total number of photons given by a scintillator $N_{ph,scin}$ is given in equation (3.22), where Y is the photon yield and E_γ is the energy of the incoming photon.

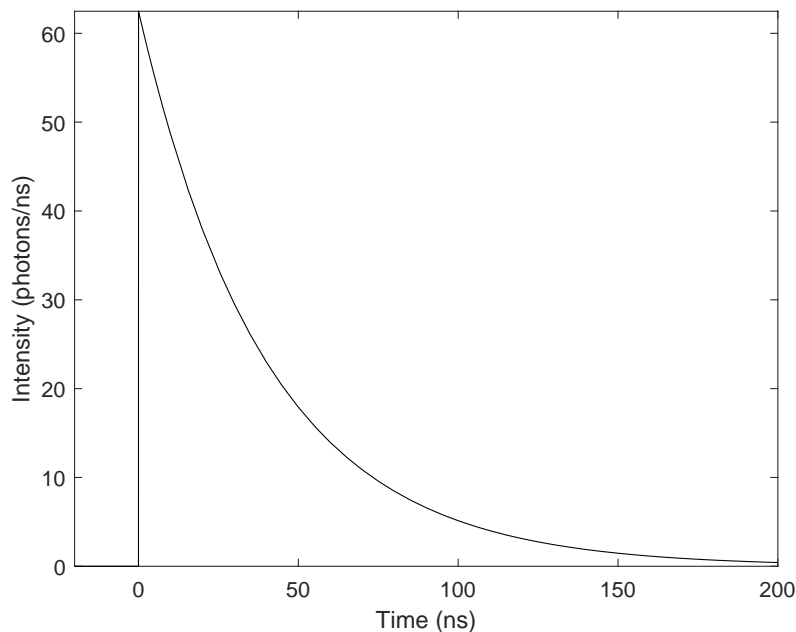
$$N_{ph,scin} = Y \cdot E_\gamma \quad (3.22)$$

The scintillator to be used is only given with a decay time constant; therefore (3.20) and (3.21) will be suitable to use. The light yield (Y) and decay time constant (τ_{scin}) for the scintillator to be used are given in table 3.3, and are obtain from [25].

Parameter	Value	Unit
τ_{scin}	40	ns
Y	25	photons/keV

Table 3.3: Parameters for LYSO scintillator used.

Plotting equation (3.20) combined with equation (3.22) for $E_\gamma = 100 \text{ keV}$ and values from table 3.3 is shown in figure 3.15. This is the expected light output from the scintillator.

Figure 3.15: Expected signal from LYSO scintillator (100 keV γ -photon), calculated with equation (3.20) and (3.22).

The LYSO-scintillator contains a radioactive isotope ^{126}Lu ; this results in self-counts. ^{126}Lu which is a beta emitter; which decays in to gamma-rays of 88 keV, 202 keV, and 307 keV. This will give peak in the energy spectrum at 88 keV, (88 keV + 202 keV), (88 keV + 307 keV), and (88 keV + 202 keV + 307 keV). This activity gives a total rate of 39 counts/s/g, and the density of LYSO is 7.1 g/cm^3 . [26]

Which of the peaks in the energy spectrum dominates is dependent on the size of the scintillator; see, for example, [27].

3.4.3 Signal from SiPM Coupled to Scintillator

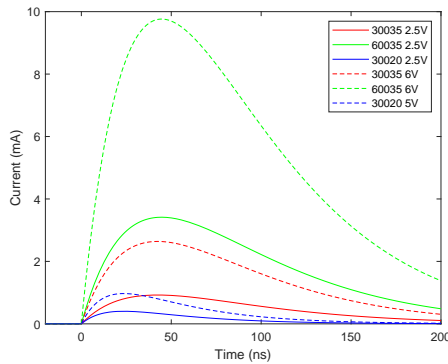
Combining equations (3.21) and (3.16) will give the total signal shape when the scintillator and the SiPM are connected together. Here the area of the pulse must be the total charge given by the SiPM, which is equal to the charge from one microcell Q times the number of fired cells N_{fired} (given in equation (3.4)), this

gives equation (3.23), the inverse Laplace transform of this gives the signal shape in the time domain (equation (3.24)).

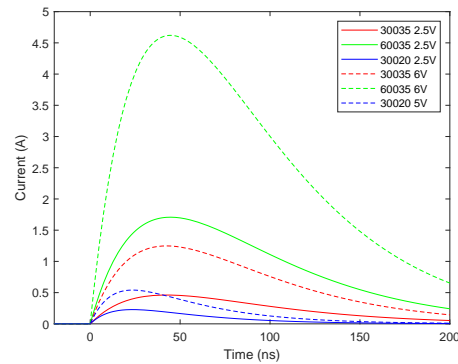
$$I(s) = \frac{QN_{fired}}{(1 + s\tau_{sipm})(1 + s\tau_{scin})} \quad (3.23)$$

$$I(t) = \frac{QN_{fired}}{\tau_{sipm} - \tau_{scin}} (e^{-t/\tau_{sipm}} - e^{-t/\tau_{scin}}) \quad (3.24)$$

The figures 3.16 and 3.17 are plotted using equation (3.24), N_{fired} was found using equation (3.4), (3.6) and (3.22). The optical coupling coefficient used is $c_{optical} = 1$ and it is assumed that all of the photon energy is seen by the scintillator (which both are upper limits). The rest of the values are from table 3.3, 3.1 and 3.2. For figure 3.16a and 3.17a the gamma photon energy was $E_\gamma = 100$ keV, and for figure 3.16b and 3.17b the gamma photon energy was $E_\gamma = 60$ MeV. The difference between figure 3.16 and 3.17 are the size of the scintillator and if the SiPM is a single unit or an array of 8×8 SiPMs. In figure 3.16 the scintillator was $50 \text{ mm} \times 50 \text{ mm} \times 50 \text{ mm}$ and the SiPM was an array of 8×8 SiPMs. In figure 3.17 the scintillator was $3 \text{ mm} \times 3 \text{ mm} \times 10 \text{ mm}$, with the $3 \text{ mm} \times 3 \text{ mm}$ coupled to the SiPM, and the SiPM was a single unit. In both figure 3.16 and 3.17 the expected signal is shown at two different overvoltage: solid line $V_{ov} = 2.5 \text{ V}$, and dashed line $V_{ov} = 6 \text{ V}$ or $V_{ov} = 5 \text{ V}$.



(a) 100 keV photon energy.



(b) 60 MeV photon energy.

Figure 3.16: Calculated signal (using equation (3.24)) from 8×8 SiPM array coupled to $50 \text{ mm} \times 50 \text{ mm} \times 50 \text{ mm}$ LYSO-scintillator.

Figure 3.16a shows signal from the lowest gamma-photon energy that is required to detect. Figure 3.16b shows the maximum signal that should be detected. These may be lower because of the optical coupling or larger time constant. In addition, the overvoltage can be adjusted to get a lower or higher signal. For the array consisting of $3 \text{ mm} \times 3 \text{ mm}$ SiPMs with $35 \mu\text{m}$ microcell (marked as 30035 in the plots) the highest signal will be a bit above 1 A (reading of figure 3.16a). If the overvoltage is slightly lowered, the highest signal will be at 1 A, and this value will be used as a requirement when choosing the preamplifier later.

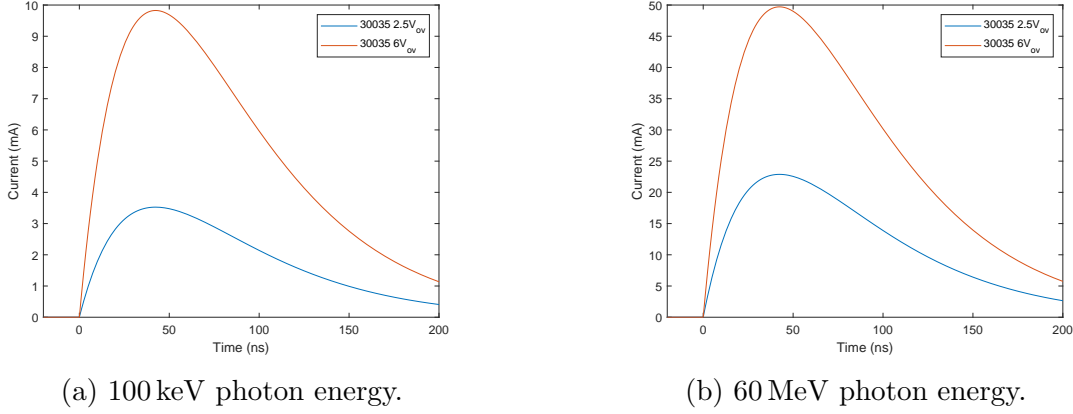


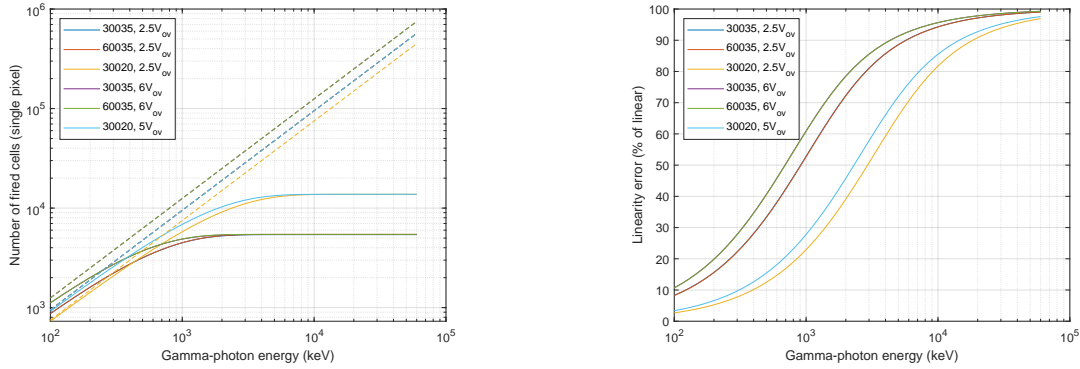
Figure 3.17: Calculated signal (using equation (3.24)) from single SiPM unit coupled to a $3 \text{ mm} \times 3 \text{ mm} \times 10 \text{ mm}$ LYSO-scintillator.

Figure 3.17a and 3.17b show the lowest and highest signal from the small scintillator and SiPM. The lowest value may be lower due to optical coupling or larger time constants. When it comes to the highest value, the SiPM is saturated long before 60 MeV and will stay the same but be proportional to the overvoltage.

3.5 Linearity of SiPM

Figure 3.18a shows the linearity of the small $3 \text{ mm} \times 3 \text{ mm} \times 10 \text{ mm}$ LYSO-scintillator, with area $A_{scin} = 3 \text{ mm} \times 3 \text{ mm}$, coupled to different single SiPMs ($3.07 \text{ mm} \times 3.07 \text{ mm}$ total area A_{sipm} with $35 \mu\text{m}$ microcells, $6.07 \text{ mm} \times 6.07 \text{ mm}$ total area A_{sipm} with $35 \mu\text{m}$ microcells, and $3.07 \text{ mm} \times 3.07 \text{ mm}$ total area A_{sipm} with $20 \mu\text{m}$ microcells), at two different overvoltages. The linear approximation (dashed line) is calculated using $N_{linear} = N_{ph,scin} \cdot PDE$, while the number of fired cells N_{fired} (solid line) is plotted using equation (3.4). Equation (3.6), (3.7) and (3.22) is used to calculate the parameters in this equation, the rest of the values needed are from table 3.1, 3.2, and 3.3. Figure 3.18b shown the error due to non-linearity N_{error} and is plotted using equation (3.25) and the results calculated for figure 3.18a.

$$N_{error}[\%] = \frac{N_{fired} - N_{linear}}{N_{linear}} \cdot 100\% \quad (3.25)$$



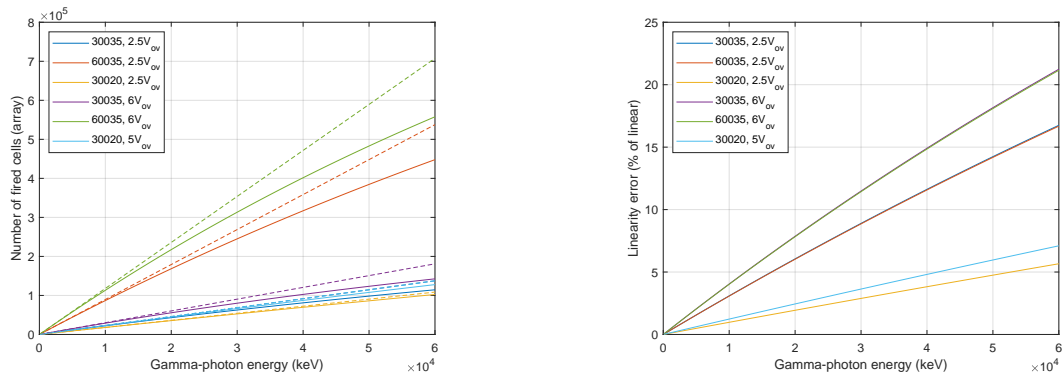
(a) Number of fired cells from SiPM using equation (3.4) (solid line) and the linear approximation (dashed line) for small scintillator and SiPM.

(b) Error due to non-linearity as percent of linear approximation for small scintillator and SiPM (note that green and red lays on top of blue and purple line).

Figure 3.18: Linearity for small scintillator and SiPM depending on absorbed gamma-photon energy in the scintillator.

Figure 3.18 shows that the linearity of the small scintillator and SiPM is not good, and for the largest gamma-photon energies it would not be possible to distinguish the values, because all the microcells will fire. But since this sensor will only be used for counting (and the energy of the gamma-photon is not important), and because the small scintillator will rarely absorb all the energy from the incoming gamma-photon (because this detector will be more towards the extreme small case to the left in figure 3.14), this non-linearity will be fine for this sensor.

Figure 3.19 is plotted in the same way as figure 3.18, but the scintillator is larger with a size $5\text{ cm} \times 5\text{ cm} \times 5\text{ cm}$, and the SiPM is an 8×8 array of the SiPM used in figure 3.18, making the area of the scintillator and the total number of microcells 64 times larger.



(a) Number of fired cells from SiPM using equation (3.4) (solid line) and the linear approximation (dashed line) for large scintillator and SiPM.

(b) Error due to non-linearity as percent of linear approximation for large scintillator and SiPM (note that green and red lays on top of blue and purple line).

Figure 3.19: Linearity for large scintillator and SiPM depending on absorbed gamma-photon energy in the scintillator.

Figure 3.19b shows that the linearity error may be up to around 20%. Lowering the overvoltage lowers the linearity error due to lower PDE. The linearity may also improve for the real detector due to the optical coupling coefficient being lower than 1 that was used in these calculations. Looking at figure 3.19a, the number of fired cells still grows at large gamma-photon energies, and these can be distinguished from each other. This means that the inverse of equation (3.4) can be used to calculate the number of photons arriving at the SiPM $N_{ph,sipm}$, and it is possible to correct for the non-linearity.

Figure 3.20 shows that the same as figure 3.19a, but the number of fired cells is shown for both all the 64 pixels and for one of the pixels alone, also the axes are logarithmic. This means that the linearity of the complete SiPM is the same as one of the pixels alone.

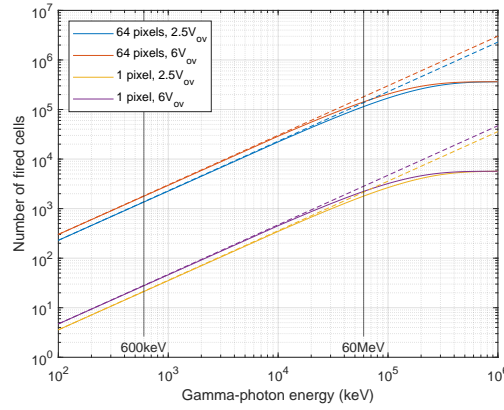


Figure 3.20: Linearity for large scintillator and SiPM, shown for all 64 pixels and 1 of the 64 pixels. The solid line is the number of fired cells, and the dashed line is the linear approximation.

3.6 Temperature Sensitivity of SiPM

The SiPM has some dependence on temperature, mainly due to the reverse breakdown voltage being temperature dependent, which then affects the overvoltage if the bias voltage is kept constant (equation (3.1)). Further, the gain and the PDE is dependent on the overvoltage. An approximation of the breakdown voltage is given in equation (3.26) (from [18])

$$V_{br}(T) = V_{br0} [1 + \beta (T - T_0)] \quad (3.26)$$

where T_0 is room temperature, V_{br0} is the breakdown voltage at temperature T_0 and β is the linear growth constant, and T is the temperature. In the data sheet for MICROFJ-SMTPA-30035-GEVB from onsemi [23] the breakdown voltage is minimum 24.2V and maximum 24.7V at 21°C and the temperature dependency of the breakdown voltage is 21.5mV/°C at 21°C. Rewriting equation (3.26) gives $V_{br} = V_{br0} + (V_{br0} \cdot \beta)(T - T_0)$, then the values will be $T_0 = 21^\circ\text{C}$, $V_{br0} = 24.45\text{V}$ (when using the average of minimum and maximum), and $(V_{br0} \cdot \beta) = 21.5\text{mV}/^\circ\text{C} \Rightarrow \beta \approx 0.8794 \times 10^{-3} \text{ }^\circ\text{C}^{-1}$, also shown in table 3.4.

Variable	Value	Unit
T_0	21	$^{\circ}\text{C}$
V_{br0}	24.45	V
β	$0.8794 \cdot 10^{-3}$	$^{\circ}\text{C}^{-1}$

Table 3.4: SiPM breakdown voltage parameters.

Figure 3.21 shows how the change in temperature affects the overvoltage. This is calculated using equation (3.26) and equation (3.1), using the parameters in table 3.4 and subtraction the mean temperature and overvoltage.

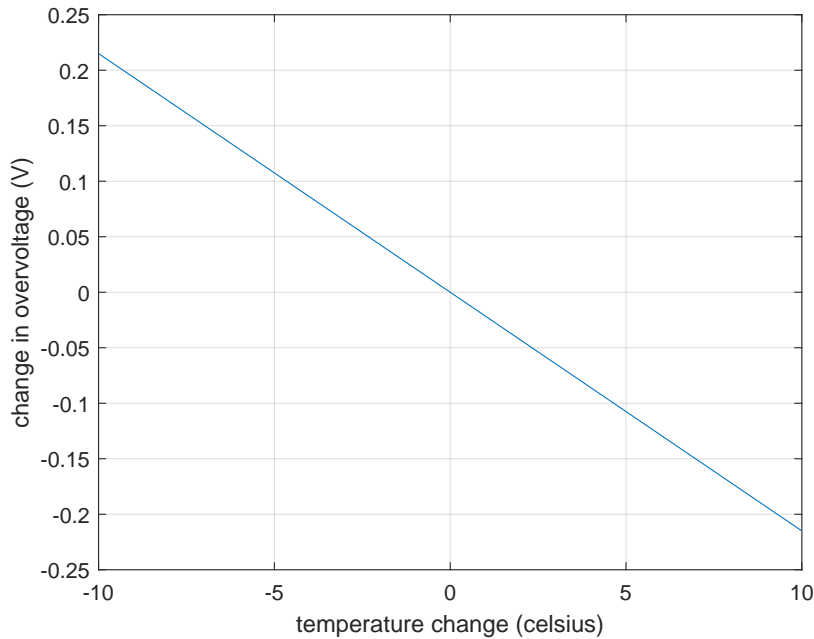


Figure 3.21: Change in overvoltage for temperature change, when bias voltage is kept constant

The overvoltage recommended in the data sheet [23] is from 1 V to 6 V. Furthermore, reading from figure 3.21 a few degrees of temperature change will change the overvoltage slightly, and there is a need to figure out how much this affects the final signal. However, delimiting the mean overvoltage to 1.25 V to 5.75 V the SiPM will be within the operating range, even if the temperature changes with 10°C .

Reading of the graph in figure 2 in the data sheet [23] the PDE can be approximated to a linear equation, which gives equation (3.27). The same can be done for the gain, reading of the graph in figure 4 in the data sheet [23], this gives equation (3.28).

$$PDE(V_{ov}) = 30\% + 3.5\%/V \cdot V_{ov} \quad (3.27)$$

$$G(V_{ov}) = 4.7143 \times 10^5 + 9.7143 \times 10^5 \text{ V}^{-1} \cdot V_{ov} \quad (3.28)$$

Figure 3.22 shows the deviation in the total output charge as percent of the mean total output charge, this deviation in percent will be the same as the deviation in

signal height, because the total charge and signal height are proportional. The total charge is given by $Q_{total} = Q \cdot N_{fired}$, Q is calculated with equation 3.2 with gain G from equation (3.28). Overvoltage is calculated using equation (3.1) and (3.26). N_{fired} is calculated the same way as for figure 3.19a, using PDE from equation (3.27) at two different gamma-ray energies: 100 keV (solid line) and 60 MeV (dashed line). Finally the deviation is calculated using equation (3.29).

$$Q_{total,error}[\%] = \frac{Q_{total}}{Q_{total,mean}} \cdot 100\% - 100\% \quad (3.29)$$

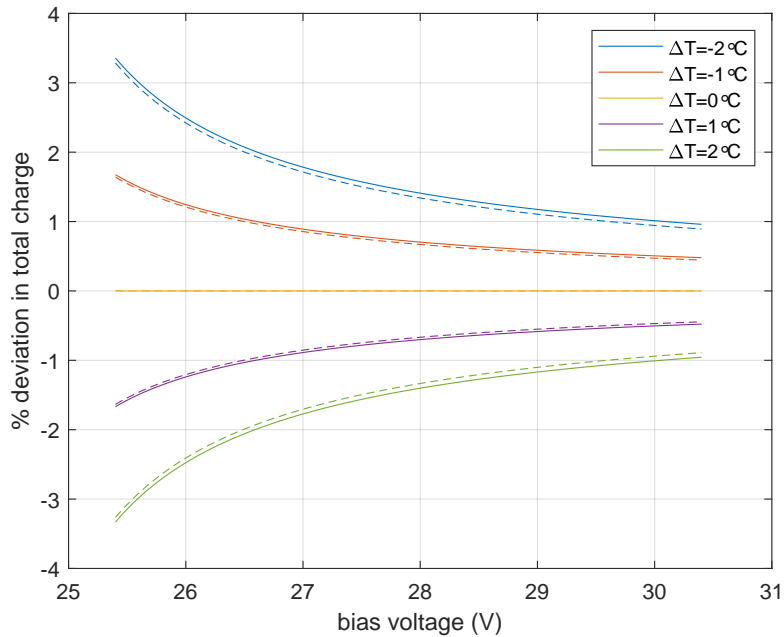
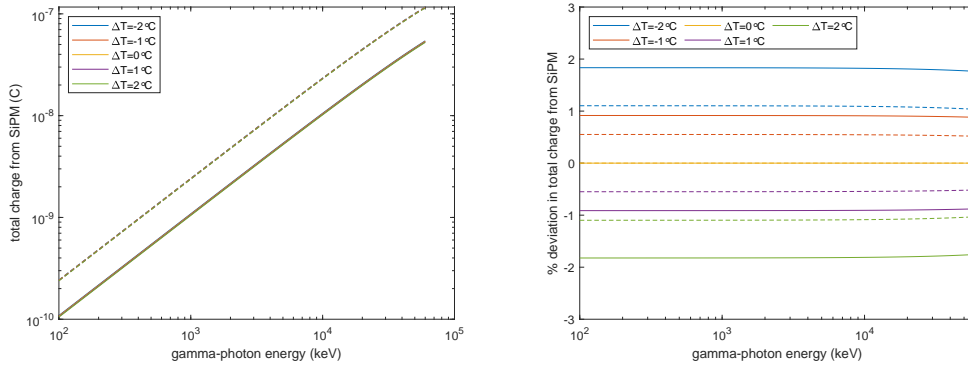


Figure 3.22: Calculated percentage deviation from total output charge at mean temperature (here 21 °C), for different constant bias voltages, using two different gamma-ray energies: 100 keV (solid line) and 60 MeV (dashed line).

Higher bias voltage (and consequently overvoltage) lowers the deviation in percent, as shown in figure 3.22. And that the deviation is mostly the same for the two gamma-photon energies, but slightly lower for the greater energies.

Figure 3.23a shows the total charge of the signal as a function of gamma-photon energies, for two different overvoltages and different temperature deviation, the total charge is calculated the same way as in figure 3.22. Figure 3.23b shown the deviation in percent of the total charge in figure 3.23a, using equation (3.29) to calculate this.



(a) Total charge in signal for different temperatures depending on absorbed energy in scintillator, and overvoltage 2.5 V (solid line) and 6 V (dashed line). (b) Deviation from total charge in signal from mean temperature depending on absorbed energy in scintillator, and overvoltage 2.5 V (solid line) and 6 V (dashed line).

Figure 3.23: Graphs showing how the temperature affects the signal height of the SiPM depending on the incoming gamma-photon energy, and for two different mean overvoltages.

Figure 3.23 shows that the deviation in percent is mostly the same for the range of gamma-photon energies. And for a mean overvoltage of 2.5 V the total charge will be within $\pm 2\%$ for a temperature change of $\pm 2^\circ\text{C}$. From this, it can be concluded there is any need to compensate for any temperature changes. In the case of large temperature changes, it is possible to change the bias voltage to keep the overvoltage constant. Some groups have developed chips that compensate for temperature by automatically adjusting the bias voltage, see for example [28]. Another option is keeping the temperature stable enough such that the overvoltage is within the operating voltage, measuring the temperature and using this to calculate the number of photons arriving at the SiPM. This can be done by working the way backward with the equations used to calculate the total charge in figure 3.23a. The last option is keeping the temperature very stable, such that the deviation in total charge is small compared to other noise sources or resolutions.

From figure 3.23b the deviation total charge is within $\pm 2\%$ for a temperature change of $\pm 2^\circ\text{C}$, and the energy resolution is expected to be around 10% which makes the 2% acceptable. And the latter solution should be good enough. However, the temperature should still be monitored close to the SiPM.

Note that increasing the temperature increases the dark current and dark count rate, as shown in [18]. Thus keeping the temperature high to keep it stable will increase the noise from the SiPM.

3.7 Measurements of SiPM

The measurements of SiPM will be used to verify some of the important properties of the SiPM, such as signal shape, length, and height. Additionally, two different readout methods are used in the measurements; one where the current signal is

converted to a voltage and read out through a series resistor, and one where the standard output of the SiPM is connected directly to a transimpedance amplifier (without a series resistance). These results will be important for the design choices in chapter 4.

3.7.1 Single Unit SiPM Measurements

The measurements in this section were taken on the MicroFJ-SMTPA-30035 (3.07 mm \times 3.07 mm SiPM with 35 μ m microcells) from onsemi. The point of these measurements was to see if the signal height and timing performance was as predicted. The measurements were taken with the setup in figure 3.24. The light source used was a Light Emitting Diode (LED) connected to a signal generator with a square pulse of with 25 ns and height 2.5 V and the bias voltage of the SiPM was 27.1 V, if not otherwise noted. There are also 50 Ω termination resistors on the signal generator and the LED (not shown in figure 3.24). The connection of the SiPM was as recommended in an application note [16], and was realized on the board in figure 3.25. The schematic for this is shown in appendix B.3.1. The standard and fast output were connected to an oscilloscope, and the measurements were captured as a waveform from the oscilloscope. These measurements are shown in figure 3.26, 3.27 and 3.28.

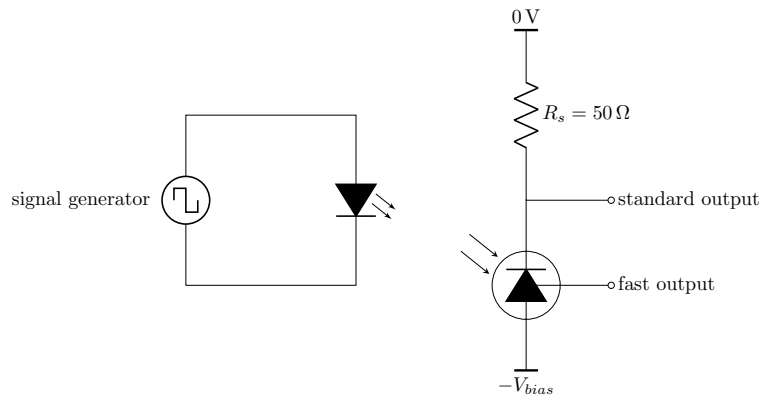


Figure 3.24: Setup for measuring signal from a single unit SiPM.

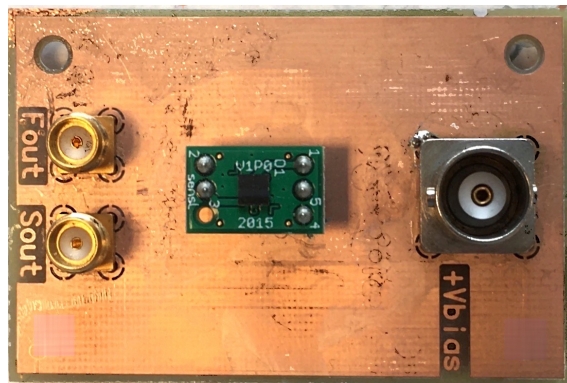


Figure 3.25: Picture of the test board used in measurements of single SiPM.

Figure 3.26 shows the signal from the SiPM when the width of the pulse from the signal generator was varied. The width of this pulse should ideally be as small as possible to get as close as possible to the impulse response of the SiPM.

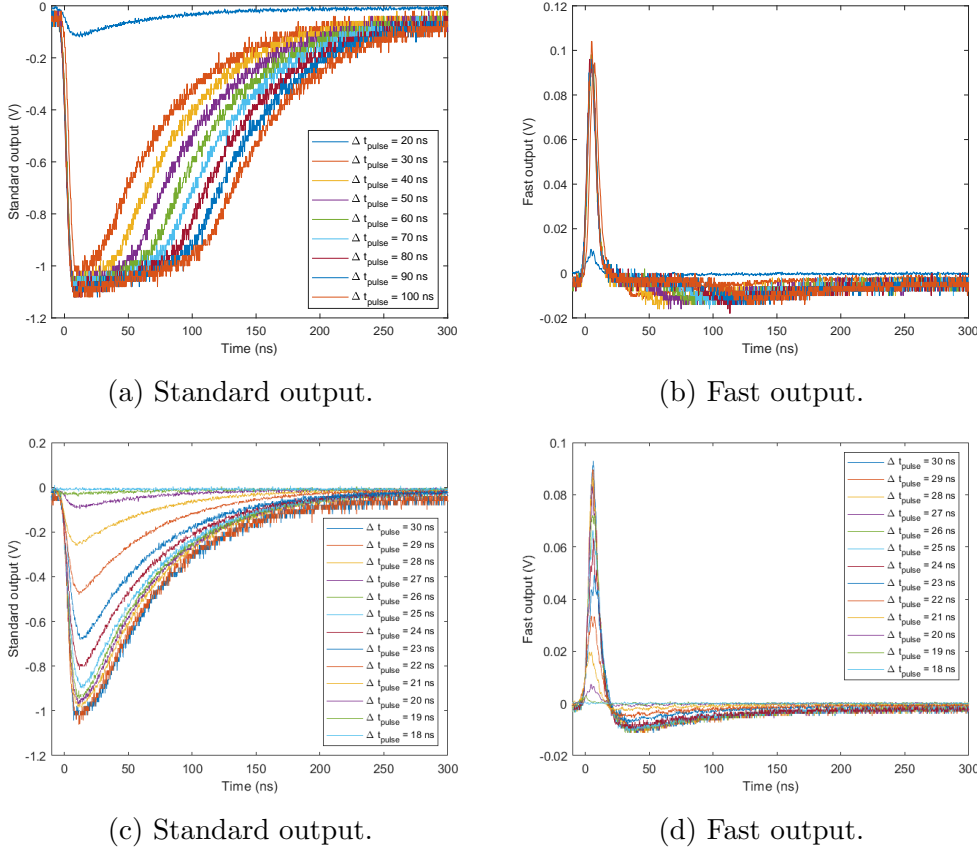


Figure 3.26: Signal from a single SiPM using different pulse width on LED light source.

It can be seen from figure 3.26a and 3.26c that a pulse width from the signal generator of 20 ns to 25 ns is the shortest pulse that can be used before the height of the signal is too low. In comparison 50 ps laser pulses were used in the application note [16]. The reason for these short pulses is likely that the termination resistors and the capacitance over the LED work as a low pass filter. Picturing a typical step response of a low pass filter, this means that the voltage from the signal generator is turned off before the voltage across the LED is able to reach its threshold voltage.

The SiPM was probably saturated (meaning that most of the microcells were triggered) for the longest pulses, see figure 3.26a. There is also a gentle slope before the LED is turned off; this can originate from microcell firing before they are fully recharged, giving out less charge than they normally would.

In figure 3.26b and 3.26d it can clearly be seen that the fast output has a high positive value when the standard output (3.26a and 3.26c) has a steep fall in the beginning, and the fast output has a value below zero when the standard output is slowly rising and returning to zero. This supports the assumption that the fast output is proportional to the derivative of the standard output, and this can similarly

be seen in figure 3.27 and 3.28.

In figure 3.27 the bias voltage over the SiPM was varied from 25 V to 30 V in steps of 1 V. The signal in figure 3.27c was filtered with a moving average filter, and the absolute value of the peak of the signal was plotted in figure 3.27d.

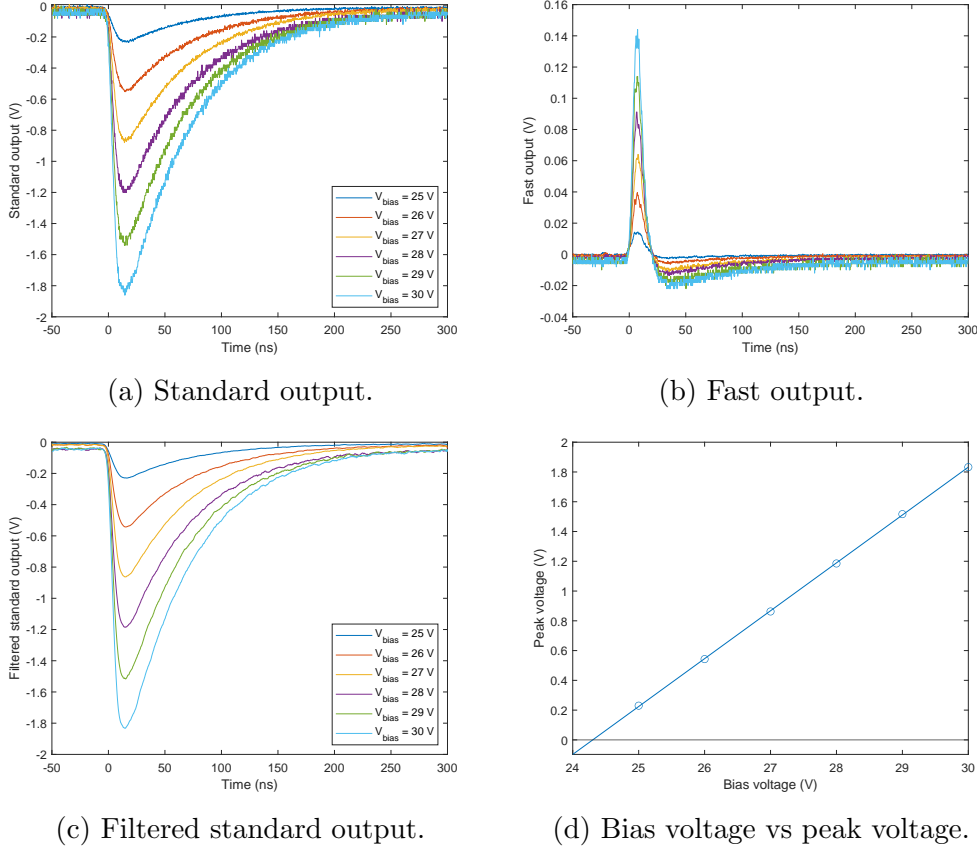


Figure 3.27: Signal from SiPM for different bias voltages, with LED as light source.

What can be concluded from figure 3.27 is that the gain of the SiPM is proportional to the overvoltage, as predicted in equation (3.2). Following equation (3.1) there will be a linear relationship between the bias voltage and the signal peak, which is also proportional to the total charge given by the SiPM.

Considering the PDE and equation (3.4) the increasing PDE with the overvoltage, the total charge (and therefore the signal height) from the SiPM should increase with more than a linear relationship, but because the SiPM was saturated with the light from the LED as shown in figure 3.26c, the number of fired microcell stays the same, and the increasing PDE will not be visible.

Comparing the highest signal in figure 3.27c, where the overvoltage was almost at 6 V, with the calculated signal from one microcell (the dashed red line in figure 3.10), it seems to agree well this the following reasoning: The peak in figure 3.10 is at approximately $22.5 \mu\text{A}$. Assuming that all the microcells are fired in figure 3.27c the peak current should be $5676 \cdot 22.5 \mu\text{A} \approx 128 \text{ mA}$. Reading this out over a 25Ω resistance (50Ω on the board in parallel with 50Ω on the oscilloscope) makes the peak voltage 3.19 V. And at last considering the time constant the peak will be at

Q_{total}/τ_{sipm} (according to equation (3.15)) and the time constant from the data sheet $\tau_{ideal} = 45$ ns was used, the time constant for this pulse will be found to be 66 ns in section 3.7.3. The relationship between the peak values can be calculated using $Q_{total}/\tau_{meas} \cdot \tau_{ideal}/\tau_{ideal} = Q_{total}/\tau_{ideal} \cdot \tau_{ideal}/\tau_{meas}$, using this on the ideal peak to estimate the measured peak gives 3.19 V \cdot 45 ns/ 66 ns \approx 2.2 V. This is slightly above, but considering that the overvoltage was a bit below 6 V, that the 25 ns pulse with from the signal generator didn't give the largest signal, and that the signal also had a rise time, the estimated peak value agrees well with the measured peak values.

In figure 3.28 the voltage over the LED was varied from 2.0 V to 2.5 V in steps on 0.1 V.

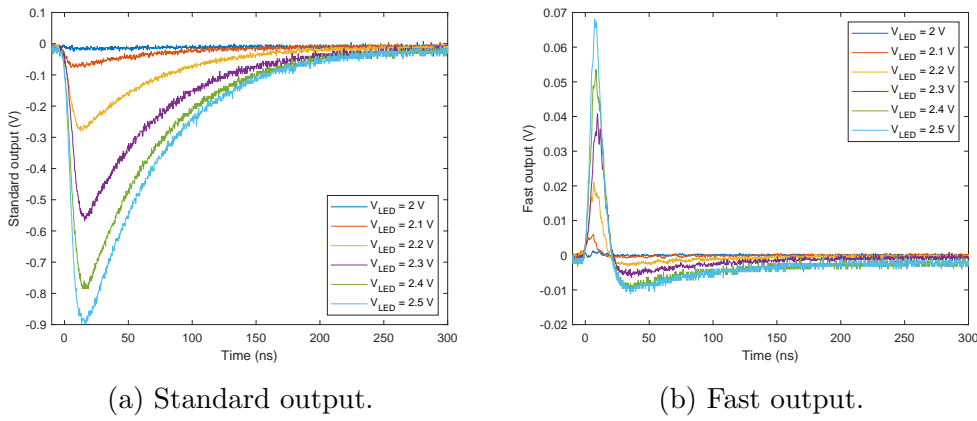


Figure 3.28: Signal from SiPM using different voltage over LED light source.

In figure 3.28 both the characteristics of the LED and the SiPM can be seen. The current through a diode is related to the voltage through an exponential function; the light intensity will then be proportional to the square of the current. This can be seen from the increasing distance between the graphs with $V_{LED} = 2.3$ V and below. The saturation of the SiPM can be seen from the decreasing distance between the graphs with $V_{LED} = 2.2$ V and above.

3.7.2 Calculating Time Constant from Measurements

To verify if the SiPM behaves as promised, it will be useful to calculate the time constant; there are several ways to do this. One of them is to fit an exponential function to the measurements in MATLAB, this was tried for the measurements taken, but it did not always fit the function correctly. An other option is to find the peak value f_{peak} of the signal then find the time where the signal equals $f_{peak} \cdot e^{-\tau/\tau} \approx 0.37 \cdot f_{peak}$. However, the full decay of the signal does not start right after the signal peak (possibly due to the LED being used). So, another alternative that circumvents this problem is to measure the time T_{90-10} from 90% to 10% of the signal peak; this will be proportional to the decay time constant. To find T_{90-10} equation (3.30) is considered. t_0 is the start of the pulse.

$$f(t) = \begin{cases} 0 & \text{for } t - t_0 < 0 \\ f_{peak} \cdot e^{-(t-t_0)/\tau} & \text{for } t - t_0 \geq 0 \end{cases} \quad (3.30)$$

From equation (3.30) the relationship between the time t_1 and t_2 where the value is 90% and 10% of the peak value can be given as in equations (3.31) and (3.32). Then the time between these is given by equation (3.33), the reason to use this time instead of just t_1 or t_2 is that it will correct for any offset in t_1 and t_2 in the case where the signal does not start exactly at $t = 0$.

$$0.9 \cdot f_{peak} = f(t_1) = e^{-(t_1-t_0)/\tau} \quad (3.31)$$

$$0.1 \cdot f_{peak} = f(t_2) = e^{-(t_2-t_0)/\tau} \quad (3.32)$$

$$T_{90-10} = t_2 - t_1 \quad (3.33)$$

Solving the equations (3.31), (3.32) and (3.33) gives equations (3.34), (3.35) and (3.36).

$$t_1 = t_0 - \tau \cdot \ln(0.9) \quad (3.34)$$

$$t_2 = t_0 - \tau \cdot \ln(0.1) \quad (3.35)$$

$$T_{90-10} = \tau \cdot (\ln(0.9) - \ln(0.1)) \quad (3.36)$$

Solving equation (3.36) for τ the time constant can be calculated with equation (3.37).

$$\tau = \frac{T_{90-10}}{\ln(0.9) - \ln(0.1)} \quad (3.37)$$

The measurements taken to find T_{90-10} are illustrated in figure 3.29. t_1 and t_2 are found by measuring the time where the signal is 90% of the maximum and 10% of the maximum after the rise of the signal. Then equation (3.33) is used to find T_{90-10} then the time constant is calculated using equation (3.37).

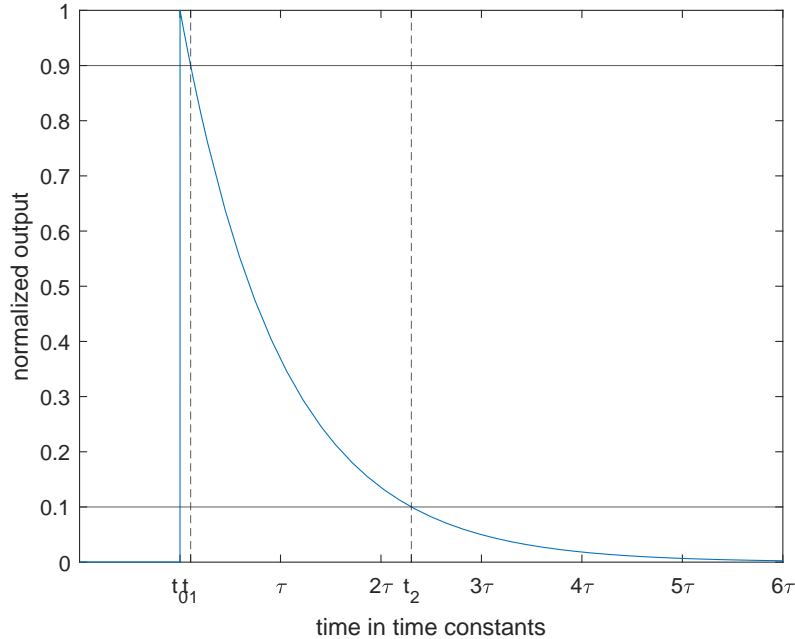


Figure 3.29: General exponential decay (as in equation (3.30)), showing the different values found in measurement and used to calculate the decay time constant.

3.7.3 Time Constant in Single Unit SiPM

Here the same measurements as in figure 3.27a and 3.28a were used to find the time constant, excluding those signals that were too low to give any reasonable answers. Because there was some noise in the measurements a moving average filter with a span of 20 was used, like in figure 3.27c. Using a large span of the average filter would increase the bandwidth of the signal, but 5 looks fine in figure 3.27c, also because the data is discrete it was not possible to fit values at exactly 90% and 10% of the maximum, so t_1 and t_2 was found using the average of the last value above and the first value below 90% or 10% (after the data was multiplied by -1 to make a “positive pulse”). The results of ten of these measurements is an average of 66 ns and a standard deviation of 3 ns, also shown in table 3.5.

The measured time constant (66 ± 3) ns is higher than the 45 ns promised for the TSV package¹ in the data sheet [23]. This could be because of the 50Ω series resistor looking at equation (3.9) and (3.13) this would increase the total decay time. It could also be due to the light diode, the signal from the signal generator had a pulse width of 25 ns, but the light pulse from the diode might be longer due to the resistance in the signal generator and the capacitance creating a low pass filter. Another possibility is that the SMTPA evaluation board² makes the signal slower, it even says in the data sheet [23] that “it should be noted that the timing performance from this board will not be optimized” ([23]), and that the SMA evaluation board³ is recommended when timing performance is required.

3.7.4 SiPM with Scintillator

A scintillator was attached to the SiPM to see how they work together. The measurements were taken with the same setup as in section 3.7.1, except that the LED was turned off, bias voltage was $-V_{bias} = 30.0$ V, and the scintillator was used as a light source. The scintillator used was a LYSO-crystal with dimensions around $8 \text{ mm} \times 8 \text{ mm} \times 40 \text{ mm}$, and was coupled to the SiPM with a small silicone pillow, the same that was used for Atmosphere-Space Interactions Monitor (ASIM), on the outside of the LYSO there was reflective tape. A picture of the setup is shown in figure 3.30.

¹Package using a TSV (Through Silicon Via) process, developed by onsemi for the J-series SiPM [23].

²Evaluation board (MicroFJ-SMTPA-XXXXX) for the MICROFJ-30035-TSV SiPM, the TSV sensor sits on a small PCB with through hole pins, named TSV Pin Adapter board (SMTPA) [23].

³Evaluation board (MicroFJ-SMA-XXXXX) for the MICROFJ-30035-TSV SiPM using female SMA (SubMiniature A) connectors [23].

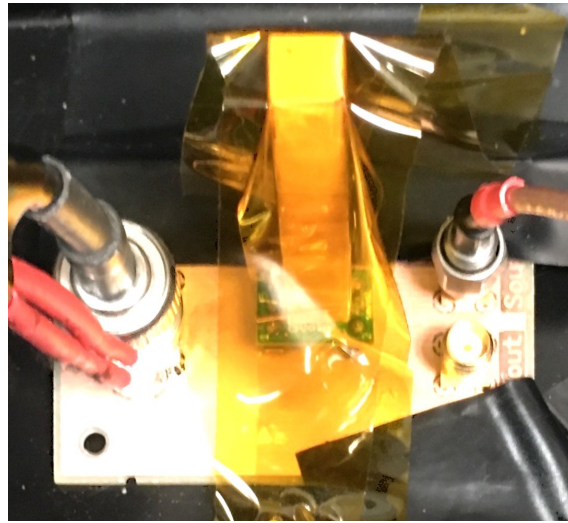


Figure 3.30: Picture of the test board used in measurements of single SiPM with small scintillator attached.

Figure 3.31 shows a few pulses from the SiPM and LYSO without any radioactive source used. The pulses seen here could be cosmic background radiation but is most likely pulses from the LYSOs intrinsic radiation, because the LYSO has a high rate of self counts from a radioactive isotope in the material it is made of.

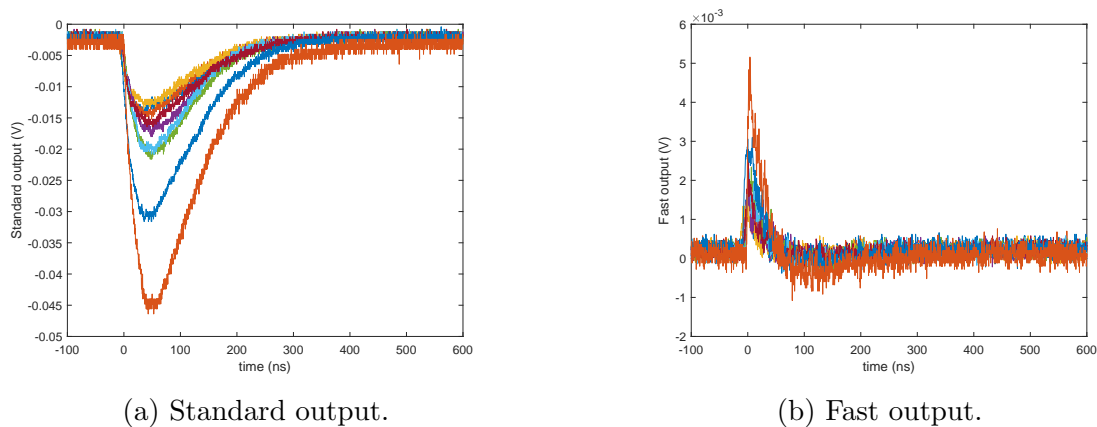


Figure 3.31: A few measured pulses from SiPM with LYSO-scintillator.

Figure 3.32 is the same pulses as figure 3.31, but the pulses are filtered with a running average filter, to remove some noise.

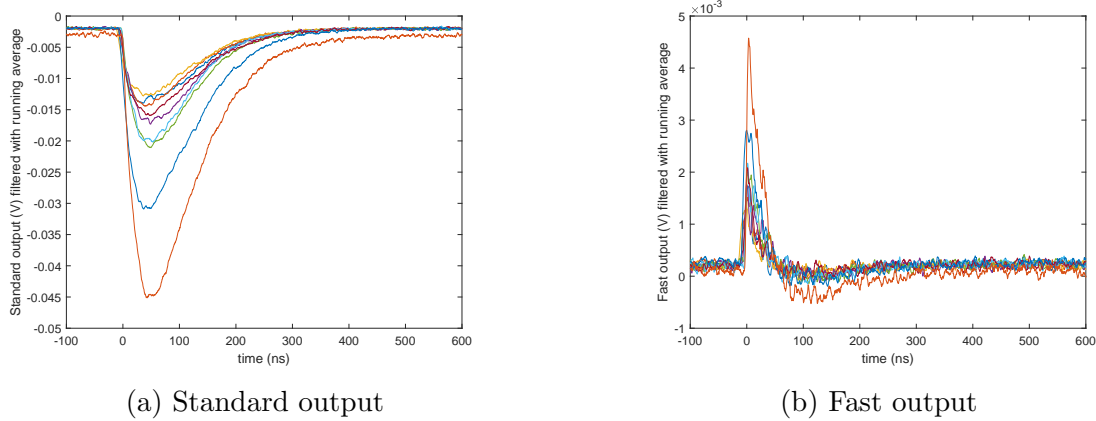


Figure 3.32: A few measured pulses from SiPM with LYSO-scintillator

Comparing figure 3.32 with the fast output in figure 3.26, 3.27 and 3.28, the undershoot of the fast output is more visible in figure 3.32 and the pulse (above zero) is wider. This agrees well with the fast output being proportional to the derivative of the standard output, since the slope of the falling and rising edge is more equal here, compared to figure 3.26, 3.27 and 3.28.

In figure 3.33 the standard output (from figure 3.32a) is normalized, the black line is a calculation of the pulse using equation (3.24). The values used was the time constant for the LYSO $\tau_{lyso} = 40$ ns (from table 3.3), $\tau_{sipm} = 66$ ns (the measured mean value from section 3.7.3), and QN_{fired} was chosen such that the peak value is normalized to 1.

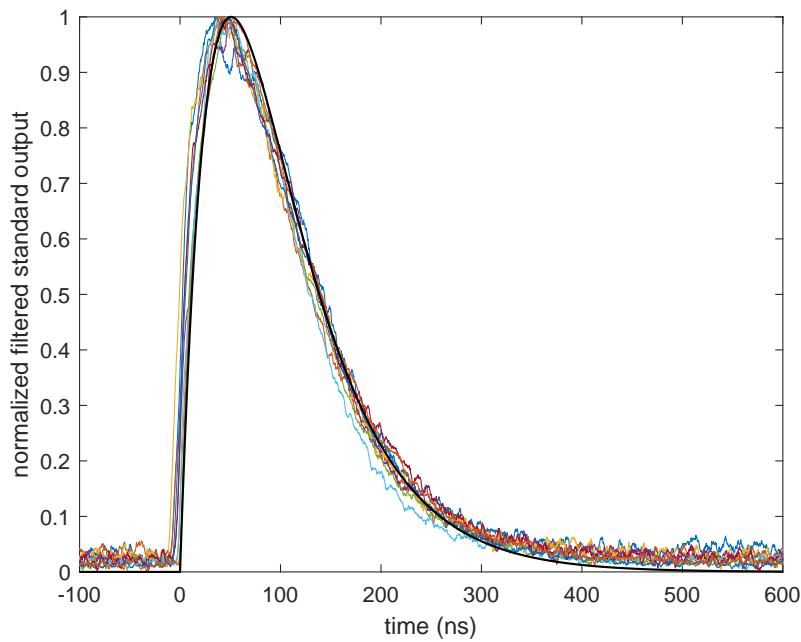


Figure 3.33: Pulses in figure 3.32a normalized and plotted with expected pulse shape

From figure 3.33 the black line fits well with the measured pulses, and it shows

that equation 3.24 is a good approximation of the pulse shape from the LYSO coupled to SiPM.

The setup in figure 3.30 was then connected to an ADC (instead of the oscilloscope) connected to a computer where LabVIEW was used for data acquisition. The negative peak value of the signal was saved as is for each pulse; no filtering was done, and the signal was as shown in figure 3.31a.

Figure 3.34 shows the measured energy spectrum of LYSO self-counts. As mentioned in section 3.4.2 the should be at 88 keV, (88 keV + 202 keV), (88 keV + 307 keV), and (88 keV + 202 keV + 307 keV). However, only three is visible here, this is possibly due to noise and the (88 keV + 202 keV) peak and (88 keV + 307 keV) peaks looks like one peak. Also, the activity of LYSO is high, using the numbers presented in section 3.4.2 the rate of this LYSO will be $7.1 \text{ g/cm}^3 \times 39 \text{ counts/s/g} \times 0.8 \text{ cm} \times 0.8 \text{ cm} \times 4 \text{ cm} \approx 700 \text{ counts/s}$, which is high compared to background or cosmic radiation.

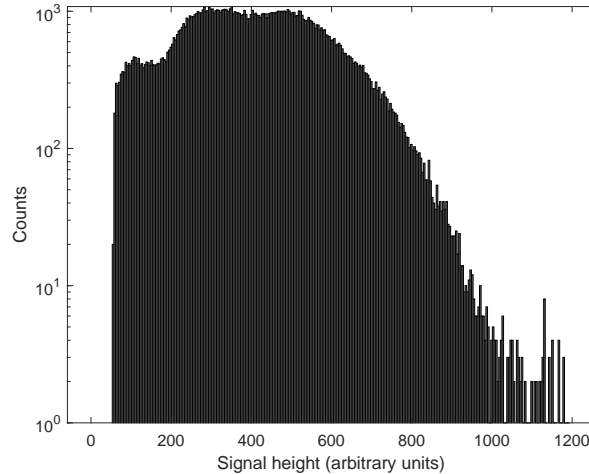
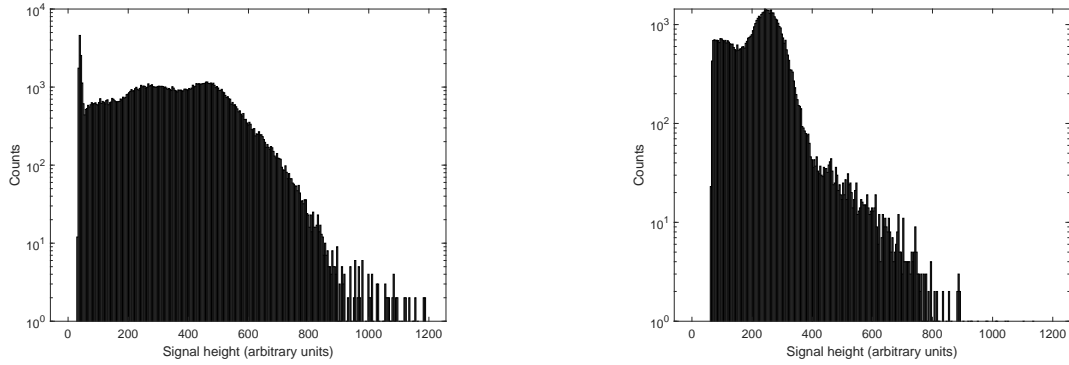


Figure 3.34: Measured energy spectrum, for LYSO self-counts.

Further, the radiation from two radioactive sources were measured; ^{137}Cs and ^{133}Ba . The histograms for these are shown in figure 3.35.



(a) Measured energy spectrum of cesium, using LYSO-scintillator.

(b) Measured energy spectrum of barium, using LYSO-scintillator.

Figure 3.35: Measured energy spectrum from radioactive sources (LYSO self-counts are not subtracted).

Figure 3.35a shows little difference from the self-counts in figure 3.34, so most of the counts here are self-counts. But the rightmost peak is slightly higher and shifted to the right. This is likely the 662 keV radiation from the Cesium. The high peak close to the threshold is probably just noise.

The barium (shown in figure 3.35b) had a high count rate (of a few kHz) and the LYSO self-counts is much less visible here. This histogram has two visible peaks at 100 arbitrary units and 250 arbitrary units, while barium has several peaks in the energy spectrum, of those that might be visible here are 276 keV, 302 keV, 356 keV, and 384 keV. The peak at 100 arbitrary units could be from both 276 keV and 302 keV, and the peak at 250 arbitrary units could be from both 356 keV and 384 keV.

3.7.5 Measurements from Array

Measurements from each pixel in the SiPM array (ARRAYJ-30035-64P-PCB) were taken with the breakout board from onsemi, ARRAYJ-BOB3-64P, which was connected as recommended in the data sheet [29]. A picture of the setup is shown in figure 3.36, and a schematic for the setup is shown in figure 3.37, the main difference here from the single SiPM readout, is that the series resistor is moved to the anode of the SiPM and the standard output is Alternating Current (AC)-coupled (with the 10 nF capacitor) to the oscilloscope. For this setup AC-coupling is necessary; otherwise, the standard output would be referred to $-V_{bias}$, which does not work for the oscilloscope. The rest of the setup was the same as in section 3.7.1.

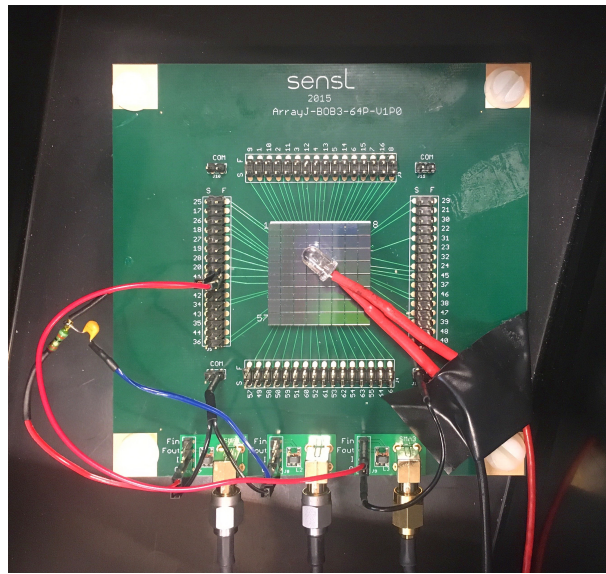


Figure 3.36: Picture of breakout board from onsemi, ARRAYJ-BOB3-64P, with the ARRAYJ-30035-64P-PCB SiPM array.

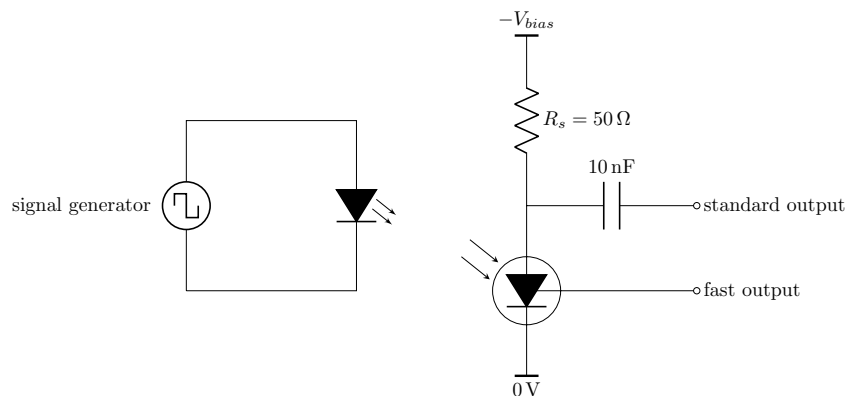


Figure 3.37: Setup for measuring signal from SiPM array

One pulse from each pixel is plotted in figure 3.38. The shape of the signal in each pixel is similar to one another, but the height differs. As seen in figure 3.36 the LED had a different distance from the different pixels in the SiPM which gives different light intensity seen by that pixel and therefore different signal height. Comparing this signal shape to the measurements in section 3.7.1 the signal from the breakout board is longer, and there are also some oscillations on top of the signal; this is especially visible on the fast output. This could come from reflections in the cables due to bad termination or stray impedance in the breakout board or the cables; the longer signal can also come from the latter.

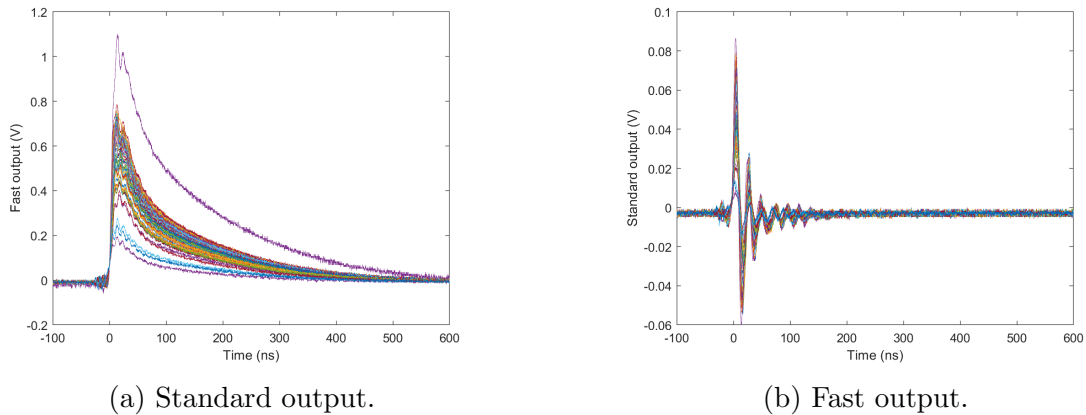


Figure 3.38: Measurements from SiPM array using the breakout board from onsemi.

Connecting several pixels together in parallel was tried on the breakout board but did not give any useful results other than the observation of an even longer pulse length.

Therefore a test board to examine how different number of pixels connected and different values of the series resistance was made. Pictures of this board is shown in figure 3.39, and the schematic is shown in appendix B.3.2. 10 pixels in the array was connected in parallel via switches, such that the number of pixels from 1 to 10 can be chosen. 10 $50\ \Omega$ resistors was connected the same way, which makes the series resistance $R_s = 50\ \Omega/n$, where n is the number of resistors connected in parallel. Otherwise, the setup was equal to the breakout board in figure 3.36 and 3.37.

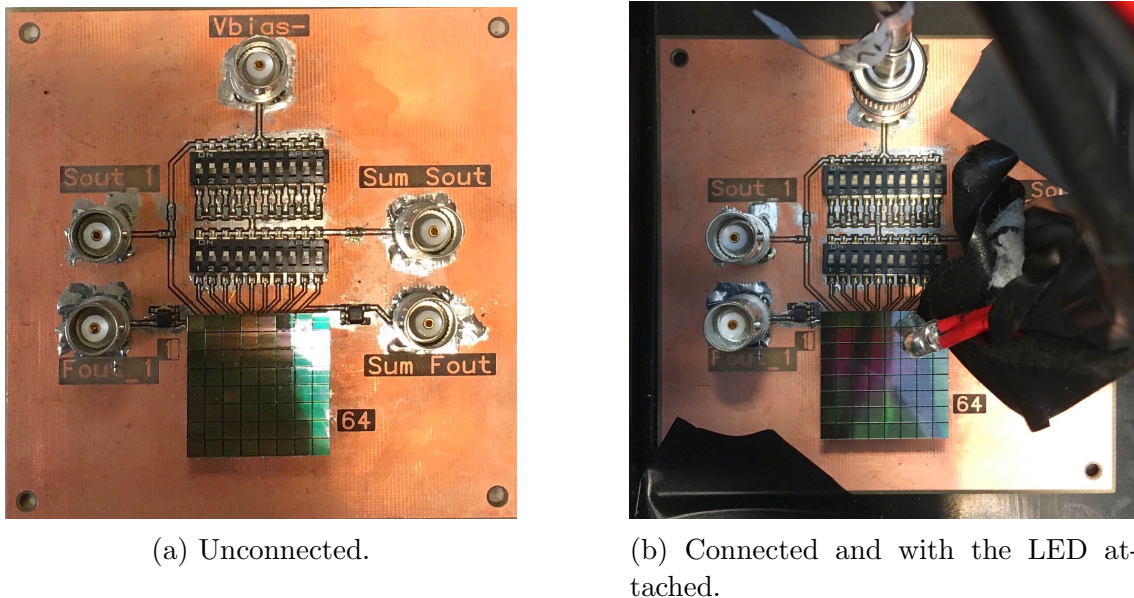


Figure 3.39: Pictures of test board used for characterizing the signal with different number of pixels connected and different series resistor values.

Ten pulses of each combination of 1 to 10 pixels and 1 to 10 resistors were recorded. A selection of these are plotted in figure 3.40, 3.41 and 3.42.

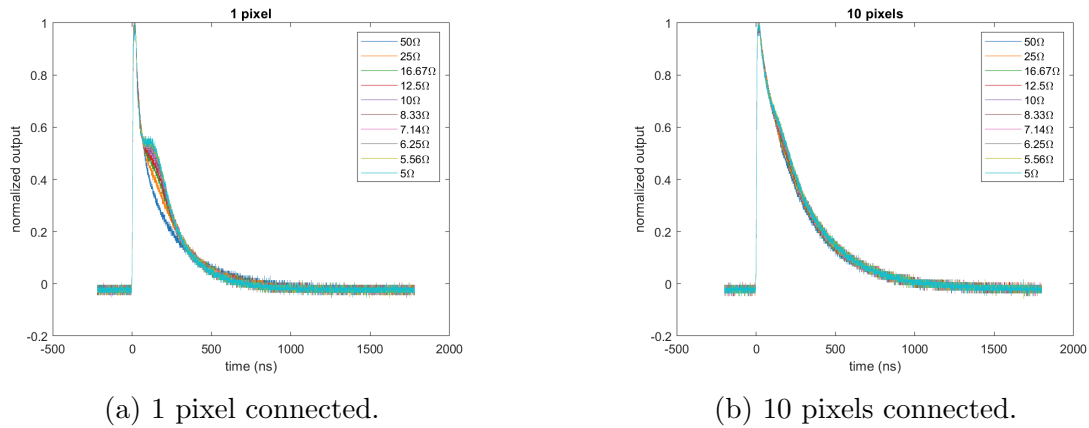


Figure 3.40: Selection of pulses from a constant number of pixels in the SiPM array using different series resistors.

Considering the pulse shape in figure 3.40 the pulse shape does not look shorter for lower series resistor values, neither for 1 or 10 pixels. This does not agree well with the time constant given in equation 3.12. For 1 pixel, the shape changes, and a bump on the pulse arises for low resistor values. This could come from a zero in the transfer function, or reflections from the LED inside the dark box, but this is not the case for the other measurements using the LED, so this is unlikely. Further, no effort was made to figure out what this was due to good results when using amplifier readout (section 3.7.6) of the SiPM. with equation 3.12

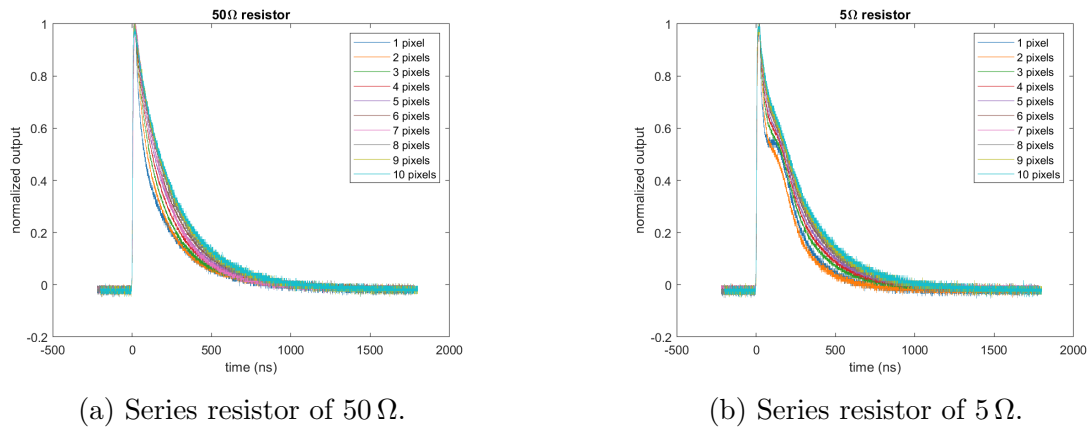


Figure 3.41: Selection of pulses from SiPM array using constant series resistor, and varying number of pixels.

Figure 3.41 shows that increasing the number of pixels, increases the pulse length, this fits well with equation (3.12). But there is not a significant difference between 50Ω and 5Ω series resistance, and there is also a bump for low number of pixels and 5Ω series resistance.

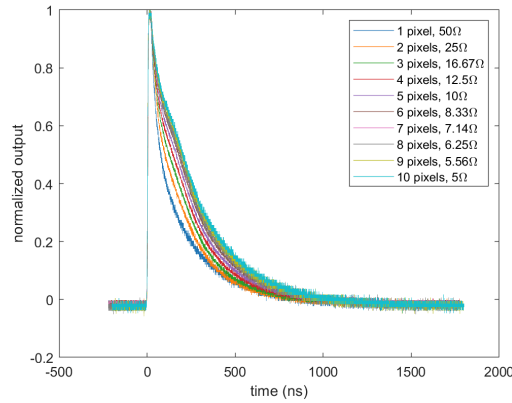
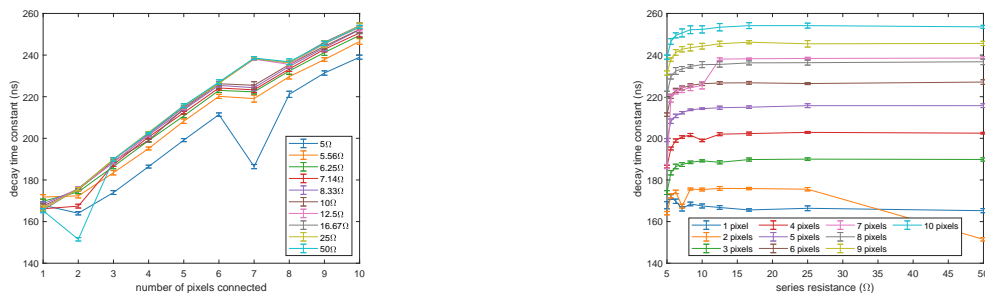


Figure 3.42: Selection of pulses from SiPM array using increasing number of pixels and decreasing series resistance

From equation (3.12) the number of pixels and series resistance should cancel each other out, and the recovery time constant (and signal length) should be the same when there is the same number of pixels and resistors are connected in parallel. The pulses in figure 3.42 does not fit in to this.

The time decay time constant for each combination of number of pixels and series resistor values were calculated, as described in section 3.7.2, with the mean value and standard deviation for the ten recordings of each combination, this is visualized in figure 3.43



(a) Decay time constant as a function of number of pixels for different resistor values.

(b) Decay time constant as a function of resistor values for different number of pixels.

Figure 3.43: Plot of decay time constant for varying number of pixels and resistor values, measured as described in section 3.7.2 from measurements with different number of pixels and resistor values, plotted with error bars for the standard deviation of 10 measurements.

From figure 3.43 the time constant does not seem to change much when the series resistor is varied; it changes just a bit for the lowest resistor values, and the time constant definitely increases with an increasing number of pixels. Some values do not follow the trend of the other measurements; for 2 and 7 pixels connected, this could be because of this bump that sometimes comes forward. However, again, no effort was made to figure this out.

3.7.6 Measurements from Array with Amplifier Readout

A different approach for the readout of the SiPM is with the standard output connected to an amplifier (this is also described in the application note [16]). A picture of the test board and setup is shown in figure 3.44, and the schematic for this board is shown in appendix B.3.3. Testing this is to see what readout method works the best and make sure that the LMH6629 amplifier works.

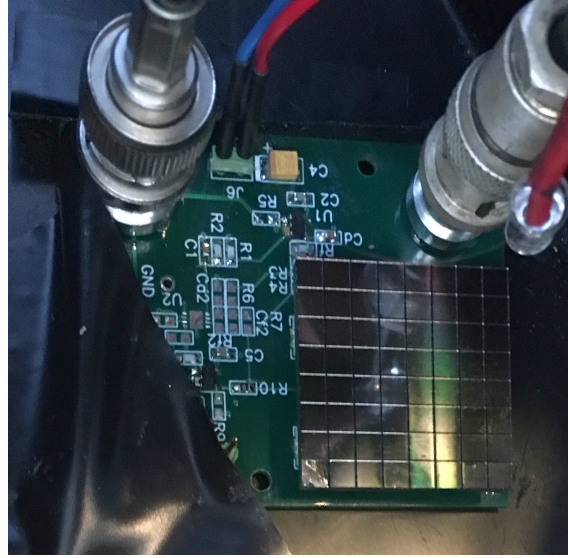


Figure 3.44: Picture of test board used for characterizing the signal from the SiPM, with a amplifier used for read-out.

A simplified circuit diagram of this readout method is shown in figure 3.45. Only 16 pixels are used for this test, and the other 48 pixels are left unconnected. The series resistance R_s can be shorted or set to a very low value, effectively connecting the anode of the SiPM pixels to virtual ground (or another common-mode). The current signal from the SiPM is converted to a voltage and shaped through the feedback resistor R_f and capacitor C_f . The circuit on the non-inverting input of the amplifier sets the common-mode the signal is referred to, and the amplifier will adjust the common-mode on the inverting input to be the same. If this common-mode is not set to ground, the supply voltage V_{bias} must be adjusted such that the voltage drop between cathode and anode is as recommended in the data sheet, [23].

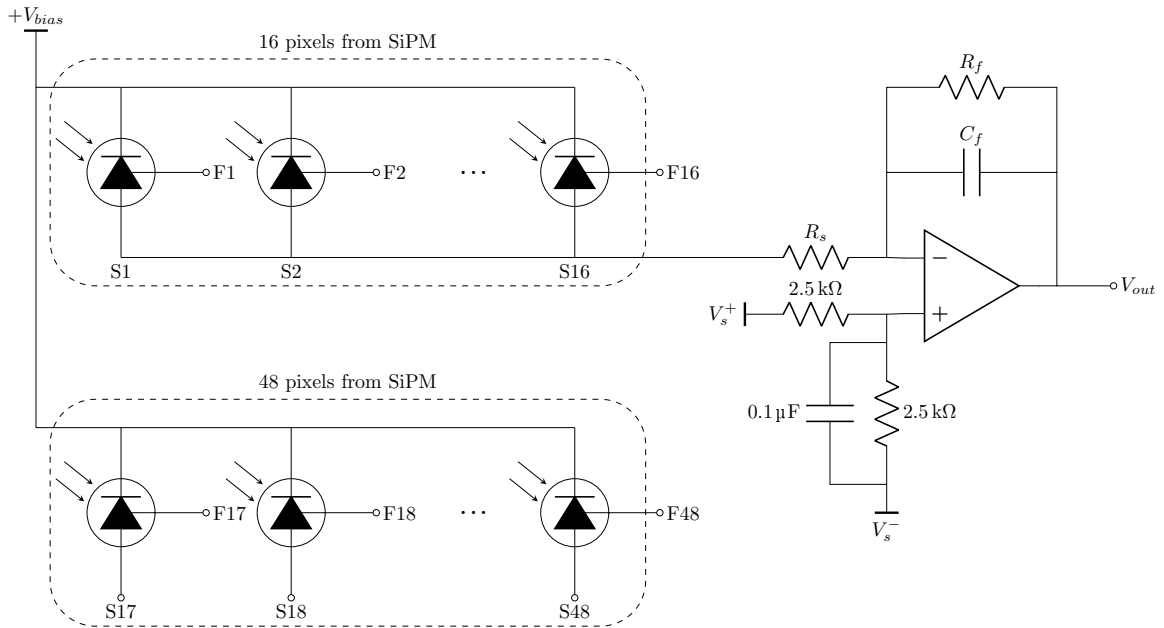
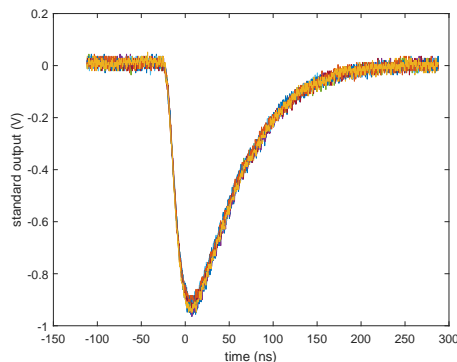
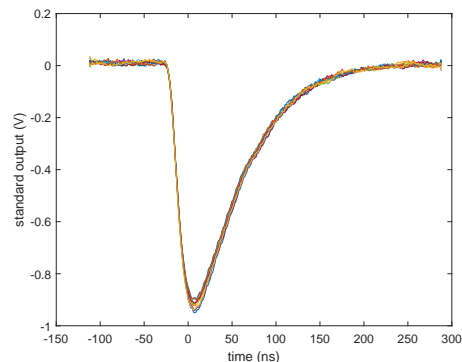


Figure 3.45: Setup for measuring signal from SiPM array using preamplifier for readout. A LED was used as the light source (but is not shown in this diagram).

For this measurements amplifier was supplied with a single supply of 5 V, and the common-mode on the input was set to 2.5 V, which is in the middle of the supply, it might be useful to adjust this to maximize the range of an ADC. The values of the feedback resistor and capacitor was $R_f = 50 \Omega$ and $C_f = 200 \text{ pF}$, and the series resistor R_s was shorted. The bias voltage was set to 30.2 V (which would correspond to 27.7 V if the common-mode on the anode was 0 V). A LED was used as the light source (not shown in the diagram in figure 3.45), with a pulse width 20 ns and height of 2.250 V, these are both in the lower range of what was used for the single SiPM readout, see figure 3.26c and 3.28a. A few pulses were recorded and plotted in figure 3.46, the pulses in figure 3.46b are filtered with a running average filter.



(a) Unfiltered



(b) Filtered with average filter of 20 samples

Figure 3.46: Pulse from 16 pixel of the SiPM array connected amplifier, and LED as light source.

What can be concluded from figure 3.46 is that the timing performance of the SiPM is much better when using an amplifier for the readout, compared to reading the voltage over a resistors (as were done in previous measurements). The time constant for this was measured as described in section 3.7.2 and resulted in an average of 52 ns and a standard deviation of 1 ns, from ten measurements, also shown in table 3.5.

To get an idea of what the signal looks like when the current from the SiPM is too high the voltage over the SiPM and LED was varied, this is shown in figure 3.47. What can be concluded from these measurements is that the signal gets a different shape when the signal is too high. And at least for the varying LED-voltage, the signal gets longer for higher signals when the amplifier is saturated.

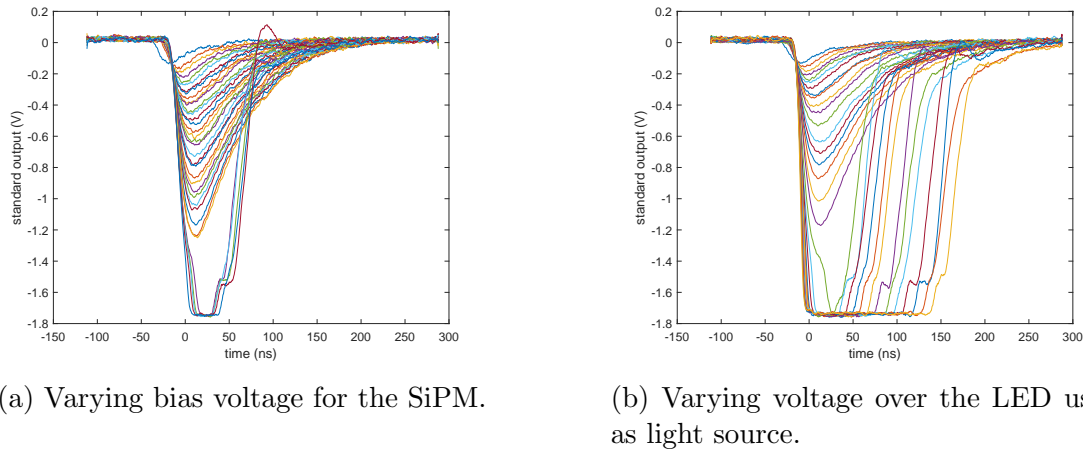


Figure 3.47: Filtered output from 16 pixel of the SiPM array connected amplifier, and LED as light source.

3.7.7 Comparison of Measurements and Biasing and REad-out Circuits

To compare the different readout methods tested, a selection of normalized pulses from the measurements were plotted in figure 3.48. Also the measured decay time constants is gathered in table 3.5.

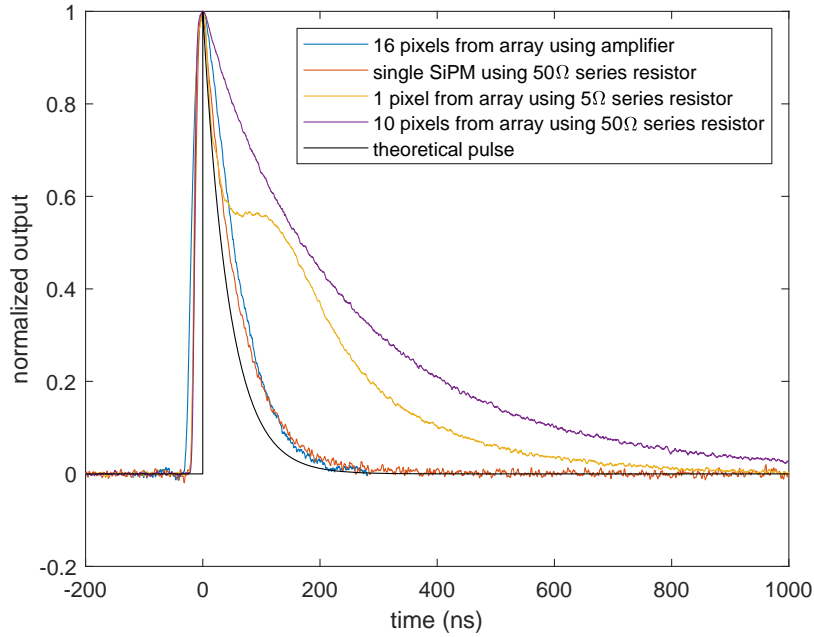


Figure 3.48: Comparison of pulses from the different biasing and readout methods used.

Figure 3.48 shows that readout using an amplifier is the best when it comes to timing performance; it is the fastest to return to the baseline. But has the slowest rise time, which comes from the shaping done by the feedback resistor and capacitor. Looking at the time constants in table 3.5 the array with amplifier readout has the lowest time constant out of the measurements, and is getting very close to the 45 ns promised in the data sheet [23].

	Measured time constant (ns)
Theoretical	45
Single pixel with series resistor	66 ± 3
Array with series resistor - minimum	151.5 ± 0.8
Array with series resistor - maximum	254 ± 1
Array with amplifier	52 ± 1

Table 3.5: Comparison of different decay time constants measured for different SiPMs and measurement setups.

Front-End Electronics

In chapter 3 it was shown that reading the SiPM out with a preamplifier, was the optimal solution (see for example figure 3.48). This preamplifier can be implemented as a CSA or a transimpedance amplifier. Further, the signal will go through a shaping circuit, reducing bandwidth and improving noise to optimize the energy resolution and high or low-frequency components of the signal to optimize the timing resolution. The dynamic range and the Nyquist theorem will be regarded when considering the shaping (and also choice of ADC).

4.1 Theory of CSA and CR-RC Shapers

The majority of the contents of this section are based on [30]; the rest is considered general knowledge or is a further result of the theory in [30].

4.1.1 Charge Sensitive Amplifier

A current signal can be converted into voltage and shaped with a circuit starting with a CSA. A circuit diagram of the CSA is shown in figure 4.1. The CSA is a type of transimpedance amplifier that gives an output voltage corresponding to the integral of the input current.

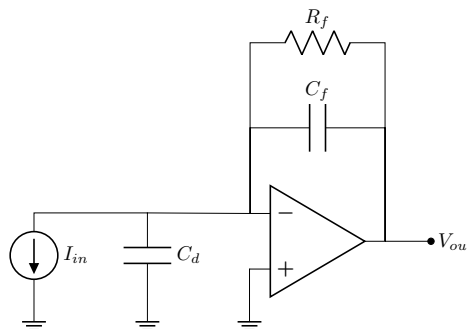


Figure 4.1: Charge Sensitive Amplifier (CSA), adopted from [30].

Assuming that the core amplifier has infinite gain and bandwidth and that the feedback resistor R_f is infinite, the output in the time domain is given by equation (4.1). Taking the Laplace transform of equation (4.1) gives the output of the CSA in the frequency domain, equation (4.2).

$$V_{out}(t) = \frac{1}{C_f} \int I_{in}(t) dt \quad (4.1)$$

$$V_{out}(s) = \frac{I_{in}(s)}{sC_f} \quad (4.2)$$

Where V_{out} is the output voltage of the CSA, C_f is the feedback capacitor, and I_{in} is the input current. Shuffling equation (4.2) to find the transfer function gives equation (4.3).

$$T_{csa}(s) = \frac{V_{out}(s)}{I_{in}(s)} = \frac{1}{sC_f} \quad (4.3)$$

From equation (4.2) assuming that the input can be approximated to a Dirac δ function, $I_{in}(t) = Q_{in}\delta(t)$, the output voltage is given by equation (4.4) and (4.5), where Q_{in} is the total charge of the current pulse and $u(t)$ is the heaviside step function.

$$V_{out}(t) = \frac{Q_{in}}{C_f} u(t) \quad (4.4)$$

$$V_{out}(s) = \frac{Q_{in}}{sC_f} \quad (4.5)$$

4.1.2 CR-RC Shaper

Now that the input current has been integrated and converted to voltage, the signal can be shaped. This can be done with a CR-RC shaper; a practical implementation of this is shown in figure 4.2. After the CSA, there is a differentiator (high pass filter) followed by a low pass filter.

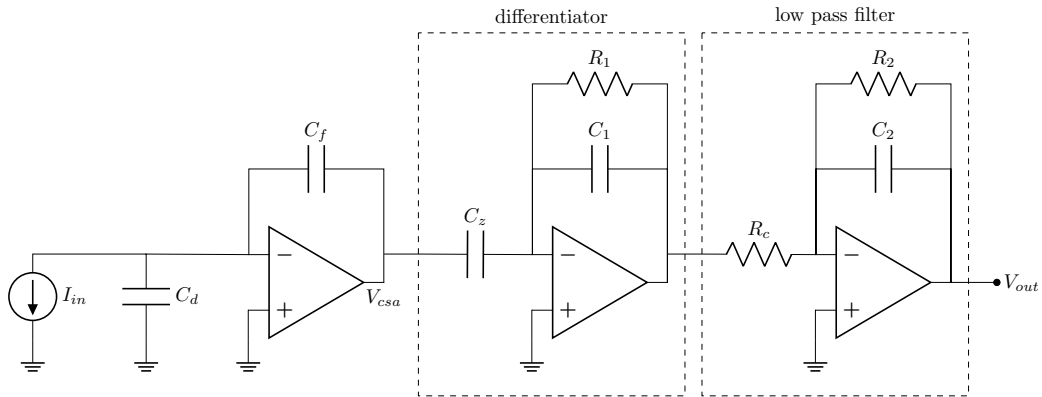


Figure 4.2: Practical implementation of CSA with CR-RC, adopted from [30].

The differentiator (high pass filter) will have the transfer function in equation (4.6), the low pass filter will have the transfer function in equation (4.7). Also the shaping time constant was chosen to be $\tau_{shaper} = R_1C_1 = R_2C_2$.

$$T_{high\ pass}(s) = \frac{sR_1C_z}{sR_1C_1 + 1} = \frac{C_z}{C_1} \frac{s\tau_{shaper}}{s\tau_{shaper} + 1} \quad (4.6)$$

$$T_{low\ pass}(s) = \frac{R_2}{R_c} \frac{1}{sR_2C_2 + 1} = \frac{R_2}{R_c} \frac{1}{s\tau_{shaper} + 1} \quad (4.7)$$

The CR-RC shaper can be extended with several low pass filters to form a CR-RCⁿ shaper, where n is the number of low pass filters in the shaper. Combining the transfer functions in equation (4.3), (4.6) and (4.7) gives the transfer function of the whole CR-RCⁿ shaper, this is shown in equation (4.8). k is the gain of the complete circuit, and is equal to the product of the gain at each stage.

$$T_{shaper,1}(s) = \frac{k}{(1 + s\tau_{shaper})^{n+1}} \quad (4.8)$$

Assuming a Dirac delta pulse input with charge Q_{in} and taking the inverse Laplace transfer gives the impulse response of the circuit, given in equation (4.9).

$$V_{out}(t) = Q_{in} \frac{k}{\tau_{shaper}} \frac{1}{n!} \left(\frac{t}{\tau_{shaper}} \right)^n e^{-\frac{t}{\tau_{shaper}}} \quad (4.9)$$

In figure 4.3 equation (4.9) is plotted for different order filters, where the number of low pass filters is $n = 1, 2, 3$ and 4. $Q_{in}k/\tau_{shaper}$ is set to 1 V and the time constant τ_{shaper} is kept constant at 100 ns.

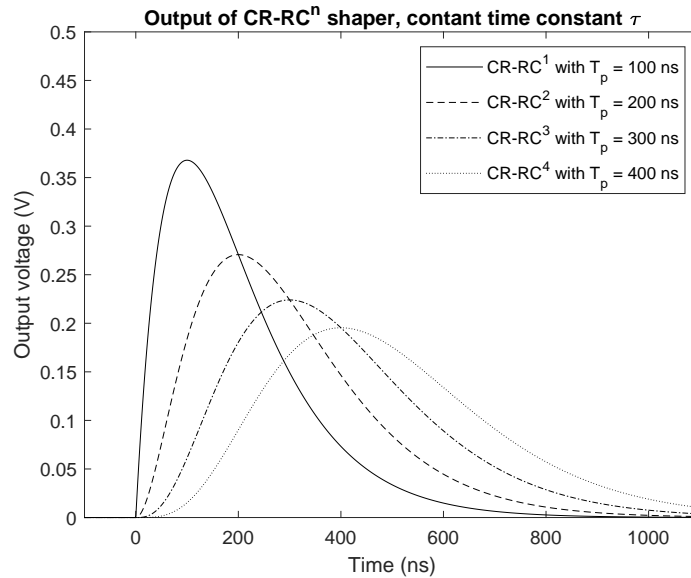


Figure 4.3: Output of CR-RCⁿ filter, with constant time constant $\tau = 100$ ns, adopted from [30].

Setting the derivative of equation (4.9) with respect to time to zero, gives the peak time $T_p = n\tau_{shaper}$. Thus the time constant can be adjusted to obtain the same

peak time for different order filters, $\tau = n/T_p$. Figure 4.4 shows equation (4.9) where the time constant is adjusted to give a constant peak time of 100 ns. The output is also normalized by dividing (4.9) by its peak value, which is obtained by inserting $t = T_p$.

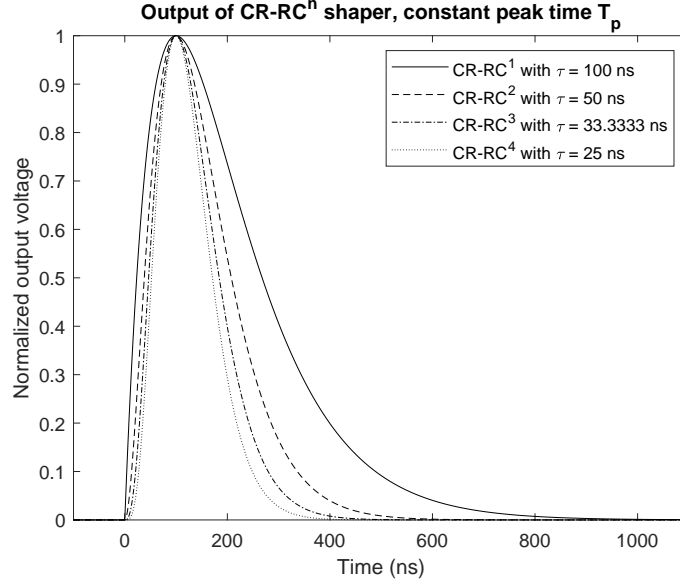


Figure 4.4: Normalized output of CR-RCⁿ filter, with constant peak time $T_p = 100$ ns, adopted from [30].

Figure 4.3 and 4.4 show that the signal can be made narrower by using a higher order filter or longer or shorter by making the time constant longer or shorter.

A CR²-RCⁿ shaper can be made by adding an extra differentiator, like the one in figure 4.2. The differentiator has a transfer function given by equation 4.6, multiplying this with equation (4.8) gives the transfer function for a CR²-RCⁿ shaper, equation (4.10). Assuming the input is equal to $Q_{in}\delta$ and taking the inverse Laplace transform gives equation (4.11).

$$T_{shaper,2}(s) = k \frac{s\tau_{shaper}}{(1 + s\tau_{shaper})^{n+2}} \quad (4.10)$$

$$V_{out}(t) = Q_{in} \frac{k}{\tau_{shaper}} \left(\frac{1}{n!} \left(\frac{t}{\tau_{shaper}} \right)^n e^{-t/\tau_{shaper}} - \frac{1}{(n+1)!} \left(\frac{t}{\tau_{shaper}} \right)^{n+1} e^{-t/\tau_{shaper}} \right) \quad (4.11)$$

Plotting equation (4.11) and using the same values as in figure 4.3 gives the plot in figure 4.5. Comparing figure 4.3 and 4.5, the CR²-RCⁿ shaper has some undershoot. This makes it easier to separate the pulses from each other, but may lead to baseline drift.

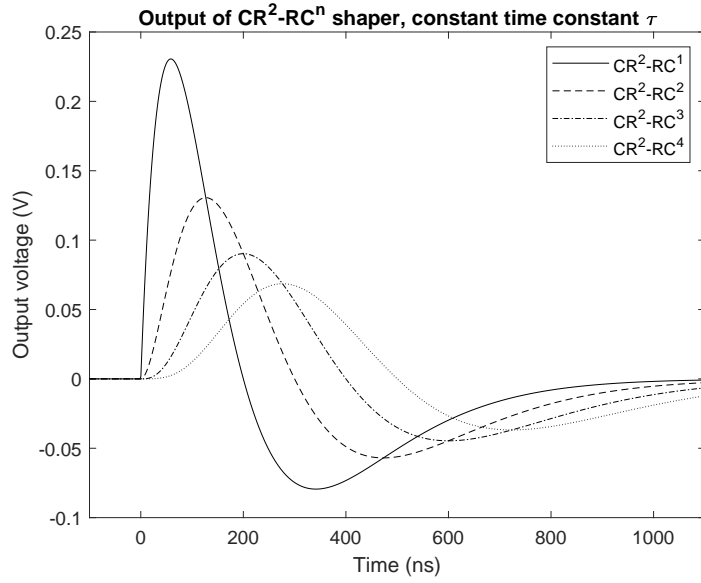


Figure 4.5: Output of CR^2-RC^n filter, with constant time constant $\tau = 100$ ns.

4.1.3 Noise in CSA and $CR-RC^n$

Figure 4.6 illustrates the front-end amplifier with noise sources; they can be categorized as series noise and parallel noise. Series noise is any noise modeled as a voltage source in series with the input of the amplifier, and parallel noise is any noise source modeled as a current source in parallel with the amplifier input.

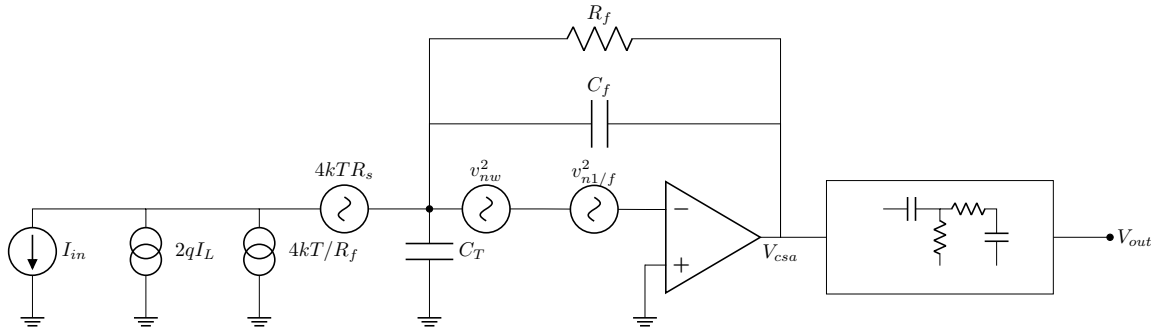


Figure 4.6: Noise sources in CSA, adopted from [30].

The total output noise (integrated over all frequencies) of the $CR-RC^n$ shaper is given by equation (4.12) for white series noise, equation (4.13) for $1/f$ series noise, and equation (4.14) for white parallel noise. Where v_{nw}^2 represents all the white noise sources referred to the amplifier input, A_f corresponds to the $1/f$ noise source, and i_n^2 represents all the white noise sources in parallel to the amplifier input. C_T is the terminal capacitance, which is equal to the sensor capacitance in addition to all other capacitances between the amplifier input and ground.

$$\langle v_{out}^2 \rangle_{nw} = v_{nw}^2 \left(\frac{C_T}{C_f} \right)^2 \frac{B(\frac{3}{2}, n - \frac{1}{2})}{4\pi T_p} n \quad (4.12)$$

$$\langle v_{out}^2 \rangle_{n1/f} = A_f \left(\frac{C_T}{C_f} \right)^2 \frac{1}{2n} \quad (4.13)$$

$$\langle v_{out}^2 \rangle_{ni} = \frac{i_n^2}{C_f^2} \frac{B(\frac{1}{2}, n + \frac{1}{2})}{4\pi n} T_p \quad (4.14)$$

Now the noise can be compared to the output voltage for the signal. The shaper impulse response given by equation (4.15), which is equal to equation (4.9) when $C_z/C_1 = 1$. By inserting $Q_{in} = q$, where q is the electron charge ($q = 1.6022 \cdot 10^{-19}C$), and $t = T_p = n\tau_{shaper}$ the output voltage for a signal of one electron is given by equation (4.16).

$$V_{out}(t) = \frac{Q_{in}}{C_f} \frac{1}{n!} \left(\frac{t}{\tau_{shaper}} \right)^n e^{-\frac{t}{\tau_{shaper}}} \quad (4.15)$$

$$V_{out,peak} = \frac{q}{C_f} \frac{n^n}{n!} e^{-\frac{t}{\tau_{shaper}}} \quad (4.16)$$

Dividing the output noise by the peak voltage from one electron gives the Equivalent Noise Charge (ENC). Equations (4.12), (4.13), and (4.14) are added together to find the total voltage noise squared. This is divided by the square of equation (4.16) to find the ENC squared, given by equation (4.17). Where the first addend is white series noise, the second is flicker series noise, and the third is parallel noise. The indexes N_w , N_f and N_i in equation (4.17) is given by equation (4.18), these are only dependent on the filter order and the type of noise.

$$ENC^2 = \frac{1}{q^2} \left(v_{nw}^2 N_w C_T^2 \frac{1}{T_p} + N_f A_f C_T^2 + i_n^2 N_i T_p \right) \quad (4.17)$$

$$N_w = \frac{B(\frac{3}{2}, n - \frac{1}{2})}{4\pi} n \frac{n!^2 e^{2n}}{n^{2n}}, \quad N_f = \frac{1}{2n} \frac{n!^2 e^{2n}}{n^{2n}}, \quad N_i = \frac{B(\frac{1}{2}, n + \frac{1}{2})}{4\pi n} \frac{n!^2 e^{2n}}{n^{2n}} \quad (4.18)$$

Figure 4.7 shows the contributions of series noise, 1/f noise (flicker noise) and parallel noise of a first order CR-RC shaper ($n = 1$). The values used in the plot are $v_{nw}^2 = 8.3 \times 10^{-18} V^2/Hz$, $i_n^2 = 2.24 \times 10^{-27} A^2/Hz$, $A_f = 8 \times 10^{-13} V^2$ and $C_T = 2$ pF, which are taken from an example in [30]. The total ENC is plotted using the square root of equation (4.17). The contribution from series, flicker and parallel noise are plotted using the square root of each addend in equation (4.17).

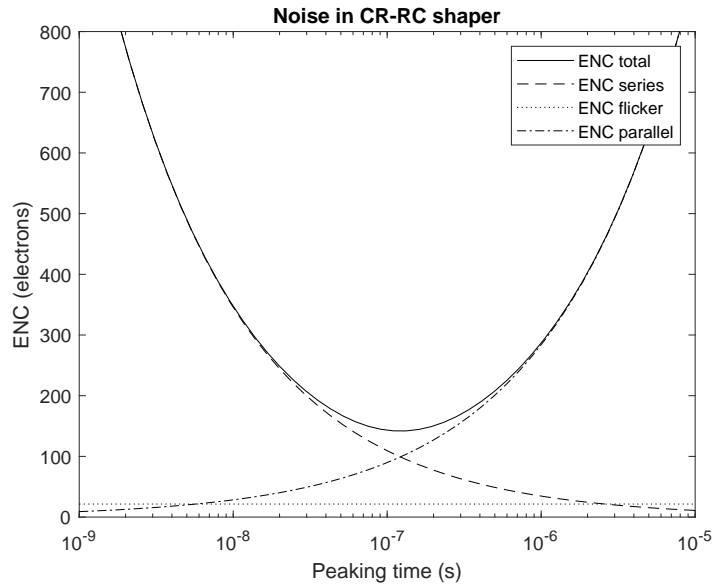


Figure 4.7: General plot of Equivalent Noise Charge, showing the contribution of series, flicker and parallel noise, adopted from [30].

Figure 4.8 shows the ENC when different order shapers are used, the square root of equation (4.17) are plotted with the same values as in figure 4.7 and n from 1 to 7. For applications where a high count rate and low noise are desired, the 2. order seems to be the best. Note that the input is assumed to have a δ -like shape.

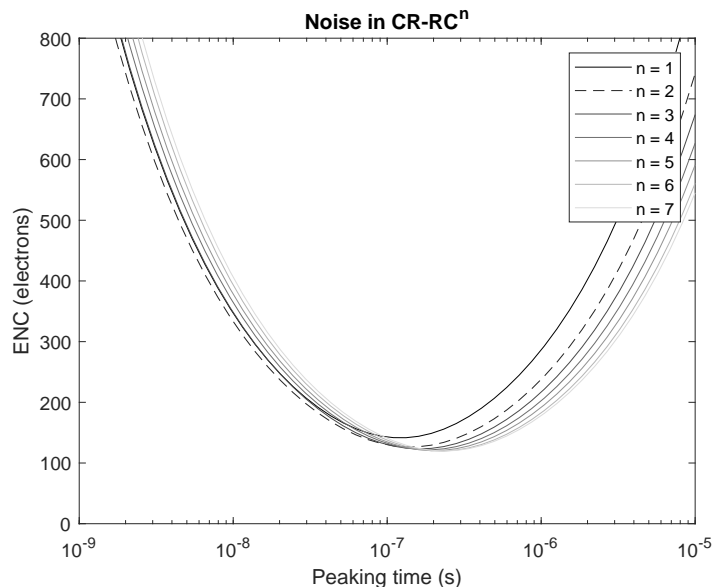


Figure 4.8: General plot of Equivalent Noise Charge for different order shapers

4.1.4 CSA with Finite Feedback Resistor

For an ideal CSA with an infinite feedback resistor, the output voltage (of the CSA) will grow indefinitely, meaning the voltage will just grow higher and higher. Real

amplifiers are limited by their supply voltage, and the output can not be larger than this. Therefore the output must at some point return to zero, and a finite feedback resistor R_f is needed. The transfer function of the CSA is then given by equation (4.21) instead of equation (4.2), now the output voltage for the shaper is given by equation (4.19) in the frequency domain, and equation (4.20) when the input has a δ -like shape.

$$V_{out}(s) = I_{in}(s) \frac{R_f}{1 + s\tau_f} \frac{sC_z R_1}{(1 + s\tau_{sh})^2} \frac{R_2}{R_c} \quad (4.19)$$

$$V_{out}(t) = Q_{in} \left[\frac{C_z R_f R_1 R_2}{R_c \tau_{sh} (\tau_f - \tau_{sh})} \left(\frac{t}{\tau_{sh}} \right) e^{-\frac{t}{\tau_{sh}}} + \frac{C_z R_f R_1 R_2}{R_c (\tau_{sh} - \tau_f)^2} \left(e^{-\frac{t}{\tau_{sh}}} - e^{-\frac{t}{\tau_f}} \right) \right] \quad (4.20)$$

Plotting equation (4.20) gives the graph in figure 4.9, when $R_f = 20 \text{ M}\Omega$, $C_f = 100 \text{ fF}$, $C_z = 5 \text{ pF}$, $R_1 = R_2 = 100 \text{ k}\Omega$, $C_1 = C_2 = 200 \text{ fF}$ and $R_c = 36.79 \text{ k}\Omega$. And the time constants are given by $\tau_f = R_f C_f$ and $\tau_{sh} = R_1 C_1 = R_2 C_2$. Figure 4.9 shows that after the pulse the output of the shaper will be lowered and return slowly to zero, if there is another pulse in close proximity to the first one the peak of the second pulse will be slightly lower, and the voltage after the second pulse will be even lower than after the first pulse, this is shown in figure 4.10.

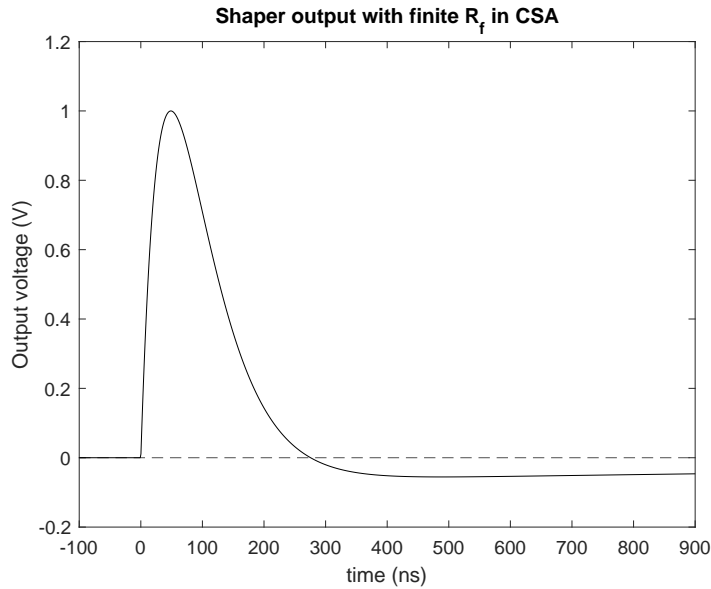


Figure 4.9: Impulse response of CR-RC shaper with finite feedback resistance, adopted from [30].

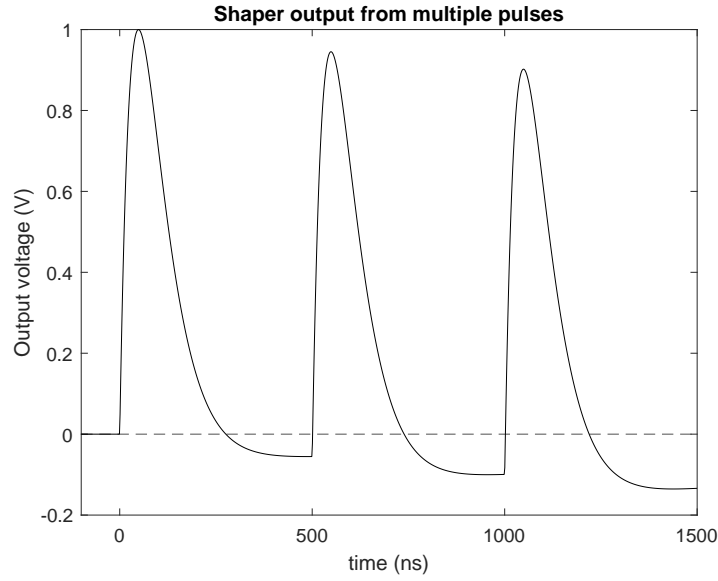


Figure 4.10: Output CR-RC shaper with finite feedback resistance, when multiple pulses hit, showing each pulse is lower than the previous, adopted from [30].

Transimpedance Input Stage

For a CSA with finite feedback resistance the transfer function is given by equation (4.21), then the impulse response is given by equation (4.22). The response of the CSA with finite feedback resistor is now identical to the ideal CSA and the differentiator (in figure 4.2). Adding a low pass filter, as shown in figure 4.11, and choosing $\tau_f = \tau_{sh}$ gives a transfer function (equation (4.23)) which is identical to the equation for the ideal CSA with the differentiator and a low pass filter, figure 4.2 and equation (4.8). More low pass filters can be added to give a higher order filter.

$$T_{csa}(s) = \frac{R_f}{1 + sR_fC_f} = \frac{R_f}{1 + s\tau_f} \quad (4.21)$$

$$V_{out}(t) = \frac{Q_{in}}{C_f} e^{-\frac{t}{\tau_f}} \quad (4.22)$$

$$T(s) = \frac{R_f R_{sh}}{R_c} \frac{1}{(1 + s\tau_{sh})^2} \quad (4.23)$$

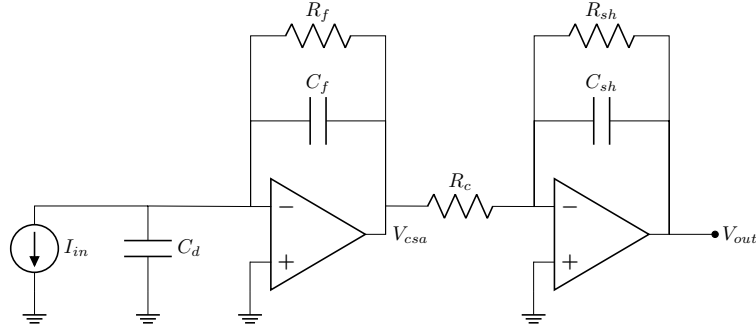


Figure 4.11: Shaper with CSA working in transimpedance mode, when R_f is small, adopted from [30].

The input stage can now be said to work in transimpedance mode. The drawback of this is that the low value of the feedback resistor R_f will cause high parallel noise. The noise from R_f is shown in figure 4.6, and is given by $i_{R_f}^2 = 4kT/R_f$, meaning that the lower R_f is the more parallel noise it produces. However, as seen in figure 4.7, the parallel noise is only dominant for large peak times, and equation (4.17) shows that the parallel noise is not dependent on the terminal capacitance C_T . This means that for an application where the sensor capacitance and the event rate is high, the noise from R_f is small compared to the other noise sources, and this approach is good.

4.2 Shaping of Signal from SiPM

Since the time constants of the SiPM and the LYSO scintillator is relatively close the value of the shaping time constant that will be used, the input can no longer be assumed to be a δ -like pulse. Combining equation (3.23) with equation (4.8) and (4.10), gives the total output in the frequency domain, equation (4.24) and (4.25).

$$V_{out,tot,1}(s) = \frac{QN_{fired}k}{(1 + s\tau_{sipm})(1 + s\tau_{scin})(1 + s\tau_{shaper})^{n+1}} \quad (4.24)$$

$$V_{out,tot,2}(s) = \frac{QN_{fired}k s \tau_{shaper}}{(1 + s\tau_{sipm})(1 + s\tau_{scin})(1 + s\tau_{shaper})^{n+2}} \quad (4.25)$$

Taking the inverse Laplace transform of equation (4.24) and (4.25) does not give one general solution. But inserting some example value, and then taking the inverse Laplace transform, gives a specific solution, even though it does not give every possible solution. Doing this with the values in table 4.1 gives equation (4.26) and (4.27), equation (3.2) is used to calculate the charge, the number of photons at the SiPM is calculated using equation (3.6), and N_f is calculated with equation (3.4).

Variable	Value
filter order n	2
scintillator time constant τ_{scin}	40 ns
SiPM decay time constant τ_{sipm}	45 ns
shaper time constant τ_{shaper}	10 ns
shaper gain k	1 V/A
gain of SiPM G	$6.3 \cdot 10^6$
gamma-photon energy E_γ	100 keV
photon yield Y	25 photons/keV
area of sipm A_{sipm}	$3.07^2 \text{mm}^2 \cdot 64$
area of scintillator A_{scin}	50^2mm^2
total number of microcells N_{total}	$5676 \cdot 64$
photon detection efficiency PDE	50 % = 0.50

Table 4.1: Example values used to demonstrate what the SiPM signal can look like after shaping.

$$\begin{aligned}
V_{out1,example} = & 0.0147 \cdot e^{-100000000 \cdot t} + 0.1273 \cdot e^{-2.2222 \cdot 10^7 \cdot t} - 0.1420 \cdot e^{-2.5000 \cdot 10^7 \cdot t} \\
& + 7.4708 \cdot 10^5 \cdot t \cdot e^{-100000000 \cdot t} + 1.4262 \cdot 10^{13} \cdot t^2 \cdot e^{-100000000 \cdot t}
\end{aligned} \tag{4.26}$$

$$\begin{aligned}
V_{out2,example} = & 0.0473 \cdot e^{-2.5000 \cdot 10^7 \cdot t} - 0.0364 \cdot e^{-2.2222 \cdot 10^7 \cdot t} - 0.0110 \cdot e^{-100000000 \cdot t} \\
& - 7.2056 \cdot 10^5 \cdot t \cdot e^{-100000000 \cdot t} - 2.3092 \cdot 10^{13} \cdot t^2 \cdot e^{-100000000 \cdot t} \\
& - 4.7541 \cdot 10^{20} \cdot t^3 \cdot e^{-100000000 \cdot t}
\end{aligned} \tag{4.27}$$

Plotting equation (4.26) and (4.27) gives the signal in figure 4.12.

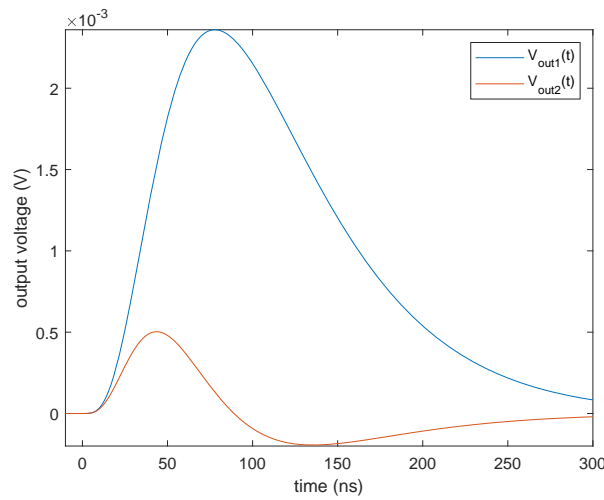
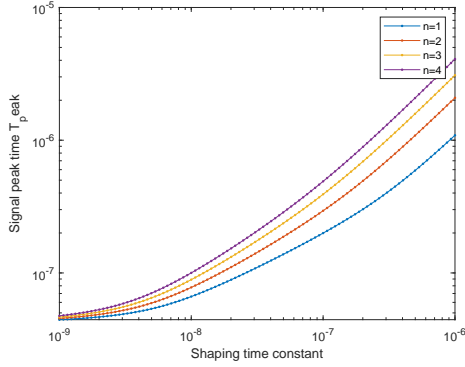


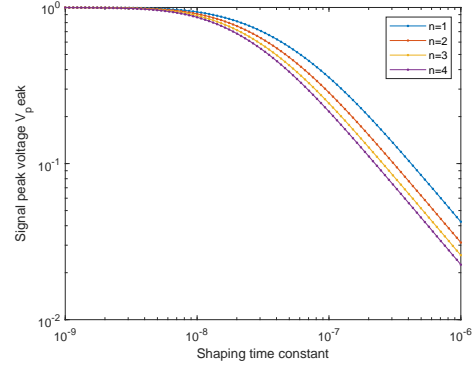
Figure 4.12: Calculated output of shaping circuit with SiPM and LYSO input

Now doing the same exercise that was used to find equation (4.26), but using different shaping time constants and normalizing the voltage peak of the input signal

to 1, gives several equations for the signal shape. Setting the derivative $\frac{dV_{out1}}{dt} = 0$ and solving for t gives the peak time T_{peak} , this is plotted in figure 4.13a versus shaping time constant $\tau_{shaping}$ for filter orders n from 1 to 4. To find the peak voltage of the signal V_{peak} the peak time is inserted into the signal shape equation, this is plotted in figure 4.13b versus shaping time constant $\tau_{shaping}$ for filter orders n from 1 to 4.



(a) Signal peak time versus shaping time constant.

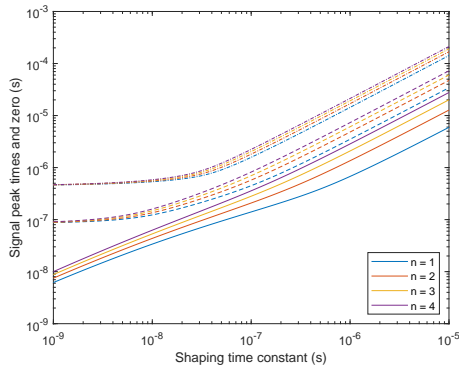


(b) Signal peak voltage versus shaping time constant.

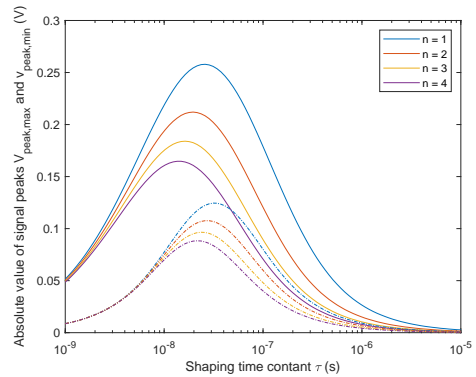
Figure 4.13: Calculated signal height and peak time for different shaper time constants and input signal with real length.

Figure 4.13 shows that the peak time and voltage do not change much for the lower shaping time constants; this is to be expected because the shaping time constant is low compared to the time constants of the input signal. At high shaping time constants, they approach their theoretical values.

Figure 4.14 is plotted using the same recipe as for figure 4.13 but with equation (4.27) instead of equation (4.26).



(a) Signal peak time versus shaping time constant.



(b) Signal peak voltage versus shaping time constant.

Figure 4.14: How shaping time constant affects a input signal with real length. Using a CR^2 - RC^n shaper, since this has a more complex shape the first peak (solid line), the second peak (dash-dotted line) and where the signal crosses the baseline between the peaks (dashed line) were plotted.

Comparing figure 4.14 and 4.13 the first peak time of the $\text{CR}^2\text{-RC}^n$ filtered signal is much lower, making it easier to distinguish pulses. But it will be harder to get good energy resolution because of the undershoot. Figure 4.14b shows that the peak values of the signals is highest around 10 ns to 100 ns.

4.2.1 Filtering of Measurements

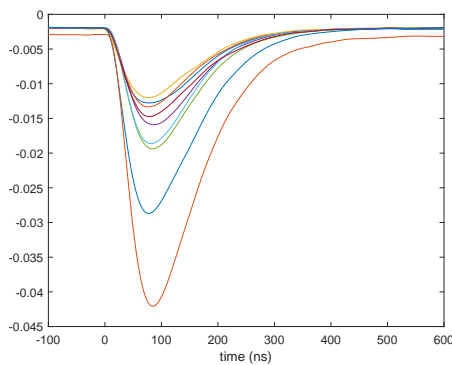
To evaluate if the signal shape in figure 4.12 is correct, a digital version of the CR-RC^n and $\text{CR}^2\text{-RC}^n$ was used on the measured pulse in figure 3.31. The relationship between the continuous and discrete frequency domain is given by equation (4.28), where s is the Laplace variable, z^{-1} is one step back in the discrete time and Δt is the sampling time. This equation is inserted into equation (4.7) and (4.6), this gives the discrete transfer functions in equation (4.29) and (4.30).

$$s = \frac{1 - z^{-1}}{\Delta t} \quad (4.28)$$

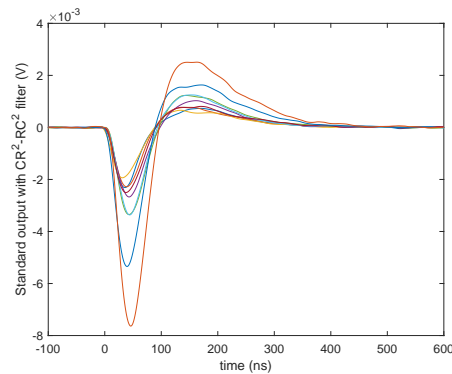
$$T_{low\ pass}(z) = \frac{k\Delta t}{(\tau_{shaper} - \Delta t) - \tau_{shaper}z^{-1}} \quad (4.29)$$

$$T_{high\ pass}(z) = \frac{k - kz^{-1}}{\left(1 - \frac{\Delta t}{\tau_{shaper}}\right) - z^{-1}} \quad (4.30)$$

The filter in equation (4.29) and (4.30) is used on the pulse measurements in figure 3.31a, the shaper time constant was chosen to be $\tau_{shaper} = 10$ ns, the gain was chosen to $k = 1$, and the sampling time on the oscilloscope was $\Delta t = 0.2$ ns. For the CR-RC^n shaper (figure 4.15a) the measured signal was filtered $n + 1 = 2 + 1 = 3$ times with the low pass filter in equation (4.29), and for the $\text{CR}^2\text{-RC}^n$ shaper (figure 4.15b) the measured signal was filtered $n + 1 = 2 + 1 = 3$ times with the low pass filter in equation (4.29) and one time with the high pass filter in equation (4.30). This was done with the `filter` function in MATLAB.



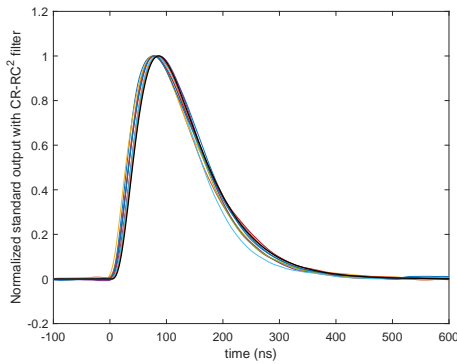
(a) Filtered with digital equivalent of CR-RC^n .



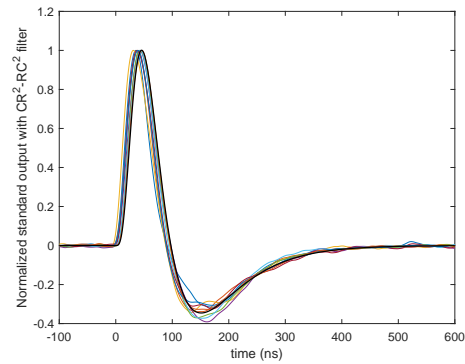
(b) Filtered with digital equivalent of $\text{CR}^2\text{-RC}^n$.

Figure 4.15: Pulse measurements from figure 3.31a (standard output of SiPM coupled with LYSO-scintillator) filtered with digital equivalent of the shaper.

Comparing figure 4.15a and 4.15b the signal will lose some height with $\text{CR}^2\text{-RC}^n$ shaper compared to CR-RC^n shaper, meaning that the $\text{CR}^2\text{-RC}^n$ shaper needs more gain. For this case of the highest pulse here the peak is at -42 mV when filtered with CR-RC^n and the difference between the peaks when filtered with $\text{CR}^2\text{-RC}^n$ shaper is -10 mV . If a $\text{CR}^2\text{-RC}^n$ shaper is used the gain should therefor be around 4 times higher than with a CR-RC^n shaper. The signal in figure 4.15 seems to have the expected form, but to investigate this further the signal in figure 4.15 was normalized and plotted together with the calculated pulse shape (black solid line) using the inverse Laplace transform of equation (4.24) and (4.25), using the same values as for the shaping filter and normalized, and $\tau_{scin} = 40\text{ ns}$ and $\tau_{sipm} = 66\text{ ns}$. This is shown in figure 4.16.



(a) Filtered with digital equivalent of CR-RC^n and normalized.

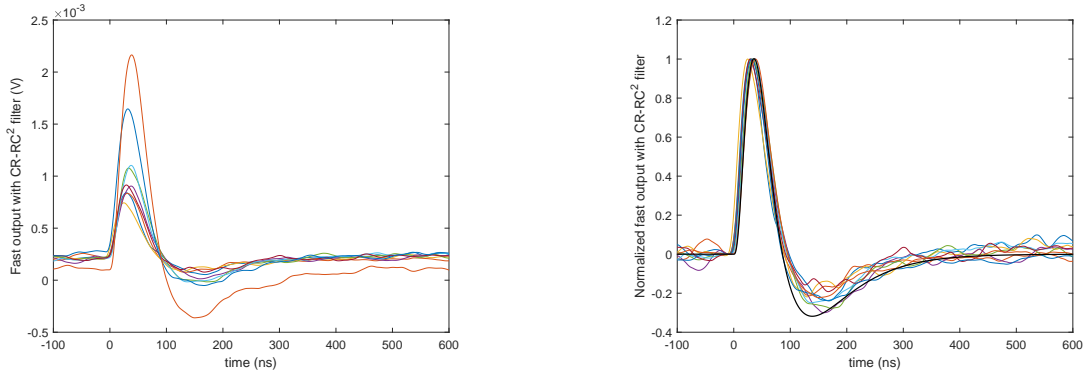


(b) Filtered with digital equivalent of $\text{CR}^2\text{-RC}^n$ and normalized.

Figure 4.16: Pulse measurements from figure 3.31a (standard output of SiPM coupled with LYSO-scintillator) filtered with digital equivalent of the shaper and normalized, the black solid line is the expected signal shape calculated with the inverse Laplace transform of equation (4.24) and (4.25).

Comparing the calculated pulse (black solid line) and the measured and filtered pulses (colored solid lines) in figure 4.16 the calculated pulse looks to be a good estimate of what the final pulse will look like.

Similar filtering and plotting was done for the fast output of the SiPM, the same CR-RC^n equivalent filtering as in figure 4.15a was used on the fast output, this is shown in figure 4.17a. Then the signals was normalized and plotted together with the expected calculated signal, for this the derivative of the calculated signal in figure 4.16a was used (using equation (4.25) with $n = 1$ instead of 2 would be the same), this gives the plot in figure 4.17b.



(a) Fast filtered with digital equivalent of $CR-RC^n$.

(b) Filtered with digital equivalent of $CR-RC^n$ and normalized, the black solid line is the expected signal shape calculated with the inverse Laplace transform of equation (4.25).

Figure 4.17: Pulse measurements from figure 3.31b (fast output of SiPM coupled with LYSO-scintillator) filtered with digital equivalent of the shaper.

The highest signal in figure 4.17a has a difference between its peaks of 2.5 mV which is lower than the high pass filtered standard output in figure 4.15b, the tail also looks noisier on the fast output. From this, it looks like the high pass filtered standard output is better than the fast output, but because the fast output has lower detector capacitance [23], it could be better when connected to a preamplifier, as shown in equation (4.17) the noise is strongly dependent on the terminal capacitance which includes the detector capacitance.

The calculated pulse in figure 4.17b seems to be a good fit, although not as good of a fit as the calculated pulses for the standard output.

4.2.2 Noise Compared to Signal from Front-End Electronics

The calculations in section 4.1.3 assumes that the input is a Dirac delta pulse, that there is a CSA and also it was just done for the $CR-RC^n$ shaper, not the CR^2-RC^n shaper. But the same procedure that was used to find the noise in section 4.1.3 can also be used here (from [30]).

The output noise is in general given by equation (4.31) (from [30]). Where S_n is the power spectral density associated with the noise source and $T_n(j2\pi f)$ is the transfer function seen from the noise source.

$$\langle v_{out}^2 \rangle = \int_0^{\infty} S_n |T_n(j2\pi f)|^2 df \quad (4.31)$$

Starting with the $CR-RC^n$ shaper the transfer function is given by equation (4.8), the square of the absolute value of the transfer function will then be given by equation (4.32) when substituting $s = 2\pi j f$ and $\tau_{shaper} = 1/(2\pi f_0)$.

$$|T(j2\pi f)|^2 = \frac{k^2}{\left(1 + \left(\frac{f}{f_0}\right)^2\right)^{n+1}} \quad (4.32)$$

Since the transfer function of the circuit is voltage per current the power spectral density (used in equation (4.31)) for each current source must be given in current. This is the case for the parallel noise, shown in equation (4.35). But the series noise will give a noise current through C_T (in figure 4.6), the power spectral density is given by equation (4.33). Also the flicker noise $v_{nf}^2 = A_f/f$ will be converted to a current through C_T , where the power spectral density is given by equation (4.34). Also $s = 2\pi jf$ was substituted in these equations.

$$i^2 = |v_n C_T s|^2 = v_n^2 C_T^2 4\pi^2 f^2 = v_n^2 C_T^2 4\pi^2 f_0^2 \left(\frac{f}{f_0}\right)^2 \quad (4.33)$$

$$i_{nf}^2 = |v_{nf} C_T s|^2 = \frac{A_f}{f} C_T^2 4\pi^2 f^2 \quad (4.34)$$

$$i_n^2 = i_{nf}^2 \quad (4.35)$$

Now inserting equations (4.35), (4.33) and (4.34) into equation (4.31) as power spectral density S_n and also inserting equation (4.32) for the transfer function, then calculating the integrals, gives the total output noise for each noise source gives equation (4.36), (4.37) and (4.38). Steps in this calculation is given in appendix D.

$$\langle v_{out}^2 \rangle_{nw} = v_{nw}^2 C_T^2 \frac{1}{4\pi\tau_{shaper}^3} k^2 B \left(\frac{3}{2}, n - \frac{1}{2} \right) \quad (4.36)$$

$$\langle v_{out}^2 \rangle_{n1/f} = A_f C_T^2 k^2 \frac{1}{2\tau_{shaper}^2} \frac{1}{n} \quad (4.37)$$

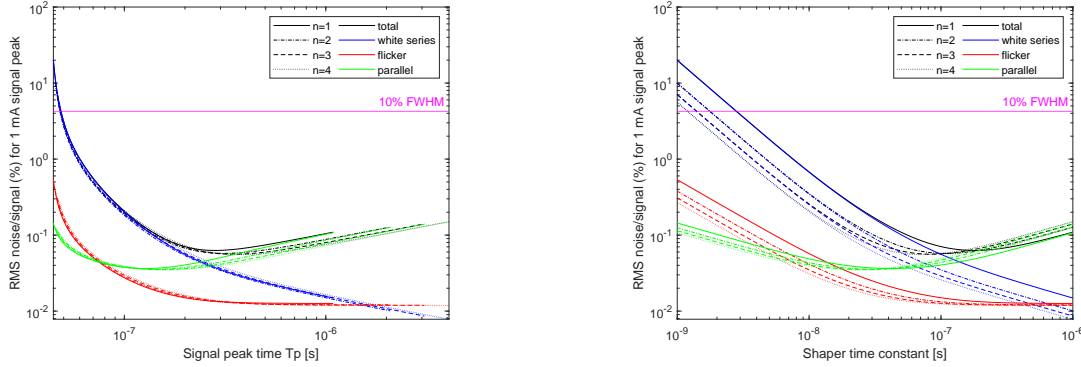
$$\langle v_{out}^2 \rangle_{ni} = i_n^2 \frac{1}{4\pi\tau_{shaper}} k^2 B \left(\frac{1}{2}, n + \frac{1}{2} \right) \quad (4.38)$$

The total noise is then calculated with equation (4.39), from [30].

$$\langle v_{out,tot}^2 \rangle = \langle v_{out,1}^2 \rangle + \langle v_{out,2}^2 \rangle + \dots + \langle v_{out,3}^2 \rangle \quad (4.39)$$

Equation (4.36), (4.37), (4.38) and the total of these using (4.39) is calculated using $v_{nw}^2 = 6.76 \times 10^{-20} \text{ V}^2/\text{Hz}$ and $A_f = 1.2182 \times 10^{-14} \text{ V}^2$ from [31], and $i_n^2 = 2 \cdot q \cdot I_L + 4 \cdot k_B T \cdot R_f$ where the unit charge is $q = 1.602 \times 10^{-19} \text{ C}$, the dark current of the SiPM is used as leakage current $I_L = 64 \cdot 1.9 \times 10^{-6} \text{ A}$ (value from [23]), the Boltzmann constant $k_B = 1.380649 \times 10^{-23} \text{ J/K}$, temperature $T = 300 \text{ K}$, and feedback resistor chosen as $R_f = 1 \Omega$ as a worst case. For the terminal capacitance $C_T = 64 \cdot 1020 \text{ pF}$ the SiPM detector capacitance is used (value from [23]), the filter order is chosen to $n = 1, 2, 3$ and 4 , and a range of shaper time constants τ_{shaper} is used.

Then the square root of equation (4.36), (4.37), (4.38) and the total of these using (4.39) was taken (to get the Root Mean Square (RMS) noise) and divided by the output signal peak, to find this the values in figure 4.13b was multiplied by the input signal peak, here chosen as 1 A which is in the lower range of pulses that will be measured. This gives the plots in figure 4.18, the signal peak time in figure 4.18a is from figure 4.13a.



(a) Percentage of noise over signal for input signal with 1 mA peak and CR-RCⁿ shaper.

(b) Percentage of noise over signal for input signal with 1 mA peak and CR-RCⁿ shaper.

Figure 4.18: Calculated RMS noise from preamplifier compared to signal peak value as a function of signal peak time and shaping time constant, for CR-RCⁿ shaper.

Figure 4.18 shows that the pulse does not need much shaping to remove enough noise for the smallest signals. Looking closely at figure 4.18b the second order filter has the lowest noise at low peak times. Besides, keeping the filter order low will prevent new noise sources not considered here by not adding additional active filters. From figure 4.18b a shaping time constant of 10 ns will remove enough noise and additionally give some margin for noise sources later in the filter, also looking at figure 4.13 this time constant does not change the peak time and value too much.

For the small scintillator (that is only useful for counting), it might be beneficial to differentiate the signal, making the pulses more distinguishable. This can be implemented by adding an extra high pass filter, like in the CR²-RCⁿ shaper.

Now considering the CR²-RCⁿ the transfer function is given by equation (4.10), the square of the absolute value of the transfer function will then be given by equation (4.40) when substituting $s = 2\pi jf$ and $\tau_{shaper} = 1/(2\pi f_0)$.

$$|T(j2\pi f)|^2 = k^2 \frac{\left(\frac{f}{f_0}\right)^2}{\left(1 + \left(\frac{f}{f_0}\right)^2\right)^{n+2}} \quad (4.40)$$

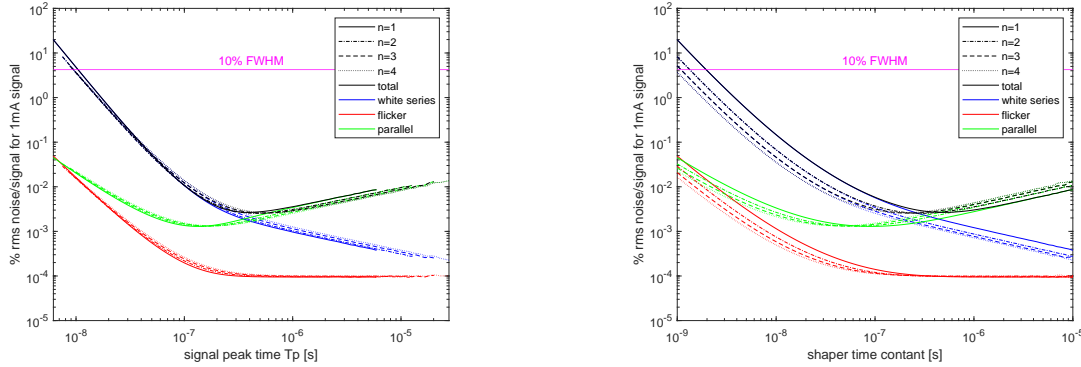
Equation (4.35), (4.33) and (4.34) is inserted into equation (4.31) as spectral density and (4.40) for the squared absolute value of the transfer function. Solving the integral gives equation (4.41), (4.42) and (4.43). Steps in this calculation is given in appendix D.

$$\langle v_{out}^2 \rangle_{nw} = v_{nw}^2 C_T^2 \frac{1}{4\pi\tau_{shaper}^3} k^2 B \left(\frac{5}{2}, n - \frac{1}{2} \right) \quad (4.41)$$

$$\langle v_{out}^2 \rangle_{n1/f} = A_f C_T^2 \frac{1}{2\tau_{shaper}^2} k^2 B \left(2, n \right) \quad (4.42)$$

$$\langle v_{out}^2 \rangle_{ni} = i_n^2 \frac{1}{4\pi\tau_{shaper}} k^2 B \left(\frac{3}{2}, n + \frac{1}{2} \right) \quad (4.43)$$

Figure 4.19 was plotted the same way as figure 4.18, but equation (4.41), (4.42) and (4.43) was used instead of equation (4.36), (4.37) and (4.38). Also the peak value and time from the first peak in figure 4.14 was used (instead of those from figure 4.13). This gives the plots in figure 4.19.



(a) Percentage of noise over signal for input signal with 1 mA peak.

(b) Percentage of noise over signal for input signal with 1 mA peak.

Figure 4.19: Calculated RMS noise from preamplifier compared to signal peak value as a function of signal peak time and shaping time constant, for CR^2 - RC^n shaper.

The noise in figure 4.19 looks mostly the same as in figure 4.18 for the domination noise levels. Therefore a shaping time constant of 10 ns would work fine for this filter as well.

4.3 Schematic and Choice of Components

As a starting point, the shaping from [1] was used. This includes these components; OPA855 for the preamplifier, THS4304 for the filter stage, and THS4505 for the ADC-driver.

4.3.1 Preamplifier

The amplifier's characteristics should be such that it can still be assumed as an ideal amplifier. Meaning that the bandwidth and gain are large enough, about a factor of ten above the bandwidth and gain for the system. The amplifier should also have low noise-also, for this case, the maximum current of the amplifier needs to be considered. This is because the current from the output of the amplifier needs to be the same as the current from the current source (since no current can go into the input for an ideal opamp), regardless of what C_f and R_f is. This is shown in figure 4.20.

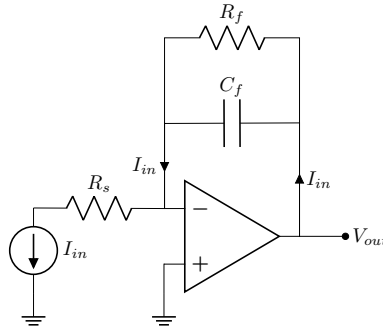


Figure 4.20: Circuit diagram of preamplifier stage with current shown.

Note that the non-inverting input in figure 4.20 is connected to ground; this can be connected to a DC-voltage to adjust the common-mode of the signal. A common-mode voltage will be useful to center the signal around ground before the ADC driver which will center it around the reference of the ADC. If the right common-mode is chosen, most of the ADCs dynamic range will be utilized.

OPA855 will be fine as a preamplifier when using a single unit of SiPM since the maximum signal that is needed to measure is around 50 mA, shown in figure 3.17b. This current is lower than the maximum that OPA855 is able to deliver from the output [32]. Also, the gain, bandwidth, and noise are within the requirements for this amplifier.

For the array of 64 SiPMs the maximum signal is larger, a bit over 1 A for the red dashed line shown in figure 3.16b. This is much more than OPA855 is able to deliver on its output and behaves oddly in simulations with large input current signals. Therefore a new amplifier is needed.

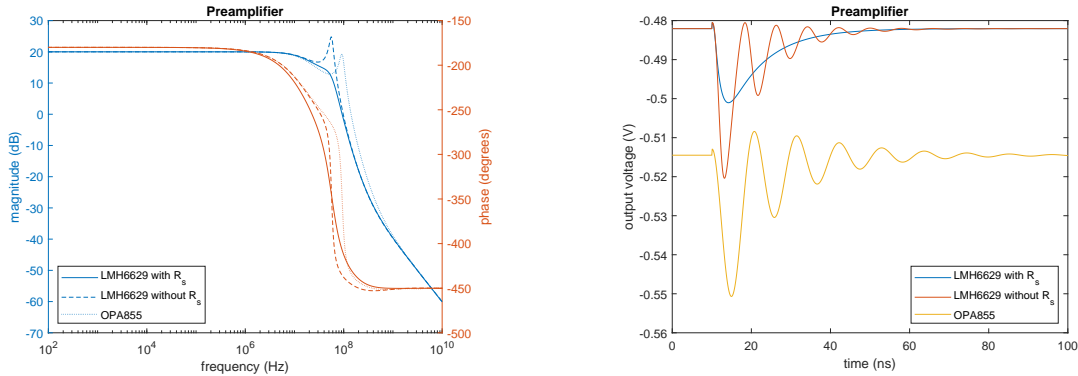
An amplifier with more than 1 A output current would be ideal (which would be able to drive the signals in figure 3.16b), but the bandwidth of such amplifier is too low (most has been around 1 MHz). The time constant for the shaping will be around 10 ns which corresponds to $100/2\pi \text{ MHz} \approx 16 \text{ MHz}$, the bandwidth of the amplifiers should be more than ten times this to still consider them ideal, thus at least 160 MHz, also there should be some room in the Gain-Bandwidth Product (GBW) to have some gain in the circuit (around 10 V/A). Therefore the amplifier should have at least 160 MHz bandwidth and as high output current as possible. The gain of the amplifier is not that important since the current signal is already high, but low noise is important since this increases Signal to Noise Ratio (SNR). OPA855 has $0.98 \text{ nV}/\sqrt{\text{Hz}}$, preferably the new amplifier should not have noise much higher than this.

Part number	GBW (MHz)	Noise at 1 kHz	Output current (mA)
OPA588	8000	1.9	80
LMH6629	4000	0.69	250
THS4271	1400	3	160
OPA2614	290	1.8	350

Table 4.2: Comparison of different amplifiers from [33].

Simulation results of the preamplifier alone are shown in figure 4.21a (frequency

response) and figure 4.21b (impulse response), this was simulated in PSpice from Texas Instruments. LMH6629 was simulated with and without any series resistance, R_s in figure 4.20, the simulation was also done with OPA855 (without R_s) to compare. The feedback resistor was $R_f = 10 \Omega$, shaping time constant was $\tau_{shaper} = 10 \text{ ns}$, the feedback capacitor was $C_f = \tau_{shaper}/R_f$ and the series resistance was set to $R_s = 0.1 \Omega$. The schematic from the simulation program is shown in appendix B.1.1 and B.1.2.



(a) Magnitude and phase from simulation of frequency response.

(b) Results from transient simulation of impulse response.

Figure 4.21: Results from simulation of preamplifier stage alone.

Both the frequency and impulse response in figure 4.21 show that LMH6629 with a small series resistor is the most stable; this will be used further. Since this resistor is so small, the wire resistance may be enough to achieve this stability in the physical implementation. However, to be sure, a slot for this R_s will be added in the PCB that can be shorted if not needed.

Since none of the amplifiers in table 4.2 can deliver the full current the SiPM array alone needs, using one preamplifier will not work. An alternative option is to have one preamplifier per SiPM-pixel in the array, then implement a summing amplifier in the filter stage. From the plots in figure 3.43a and 3.43b this option will slow down the signal the least. However, this option will take up a large area and consume more power; also, it might add more noise if the detector capacitance is no longer so large that the noise (in equation 4.17) is approximately proportional to it.

The compromise between these two options is to connect groups of pixels (this has been done in [34]), where M number of pixels are connected in parallel and into one preamplifier; this makes N number of groups which needs one preamplifier each. Then the N number of signals from the preamplifiers is combined in with a summing amplifier at the filter stage. As shown in figure 3.16b, the highest signal is a bit above 1 A (ignoring the SiPM-array with $6 \text{ mm} \times 6 \text{ mm}$ pixels, since it already has a board that reads the sum of the signal). This peak may be lower due to photons lost in the optical coupling or the signal being slower than what the data sheet promises (see for example figure 3.48), but the overvoltage can also be adjusted to make the signal lower. This means that the lowest number of groups that will work is $N = 4$ since LMH6629 can deliver up to 250 mA of current, which makes $M = 16$ pixels in each group. The pixels in each group in the SiPM array will be connected in parallel

and then be connected to the preamplifier input, similar to the measurements with the of SiPM with preamplifier (figure 3.45).

Then, the output of the four preamplifiers will be connected to one summing amplifier at the filter stage; this will be described further in section 4.3.2, a simplified illustration is shown in figure 4.22. For the single SiPM, only one preamplifier is needed (as the largest signal shown in figure 3.17b). This should also be enough for the fast output since the fast output is about a factor ten lower than the standard output (see figure 3.31b).

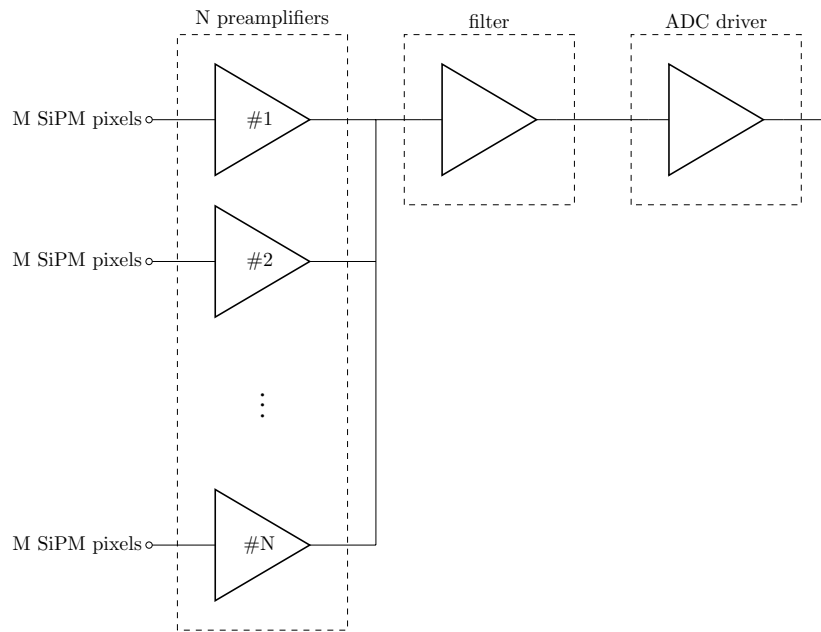


Figure 4.22: Simplified circuit showing how several amplifiers will be connected the filter and ADC driver stages.

4.3.2 Filter

In general the filter stage can be used as a high pass or low pass filter. For the front-end electronics of the SiPM array this stage could also be used as a summing amplifier, as illustrated in figure 4.23.

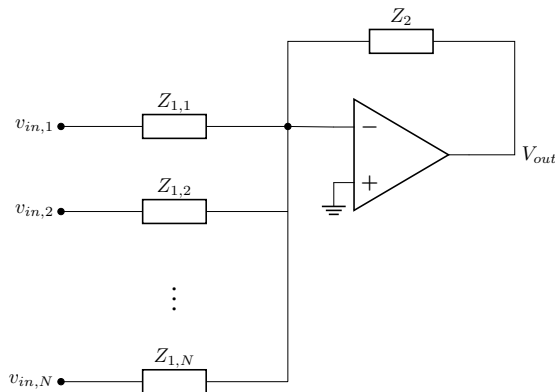


Figure 4.23: Circuit diagram of general summing amplifier.

Applying Kirchhoff's laws on the circuit in figure 4.23 and choosing $Z_1 = Z_{1,1} = Z_{1,2} = \dots = Z_{1,N}$ gives equation (4.44).

$$V_{out} = -\frac{Z_2}{Z_1} (v_{in,1} + v_{in,2} + \dots + v_{in,N}) \quad (4.44)$$

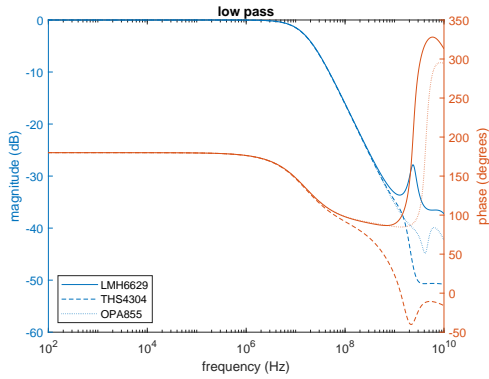
Choosing $Z_2 = R_2 \parallel (1/C_2) = R_2/(sR_2C_2 + 1)$ will make a pole in the transfer function. If $Z_1 = R_1$ the filter will be a low pass filter, with equation (4.45).

$$V_{out}(s) = -\frac{R_2}{R_1} \frac{1}{sR_2C_2 + 1} (v_{in,1} + v_{in,2} + \dots + v_{in,N}) \quad (4.45)$$

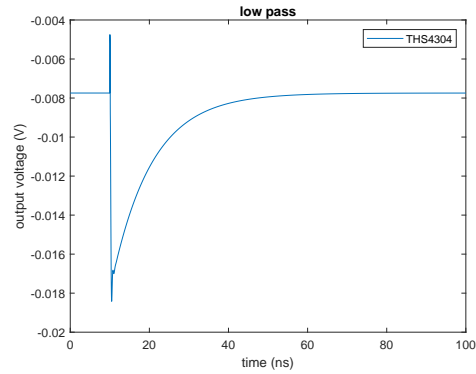
If $Z_1 = 1/(sC_2)$ the filter will be a high pass filter with equation with equation (4.46).

$$V_{out}(s) = -\frac{sR_2C_1}{sR_2C_2 + 1} (v_{in,1} + v_{in,2} + \dots + v_{in,N}) \quad (4.46)$$

The filter stage was simulated for a simple low pass and high pass filter (with just one input) for a few different amplifiers. The results of the frequency response is shown in figure 4.24a for the low pass filters and figure 4.25a for the high pass filter, the results of the impulse response is shown in figure 4.24b for the low pass filters and figure 4.25b for the high pass filter. The values used was $R_1 = 1 \text{ k}\Omega$, $R_2 = 1 \text{ k}\Omega$, $\tau_{shaper} = 10 \text{ ns}$, $C_2 = \tau_{shaper}/R_2 = 10 \text{ pF}$ and $C_1 = 4 \cdot C_2 = 40 \text{ pF}$ (these are the same variables as used in equation (4.45) and (4.46)). Also the schematic from PSpice is shown in appendix B.1.1 and B.1.2. Note that in figure 4.24b the simulation results for two of the amplifiers are not shown, since they were unstable in this configuration.

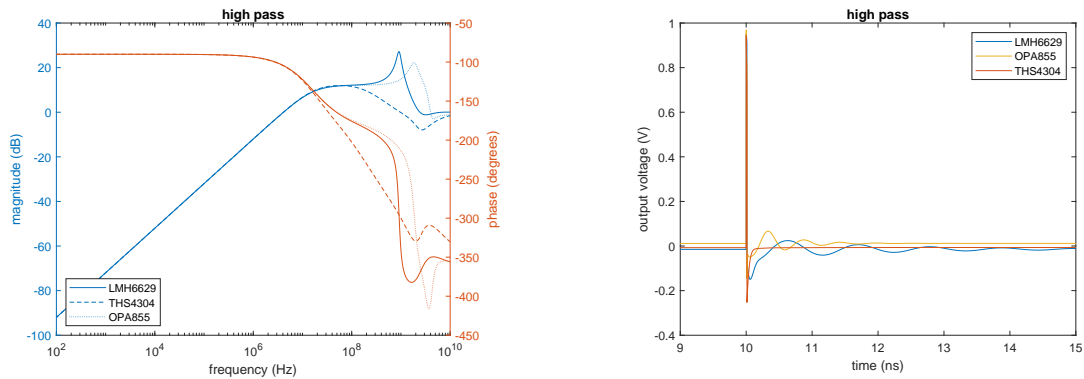


(a) Magnitude and phase from simulation of frequency response.



(b) Results from transient simulation of impulse response.

Figure 4.24: Results from simulation of low pass filter stage alone.



(a) Magnitude and phase from simulation of frequency response.

(b) Results from transient simulation of impulse response.

Figure 4.25: Results from simulation of high pass filter stage alone.

From figure 4.24 and 4.25 it can be concluded that THS4304 will work best (out of the tested amplifiers) filter stage. And as seen in the impulse response, this will also work for both high pass and low pass filters.

4.3.3 ADC Driver

The ADC driver converts the single ended input signal and outputs a differential signal, which is ideal for the ADCs [35, 36]. It also centers the signal around a common mode DC level given by the ADC. The circuit for this was mostly kept as in [1], and a circuit diagram is shown in figure 4.26. When used with one input, the values of the resistors and capacitors were changed to obtain the desired time constants in the filter.

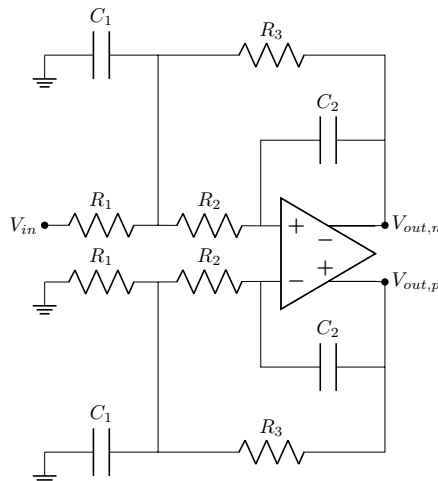


Figure 4.26: Circuit for ADC driver stage, using a second order low pass multiple-feedback filter, as in [1].

Applying Kirchhoff's laws to the circuit in figure 4.26 (looking at only one side of the filter) gives the transfer function in equation (4.47), the variables in the equation

is shown in figure 4.26. The transfer function for a filter with two equal poles is given in equation (4.48), where $\tau = RC$ and R and C is a resistance and a capacitance.

$$T_{ADC\ driver}(s) = \frac{V_{out}(s)}{V_{in}(s)} = \frac{-R_3/R_1}{s^2 R_2 R_3 C_1 C_2 + s \left(\frac{R_2 R_3}{R_1} + R_3 + R_2 \right) C_2 + 1} \quad (4.47)$$

$$T_{2\ poles}(s) = \frac{-k}{(s\tau + 1)^2} = \frac{-k}{s^2 R^2 C^2 + 2sRC + 1} \quad (4.48)$$

Comparing the equations (4.47) and (4.48) gives the set of equations in equation (4.49).

$$\frac{R_3}{R_1} = k, \quad R_2 R_3 C_1 C_2 = R^2 C^2, \quad \left(\frac{R_2 R_3}{R_1} + R_3 + R_2 \right) C_2 = 2RC \quad (4.49)$$

Solving equation (4.49) and choosing $R_3 = R$ and $C_2 = C$ to get one simple solution gives the resistor and capacitor values in equation (4.50).

$$R_1 = \frac{1}{k}R, \quad R_2 = \frac{1}{k+1}R, \quad R_3 = R, \quad C_1 = (k+1)C, \quad C_2 = C \quad (4.50)$$

It was shown in section 4.3.1 that four preamplifiers are needed, the signal from these can be summed in the next amplifier stage. In the case where the filter stage is skipped, the ADC driver can be used as a summing amplifier instead. The circuit diagram for this is shown in figure 4.27.

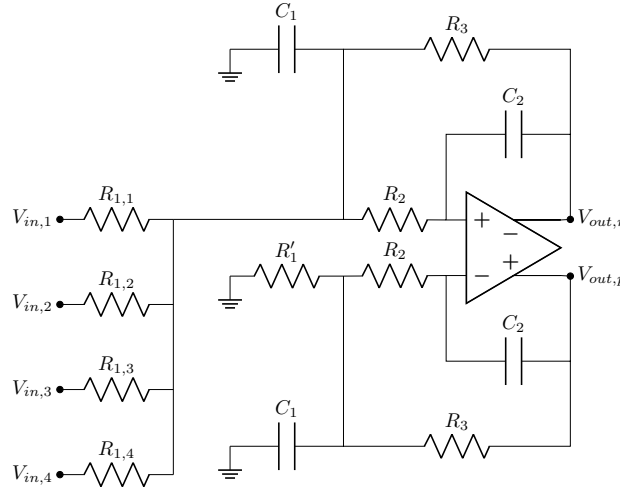


Figure 4.27: Extended ADC driver (in figure 4.26) to be used as a summing amplifier.

Setting the resistors $R_{1,1} = R_{1,2} = R_{1,3} = R_{1,4} = R_1$ and applying Kirchhoff's laws (looking at the upper half of the circuit in figure 4.27) gives the output in equation (4.51).

$$V_{out,ADC\ driver}(s) = \frac{-(R_3/R_1) \cdot (V_{in,1} + V_{in,2} + V_{in,3} + V_{in,4})}{s^2 R_2 R_3 C_1 C_2 + s \left(4 \frac{R_2 R_3}{R_1} + R_3 + R_2 \right) C_2 + 1} \quad (4.51)$$

Comparing the equations (4.51) and (4.48) gives the set of equations in equation (4.52).

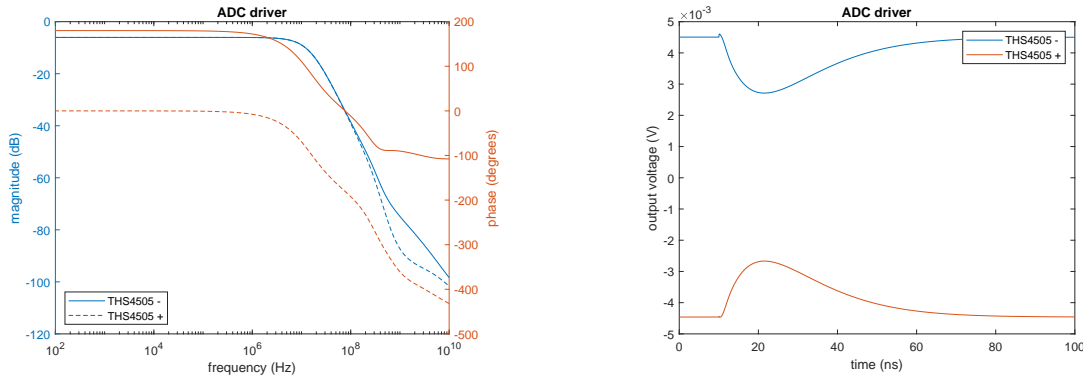
$$\frac{R_3}{R_1} = k, \quad R_2 R_3 C_1 C_2 = R^2 C^2, \quad \left(4 \frac{R_2 R_3}{R_1} + R_3 + R_2\right) C_2 = 2RC \quad (4.52)$$

Solving equation (4.52) and choosing $R_3 = R$ and $C_2 = C$ to get one simple solution gives the resistor and capacitor values in equation (4.53).

$$R_1 = \frac{1}{k}R, \quad R_2 = \frac{1}{4k+1}R, \quad R_3 = R, \quad C_1 = (4k+1)C, \quad C_2 = C \quad (4.53)$$

R'_1 needs to be equal to $R_1/4$ to give the correct output, and R'_1 is equivalent to four of R_1 connected to ground in parallel.

Figure 4.28 shows results from simulations of frequency response and impulse response. Here the simple ADC driver (in figure 4.26) is simulated, the values used was $R = 1 \text{ k}\Omega$, $\tau_{shaper} = 10 \text{ ns}$, $C = \tau_{shaper}/R = 10 \text{ pF}$ and $k = 1$, this gives the specific values for each resistor and capacitors (as shown in figure 4.26): $R_1 = R/k = 1 \text{ k}\Omega$, $R_2 = R/(k+1) = 500 \Omega$, $R_3 = R = 1 \text{ k}\Omega$, $C_1 = C \cdot (k+1) = 20 \text{ pF}$ and $C_2 = C = 10 \text{ pF}$. The amplifier used was THS4505. Schematics from the simulation program PSpice is shown in appendix B.1.1 and B.1.2.



(a) Magnitude and phase from simulation of frequency response.

(b) Results from transient simulation of impulse response.

Figure 4.28: Results from ADC driver simulation alone.

The results in figure 4.28 show that THS4505 will work fine as a ADC driver and that the filtering circuit around works as expected.

4.3.4 Diode Clippers

For LMH6629 the absolute maximum ratings are listed for single supply, the maximum analog input voltage is given as -0.5 to V_S , if using a dual supply $\pm V_S$ should be within this. For 5V single supply the typical output voltage range is 0.82V to 4.19V, for a dual supply of $\pm 2.5 \text{ V}$ this should correspond to -1.68 V to 1.69 V . The typical output voltage swing for THS4304 is 1.1 V to 3.9 V and is also given

for 5V single supply, this corresponds to ± 1.4 V for dual supply of ± 2.5 V. All the values for the amplifiers LMH6629, THS4304 and THS4505 are found in their data sheets [31, 37, 38], a summary of the relevant values are in table 4.3, the inputs are absolute maximum ratings. V_S is the supply voltage, for LMH6629 and THS4304 it is 2.5 V and for THS4505 it is 5 V.

Amplifier	LMH6629	THS4304	THS4505
Input voltage (V)	$\pm V_S$	$\pm V_S$	$\pm V_S$
Differential input voltage (V)	3	2	4
Output voltage swing (V)	-1.68 to +1.69	± 1.4	$\pm 8^1$
Output current (mA)	250	140	130 ¹

Table 4.3: Analog input and output range for amplifiers.

The connection between LMH6629 and THS4304 should not be a problem since both will have a supply voltage of ± 2.5 V; therefore, the output of LMH6629 will never exceed ± 2.5 V which will be the maximum input voltage on THS4304. The output of LMH6629 will be connected to the inverting input of THS4304, and the non-inverting input will be connected to ground or a DC voltage. The maximum differential input voltage is at 2V, and the inverting input can only be between -1.68 V and 1.69 V, so this will be fine as long as the non-inverting input is between -0.31 V and 0.32 V. When it comes to THS4505, the inverting input will be connected to THS4304, which can only deliver ± 1.4 V and the non-inverting input will be connected to ground (through some filtering circuit), so will not be any problems here.

Also the input of the ADCs needs to be considered, the input voltages that the analog inputs (that will be connected to the output of THS4505) are listed in table 4.4, and are from the data sheets [36, 35].

ADC	ADS5404	AD9257
Minimum input voltage (V)	-0.5	-0.3
Maximum input voltage (V)	$AVDD33 + 0.5$	+2.0

Table 4.4: Absolute minimum and maximum input voltage to the analog inputs on the ADCs.

The inputs of the ADCs will be connected to the output of THS4505; the differential output swing is ± 8 V, looking at the overdrive recovery for single ended output in the data sheet [38], it looks like each output has a range of around -4 V to 4 V, this is clearly beyond what the input of the ADCs can withstand, as shown in table 4.4. Therefore it is necessary to put diode clippers between these to protect the ADC input; these can be connected as shown in figure 4.29.

¹Differential (meaning that this value is for the difference between the two outputs of the amplifier)

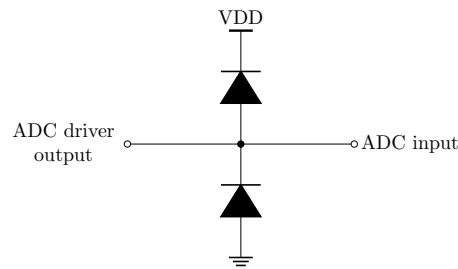


Figure 4.29: Common connection for diode clippers, if the signal is above VDD or below ground the signal will be clipped.

Connection the diodes as in figure 4.29 means that the signal will be cut a bit above VDD and a bit below ground, how much depends on the forward voltage across the diode. For AD9257 $AVDD = 1.8\text{ V}$ can be used (as VDD), since the maximum is at 2.0 V the forward voltage on the diode is ideally 0.2 V , the minimum is at -0.3 V compared to ground. For ADS5404 the signal can be 0.5 V below ground and above $AVDD33 = 3.3\text{ V}$, so a diode with forward voltage equal to or below 0.5 V will be fine.

Therefore a diode with low forward voltage should be used; this was read at 100 mA from the data sheets², this value is usually easy to find, and it gives some margin because THS4505 can give up to 130 mA in differential output current, meaning that each output can give up to 65 mA . Additionally, the diode should have low capacitance not to affect the signal's bandwidth. The forward voltage at 100 mA and capacitance at 1 V reverse voltage is plotted for different diodes in figure 4.30.

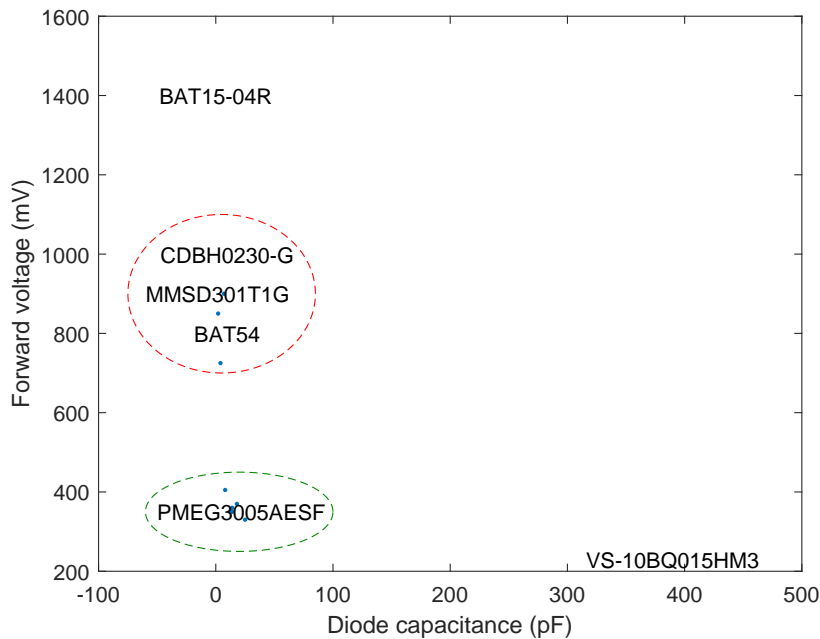


Figure 4.30: Diode capacitance and forward voltage for different diodes

²A numerous amount of diodes were looked at, and forward voltage noted, therefore most of these is not in the reference list, but the ones that will be used are.

The groups marked with a red and green ring in figure 4.30 is zoomed in on and shown in figure 4.31a and 4.31b.

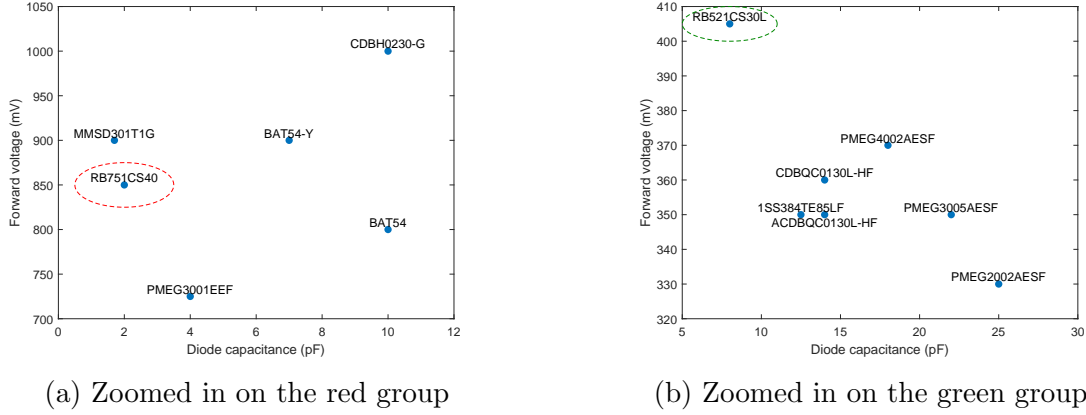


Figure 4.31: Diode capacitance and forward voltage for a selection of diodes

Further, either RB751CS40 (with data sheet [39]) or RB751CS30L (with data sheet [40]) will be used. RB751CS40 has lower capacitance but higher forward voltage, while RB751CS30L has lower forward voltage but higher capacitance, a slot that fits either of these diodes will be added to the PCB.

4.3.5 Analog to Digital Converters

There are two ADCs on the High-Speed ADC Board, some of the relevant parameters are shown in table 4.5, and are from the data sheets [35, 36]. These two ADC provide two versions of a compromise between sampling rate and the number of bits. Therefore it must be considered if or what these will be used for.

ADC	ADS5404	AD9257
Number of bits	12	14
Effective number of bits	9.8	12.3
Sampling rate (MHz)	500	65
Number of channels	2	8

Table 4.5: ADC parameters.

When choosing which ADC should be used for what, both the dynamic range needed (the number of bits) and the frequency content of the signal are considered. Nyquist sampling theorem states what the sampling frequency f_s must be in relation to the maximum frequency if the signal f_{MAX} ; this is shown in equation (4.54).

$$f_s \geq 2f_{MAX} \quad (4.54)$$

Figure 4.32 shows the frequency content of the signal from SiPM and LYSO shaped with CR-RC², with different shaper time constants. This is plotted using equation (4.24), with filter order $n = 2$, time constants for SiPM and LYSO from

table 3.3, 3.1, and 3.2, and kQN_{fired} is set to a value that normalizes the function. The Laplace variable $s = 2\pi jf$, where $j = \sqrt{-1}$ and f is the frequency (x-axis on the plot). The decibel value is found using equation (4.55), where V_{in} is a unit impulse. Also two lines are added to show $f_s/2$ for both ADCs.

$$dB = 20 \log_{10} \left(\frac{V_{out}}{V_{in}} \right) \quad (4.55)$$

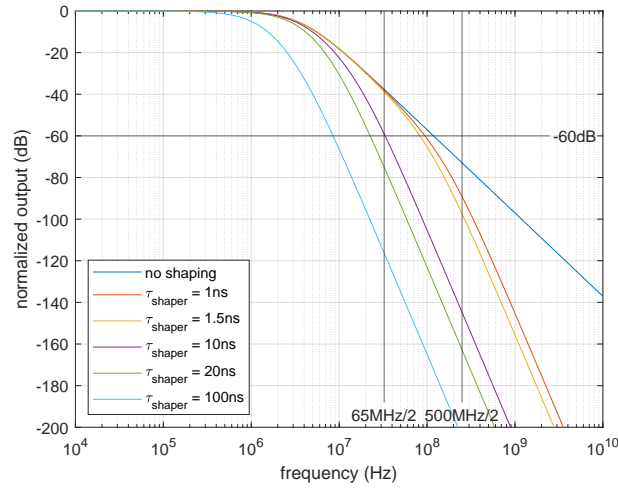


Figure 4.32: Normalized frequency content of signal from SiPM, LYSO-scintillator and CR-RCⁿ filter.

Figure 4.33 is plotted in the same way as figure 4.32, but equation (4.25) is used instead and $kQN_{fired}\tau_{shaper}$ is set to a value that normalizes the function. Figure 4.32 shows the frequency content of the signal from SiPM and LYSO shaped with CR²-RC². The frequency content of the fast output of the SiPM with a CR-RC² would be the same since the fast output is the derivative of the standard output, and the plot is normalized.

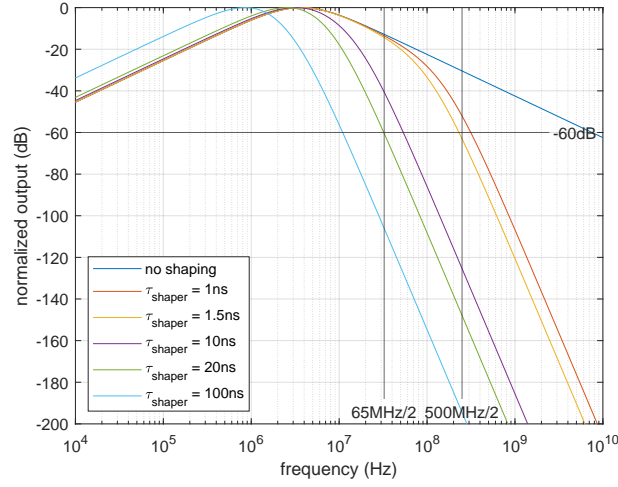


Figure 4.33: Normalized frequency content of signal from SiPM, LYSO-scintillator and $\text{CR}^2\text{-RC}^n$ filter, this will also be similar to using the fast output of the SiPM and CR-RC^n filter.

This signal has frequency components up to infinity, but assuming everything under -60 dB is low enough to ignore, f_{MAX} can be set to where the signal crosses the -60 dB-line. Considering the plot in figure 4.32, using a sample rate of 500 MHz is enough to capture the signal without any shaping, if using a sample rate of 65 MHz the shaping time constant needs to be at least 10 ns to capture the signal. For the plot in figure 4.33, using a sample rate of 500 MHz is enough to capture the signal for shaping time constants above 1.5 ns, if using a sample rate of 65 MHz the shaping time constant needs to be at least 20 ns to capture the signal. Moreover, theoretical values (from the data sheets) for the SiPM and LYSO time constants are used; from measurements, these are higher, which makes the maximum frequency lower and the margin to Nyquist sampling theorem larger.

When it comes to the dynamic range ADS5404 has 12 bits (table 4.5), this gives $2^{12} = 4096$ different levels, these can be represented with values from 0 to 4095. Assuming that the relationship between the γ -photon energy and the ADC-input is linear and the whole ADC-range can be used; 60 MeV would be at 4095, 662 keV would be at 45.2 and 100 keV would be at 6.83. In the case of AD9257 which has 14 bits, which gives 16384 levels and a range from 0 to 16383; 60 MeV would be at 16383, 662 keV would be at 180.7 and 100 keV would be at 27.3.

The quantitation error of an ADC can be calculated using equation (4.56), where V_{max} is the maximum input signal, V_{min} is the minimum input signal, and n is the number of bits.

$$\Delta V_{\text{quantization error}} = \frac{V_{max} - V_{min}}{2^n} \quad (4.56)$$

Equation (4.57) is the PDF for a uniform distributing, where a or δ is the width of the PDF. Equation (4.58) is the PDF of a normal distributing, where σ is the standard deviation. μ is the mean value. The relationship between the uniform and standard deviation is given by equation (4.59). Further, the standard deviation can

be converted to a FWHM (of a normal distribution) using equation (4.60).

$$f(x) = \begin{cases} \frac{1}{a} & \text{for } |x - \mu| \leq \frac{a}{2} \\ 0 & \text{for } |x - \mu| > \frac{a}{2} \end{cases} \quad (4.57)$$

$$f(x) = \frac{1}{\sigma\sqrt{2\pi}} \exp\left[-\frac{(x - \mu)^2}{2\sigma^2}\right] \quad (4.58)$$

$$\sigma = \frac{a}{2\sqrt{3}} \quad (4.59)$$

$$FWHM = 2\sqrt{2 \ln 2} \sigma \quad (4.60)$$

ΔE is the quantization error uniformly distributed, σ_E is the standard deviation of the quantization error and $FWHM_E$ is the FWHM of the quantization error. These are calculated using 60 MeV as maximum signal, 0 as minimum signal, the effective number of bits for n , and the equations (4.56), (4.59), and (4.60). The result is given in table 4.6

ADC	ADS5404	AD9257
Bits	12	14
Range	0 – 4095	0 – 16383
Range (keV)	0 – 60000	0 – 60000
Effective number of bits	9.8	12.3
ΔE (keV)	67.3	11.9
σ_E (keV)	19.4	3.4
$FWHM_E$ (keV)	45.7	8.1

Table 4.6: Quantization error from the ADC, for different error distributions. Also assuming the adc input is proportional to the gamma-photon energy, and not looking at any other noise sources.

From figure 4.32 and 4.33 and table 4.6 it can be concluded what ADC to use. For the large scintillator with SiPM array energy resolution is important, so AD9257 (which has the most bits) should be used to achieve this, also figure 4.32 shows that a shaping time constant of $\tau_{shaper} = 10$ ns is enough which was also concluded from figure 4.18b to filter out enough noise. If using the fast output or has a high pass filter on the standard output, reading of figure 4.32, the shaping time constant should be at least 20 ns, which still gives a lower peak time than the standard output with just low pass filters and shaping time constant 10 ns (this can be read from figure 4.13a and 4.14a).

For the small scintillator that only will be used for counting, the ADS5404 can be used since energy resolution is not needed for this 12 bits is more than enough, and it will be beneficial to choose the ADC with the highest sampling rate. This means that even with a small shaper time constant enough of the signal will be captured (as shown in figure 4.32 and 4.33). Also the difference between the highest and lowest pulses won't be as high, as shown in figure 3.18 this sensor will be very non-linear, also comparing the pulses in figure 3.17a and 3.17b the highest signal will only be around 6 times higher than the lowest signal. And the quantitation error won't affect this measurement as much as predicted in table 4.6.

4.3.6 Other Schematic Options

Since it can be concluded from figure 4.8 and 4.18a that a second order shaper would give the lowest noise compared to the signal, there is only a need for three poles in the amplifying and shaping circuit. The preamplifier has one pole while the ADC driver has two; therefore, an option to skip the filter stage is added (but it is left there in case it might be needed).

Additionally, some options to read both outputs from the SiPM or to have two channels for one of the outputs are added. The reasoning for this is to have one output with better energy resolution, the standard output with CR-RCⁿ shaping, and one output with better timing resolution, either the fast output with CR-RCⁿ shaping or the standard output with CR²-RCⁿ shaping. It would also be possible to have two channels from the same SiPM output with different gain; this could be useful in the case where the quantization error from the ADC becomes dominating. A simplified diagram of the implementation is shown in figure 4.34.

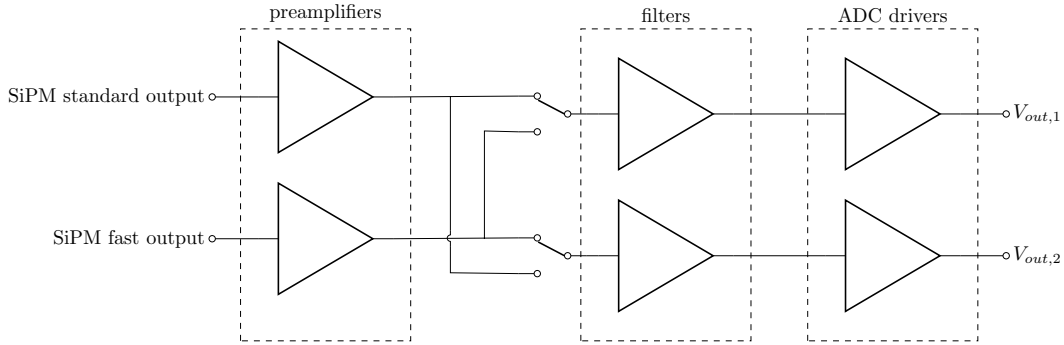


Figure 4.34: Option added to board, where the fast and the standard output can be used, or two of either can be used, for example for applying different gain of different filter types.

4.4 Simulation of Complete Circuit

4.4.1 AC-Response of Summing Configuration

A simulation of the front-end electronics for the SiPM array is done in PSpice from Texas Instruments. In this section the AC-analysis is considered to see if the circuit works as expected, and also to determine the noise. The schematic from the simulation program is shown in appendix B (section B.2.1).

If nothing else is noted the values used for the simulation was $\tau_{shaper} = 10$ ns for all stages, $R_s = 0.1 \Omega$, $R_f = 10 \Omega$ and $C_f = \tau_{shaper}/R_f$ for the preamplifier. For the filter stage $R_2 = R = 1$ k Ω and $C_2 = \tau_{shaper}/R_2$, when used as a low pass filter the gain (also referred to as summing gain or low pass gain) was $k_{sum} = 1$ and $R_1 = R_2/k_{sum}$ and when used as a high pass filter the gain was $k_{high\ pass} = 1$ and $C_1 = k_{high\ pass} \cdot C_2$. The resistors and capacitors for the ADC driver was calculated using equation (4.53) and $R'_1 = R_1/4$ on the components shown in figure 4.27, and $R = 1$ k Ω and $C = \tau_{shaper}/R$, if connected to the low pass or high pass filter the gain

$k = k_{ad} = 1$ and when used as a summing amplifier (taking in the inputs from the preamplifiers) the gain was $k = k_{sum} = 1$.

The results of the simulation are shown in the following figures: figure 4.35 shows the gain at each stage of the circuit compared to the input of the preamplifier, figure 4.36 shows the corresponding phase to the gain in figure 4.35, and figure 4.37 shows the output noise spectral density simulated at each output/output options.

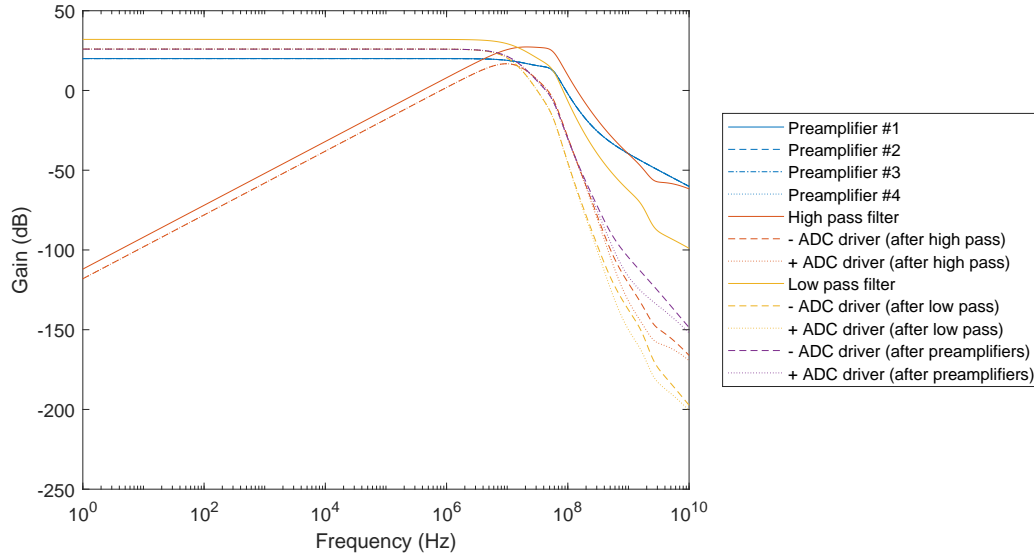


Figure 4.35: Gain of frequency response using time constant $\tau_{shaper} = 10$ ns, feedback resistor in preamplifier $R_f = 10 \Omega$, other resistors around $1 \text{ k}\Omega$, and gain of the summing amplifier equal to 1.

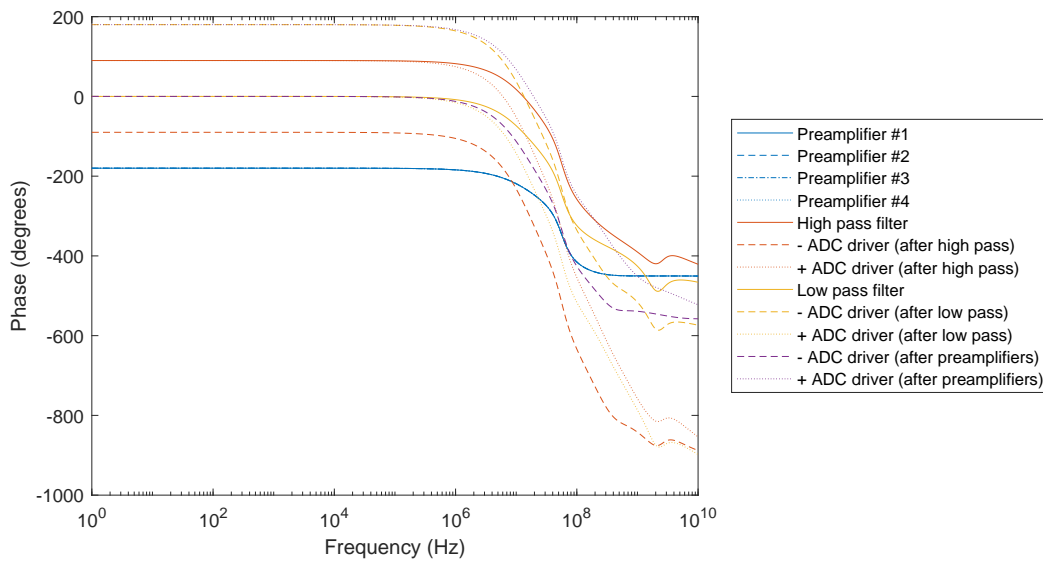


Figure 4.36: Phase of frequency response using time constant $\tau_{shaper} = 10$ ns, feedback resistor in preamplifier $R_f = 10 \Omega$, other resistors around $1 \text{ k}\Omega$, and gain of the summing amplifier equal to 1.

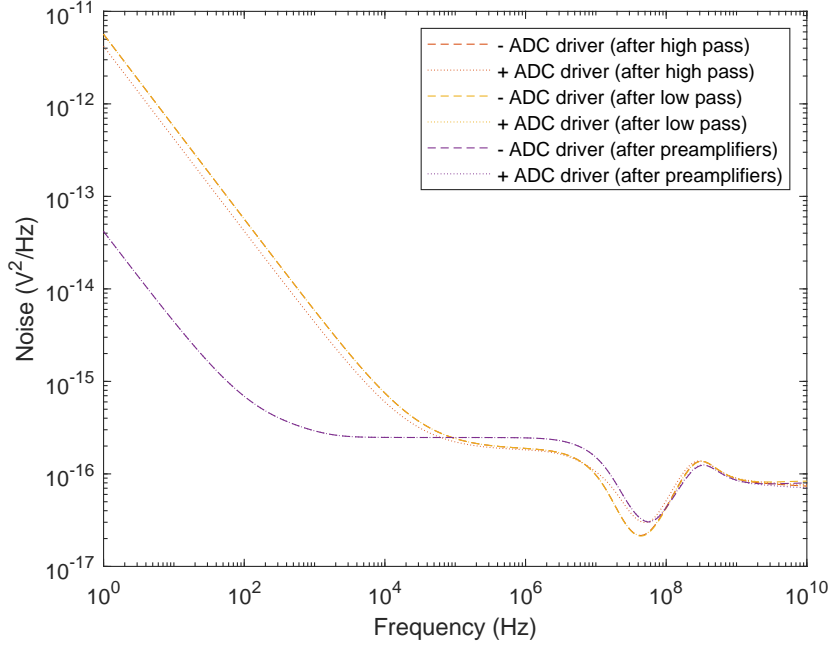


Figure 4.37: Output noise spectral density on the different outputs when using time constant $\tau_{shaper} = 10$ ns, feedback resistor in preamplifier $R_f = 10 \Omega$, other resistors around $1 \text{ k}\Omega$, and gain of the summing amplifier equal to 1.

To find the total noise the noise spectral density in figure 4.37 is integrated from 1 Hz to 5×10^7 Hz to get the average of the squared noise, then the square root is taken to get the RMS noise. This is shown in table 4.7.

Some values were varied to see if the noise level improved, while the rest were kept as described earlier. The varied values were the gain of the low pass filter and the summing ADC driver k_{sum} , the feedback resistor in the preamplifier R_f , the basis resistor R (used to calculate the resistor in filter stage and ADC driver stage), and the shaper time constant τ_{shaper} .

ADC driver output	Variation				
	-	$k_{sum} = 0.25$	$R_f = 20 \Omega$	$R = 100 \Omega$	$\tau_{shaper} = 20 \text{ ns}$
+ after high pass	54	59	65	45	47
- after high pass	59	59	65	45	47
+ after low pass	54	49	60	45	45
- after low pass	54	49	60	45	45
+ after preamplifier	67	47	75	57	53
- after preamplifier	67	47	75	57	53

Table 4.7: Output RMS noise from simulated amplifying and shaping circuit in μV_{rms} (square root of integral of figure 4.37 and equivalent plots, when some of the values are changed).

Looking at the values in table 4.7 changing the gain at the summing stage (low pass filter or preamplifier with preamplifier input) slightly decreases the noise. However, the noise does not decrease by one-fourth like the gain. This means that a lot

of the noise comes from after the gain stages. Also, doubling the preamplifier gain R_f to $20\ \Omega$ increases the noise but does not double it; this also suggests that a great deal of noise comes from after the preamplifier stage.

Lowering the resistor values from around $1\ \text{k}\Omega$ to $100\ \Omega$ also lowers the noise. This can be explained by the noise in a basic RC-low pass filter, where the resistor is the only noise source, the squared output noise is equal to kT/C , meaning that a higher capacitor lowers the noise. The capacitor values increase when the resistor values decrease to get the same shaper time constants. This seems to lower the noise the most for the shaper with a low or high pass filter stage, but this will increase power consumption because the voltage V stays the same while the resistor R is decreased, so the power P will be $P = V^2/R$ and are inversely proportional to R .

Moreover, increasing the shaping time constant lowers the noise; a higher shaper time constant corresponds to a lower cutoff frequency. Consequently, more of the high-frequency noise is filtered out. Also, note that the ADC driver directly connected to the preamplifier has higher noise for most of the variations. The same shaper time constant was used for all the filter types, and the shaper with a low pass stage will be a third order CR-RC shaper, filtering out more noise and slowing down the signal more. The shaper with a high pass filter will filter out more of the low-frequency noise. While the preamplifier ADC driver direct connection is a second order CR-RC shaper, filtering out less noise but keeping more of the fast components of the signal. Another advantage of removing this filter stage is removing another power consumer and noise source.

Using the k_{sum} variation and looking at the outputs after the preamplifier ADC direct connection, the ADC will see the output equivalent noise as two voltage noise sources in series. The total output noise can therefore be calculated using equation (4.39). That makes the total squared noise for this option $\langle v_{out,tot}^2 \rangle = (47\ \mu\text{V})^2 + (47\ \mu\text{V})^2 = 4418\ \mu\text{V}^2$ and the RMS noise $v_{out,tot,rms} = \sqrt{\langle v_{out,tot}^2 \rangle} = 66\ \mu\text{V}$.

This can be converted to a FWHM distribution through equation (4.60), where σ is the standard deviation and is the same as RMS as long as the mean value is zero, which is the case for noise. This gives $v_{out,tot,fwhm} = 157\ \mu\text{V}$. If the complete ADC range of the AD9257 is used the peak of the 60 MeV will be at 2 V, assuming that the peak of the output signal is proportional to the gamma-photon energy 661 keV will be at approximately 20 mV. That makes the ratio of noise over signal $FWHM_{noise} = 157\ \mu\text{V}/(20\ \text{mV}) = 0.8\ \%$, and this will not contribute much to worsening the energy resolution of the detectors.

This noise can then be added together with other deviations: The linearity error from section 3.5 can be read of from figure 3.19b, and is about 2.5 % at 662 keV. Converting this from a uniform to the FWHM of normal distribution (using equation (4.59) and (4.60)) gives a deviation of $FWHM_{lin} = 1.36\ \%$. Temperature deviation from section 3.6 should be less than $FWHM_{temp} = 2\ \%$. Converting this from a uniform to the FWHM of normal distribution (using equation (4.59) and (4.60)) gives a deviation of 1.70 %. Quantization error from ADC (table 4.6) is $FWHM_{adc} = 8.1\ \%$. And assuming the output of the scintillator has an energy resolution of 10 %. And the output is proportional to the signal from the scintillator so that it will contribute with $FWHM_{scin} = 10\ \%$ on the output as well. Adding all of this together

gives the total energy resolution:

$$\begin{aligned}
 FWHM_{tot} &= \sqrt{FWHM_{lin}^2 + FWHM_{temp}^2 + FWHM_{adc}^2 + FWHM_{noise}^2 + FWHM_{scin}^2} \\
 &= \sqrt{(1.36\%)^2 + (1.70\%)^2 + (8.1\%)^2 + (0.8\%)^2 + (10\%)^2} \\
 &\approx 13.1\%
 \end{aligned}$$

Note that the noise sources in the SiPM is ignored here; this is because the signal from the scintillator and SiPM is so large the dark counts, crosstalk and afterpulsing is negligible.

4.4.2 Time Domain Simulation with Realistic Input (Summing Configuration)

Figure 4.38 shows the results from a time domain simulation of the same circuit as in section 4.4.1, using the $k_{sum} = 0.25$ variation shown in table 4.7. But the input was different, the input was a exponential decay function with rise time constant 40 ns and decay time constant 45 ns with a peak current of 250 mA. Also a schematic from this simulation is shown in appendix B.2.2. Note that the common mode on the ADC driver was set to ground, this will be set to an reference from the ADC on the final board.

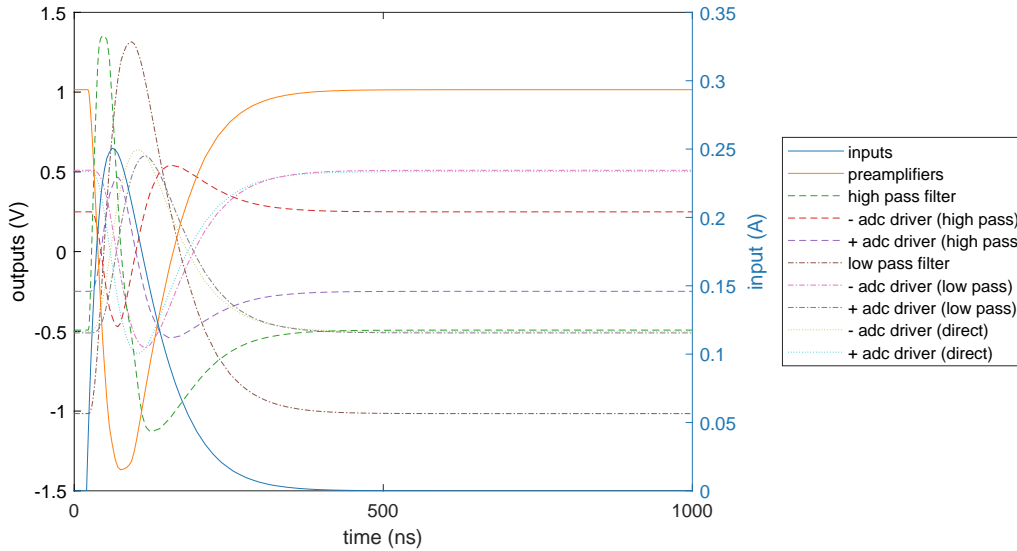


Figure 4.38: Time domain simulation of complete circuit with summing configuration using realistic input.

Looking at the simulation results 4.38 using $R_f = 10\ \Omega$ was a bit too high for an input signal with peak 250 mA, this can be seen at the ADC driver outputs that should be between $\pm 0.5\ \text{V}$ (to get a peak-to-peak voltage up to 2 V which AD9257 can measure [35]). The baseline of the ADC driver output is very close to $-0.5\ \text{V}$ and $0.5\ \text{V}$, this might need some adjustment in case the baseline is clipped when noise is added.

In general, the outputs from the circuit work as expected; this was also tried for some different variations but was not considered interesting to show here.

When it comes to the simulation without any summing amplifier that will be used for the single unit SiPM or the fast output, it should work fine; this is because the more complex version with summing works.

Discussion and Conclusion

5.1 Discussion and Conclusion

Detailed knowledge about the SiPM was acquired both alone and for scintillation light detection. Equations were found, estimates for the relevant characteristics of the SiPM were made, and the most essential/controversial was verified through measurements. This includes, among other things, signal shape, height, and length from the SiPM, and signal shape of the SiPM coupled to LYSO-scintillator (the height of this signal should be verified from measurements with the correct coupling material is used).

The large signal of the SiPM was confirmed (see, for example, the discussion after figure 3.27.). The signal length was highly dependent on the readout method, see for example figure 3.48, but for the fastest readout method the signal length was close to the theoretical value, (52 ± 1) ns compared to 45 ns. The signal shape was, for the most part, as expected, see figure 3.48. There were some exceptions, but these were not thoroughly examined due to better results from newer measurements. In general, the SiPM with LED as a light source had a slower rise time than predicted, but this is probably due to the characteristics of the LED. For the SiPM with a scintillator, the calculated signal shape was a good estimate, also with filtering.

A suitable way to bias and read out the SiPM was found based on equations for the signal shape and application notes and verified through measurement. From this, it was concluded that the best way was to use a transimpedance amplifier for amplifying and converting the current signal to a voltage. The SiPM was also biased using the amplifier input for virtual ground (or a different common-mode) and an external power supply on the other end. This especially made a difference for the SiPM array, and the time constant was very close to the theoretical value.

Due to the temperature sensitivity of the SiPM, it was calculated how much this would affect the system, and the conclusion was to keep the temperature relatively stable and monitor the temperature. If the temperature is kept within $\pm 2^\circ\text{C}$ the deviation in signal height should be within $\pm 2\%$.

The SiPM output will not have linear behavior close to saturation. Therefore there what a need to figure out how much this would affect the sensor. Some calculations for the linearity were done. These showed that the linearity of the large

scintillator and the SiPM would be good, within 20 %. And it will also be possible to correct for if enough of the parameters are known. The linearity may also be better than shown in the calculation, due to photons lost in the optical coupling and lower PDE due to the spectrum of wavelengths from the scintillator. For the single SiPM the linearity was poor, and the highest energies impossible to distinguish. However, this does not matter because of the properties of the small scintillator and the fact that it will be used for counting only.

What can be concluded from the investigation of the SiPM sensor is that it will be suitable as a scintillation light detector for the chosen LYSO scintillators.

A design for front-end electronics for the SiPM was made. This includes a preamplifier, filter stage (optional) and ADC driver. The preamplifier is a transimpedance amplifier, the filter stage can be used as a first order low pass or high pass filter, and the ADC driver is implemented using with a second order low pass filter. With this implementation, preamplifier, filter, and ADC driver are used for shaping.

Noise in the shaping circuit was calculated for different shaping time constants, and a shaping time constant was chosen such that the height and the length of the signal were not changed significantly. However, the noise was low enough, plus some generous margin. The noise from simulations of this circuit was much higher because only the noise from the preamplifier was considered in the calculations, and the simulations included the other amplifiers and passive components. But, the noise was still small enough not to make a significant impact on the energy resolution, as it was concluded in section 4.4 that the noise would contribute with an error of 0.8 % (FWHM) at the lowest signal.

Adding up noise sources and deviations (from temperature sensitivity, linearity, ADC quantization error and noise), and assuming the energy resolution of the scintillator alone is 10 %, the total energy resolution at 662 keV would be 13.1 %. This is well within the 25 % requirement, and close to the ideal value of 10 %. At larger gamma-photon energies, the non-linearity will dominate at 20 %, and if assuming the scintillator has an energy resolution of 10 % here as well, this will barely be within the 25 % requirement, but this can be corrected for.

When it comes to the signal length the peak time needs to be below 100 ns to distinguish the pulses at high count rates. Looking at the pulses in figure 4.16a, 4.17b and 4.17c, the peak times were at approximately 85 ns for standard output with low pass filters, 45 ns for standard output with additional high pass filter and 35 ns for fast output with low pass filters, which were all within the requirement. The shaping time constant used here was 10 ns.

The Nyquist theorem was considered, and for the standard output with low pass filters, no shaping was needed for the 500 MHz ADC, and a shaping time constant of at least 10 ns was needed for the 65 MHz ADC. For the standard output with additional high pass filter (or fast output with low pass filters) the shaping time constant needs to be at least 1.5 ns for the 500 MHz ADC, and a shaping time constant of at least 20 ns is needed for the 65 MHz ADC. These are not absolute limits, since the frequency content of the signal in principle extends to infinity, but the limit was chosen at -60 dB.

A solution of preamplifiers for the SiPM array was designed. This included dividing the array outputs into four groups; in each group, the outputs are shorted

together and connected to the amplifier. The amplifier chosen was LMH6629, which has high bandwidth and can deliver high current. This amplifier was also tested with 16 of the pixels in the SiPM array.

To sum up, this thesis contributes to upgrading the UIB-BGO instrument that will be used for the ALOFT campaign by investigating the properties of the SiPM sensor and designing suitable front-end electronics.

5.2 Further Work

Although a design of the front-end electronics has been made, the PCB that it sits on must be finalized and assembled. Also a PCB for mounting and connecting the SiPM needs to be made.

Some decisions for the design are still to be made; the gain of the circuit will need to be set after measurements using the correct coupling material between the SiPM and scintillator. And the position of the preamplifier, if it needs to sit close to the SiPM or can sit on the main board. The preamplifier might need to sit close to the SiPM due to the length of the signal from the SiPM being very dependent on how it is connected—also, the stability of the preamplifier is a factor here. The drawback of having the preamplifier on the same board as the SiPM is added complexity to that board.

Summary of Design

This appendix summarizes the design choices of the thesis.

In general, the suggestion is to have one channel for each standard and fast output on both the SiPM array and the single SiPM unit. Also the filter stage should be skipped, and only preamplifier and ADC driver used. This results in a signal chain: SiPM output \rightarrow preamplifier \rightarrow ADC driver \rightarrow diode clippers \rightarrow ADC input.

The components used for each stage are: LMH6629 for preamplifier, THS4304 for filter stage, and THS4505 for ADC driver.

Figure A.1 shows a simplified circuit diagram for adjusting the common-mode of the signal, where a voltage divider connected to the power supply controls the input voltage. This can be used on the preamplifier and the filter stage. It would not work good on the ADC driver because of the feedback loop on both inputs. The components in the voltage divider will be referred to with the manes shown in figure A.1.

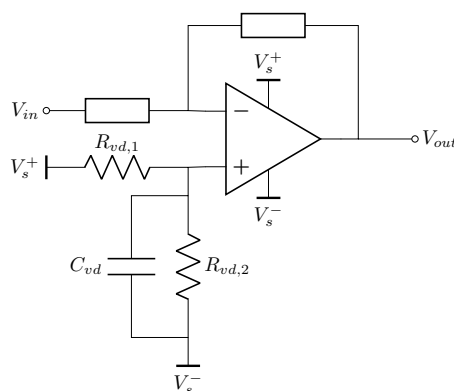


Figure A.1: Simplified diagram of preamplifier of filter stage, showing a voltage divider for adjusting the common-mode, as well as the supply voltage.

The first to consider is the standard output of the SiPM array. This will be divided into four groups where each pixel is connected in parallel and into a preamplifier, resulting in four groups of SiPM pixels and preamplifiers. The non-inverting

inputs on the preamplifier will be set to a DC-voltage of 1 V to adjust the common-mode and center the signal around ground. This may need to be lowered slightly in the case where the baseline is clipped by the ADC, but the leakage current SiPM may already give the baseline some margin from the dynamic range of the ADC. The common-mode is implemented with a voltage divider as in figure A.1. The common cathode on the SiPM must be connected to a positive bias voltage 1 V above the operating voltage (of 25.2 V to 30.7 V [23]). The signal from the preamplifiers will be summed in the ADC driver circuit with a gain of $k = 0.25$. The resistor and capacitor values are calculated using equation (4.52), $R = 1 \text{ k}\Omega$, and $C = 10 \text{ pF}$; resulting in a time constant of 10 ns. The ADC driver output should then be connected to AD9257 via a $25 \text{ }\Omega$ resistor and diode clippers using RB751CS30L (between the signal and ground, and signal and $\text{AVDD} = 1.8 \text{ V}$), and the reference output of the ADC to the common mode input of the ADC driver. The rest of the values and explanations are given in table A.1.

Stage	Component Name	Value	Comment
Preamplifier (figure 4.20)	R_f	10 Ω	R_f determines the gain of the circuit, this will need adjustment after the measurements with the right coupling material.
	C_f	1 nF	Should be equal to τ_{shaper}/R_f and needs adjustment after R_f , the capacitors can be set to a lower value in case there is stability issues.
	R_s	shorted	Could also add a small resistor ($\sim 0.1 \Omega$) if needed to make it stable.
	$R_{vd,1}$	1.5 keV	For setting the common-mode, might increase this a bit if the baseline is clipped by the ADC.
	$R_{vd,2}$	3.5 keV	For setting the common-mode, might decrease this a bit if the baseline is clipped by the ADC.
	C_{vd}	0.1 μ F	For filtering noise from the voltage divider.
Filter (figure 4.23)			Skip this stage.
ADC driver (figure 4.27)	R_1	4 k Ω	Calculated with R/k
	R'_1	1 k Ω	Equal to $R_1/4$.
	R_2	500 Ω	Calculated with $R/(4k + 1)$.
	R_3	1 k Ω	Equal to R .
	C_1	20 pF	Calculated with $C \cdot (4k + 1)$.
	C_2	10 pF	Equal to C .
	V_s^+	5 V	
V_s^-	-5 V		

Table A.1: Component values for front-end electronics for SiPM array.

When it comes to the fast SiPM array, the fast outputs from all the pixels can be shorted together and into the preamplifier output; this should mostly be the same as for the array, except for the values given in table A.2. The simple ADC driver should be used (since there is only one preamplifier), the values for this is shown in table A.3, and is calculated using 4.49, $R = 1 \text{ k}\Omega$, and $C = 10 \text{ pF}$. The connection to the ADC should be the same as for the SiPM array standard output.

The standard output (anode) of the single unit SiPM should be connected to the preamplifier, and the cathode connected to positive bias voltage 0.5 V above the operating voltage (of 25.2 V to 30.7 V [23]). The values of the components around the preamplifier should be as given in table A.2 (and table A.1 for those not given in table A.2). The preamplifier output will then be connect to the ADC driver given in table A.3. The ADC driver output should then be connected to ADS5404 via a 25 Ω resistor and diode clippers using RB751CS40 (between the signal and ground, and

signal and $AVDD33 = 3.3\text{ V}$), and the reference output of the ADC to the common mode input of the ADC driver.

The fast output of the single unit SiPM should have an equal connection as the standard output, except for those values given in table A.2.

Input signal	Component Name	Value	Comment
Array fast output	R_f	$50\ \Omega$	Around 5 times feedback resistor for standard output.
	C_f	$200\ \text{pF}$	Should be equal to τ_{shaper}/R_f and needs adjustment after R_f , the capacitors can be set to a lower value in case there is stability issues.
	$R_{vd,1}$	$3\ \text{keV}$	Centering the signal around ground and $2\ \text{V}$ peak-to-peak.
	$R_{vd,2}$	$2\ \text{keV}$	Centering the signal around ground and $2\ \text{V}$ peak-to-peak.
Single unit standard output	R_f	$50\ \Omega$	If using a overvoltage around $2\ \text{V}$ on SiPM, may be lowered if a higher overvoltage is used.
	C_f	$200\ \text{pF}$	Should be equal to τ_{shaper}/R_f and needs adjustment after R_f , the capacitors can be set to a lower value in case there is stability issues.
	$R_{vd,1}$	$2\ \text{k}\Omega$	Centering the signal around ground and $1\ \text{V}$ peak-to-peak.
	$R_{vd,2}$	$3\ \text{k}\Omega$	Centering the signal around ground and $1\ \text{V}$ peak-to-peak.
Single unit fast output	R_f	$1\ \text{k}\Omega$	If using a overvoltage around $2\ \text{V}$ on SiPM, may be lowered if a higher overvoltage is used.
	C_f	$10\ \text{pF}$	Should be equal to τ_{shaper}/R_f and needs adjustment after R_f , the capacitors can be set to a lower value in case there is stability issues.
	$R_{vd,1}$	$2.7\ \text{k}\Omega$	Centering the signal around ground and $31\ \text{V}$ peak-to-peak.
	$R_{vd,2}$	$2.3\ \text{k}\Omega$	Centering the signal around ground and $1\ \text{V}$ peak-to-peak.

Table A.2: Preamplifier component values that deviates from table A.1 for different inputs.

Stage	Component Name	Value	Comment
ADC driver (figure 4.26)	R_1	1 k Ω	Calculated with R/k
	R_2	500 Ω	Calculated with $R/(k + 1)$.
	R_3	1 k Ω	Equal to R .
	C_1	20 pF	Calculated with $C \cdot (k + 1)$.
	C_2	10 pF	Equal to C .
	V_s^+	5 V	
	V_s^-	-5 V	

Table A.3: Component values for simple ADC driver with unit gain and only one input signal.

A conclusion to skip the filter stage has been made, but the option to use it is still kept. The filter stage might be useful as a low pass filter in the case where the feedback capacitor can have a high enough value to give the desired time constant. As a high pass filter, if the quality of the fast output is poor and a CR^2 - CR^n shaper on the standard output might work better. Alternatively, as AC-coupling, if a single supply must be used instead of dual on the preamplifier. The AC-coupling would have a similar circuit as the high pass filter but a very large time constant in the feedback.

The other options kept, but not concluded to use here, are: The option to have two channels from the standard output; this will be useful if the quality of the fast output is poor and a CR^2 - CR^n shaper on the standard output might work better. Then there can be one channel with CR - CR^n shaping and CR^2 - CR^n shaping of the standard output, giving both good timing resolution and energy resolution. The option to have two channels from the standard output will also be useful in the case the SNR of the low signals is poor; then one of the channels can have high gain to increase the quality of the low signals. It is also possible to have two channels with fast output with different gain.

Since the SiPM and front-end electronics (except for possibly the preamplifier) will be on different boards, it should be possible to switch around some of the SiPM outputs. For example, if the fast output of the SiPM array is desired to use with the fastest ADC ADS5404.

Another discussion is if the preamplifier should be on the main board with the rest of the front-end electronics or the board with the SiPM mounted. It might be necessary to have the preamplifier together with the SiPM for timing performance of the SiPM and stability of the preamplifier. However, this adds complexity to that board, and if the change in timing performance and stability is insignificant, it will be easier to have the preamplifier on the main board.

Schematics

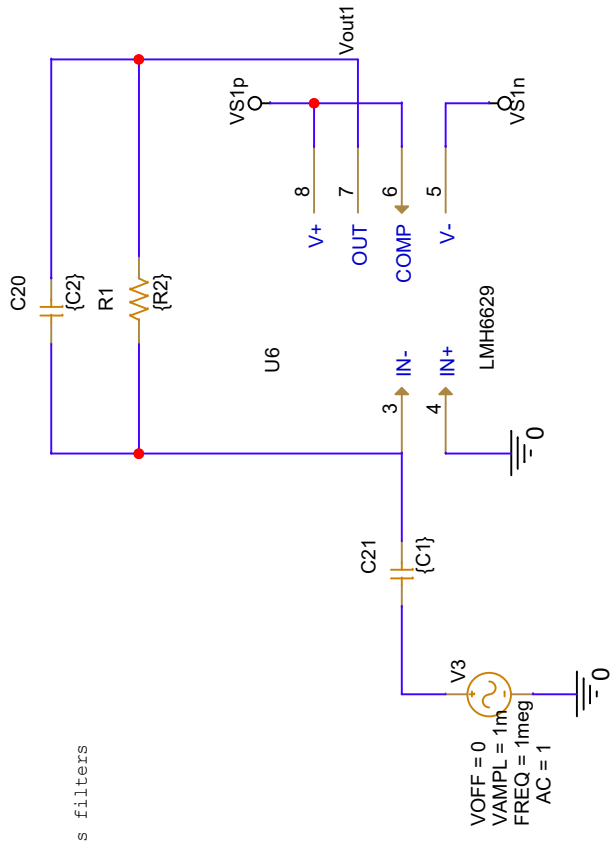
This appendix contains schematics relevant to the work done in this thesis—the schematic for simulations, test boards, and the High-Speed ADC board.

B.1 Schematic Used in Simulation of Individual Stages

These schematics were made in PSpice from Texas Instrument to do simulations in the same program.

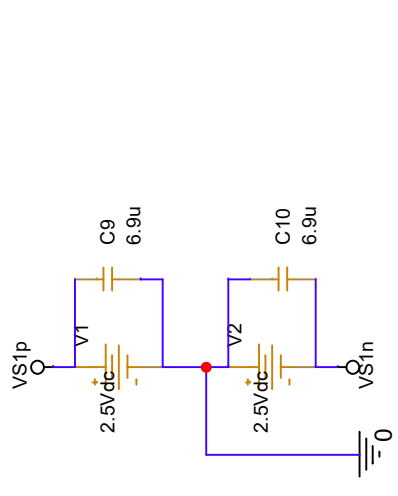
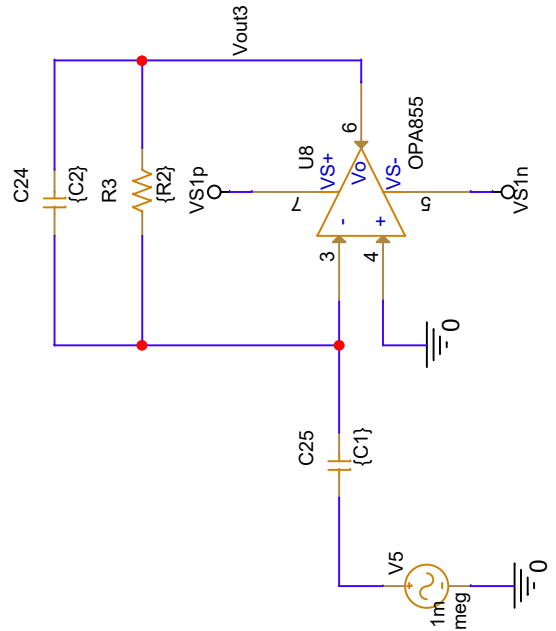
B.1.1 AC-Response

High pass filters



PARAMETERS:

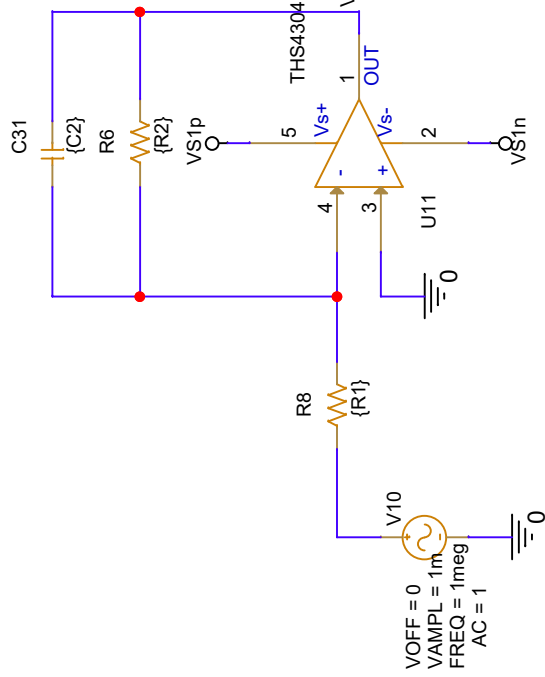
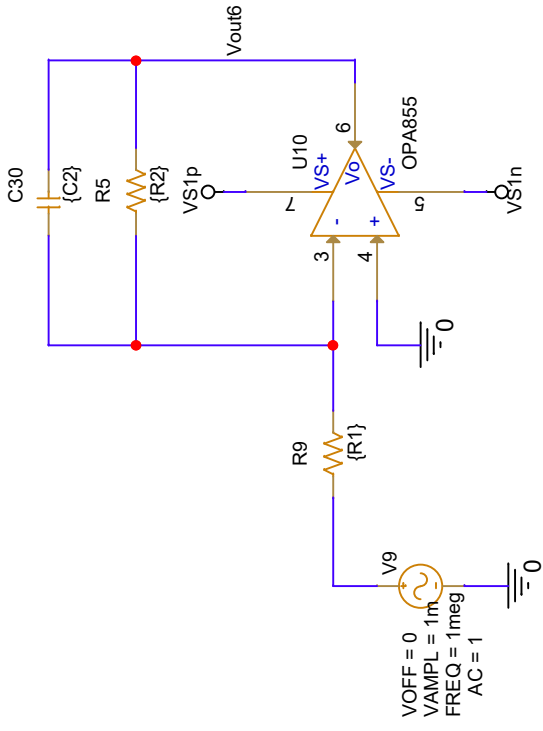
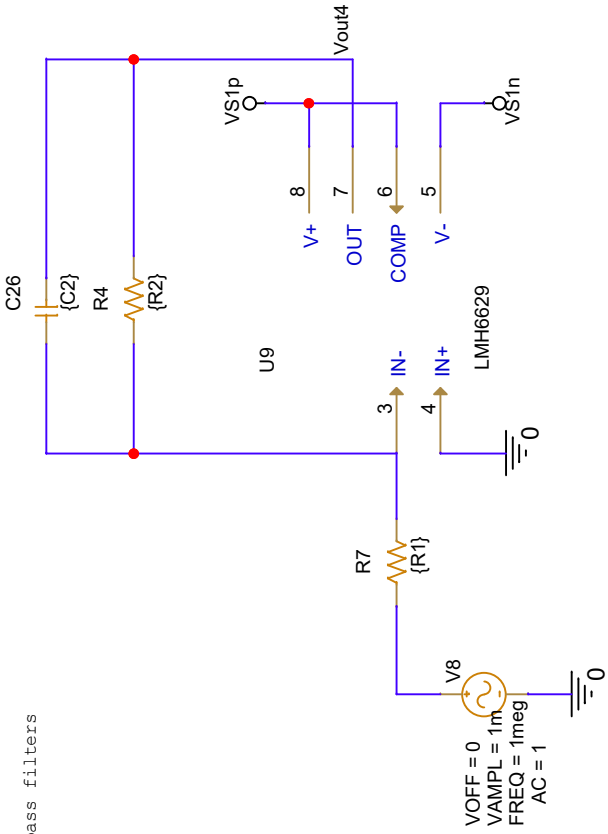
- $CF = \{\tau/R\}$
- $I_{in} = -250m$
- $R = 1k$
- $C1 = \{C2 * gain_h\}$
- $C2 = \{\tau/R\}$
- $R1 = \{R2/gain_l\}$
- $R2 = \{R\}$
- $RF = 10$
- $RS = 0.1$
- $C = \{\tau/R\}$
- $gain_h = 4$
- $gain_l = 1$
- $gain_ad = 1$
- $\tau = 10n$
- $V_{OFF} = 0$
- $V_{AMPL} = 1m$
- $FREQ = 1meg$
- $AC = 1$



Title High pass filters

Size A Document Number <Doc>

Low pass filters



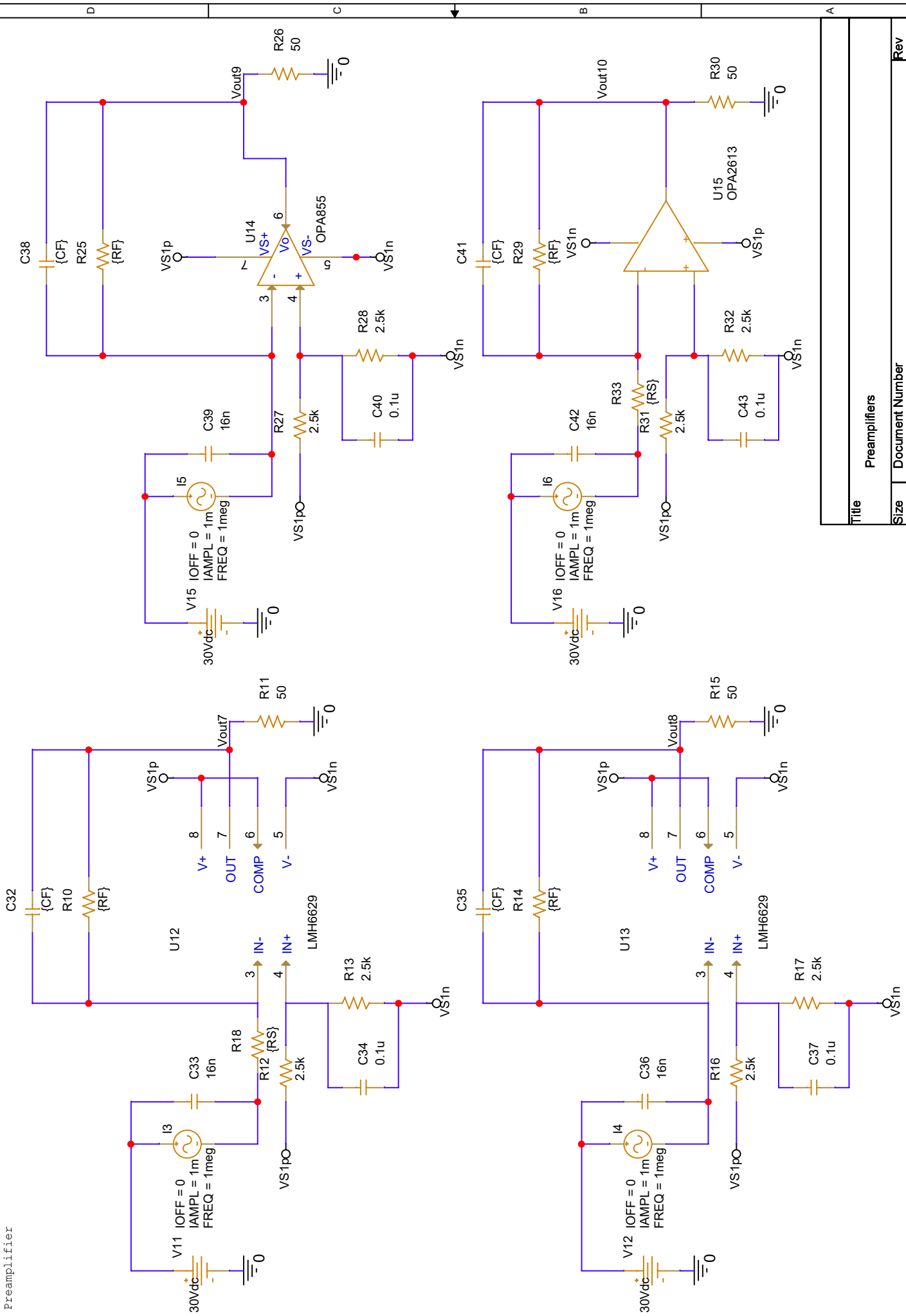
Title Low pass filters

Size A Document Number <Doc>

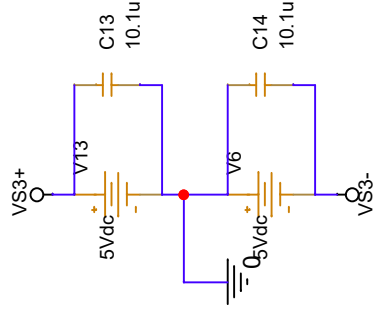
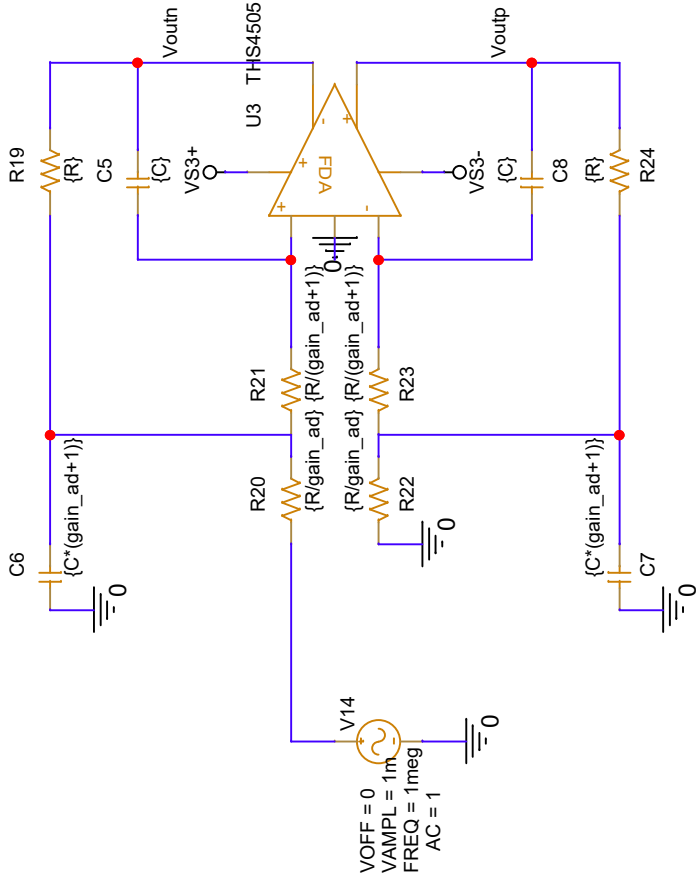
Date: Monday, May 16, 2022

Sheet 1 of 1

Rev <Rev Code>



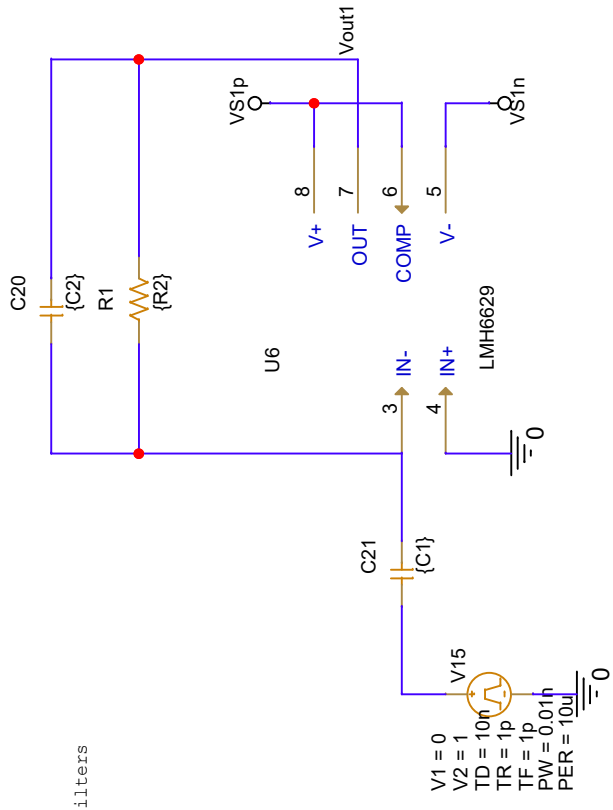
Title		Preamplifiers	
Size	A	Document Number	<Doc>
Date:	Monday, May 16, 2022	Sheet	1 of 1
Rev	<Rev Code>		



Title		ADC driver	
Size	A	Document Number	<Doc>
Date:	Monday, May 16, 2022	Sheet	1 of 1
Rev	<Rev Code>		

B.1.2 Impulse-Response

High pass filters

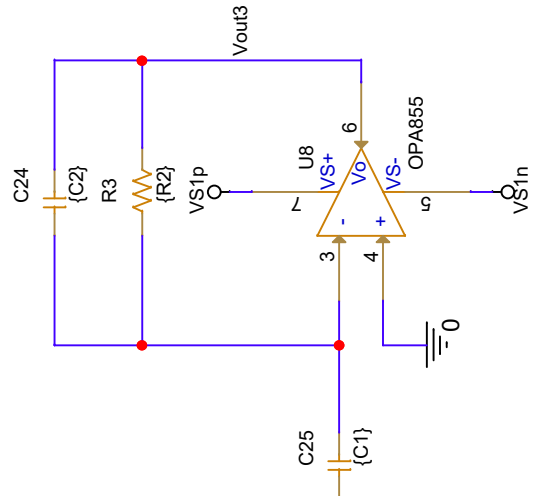
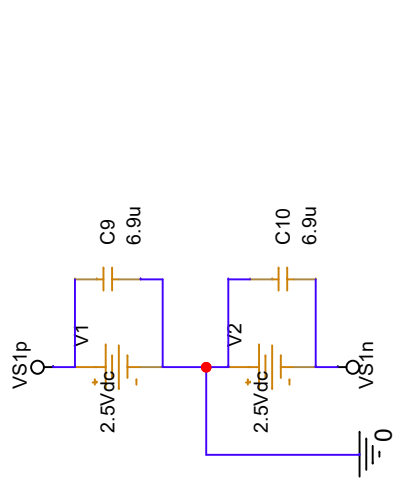


V1 = 0
V2 = 1
TD = 10n
TR = 1p
TF = 1p
PW = 0.01h
PER = 10u

PARAMETERS:

- CF = {tau/RF}
- lin = -250m
- R = 1k
- C1 = {C2*gain_h}
- C2 = {tau/R2}
- R1 = {R2/gain_l}
- R2 = {R}
- RF = 10
- RS = 0.1
- C = {tau/R}
- gain_h = 4
- gain_l = 1
- gain_ad = 1
- tau = 10n

V1 = 0
V2 = 1
TD = 10n
TR = 1p
TF = 1p
PW = 0.01h
PER = 10u

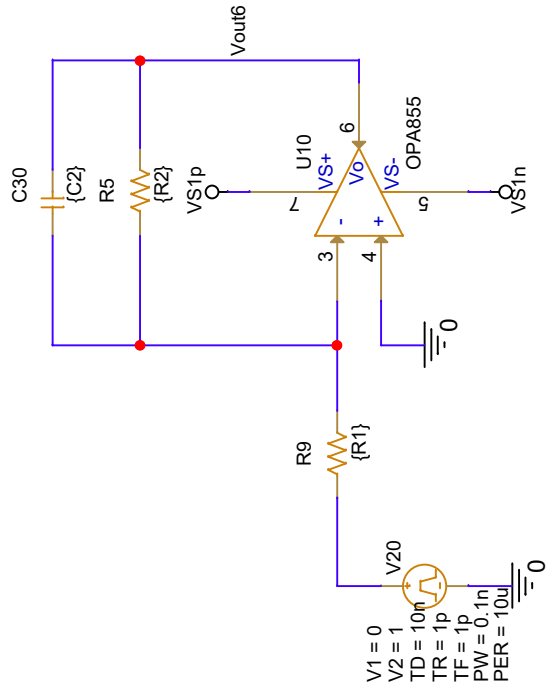
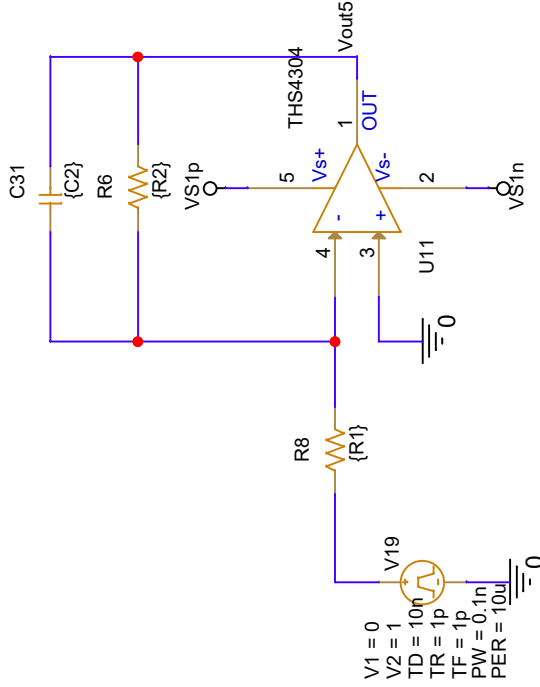
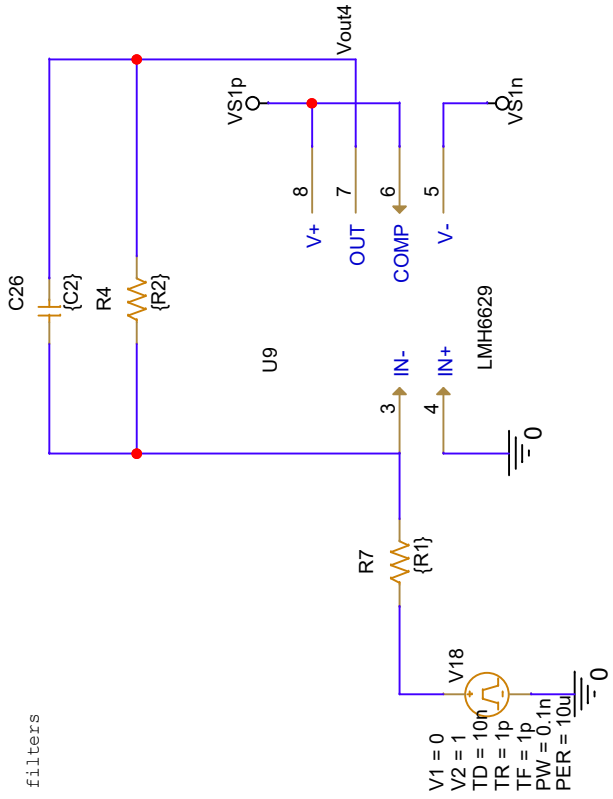


V1 = 0
V2 = 1
TD = 10n
TR = 1p
TF = 1p
PW = 0.01h
PER = 10u

Title : High pass filters

Size : A
Document Number : <Doc>

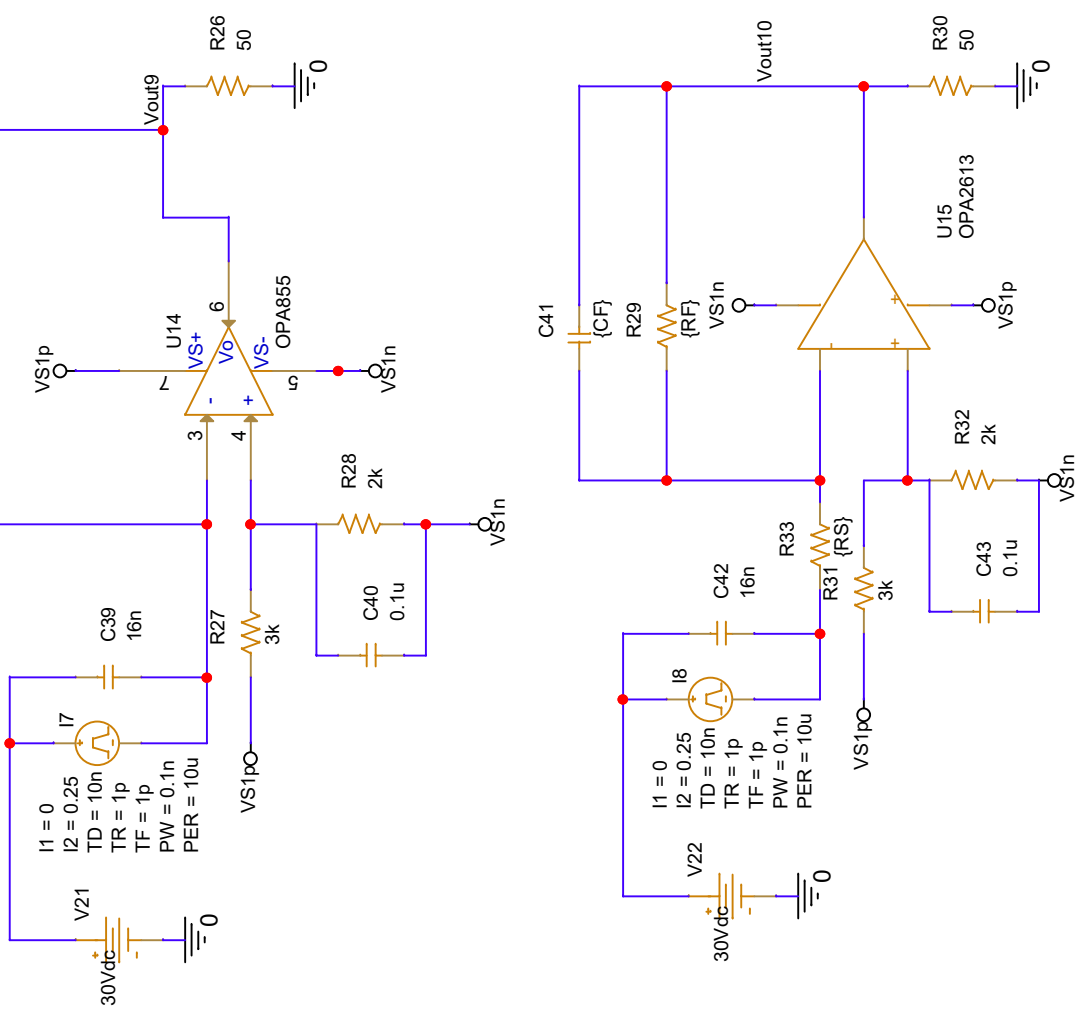
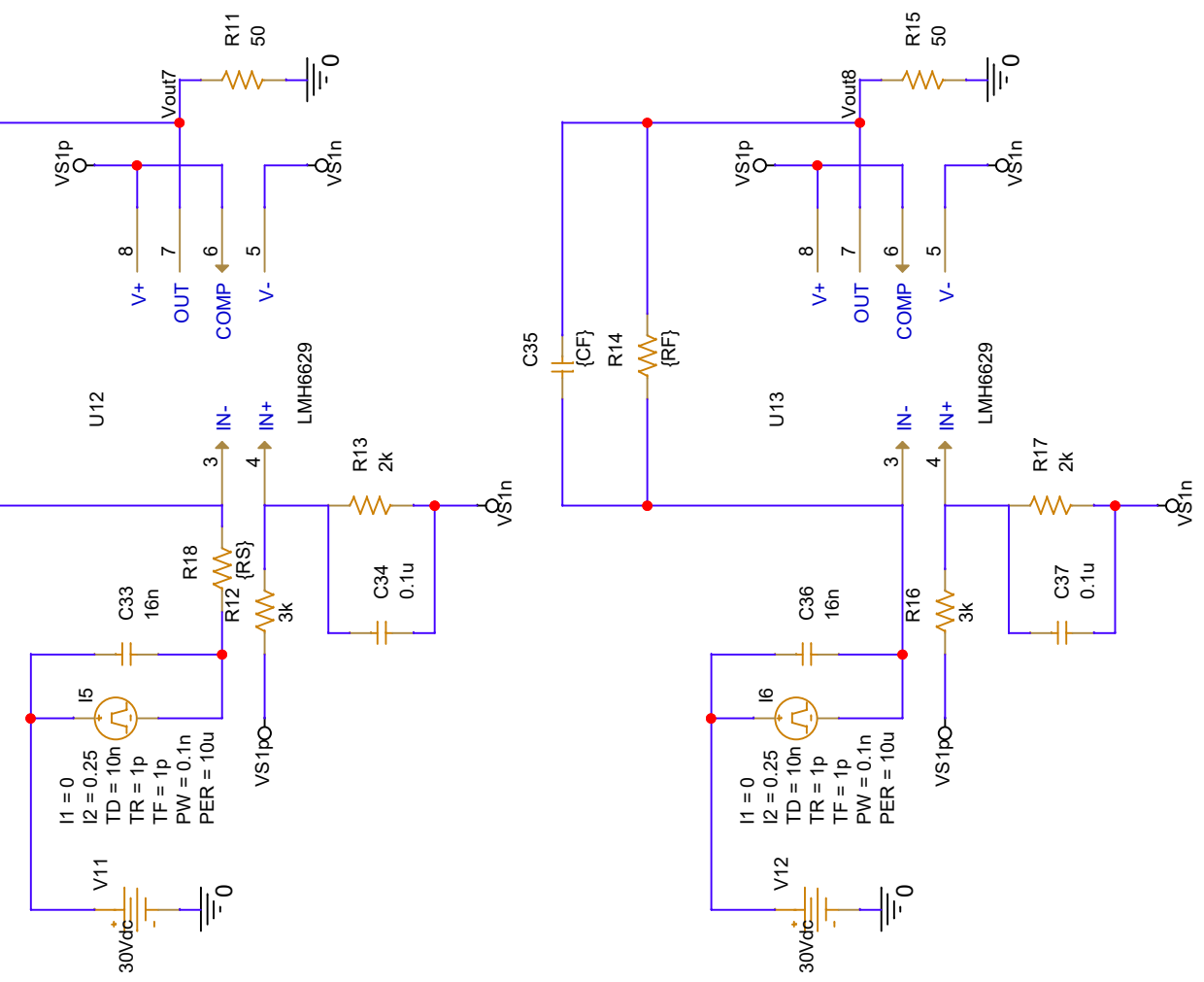
Low pass filters



Title : Low pass filters :

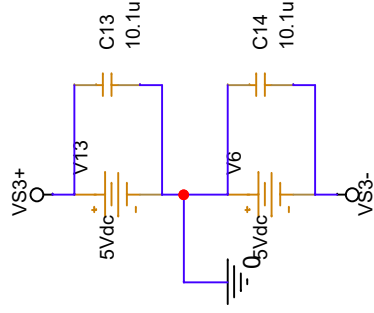
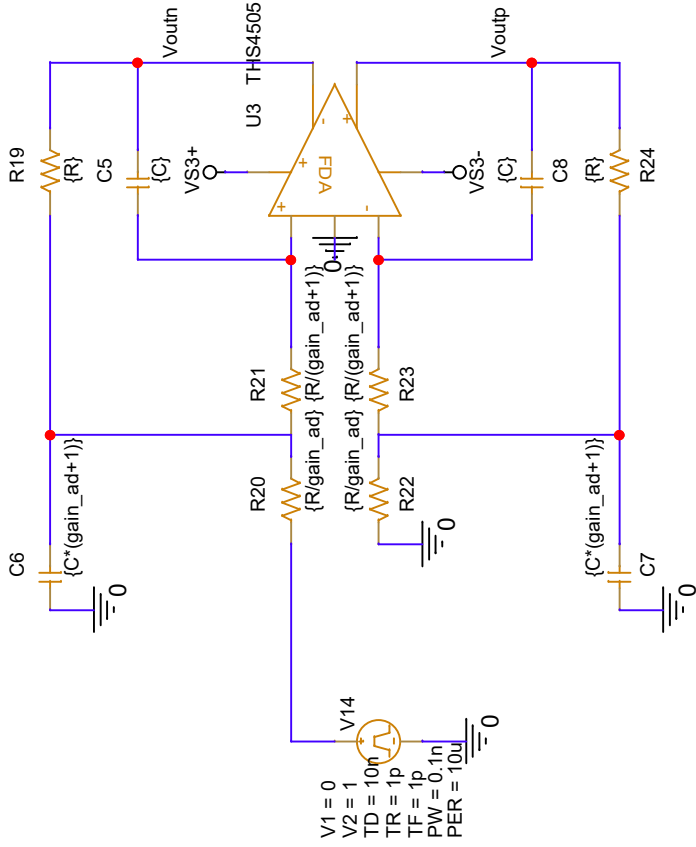
Size A Document Number <Doc>

Preamplifier



Preamplifiers

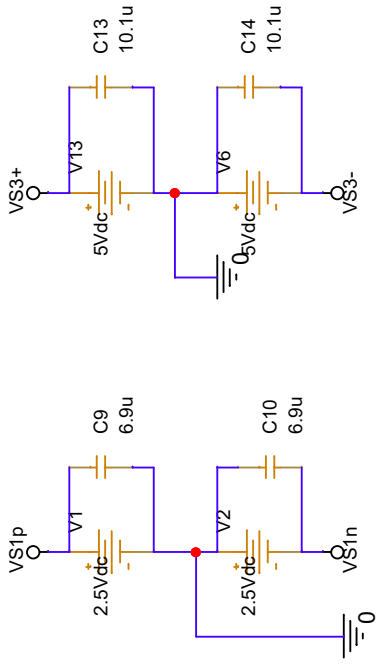
Title	Preamplifiers		
Size	A	Document Number	<Doc>
Date:	Monday, May 16, 2022	Sheet	1 of 1
Rev	<Rev Code>		



Title		ADC driver	
Size	Document Number	Rev	<Rev Code>
A	<Doc>	1	1
Date:	Monday, May 16, 2022	Sheet	1 of 1

B.2 Schematic Used in Simulation of Complete Circuit

B.2.1 AC-Response of Summing Configuration



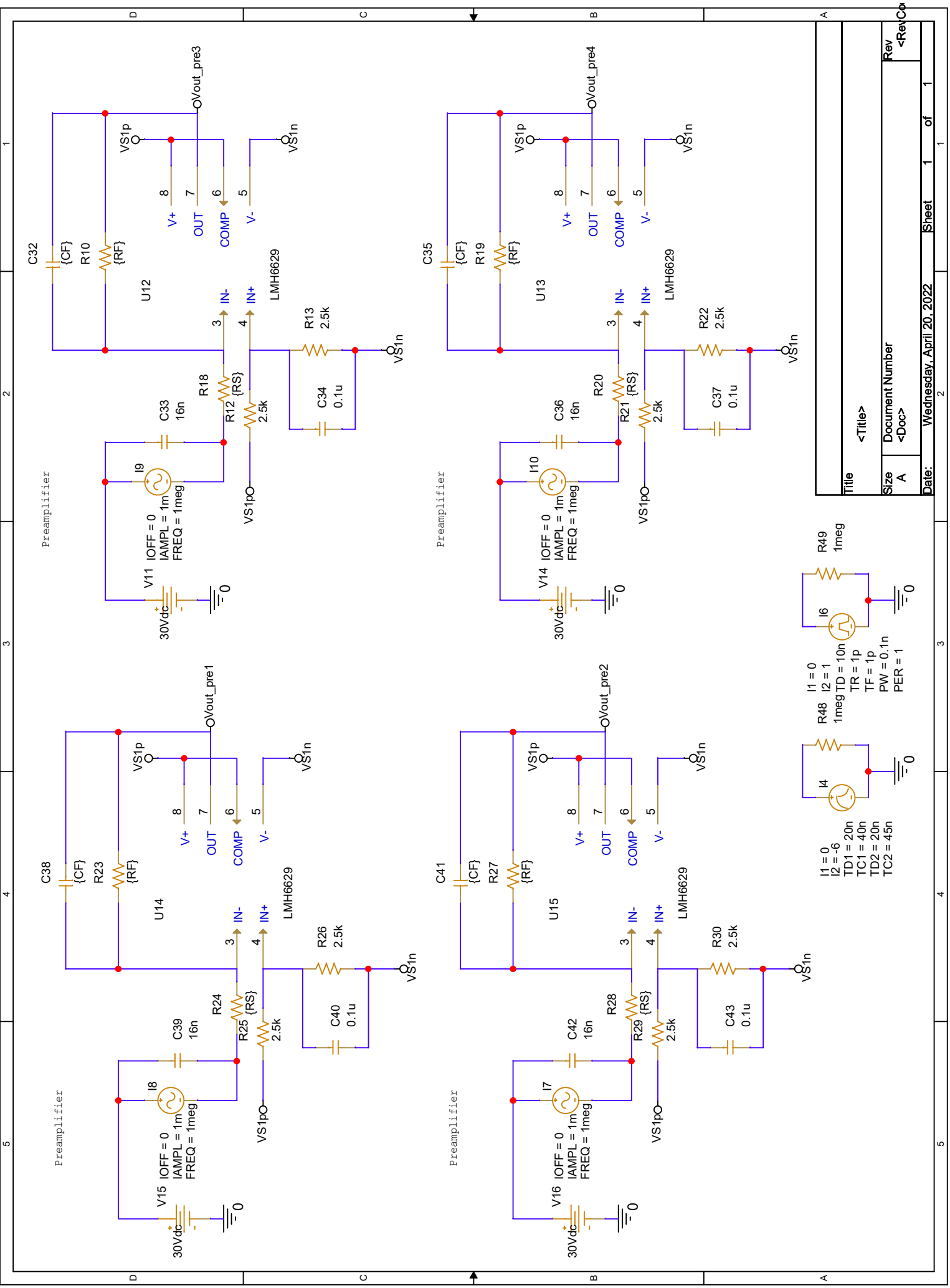
PARAMETERS:

preamp and input
 $lin = -250m$
 $RS = 0.1$
 $RF = 10$
 $CF = \{tau/RF\}$

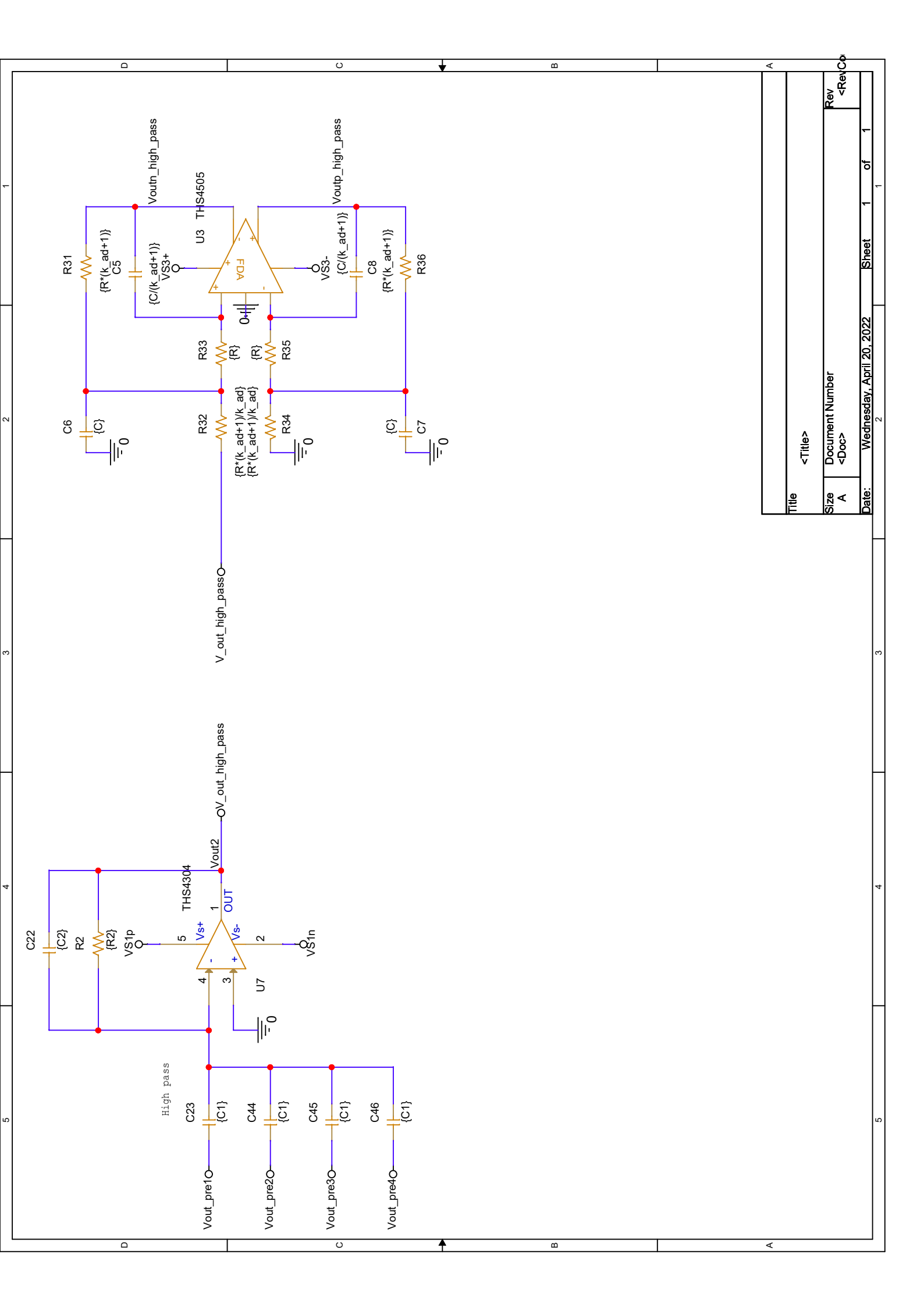
filter
 $C1 = \{C2*gain_high_pass\}$
 $C2 = \{tau/R2\}$
 $R1 = \{R2/gain_low_pass\}$
 $R2 = \{R\}$

adc driver
 $R = 1k$
 $C = \{tau/R\}$
 $tau = 10n$
 $gain_high_pass = 1$
 $gain_low_pass = 1$
 $k_ad = 1$

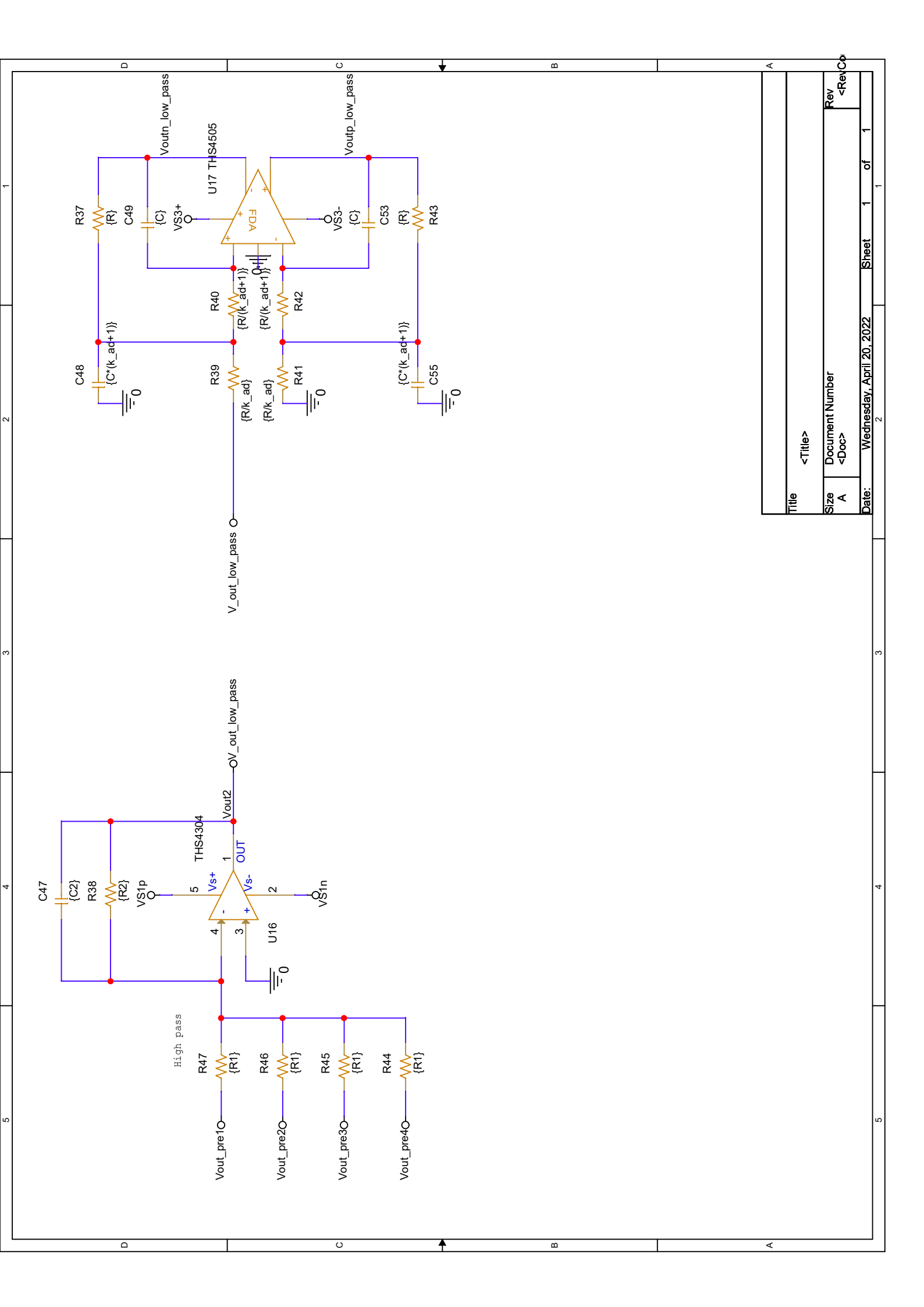
Title		<Title>	
Size	Document Number	Rev	<Rev/Co
A	<Doc>		
Date:	Wednesday, April 20, 2022	Sheet	1 of 1



Title		<Title>
Size	Document Number	<Doc>
Rev	<Rev>	
Date:	Wednesday, April 20, 2022	Sheet 1 of 1

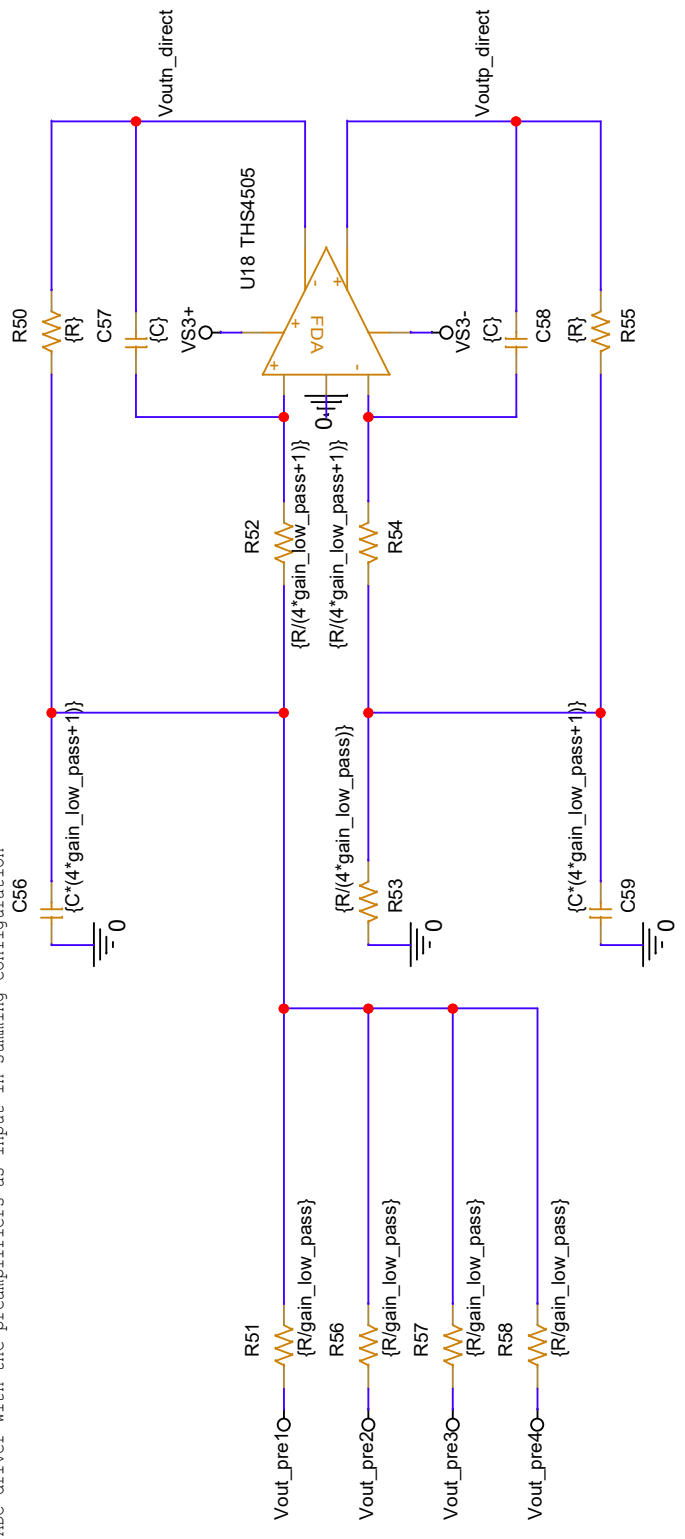


Title		<Title>	
Size	A	Document Number	<Doc>
Date:	Wednesday, April 20, 2022	Sheet	1 of 1



Title		<Title>
Size	Document Number	A <Doc>
Date:	Rev	Wednesday, April 20, 2022 <Rev>
Sheet	1 of 1	2

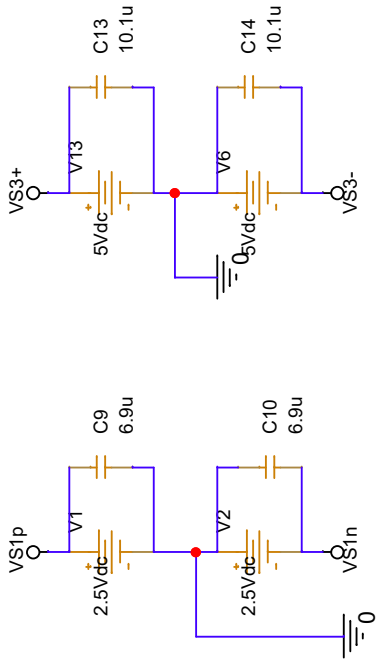
ADC driver with the preamplifiers as input in summing configuration



Title		<Title>	
Size	A	Document Number	<Doc>
Rev	<Rev>	Sheet	1 of 1
Date:	Wednesday, April 20, 2022	Sheet	1 of 1

B.2.2 Time Domain Simulation with Realistic Input (Summing Configuration)

Dual Supply for Preamplifier and Filter



PARAMETERS:

```

lin = {5,8}
RS = 0.1
RF = 10
CF = {tau/RF}

C1 = {C2*gain_high_pass}
C2 = {tau/R2}
R1 = {R2/gain_low_pass}
R2 = {R}

R = 100
C = {tau/R}
tau = 10n
gain_high_pass = 0.75
gain_low_pass = 0.25
k_ad = 1

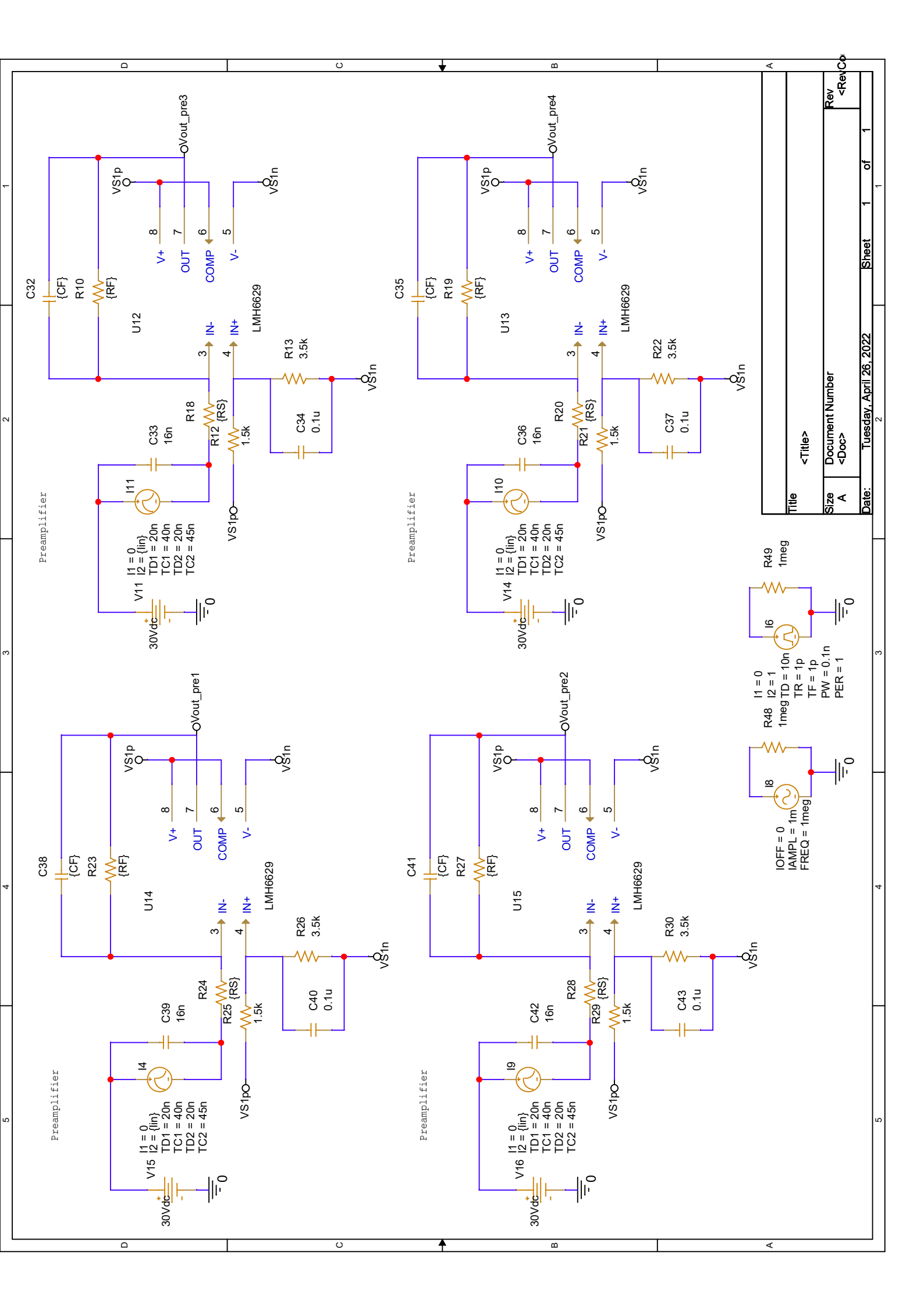
```

preamp and input

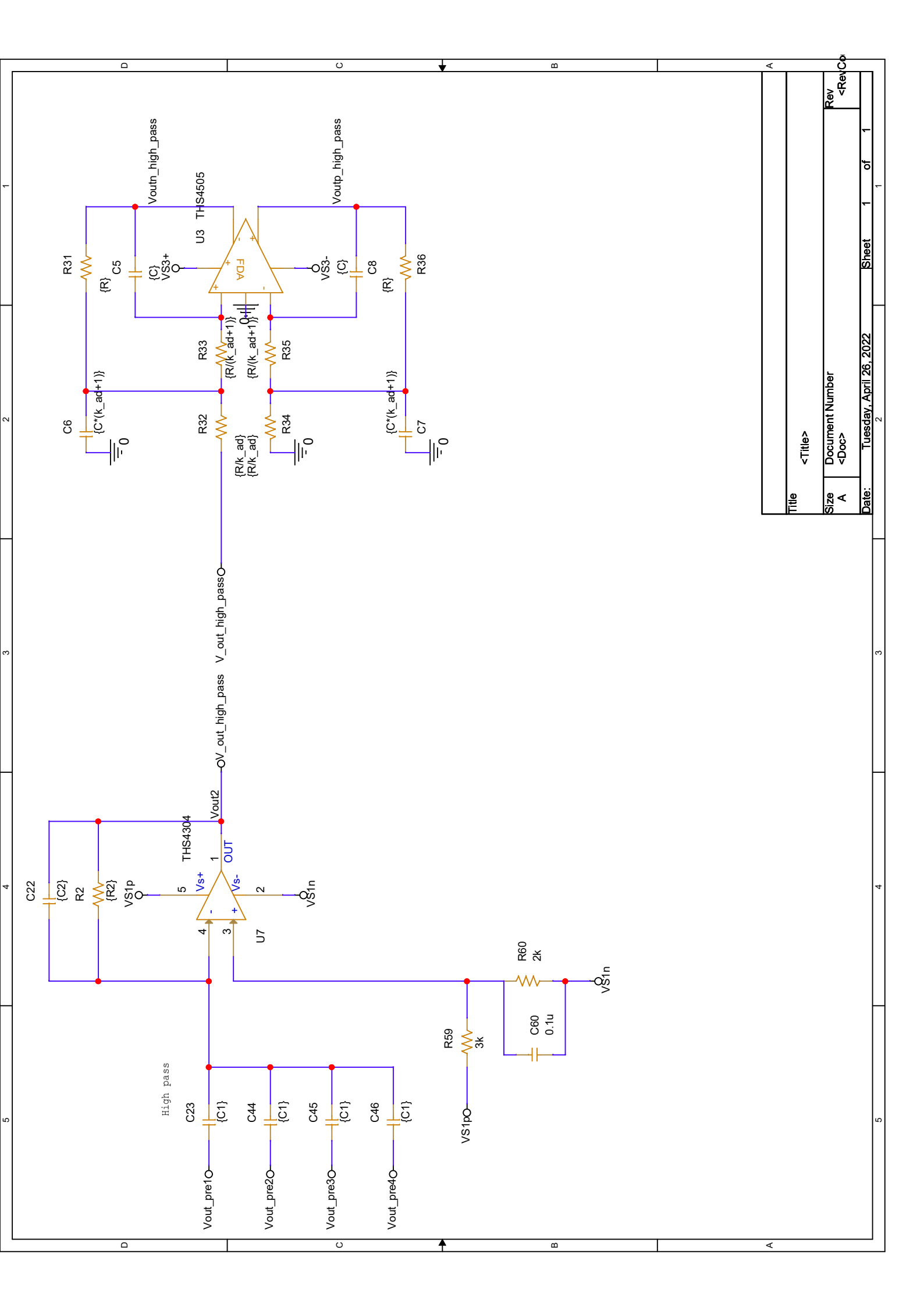
filter

adc driver

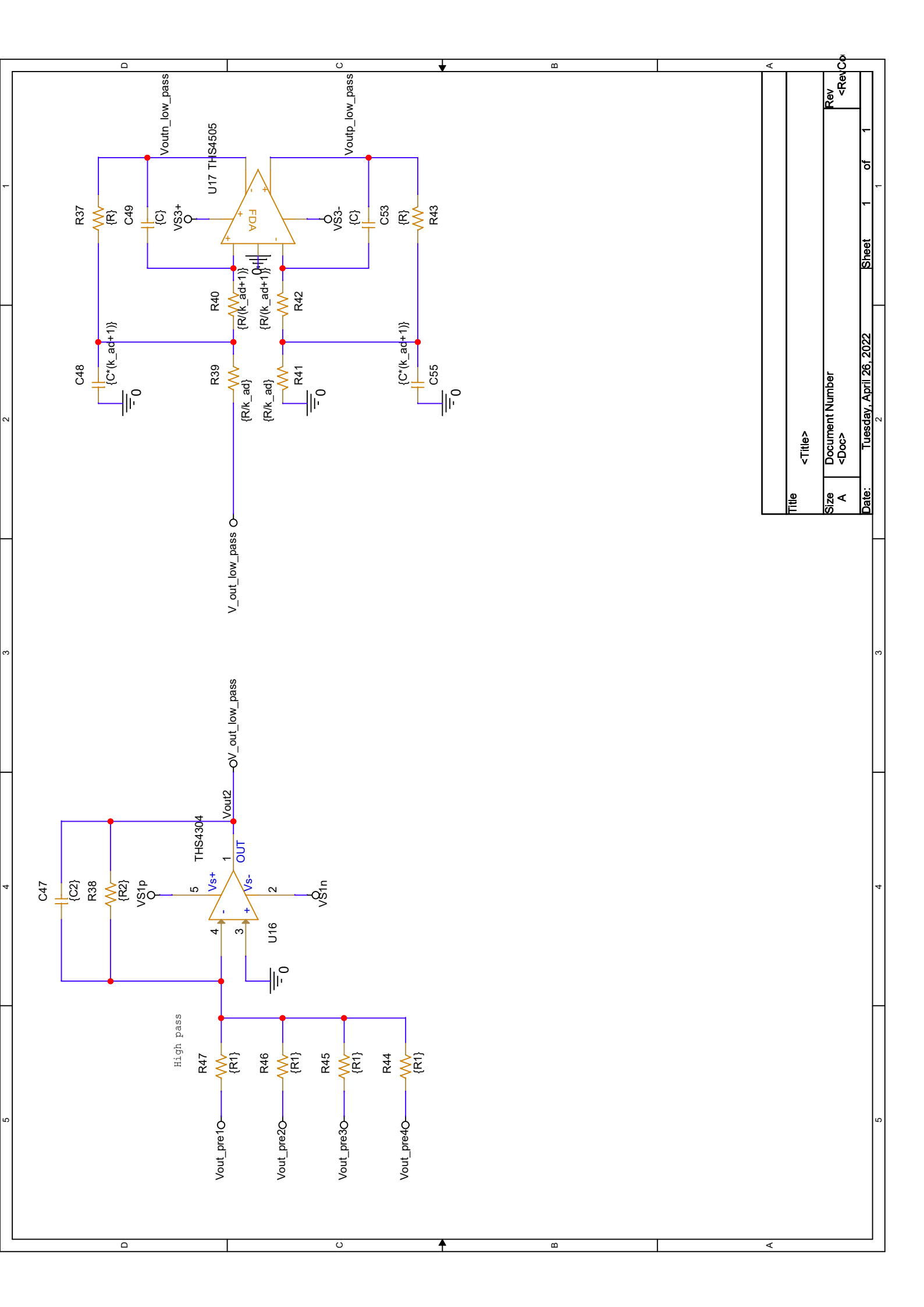
Title		<Title>	
Size	A	Document Number	<Doc>
Rev	<Rev>	Sheet	1 of 1
Date:	Tuesday, April 26, 2022	Sheet	1 of 1



Title		<Title>
Size	Document Number	Rev
A	<Doc>	<Rev>
Date:	Tuesday, April 26, 2022	Sheet 1 of 1

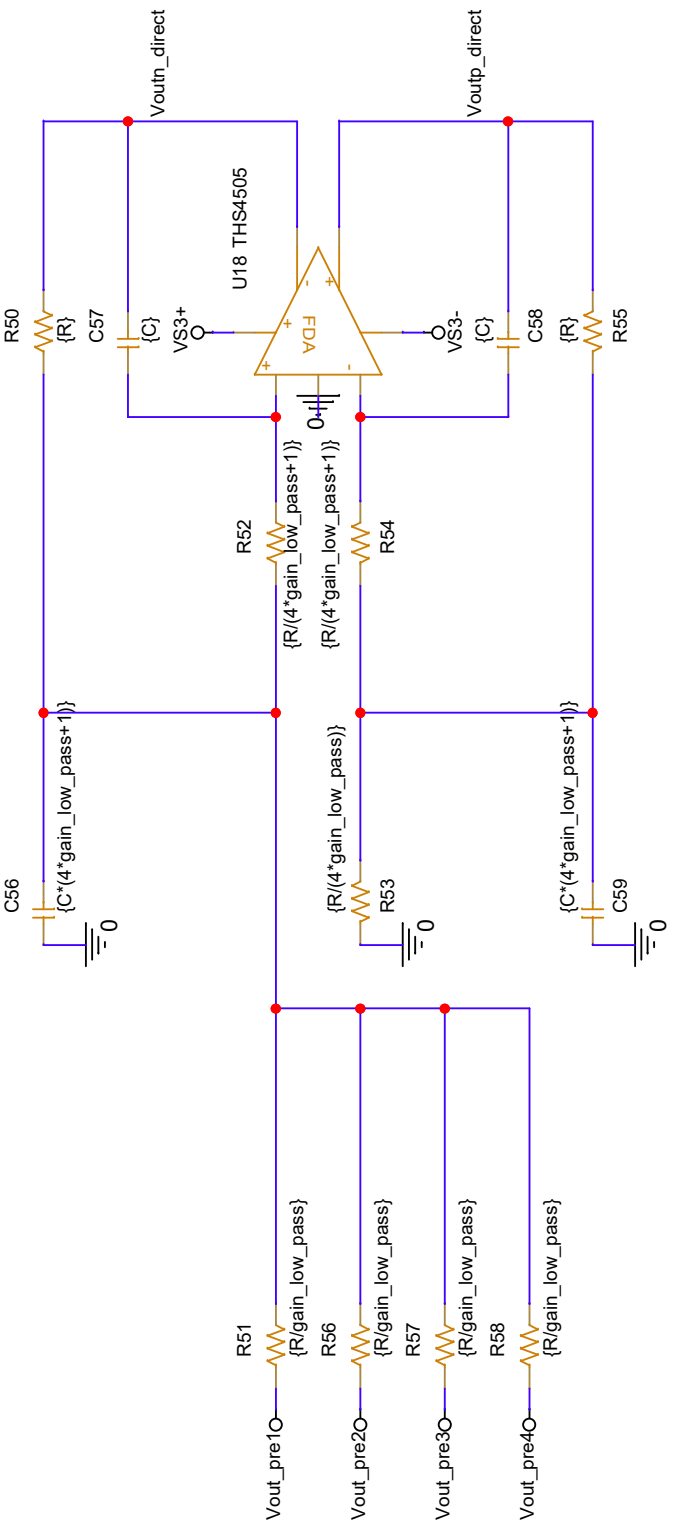


Title		<Title>	
Size	A	Document Number	<Doc>
Date:	Tuesday, April 26, 2022	Sheet	1 of 1



Title		<Title>
Size	Document Number	A
Rev	<Rev>	<Rev>
Date:	Tuesday, April 26, 2022	Sheet 1 of 1

ADC driver with the preamplifiers as input in summing configuration



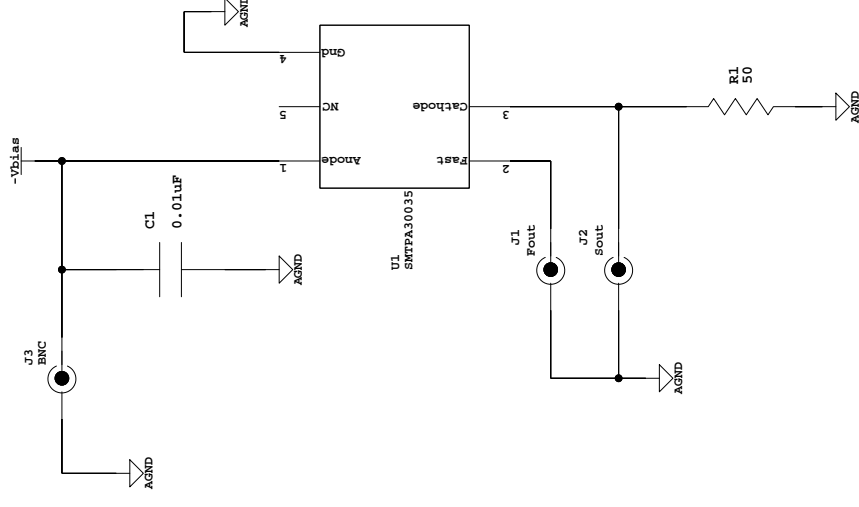
Title		<Title>
Size	Document Number	A <Doc>
Rev	<Rev>	1 of 1
Date:	Tuesday, April 26, 2022	Sheet 1 of 1

B.3 Schematics of Test Boards

This section shows the schematic for the test boards that were used in this thesis, these were all made by Senior Engineer Shiming Yang.

B.3.1 Single SiPM Test Board

6	5	4	3	2	1
Change description		Rev	Date		



University of Bergen

PROPRIETARY DATA: ALL RIGHT RESERVED. REPRODUCTION OR DISCLOSURE TO THIRD PARTIES OF THIS DOCUMENT OR ANY PART THEREOF IS NOT PERMITTED EXCEPT WITH PRIOR AND EXPRESSED WRITTEN PERMISSION.

Project

Drawn by	Date
Checked by	Date
Approved by	Date
PA approved by	Date

Drawing title

Drawing number

Rev
1

Sheet title

Sheet
1 / 1

6	5	4	3	2	1
Change description		Rev	Date		



University of Bergen

PROPRIETARY DATA: ALL RIGHT RESERVED. REPRODUCTION OR DISCLOSURE TO THIRD PARTIES OF THIS DOCUMENT OR ANY PART THEREOF IS NOT PERMITTED EXCEPT WITH PRIOR AND EXPRESSED WRITTEN PERMISSION.

Project

Drawn by	Date
Checked by	Date
Approved by	Date
PA approved by	Date

Drawing title

Drawing number

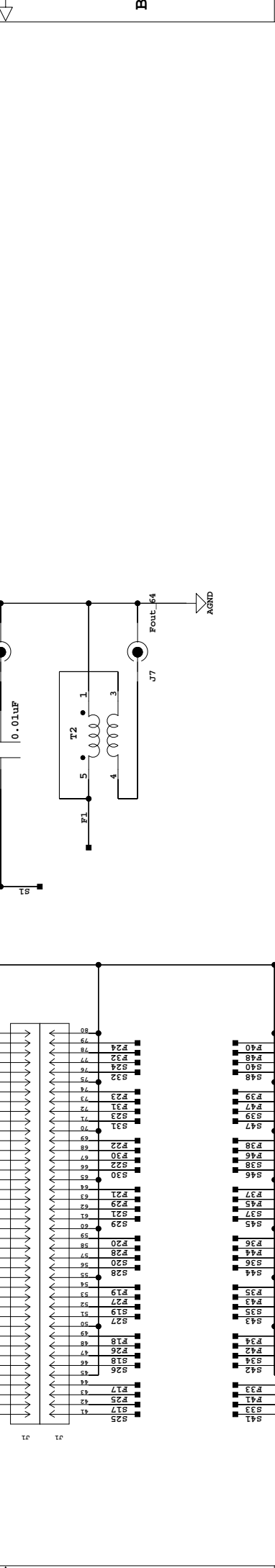
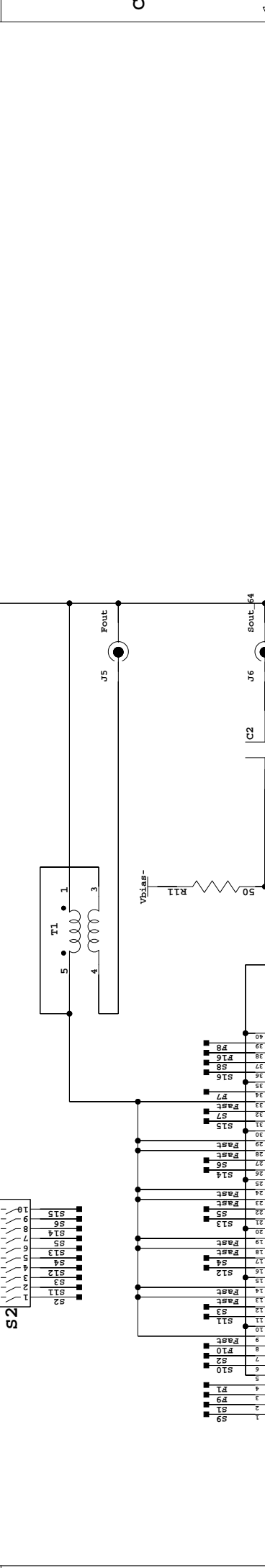
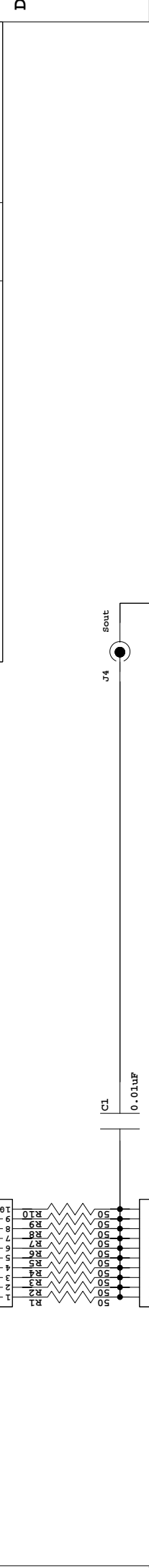
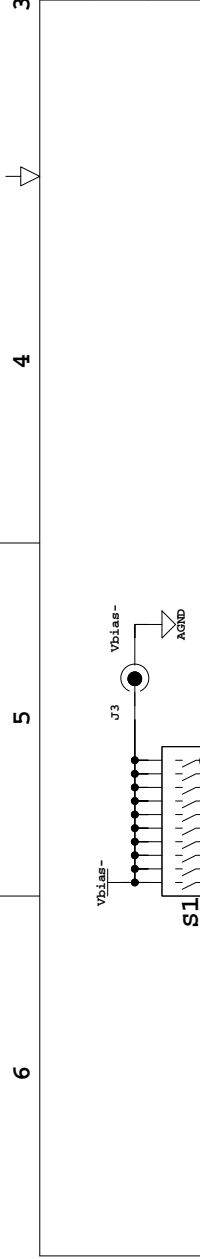
Rev
1


Sheet title

Sheet
1 / 1

B.3.2 SiPM Array Test Board for Varying Series Resistor and Number of Pixels

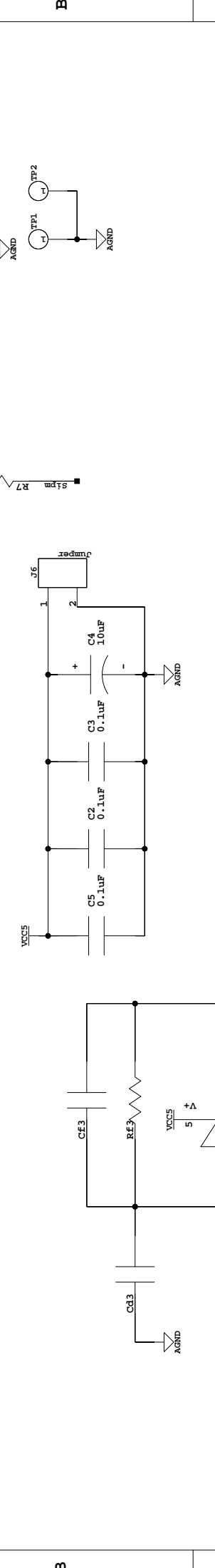
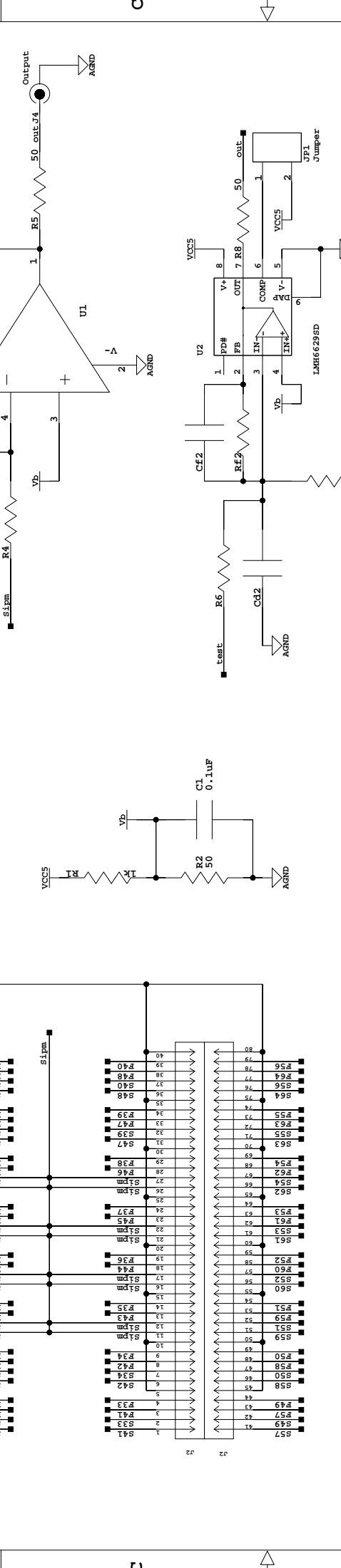
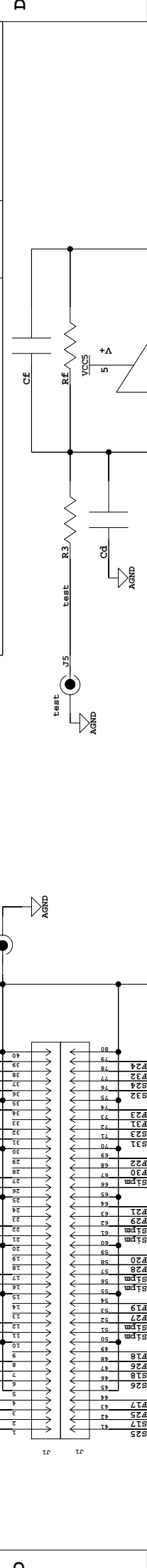
	2	1
Change description	Rev	Date



 University of Bergen		PROPRIETARY DATA: ALL RIGHT RESERVED. REPRODUCTION OR DISCLOSURE TO THIRD PARTIES OF THIS DOCUMENT OR ANY PART THEREOF IS NOT PERMITTED EXCEPT WITH PRIOR AND EXPRESSED WRITTEN PERMISSION.	
Project			
Drawn by	Date	Drawing title	Rev
Checked by	Date	Drawing number	1
Approved by	Date	Sheet title	Sheet 1 / 1
PA approved by	Date	Carrier / 1	1

B.3.3 SiPM Array Test Board with Amplifier Readout

6	5	4	3	2	1
Change description					
Rev					
Date					



 University of Bergen		Project	
Drawn by	Date	Drawing title	
Checked by	Date	Drawing number	
Approved by	Date	Rev	
FA approved by	Date	Sheet title	
		OpAmpTest / 1	
		2	1

PROPRIETARY DATA: ALL RIGHT RESERVED. REPRODUCTION OR DISCLOSURE TO THIRD PARTIES OF THIS DOCUMENT OR ANY PART THEREOF IS NOT PERMITTED EXCEPT WITH PRIOR AND EXPRESSED WRITTEN PERMISSION.

B.4 Schematic for High-Speed ADC Board

This section shows the schematic for the High-Speed ADC board. Head Engineer Bilal Hasan Qureshi is working on this board and has made this schematic. The work in this thesis has made changes to four of the ADC inputs, more specifically the pages called “Channel-A ArraySiPM-Standard”, “Channel-B ArraySiPM-Fast”, “Channel-J SingleSiPM-Standard” and “Channel-K SingleSiPM-K”.

ADC Schematic - Hierarchical Design

AD9257 Block: Octal 65 MSPS - 14 Bit ADC AD9257

ADS5404 Block: Dual 500 MSPS - 12 Bit ADC ADS5404

ZYNQ Block: ZYNQ-7Z030 FFG 676

Clock Multiplexer

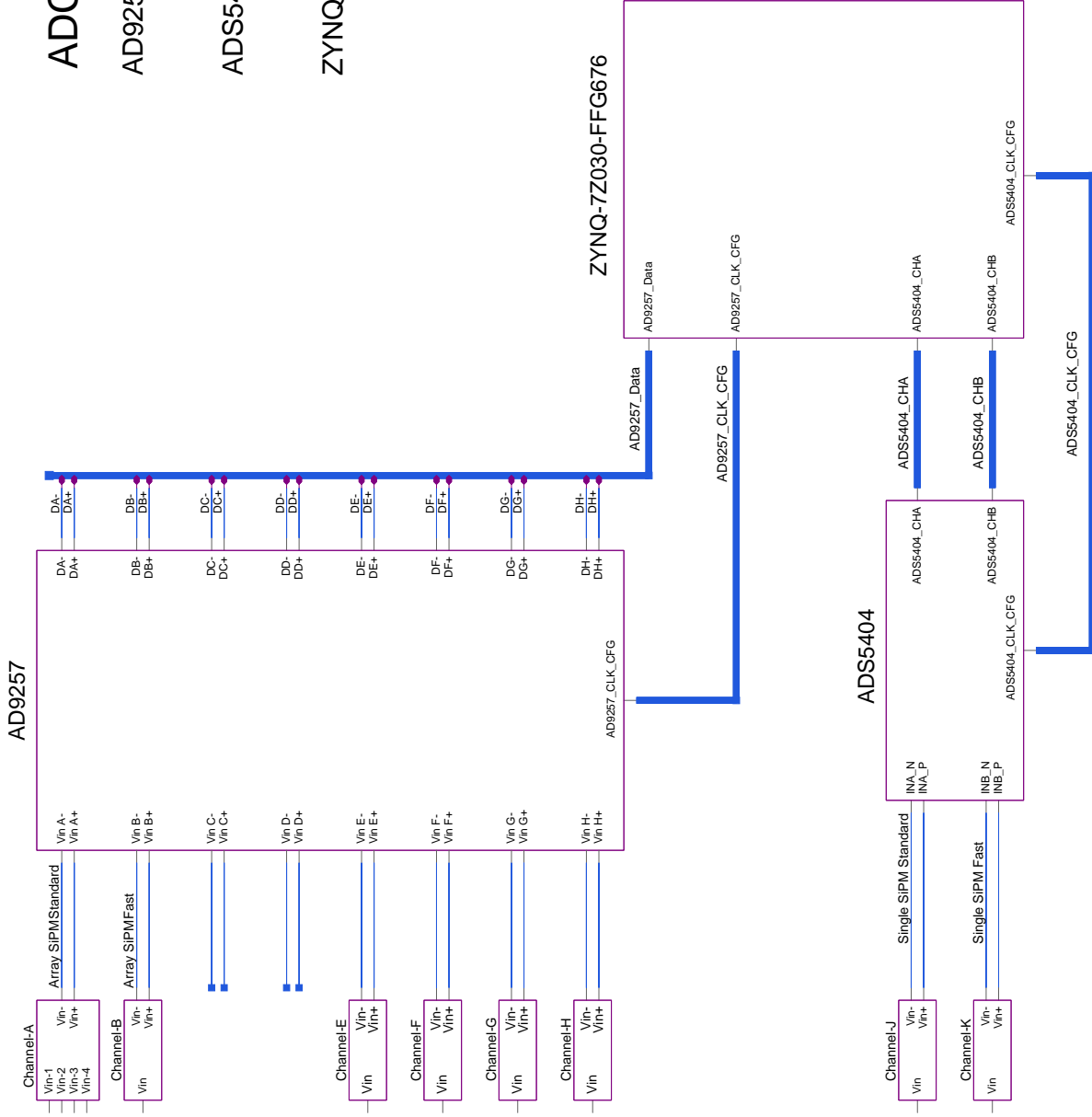
External SDRAM 512 MB DDR3L

External Flash 16 MB

USB OTG 2.0

Ethernet 1000 M

SD Card

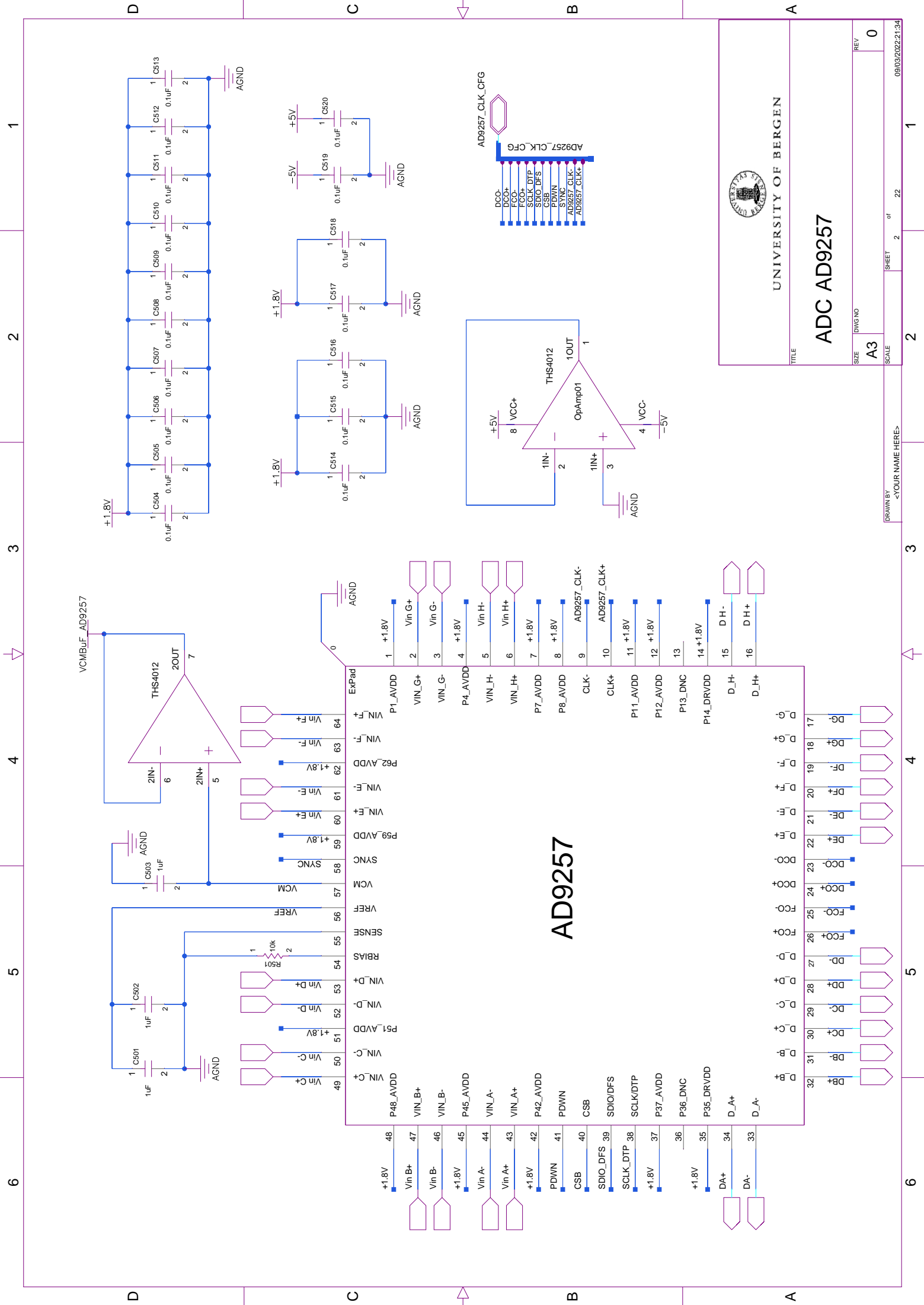


UNIVERSITY OF BERGEN

ADC-Top

TITLE	ADC-Top		
SIZE	DWG NO	SHEET	REV
A3		1 of 22	0
SCALE			

DRAWN BY <YOUR NAME HERE>



UNIVERSITY OF BERGEN

ADC AD9257

TITLE

SIZE: DWG NO. **A3** of 22 SHEET 2 of 22

SCALE

REV **0**

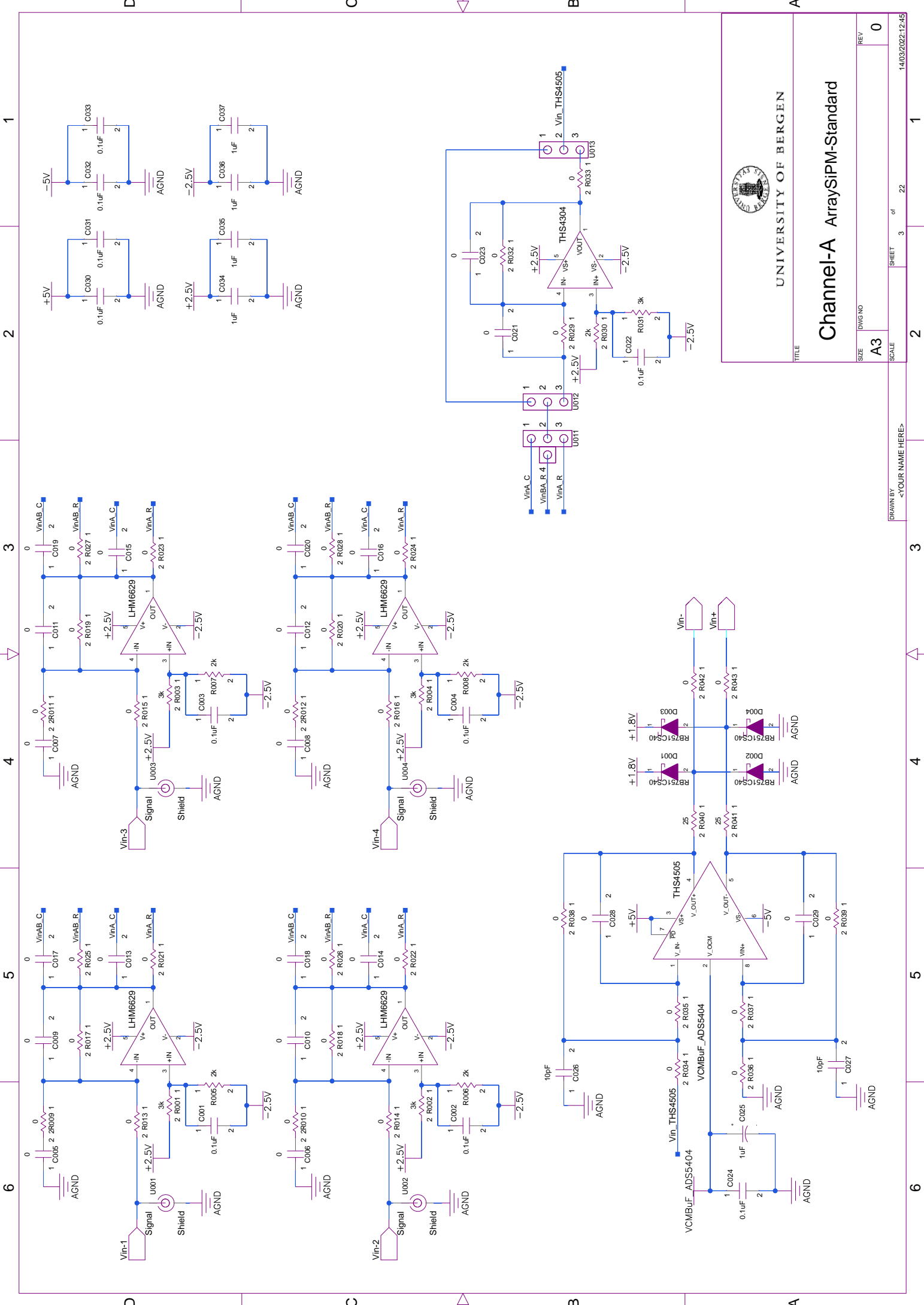
DRAWN BY: <YOUR NAME HERE> 09/03/2022, 21:34

AD9257

6 5 4 3 2 1

6 5 4 3 2 1

D C B A



UNIVERSITY OF BERGEN

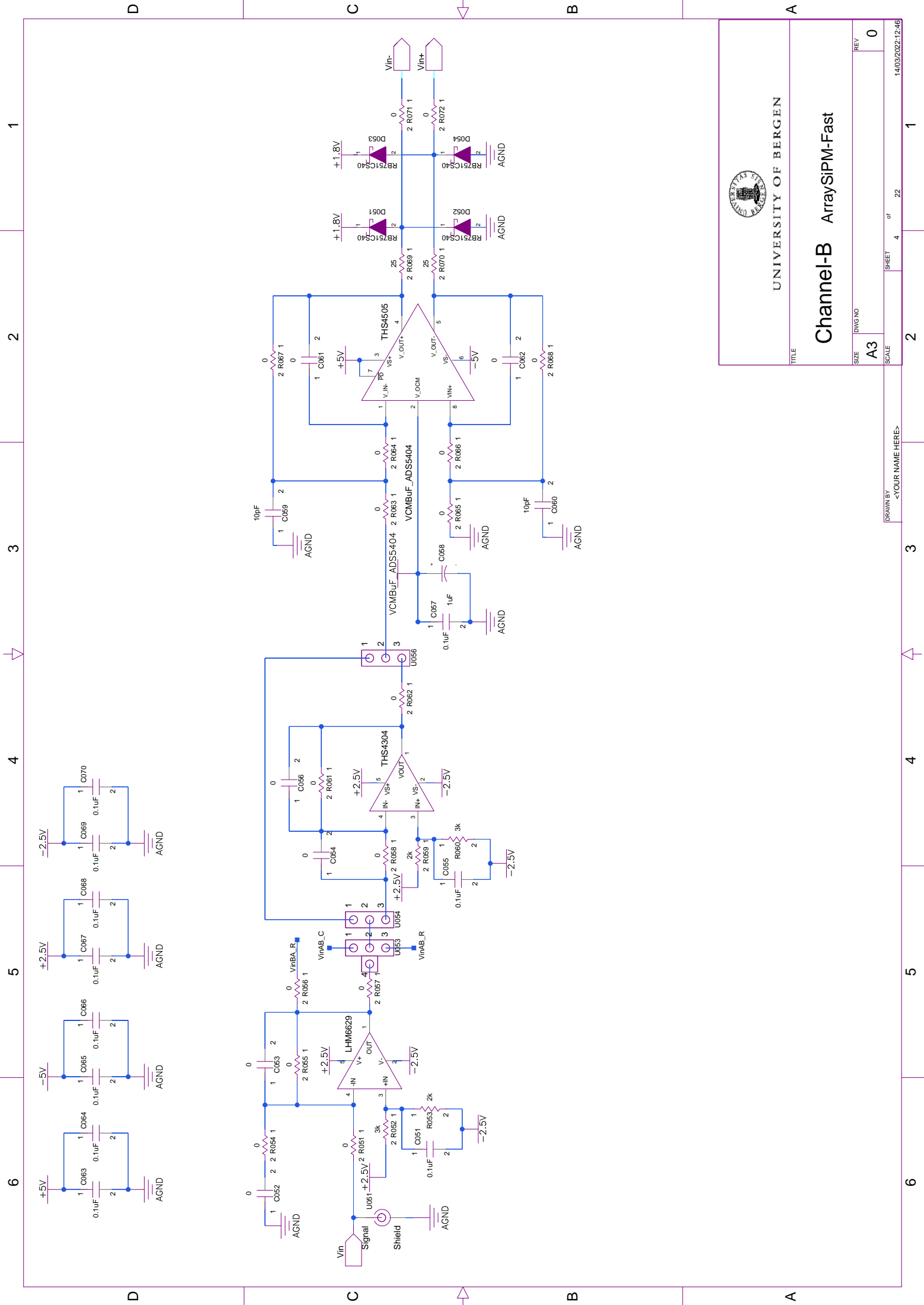
Channel-A ArraySiPM-Standard

TITLE

SIZE	DWG NO	SHEET	of	22	REV	0
A3						

DRAWN BY <YOUR NAME HERE>

14/03/2022:12:45



UNIVERSITY OF BERGEN

Channel-B ArraySiPM-Fast

TITLE

SIZE DWG NO
A3

SCALE SHEET 4 of 22

REV
0

14/03/2022:12:45

D

C

B

A

D

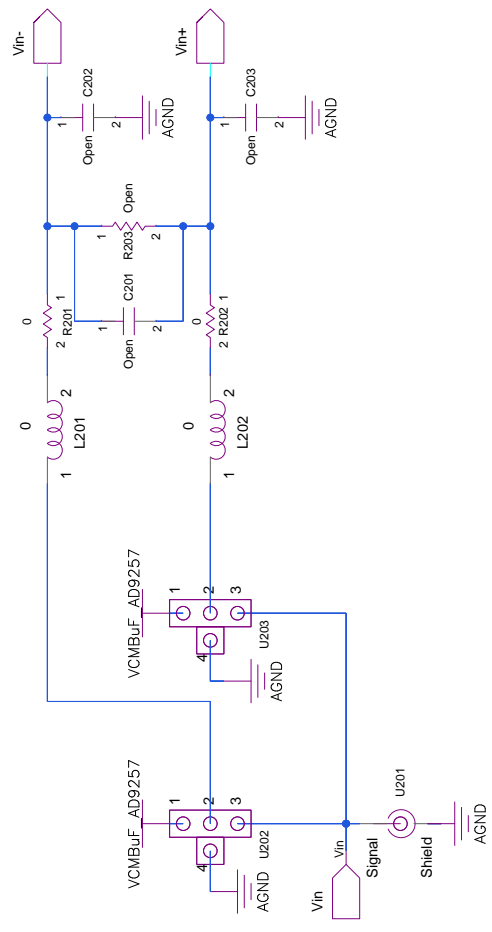
C


B

A

1 2 3 4 5 6

1 2 3 4 5 6



 UNIVERSITY OF BERGEN	
<h1>Channel-E Direct Induction</h1>	
TITLE	
SIZE	DWG NO
A3	
SCALE	
DRAWN BY	<YOUR NAME HERE>
SHEET	5 of 22
REV	0
14/03/2022:13:05	

D

C

B

A

D

C

B

A

1

2

3

4

5

6

1

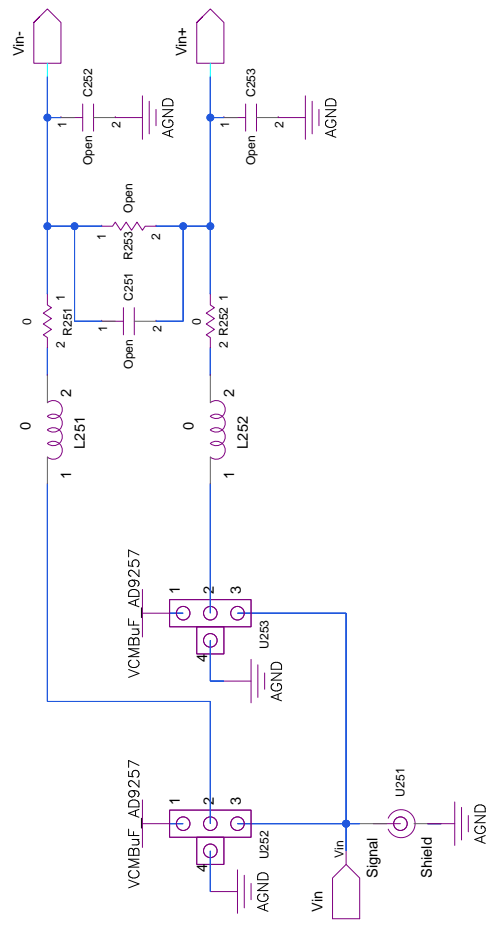
2


3

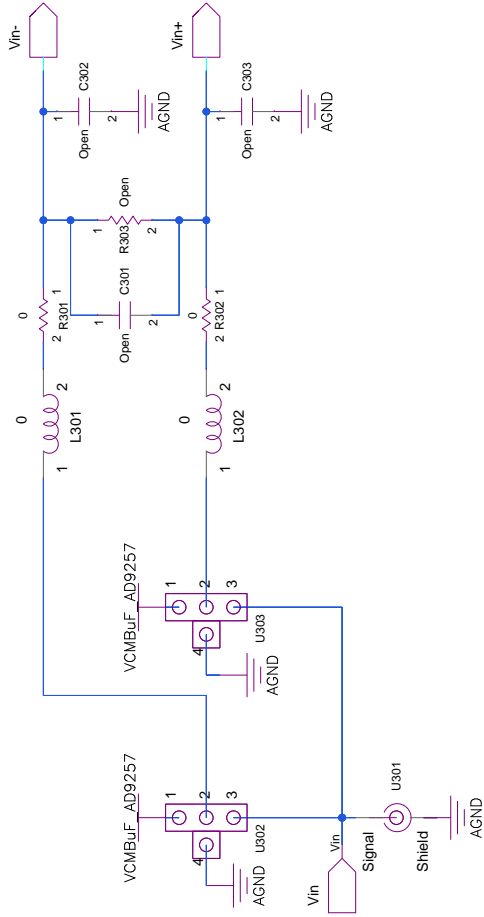
4


5

6



 UNIVERSITY OF BERGEN	
<h1>Channel-F Direct Induction</h1>	
TITLE	
SIZE	DWG NO
A3	
SCALE	
	SHEET 6 of 22
	REV 0
DRAWN BY <YOUR NAME HERE>	
14/03/2022:13:05	




 UNIVERSITY OF BERGEN
Channel-G Direct Induction

TITLE			
SIZE	DWG NO	SHEET	REV
A3		7 of 22	0
SCALE	DRAWN BY <YOUR NAME HERE>		
	2	3	1

D

C

B

A

D

C

B

A

1

2

3

4

5

6

1

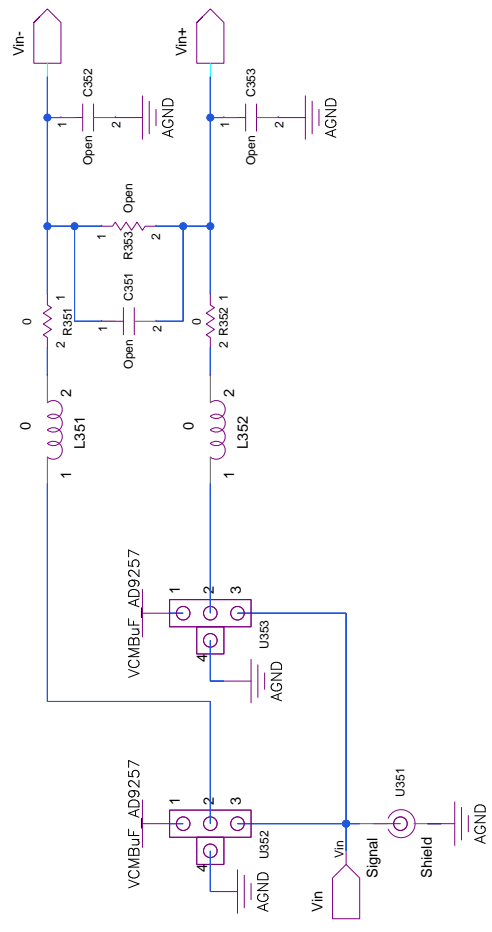
2


3

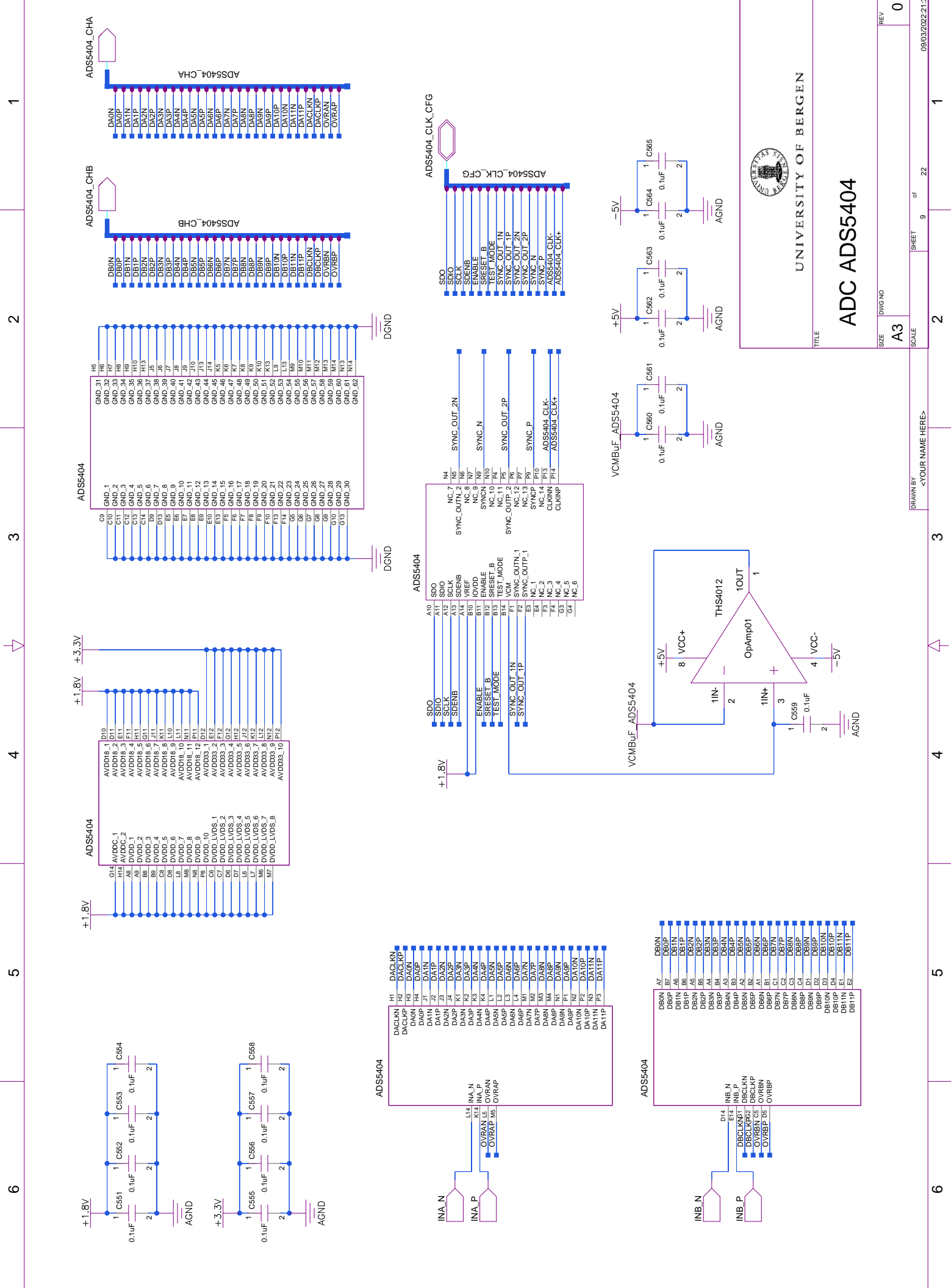
4

5

6



 UNIVERSITY OF BERGEN	
<h1>Channel-H Direct Induction</h1>	
TITLE	
SIZE	DWG NO
A3	
SCALE	
DRAWN BY	<YOUR NAME HERE>
SHEET	8 of 22
REV	0
14/03/2022:13:05	



UNIVERSITY OF BERGEN

ADC ADS5404

SIZE DWG NO
A3

SHEET 9 of 22

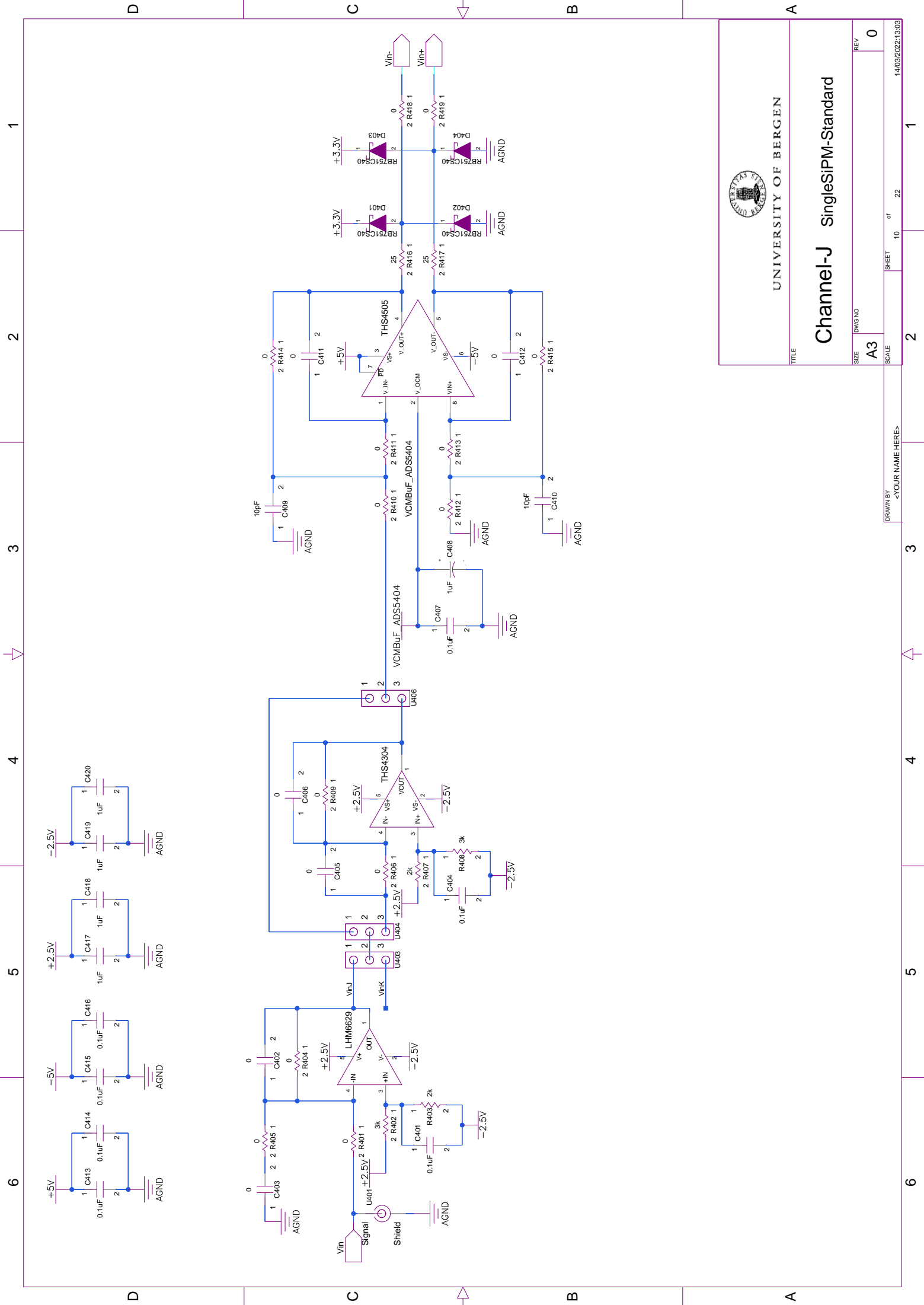
REV 0


09/03/2022, 21:34

DRAWN BY <YOUR NAME HERE> 2 3 4 5 6

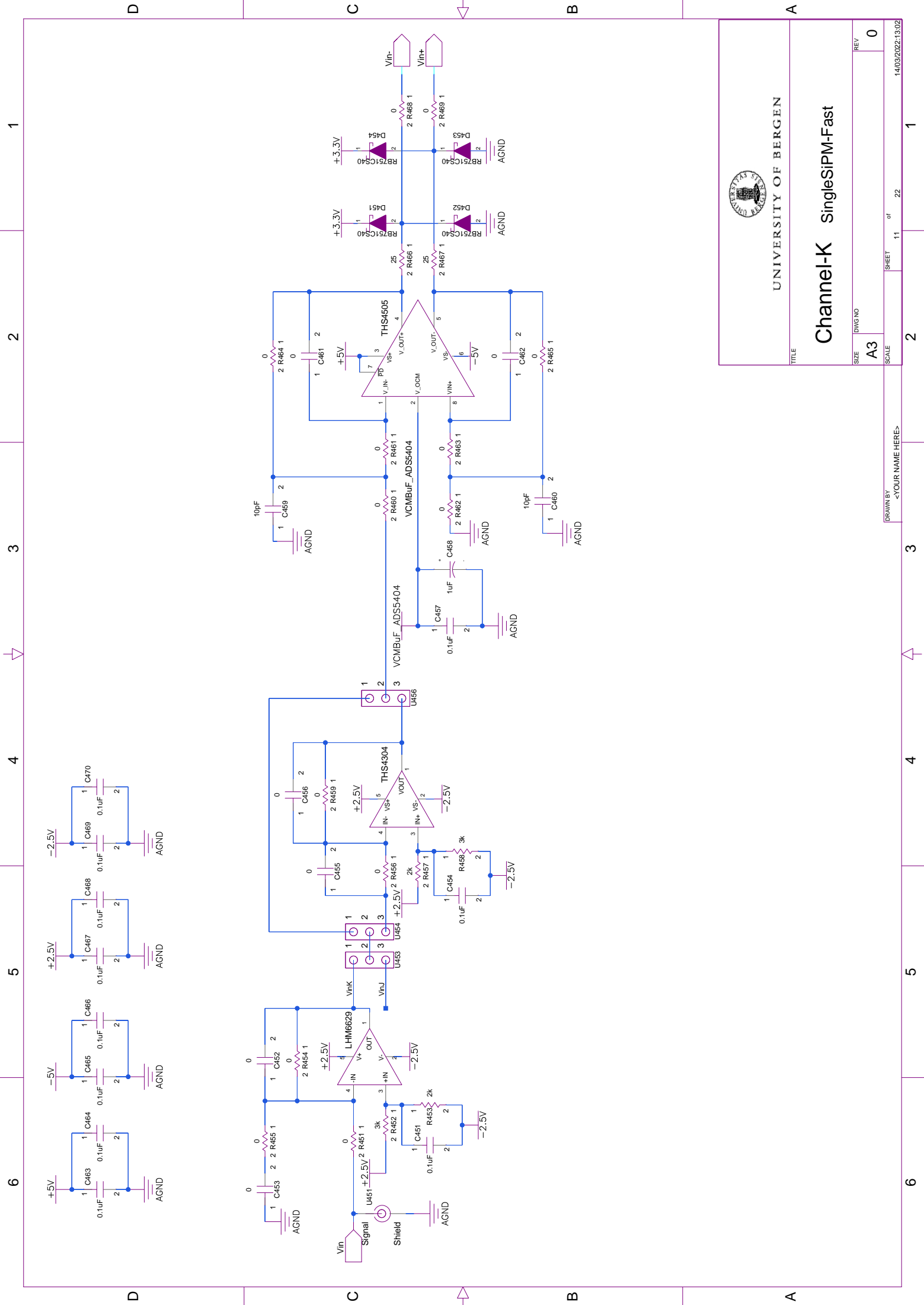
1 2 3 4 5 6


D C B A

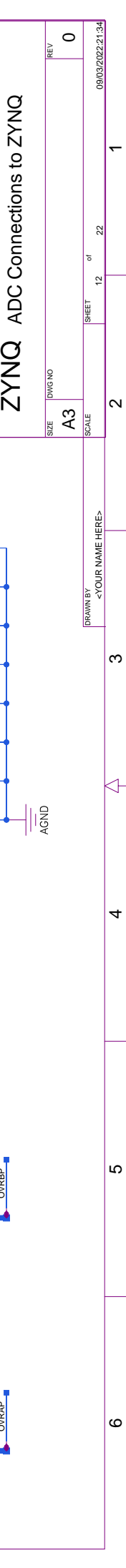
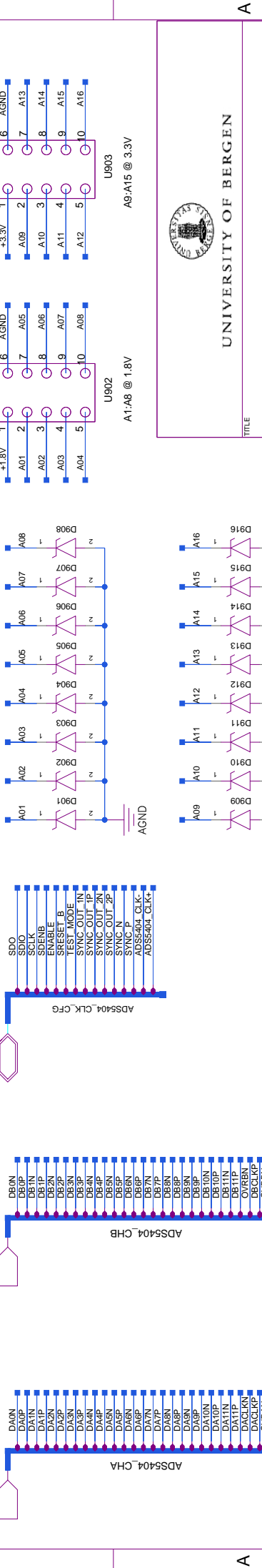
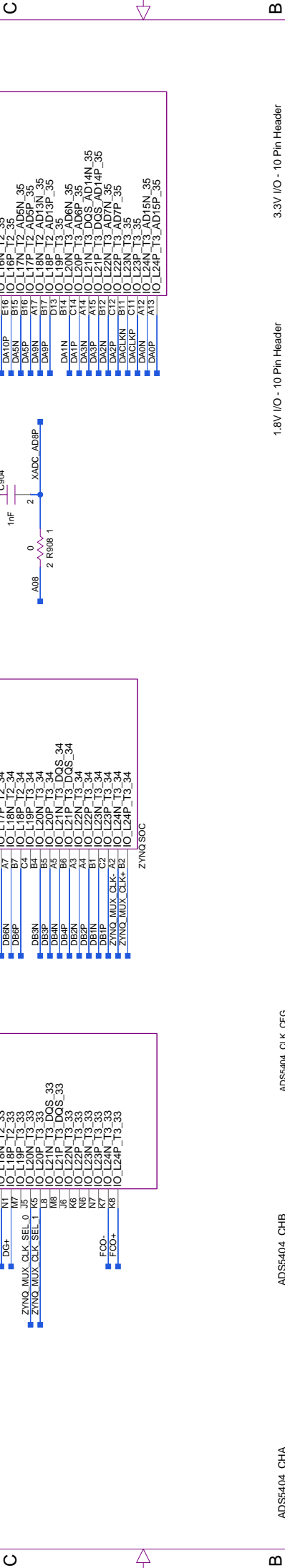


 UNIVERSITY OF BERGEN	
Channel-J SingleSiPM-Standard	
TITLE	
SIZE	DWG NO
A3	
SCALE	SHEET 10 of 22
DRAWN BY	<YOUR NAME HERE>
	1403/2022:13.03

REV	0
-----	---



 UNIVERSITY OF BERGEN	
Channel-K SingleSIPM-Fast	
TITLE	
SIZE	DWG NO
A3	
SCALE	
DRAWN BY	<YOUR NAME HERE>
SHEET	11 of 22
REV	0
1403/2022:1302	



D

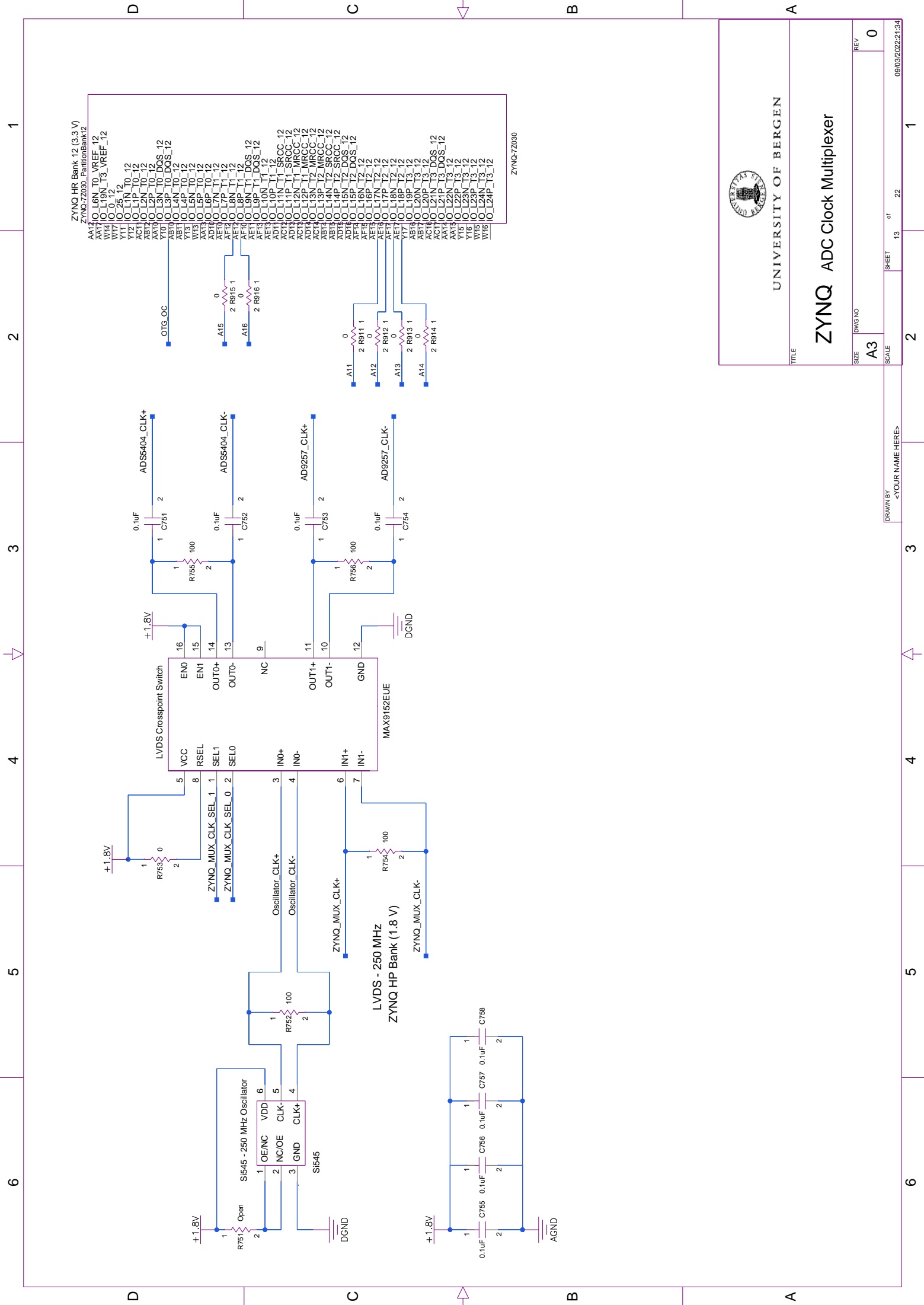
C

B

A

UNIVERSITY OF BERGEN
ZYNQ ADC Connections to ZYNQ

SIZE DWG NO **A3** SCALE **1** SHEET OF **22**
 REV **0** 09/03/2022 21:34
 DRAWN BY: <YOUR NAME HERE>



UNIVERSITY OF BERGEN

ZYNQ ADC Clock Multiplexer

TITLE

SIZE: DWG NO: **A3** SCALE: **13** of **22** SHEET

REV: **0**

DRAWN BY: <YOUR NAME HERE>

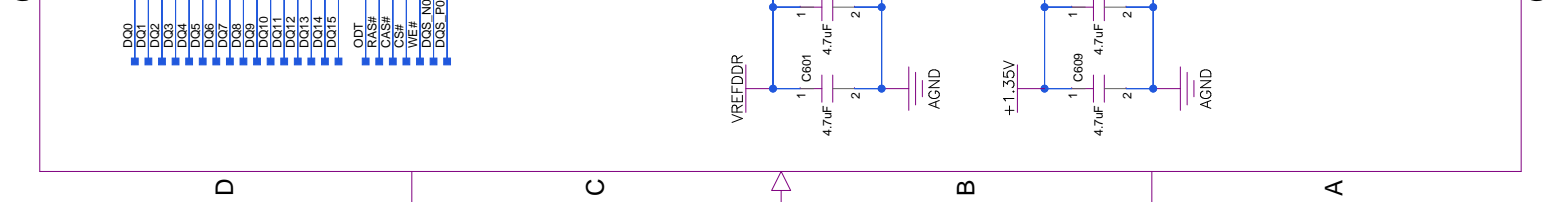
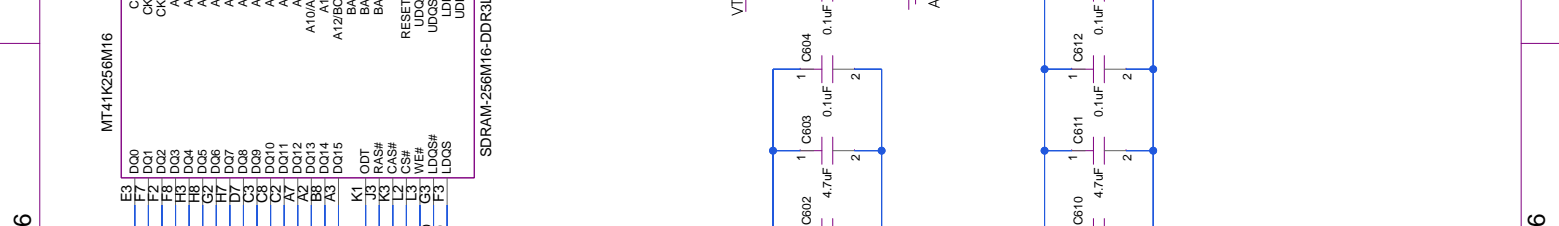
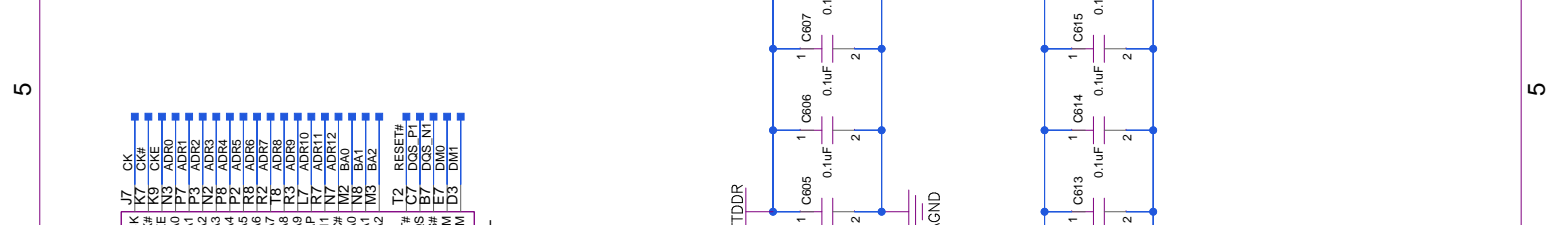
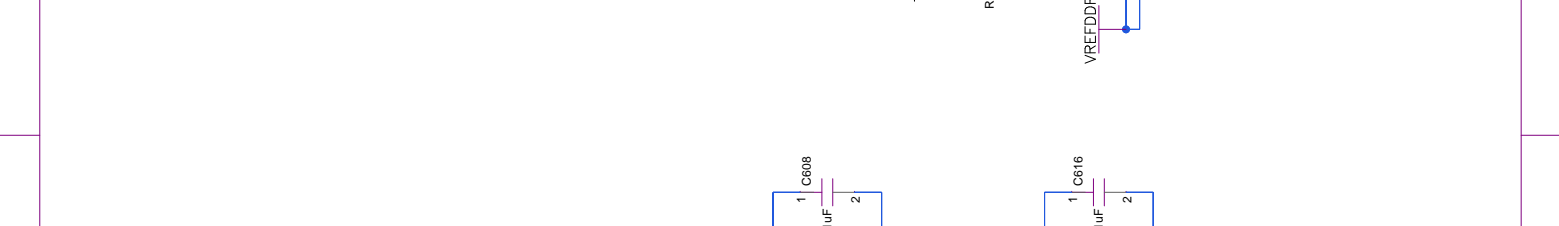
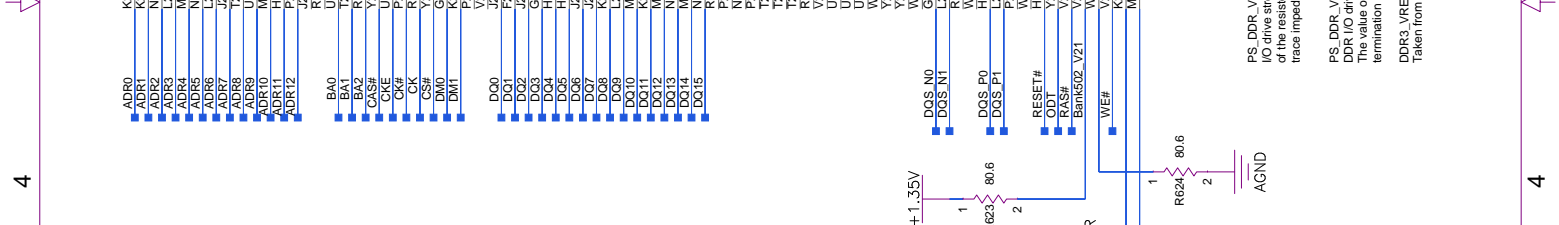
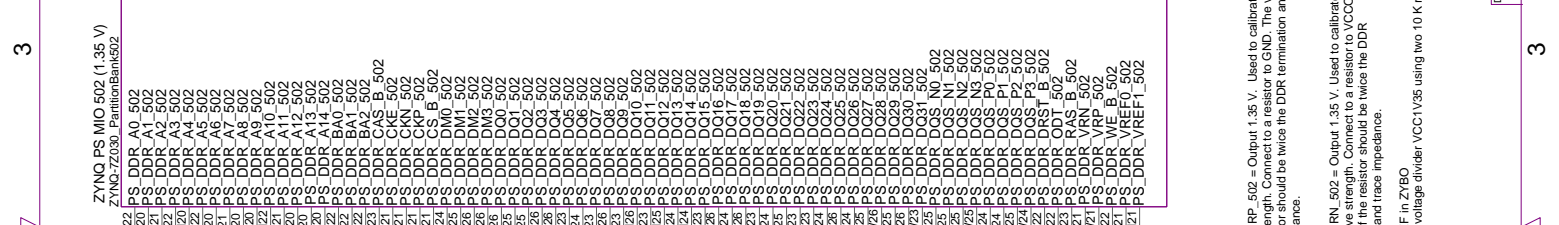
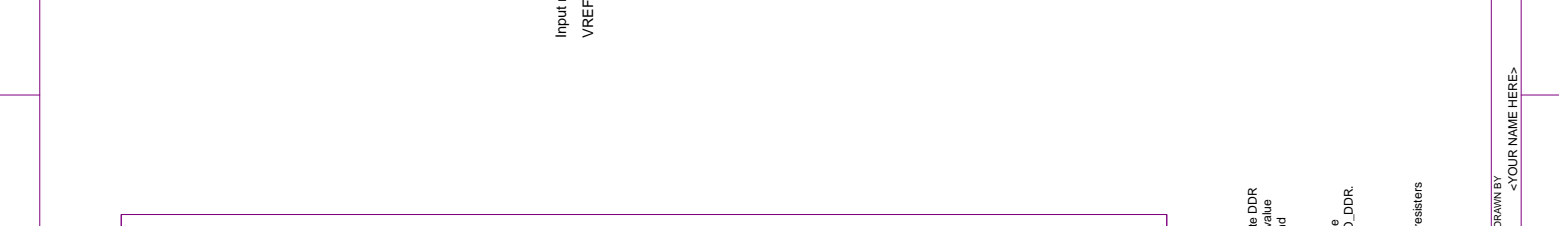
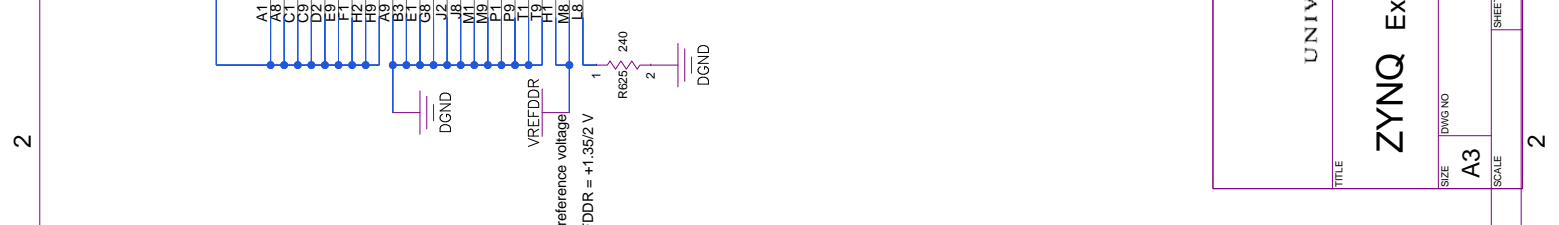
09/03/2022, 21:34

6 5 4 3 2 1

6 5 4 3 2 1

D C B A

D C B A



PS_DDR_VRP_502 = Output 1.35 V. Used to calibrate DDR I/O drive strength. Connect to a resistor to GND. The value of the resistor should be twice the DDR termination and trace impedance.

PS_DDR_VRN_502 = Output 1.35 V. Used to calibrate DDR I/O drive strength. Connect to a resistor to VCC0_DDR. The value of the resistor should be twice the DDR termination and trace impedance.

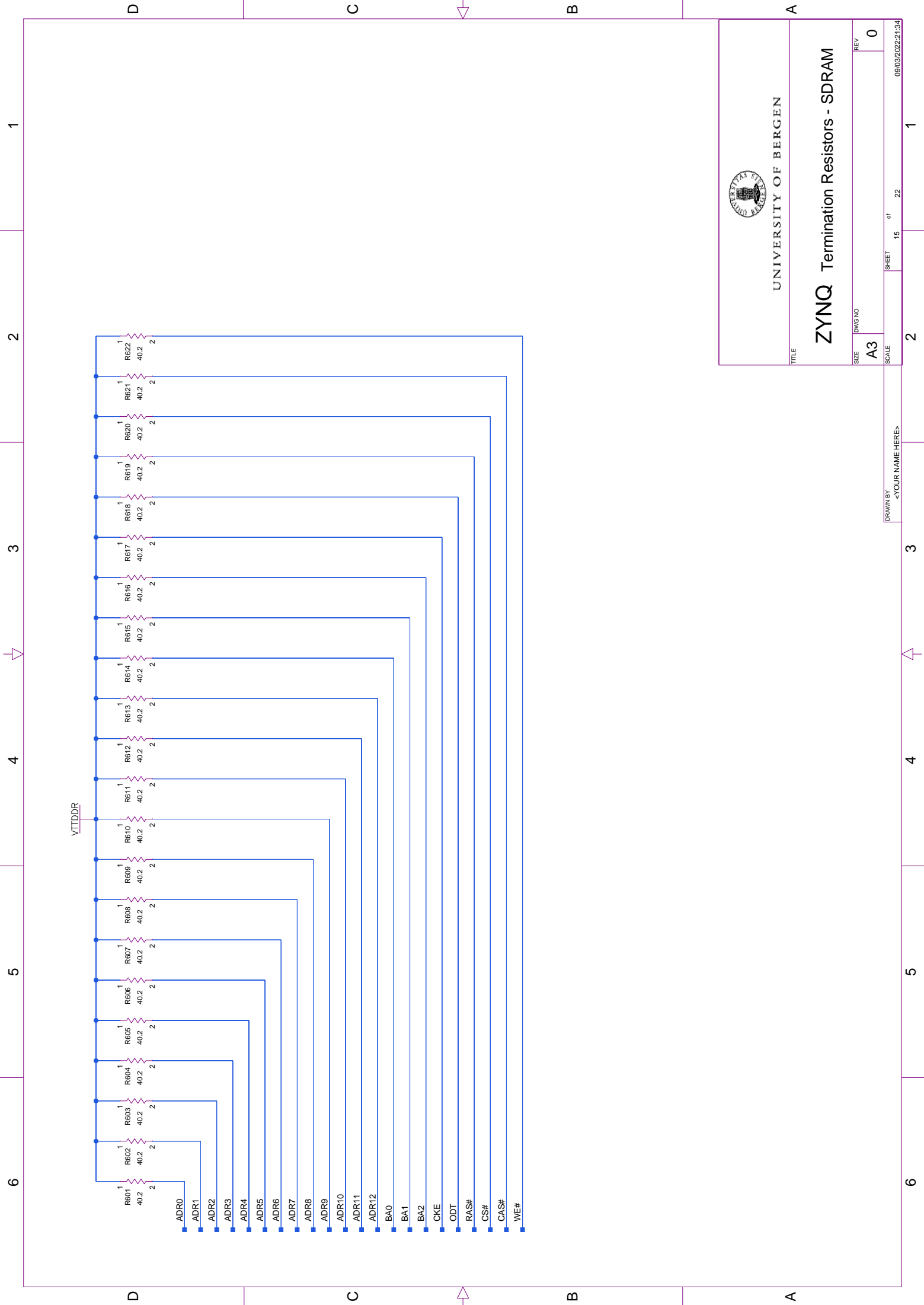
DDR3_VREF in ZYBO
Taken from voltage divider VCC1V35 using two 10-K resistors


UNIVERSITY OF BERGEN

ZYNQ External SDRAM DDR3L

REV 0

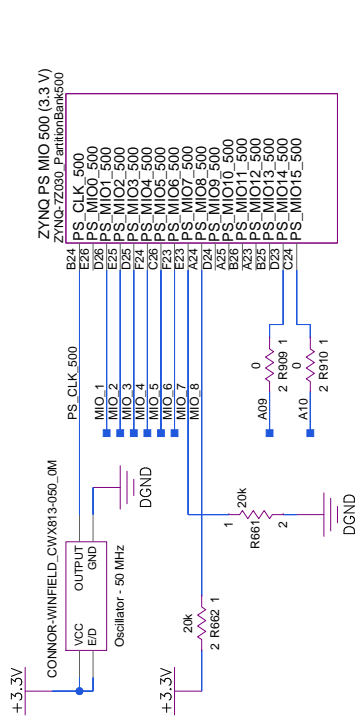
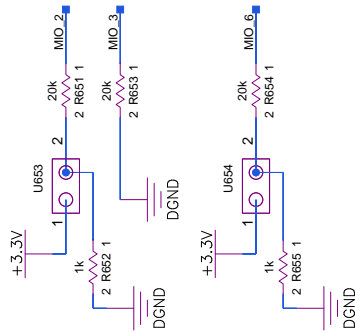
09/03/2022, 21:34



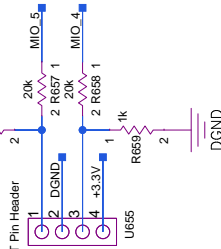
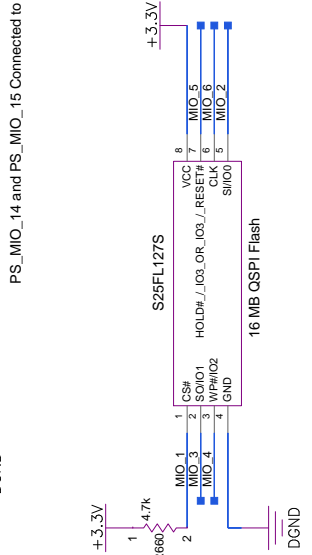
 UNIVERSITY OF BERGEN	
ZYNQ Termination Resistors - SDRAM	
TITLE	
SIZE	DWG NO
A3	
SCALE	
DRAWN BY	<YOUR NAME HERE>
SHEET	15 of 22
REV	0
09/03/2022, 21:34	



MIO[2:6] are bootstrapping pins for configuration.
 UG585 page 166 and 52
 MIO[7:8] are Voltage Mode Configuration.
 UG933 page 57
 MIO Bank 0: PS_MIO[0:15] MIO500 (3.3 V). Pull Down MIO_7 with 20 k resistor
 MIO Bank 1: PS_MIO[16:53] MIO501 (1.8 V) . Pull Up MIO_8 to VCCO_MIO0 with 20 k resistor



PS_MIO_14 and PS_MIO_15 Connected to UART



Connect 1 and 2 for JTAG
 Connect 2 and 3 for QSPI Flash
 Connect 3 and 4 for SD Card



UNIVERSITY OF BERGEN

ZYNQ QSPI Flash and BOOT

SIZE DWG NO

A3

SCALE

REV

0

09/03/2022, 21:34

DRAWN BY <YOUR NAME HERE>

SHEET 16 of 22

2

3

4

5

6

1

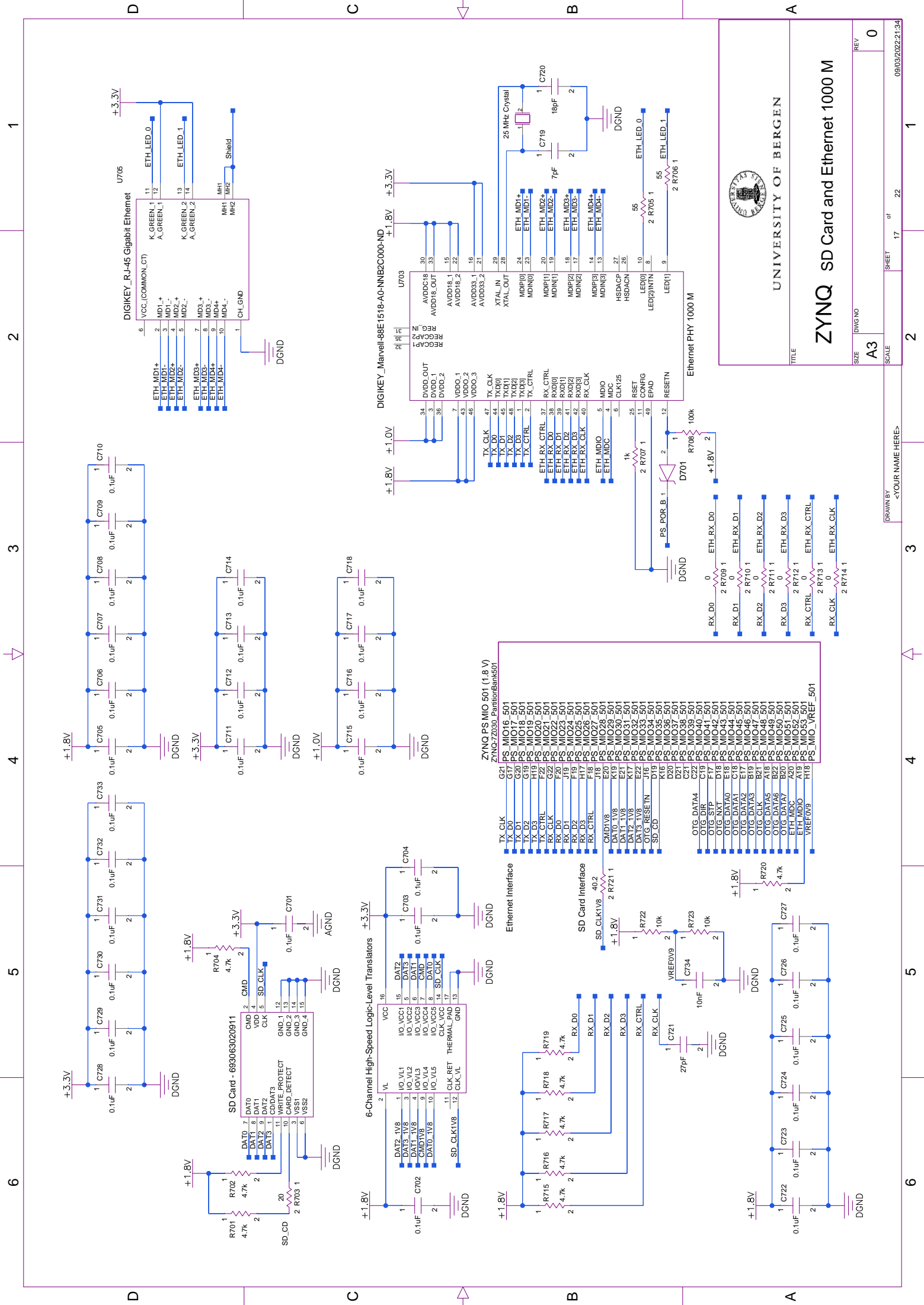
2

3

4

5

6



6 5 4 3 2 1

D C B A 3 2

DIGIKEY_RJ-45 Gigabit Ethernet

DIGIKEY_Marvell88E1518-A0-NNB2C000-ND

Ethernet PHY 1000 M

ZYNQ PS MIO501 (1.8V)

6-Channel High-Speed Logic-Level Translators

SD Card - 693063020911

UNIVERSITY OF BERGEN

ZYNQ SD Card and Ethernet 1000 M

SIZE DWG NO

A3

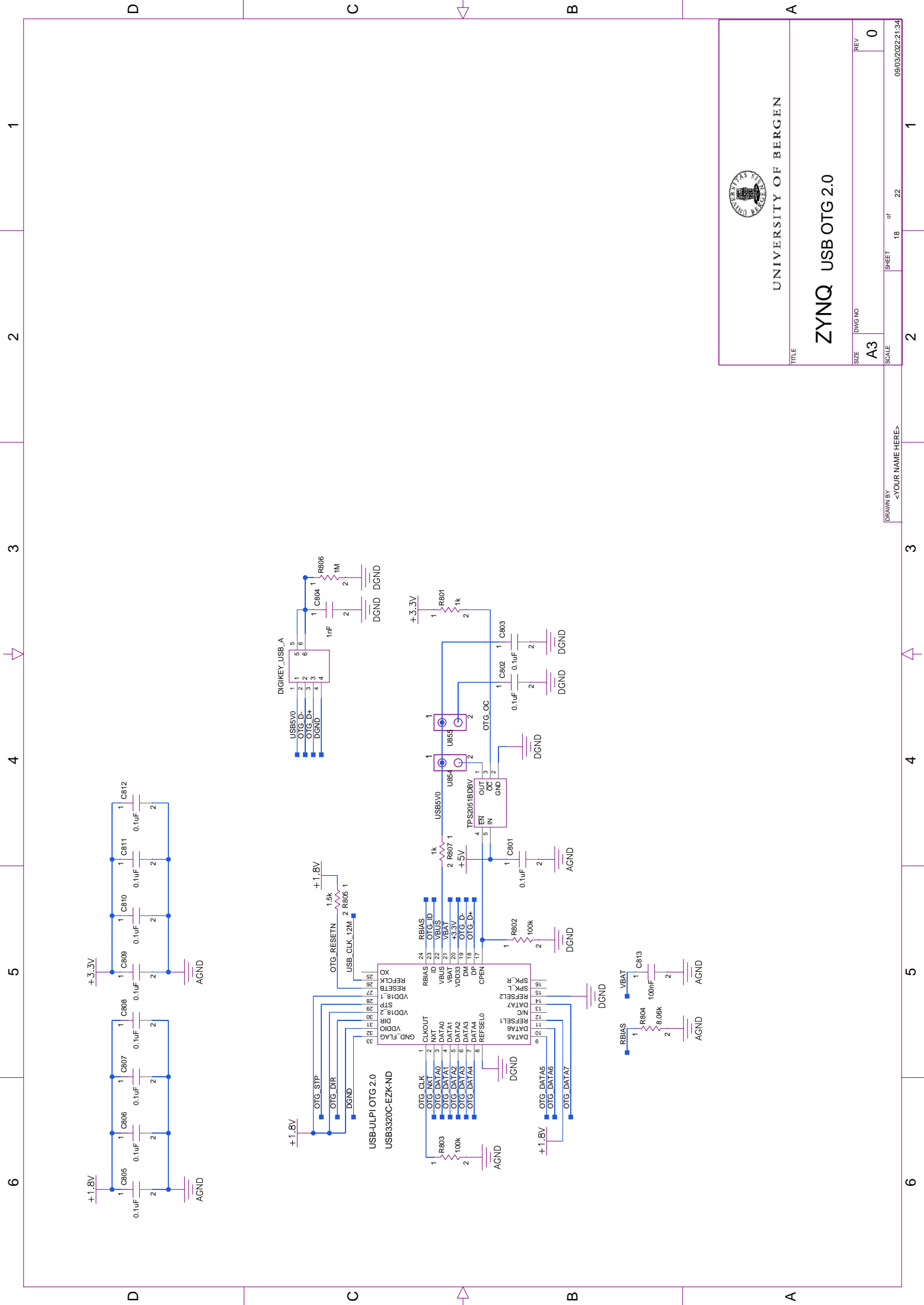
SCALE

SHEET 17 of 22

DRAWN BY <YOUR NAME HERE>


REV 0

09/03/2022, 21:34



6 5 4 3 2 1

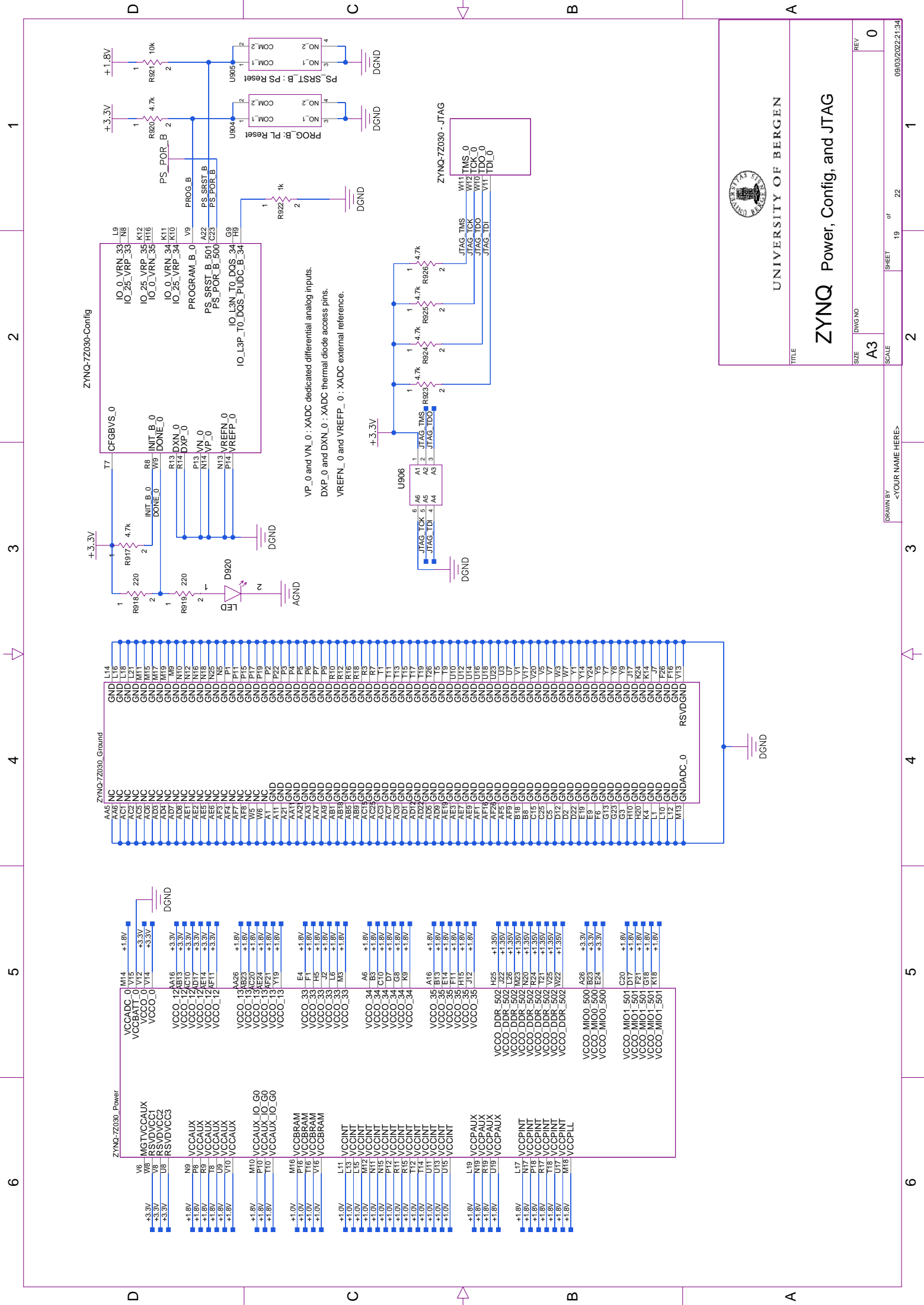
D C B A


 UNIVERSITY OF BERGEN
ZYNQ USBOTG 2.0

TITLE			
SIZE	DWG NO	SHEET	of
A3		18	22
SCALE	<YOUR NAME HERE>		
REV	0	09/03/2022, 21:34	

6 5 4 3 2 1

D C B A



1 2 3 4 5 6

1 2 3 4 5 6

UNIVERSITY OF BERGEN

ZYNQ Power, Config, and JTAG

TITLE

SIZE: DWG NO
A3

SCALE

DRAWN BY: <YOUR NAME HERE>

SHEET 19 of 22

REV 0

09/03/2022 21:34

D

C

B

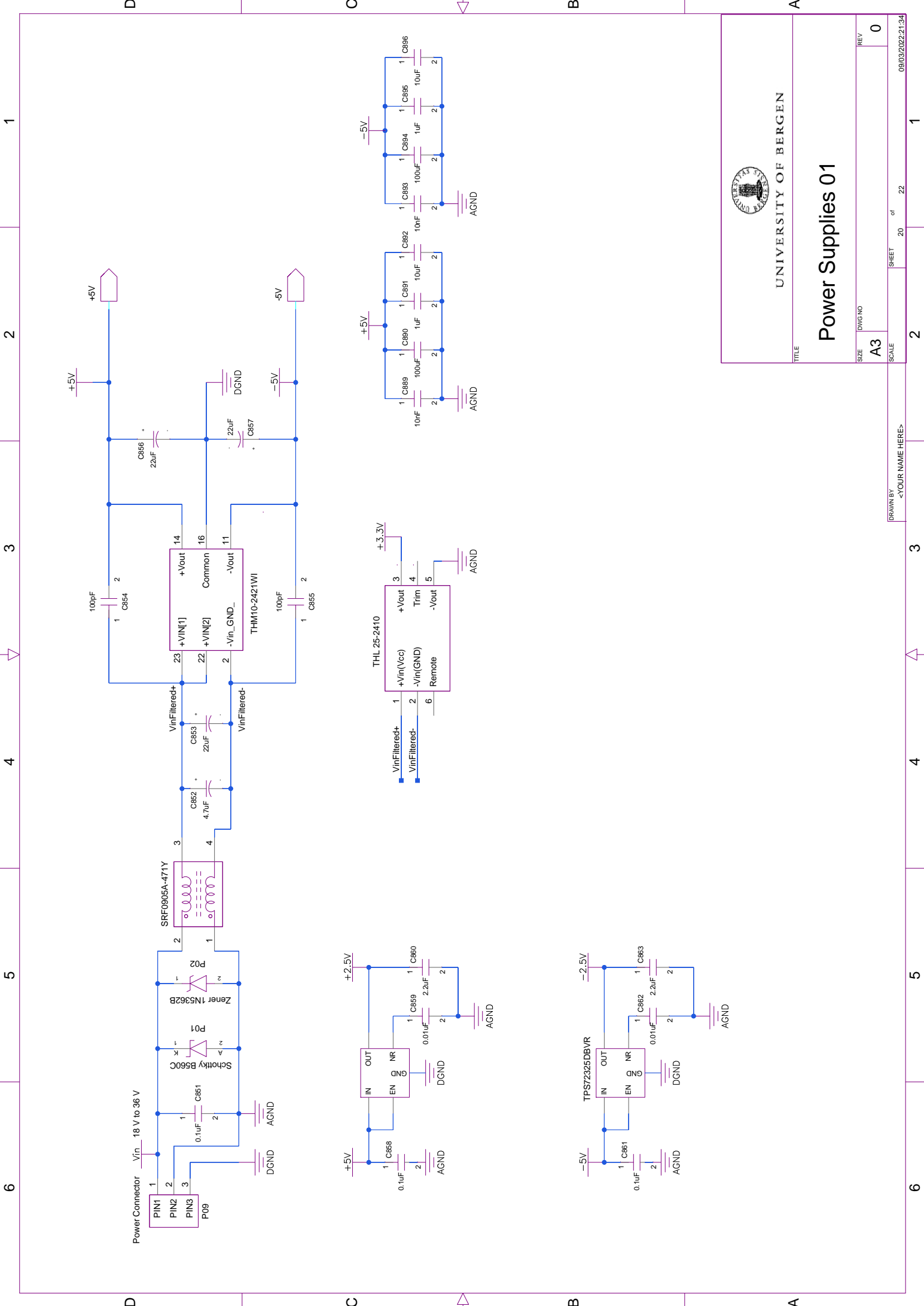
A

D

C

B

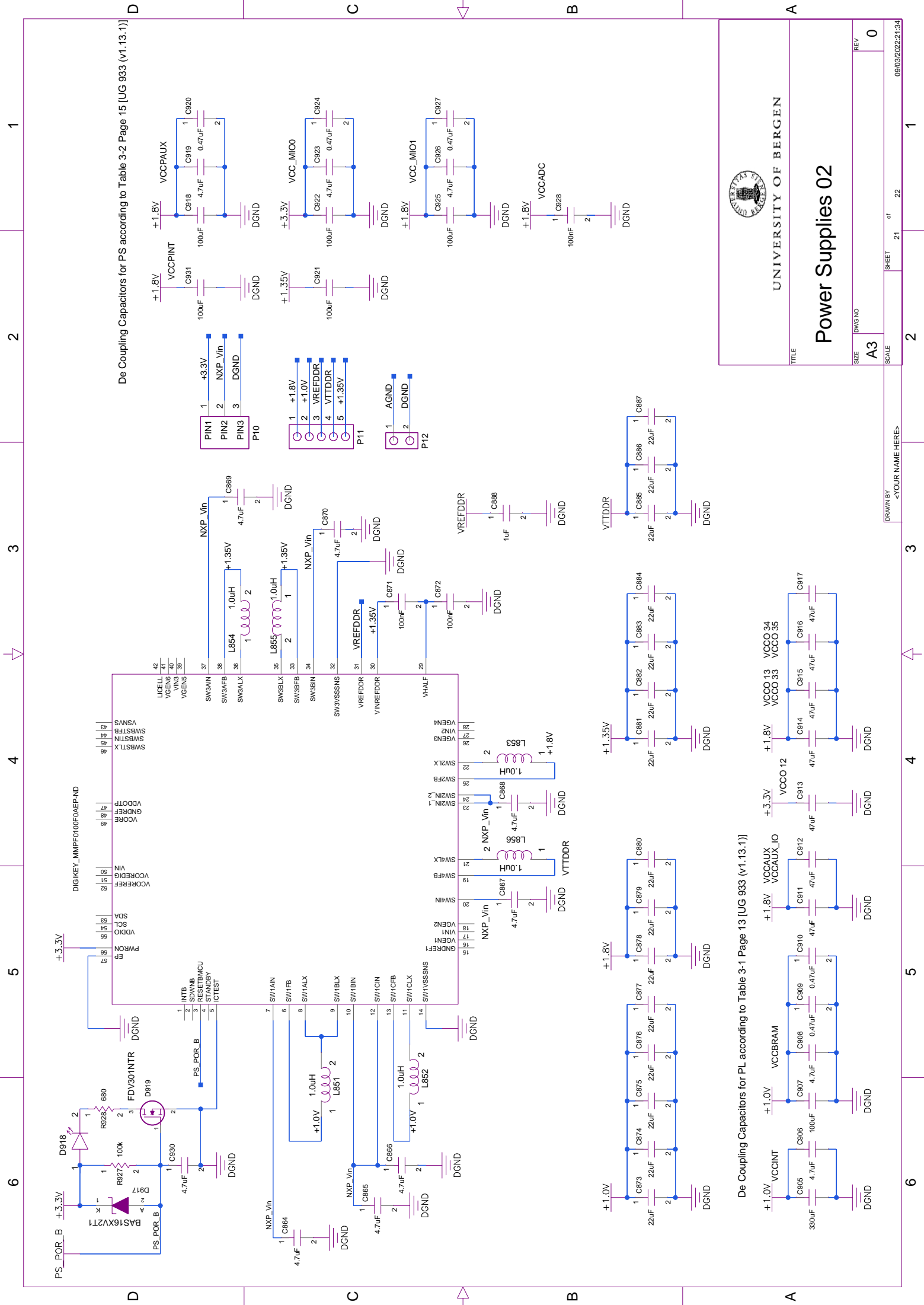
A



UNIVERSITY OF BERGEN

Power Supplies 01

TITLE: _____
 SIZE: DWG NO: _____
 SCALE: A3
 SHEET: 20 of 22
 DRAWN BY: <YOUR NAME HERE>
 REV: 0
 09/03/2022, 21:34



De Coupling Capacitors for PS according to Table 3-2 Page 15 [UG 933 (v1.13.1)]

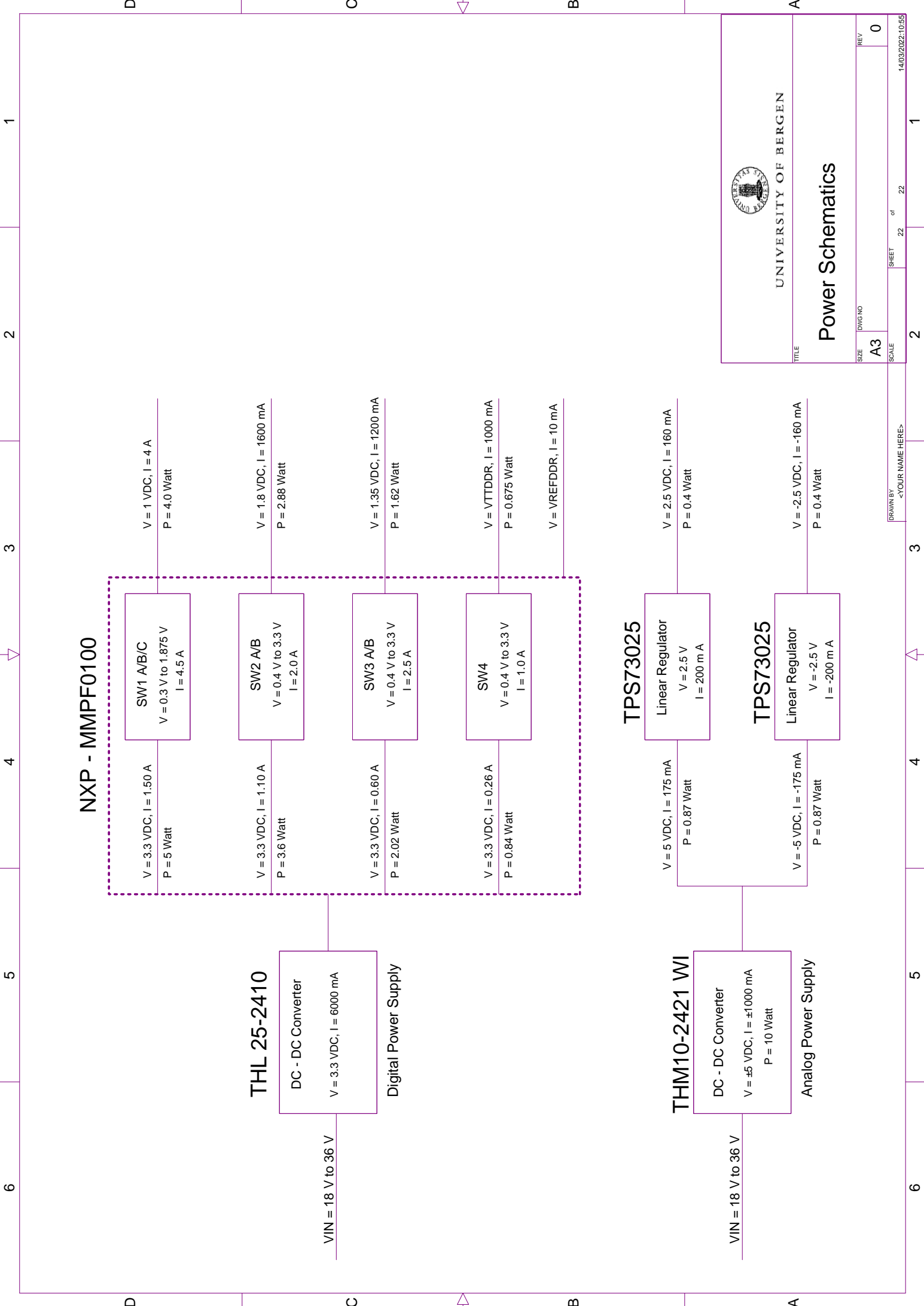
De Coupling Capacitors for PL according to Table 3-1 Page 13 [UG 933 (v1.13.1)]



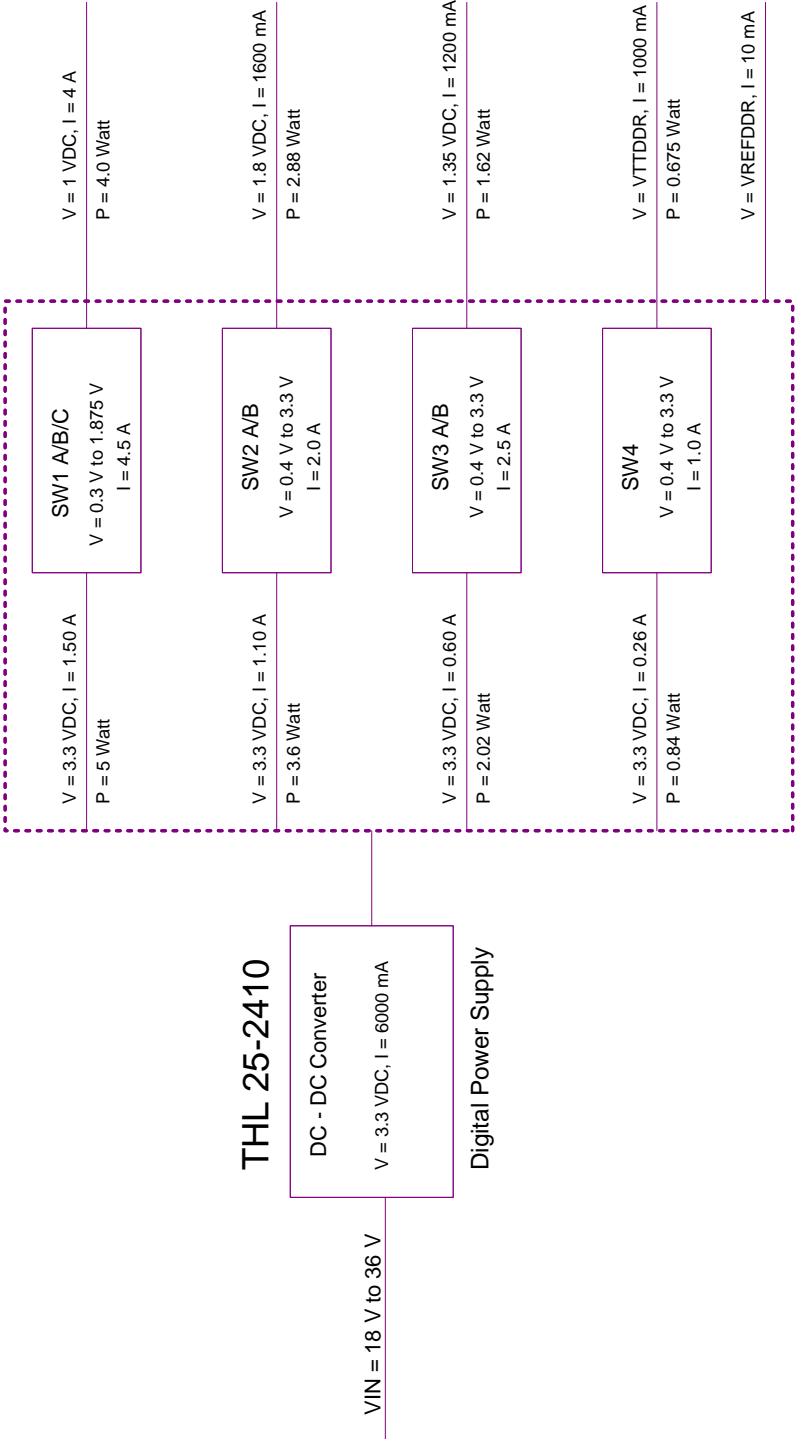
UNIVERSITY OF BERGEN

Power Supplies 02

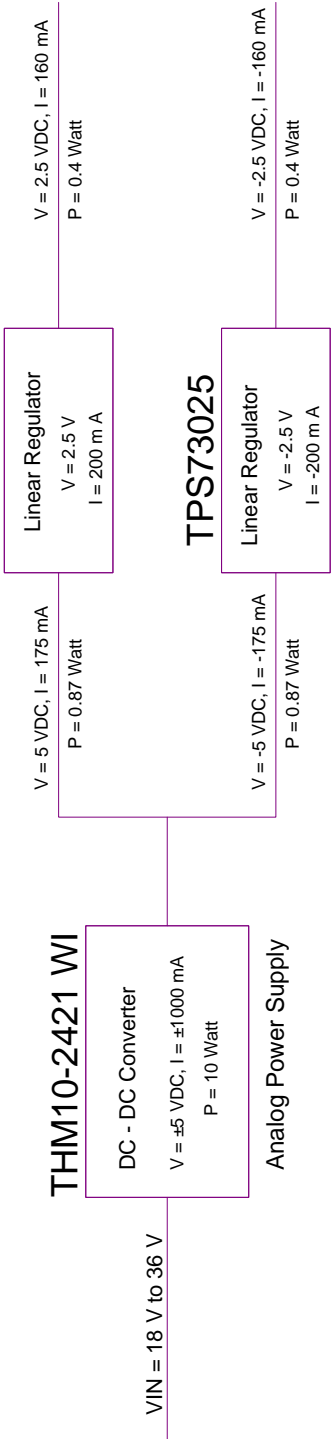
TITLE	Power Supplies 02		
SIZE	DWG NO	SHEET	REV
A3		21 of 22	0
SCALE			




NXP - MMPF0100



TPS73025



UNIVERSITY OF BERGEN



Power Schematics

SIZE: DWG NO
A3

SCALE: SHEET 22 of 22

REV: 0

14/03/2022:10:55

DRAWN BY: <YOUR NAME HERE>

Shared Files

The files that might be useful for others after this thesis is delivered are placed in a shared folder at UiB. This folder contains:

- Simulation files
- MATLAB files
- Measurement raw files
- L^AT_EXfiles

The simulation files are in a folder named `spice_sim` contains simulation files developed to use in this thesis. First, there is the simulation in LTspice used in section 3.3.1. The other simulation files are of the front-end electrons circuit and the components used. This includes the simulation files used in section 4.4: For all the individual stages in the circuit, both frequency and impulse response. For the complete circuit with a summing amplifier that can be simulated with frequency response or a transient simulation of impulse response or with a realistic input. The folder also contains simulation files of the complete circuit without summing that have not been shown here.

The `MATLAB` folder contains files for making most of the plots in this document; this includes calculated plots and plots of simulation and measured data. There are also MATLAB files for most of the calculations, which were not done by hand. Additionally, in the `MATLAB` folder, if `.csv`-files exported from the simulations.

The `Measurements` folder contains all the measurements that were taken in conjunction with this work. These are mostly oscilloscope data from SiPM measurements; these raw files is the used by the MATLAB files in the `MATLAB` folder.

Lastly, the `Thesis`-folder contains the L^AT_EXfiles that were used to create this document. This includes, among other things, a `.pdf`-file of all plots and finished and source files for the circuit diagrams shown in this document.

Intermediate Noise Calculations

This appendix is a supplement to the noise calculations in section 4.2.2.

From section 4.2.2 the output noise will be given by equation (4.31), where the transfer function is given by equation (4.32) and the spectral densities is given by equations (4.33), (4.34) and (4.35). This appendix follows the same method for solving the integrals as in [30]

$$\langle v_{out}^2 \rangle = \int_0^{\infty} S_n |T_n(j2\pi f)|^2 df \quad (4.31)$$

$$|T(j2\pi f)|^2 = \frac{k^2}{\left(1 + \left(\frac{f}{f_0}\right)^2\right)^{n+1}} \quad (4.32)$$

$$i^2 = |v_n C_{Ts}|^2 = v_n^2 C_T^2 4\pi^2 f^2 = v_n^2 C_T^2 4\pi^2 f_0^2 \left(\frac{f}{f_0}\right)^2 \quad (4.33)$$

$$i_{nf}^2 = |v_{nf} C_{Ts}|^2 = \frac{A_f}{f} C_T^2 4\pi^2 f^2 \quad (4.34)$$

$$i_n^2 = i_n^2 \quad (4.35)$$

After inserting equations (4.35), (4.33) and (4.34) into equation (4.31) as power spectral density S_n and also inserting equation (4.32) for the transfer function the integrals for the noise is given by equations (D.1), (D.2) and (D.3).

$$\langle v_{out}^2 \rangle_{nw} = \int_0^{\infty} i_n^2 \frac{k^2}{\left(1 + \left(\frac{f}{f_0}\right)^2\right)^{n+1}} df \quad (D.1)$$

$$\langle v_{out}^2 \rangle_{n1/f} = \int_0^{\infty} i_{nf}^2 \frac{k^2}{\left(1 + \left(\frac{f}{f_0}\right)^2\right)^{n+1}} df \quad (D.2)$$

$$\langle v_{out}^2 \rangle_{ni} = \int_0^\infty i_n^2 \frac{k^2}{\left(1 + \left(\frac{f}{f_0}\right)^2\right)^{n+1}} df \quad (D.3)$$

Inserting the content of equations (4.35), (4.33) and (4.34) into equation (D.1), (D.2) and (D.3), and moving the constant terms outside the integral gives equation (D.4), (D.5) and (D.6).

$$\langle v_{out}^2 \rangle_{nw} = v_{nw}^2 C_T^2 4\pi^2 f_0^2 k^2 \int_0^\infty \frac{\left(\frac{f}{f_0}\right)^2}{\left(1 + \left(\frac{f}{f_0}\right)^2\right)^{n+1}} df \quad (D.4)$$

$$\langle v_{out}^2 \rangle_{n1/f} = A_f C_T^2 4\pi^2 f_0 k^2 \int_0^\infty \frac{\left(\frac{f}{f_0}\right)}{\left(1 + \left(\frac{f}{f_0}\right)^2\right)^{n+1}} df \quad (D.5)$$

$$\langle v_{out}^2 \rangle_{ni} = i_n^2 k^2 \int_0^\infty \frac{1}{\left(1 + \left(\frac{f}{f_0}\right)^2\right)^{n+1}} df \quad (D.6)$$

These integrals in equation (D.4), (D.5) and (D.6) can be solved using the beta function, given in equation (D.7). And using the substitution in equation (D.8).

$$B(m+1, \alpha+1) = \int_0^\infty \frac{u^m}{(1+u)^{m+\alpha+2}} du \quad (D.7)$$

$$u = \left(\frac{f}{f_0}\right)^2 \rightarrow f = f_0 u^{\frac{1}{2}} \rightarrow df = f_0 \frac{1}{2} u^{-\frac{1}{2}} du \quad (D.8)$$

Inserting the substitution in equation (D.8) into equation (D.4), (D.5) and (D.6) give equation (D.9), (D.10) and (D.11).

$$\langle v_{out}^2 \rangle_{nw} = v_{nw}^2 C_T^2 2\pi^2 f_0^3 k^2 \int_0^\infty \frac{u^{\frac{1}{2}}}{(1+u)^{n+1}} du \quad (D.9)$$

$$\langle v_{out}^2 \rangle_{n1/f} = A_f C_T^2 2\pi^2 f_0^2 k^2 \int_0^\infty \frac{1}{(1+u)^{n+1}} du \quad (D.10)$$

$$\langle v_{out}^2 \rangle_{ni} = i_n^2 \frac{f_0}{2} k^2 \int_0^\infty \frac{u^{-\frac{1}{2}}}{(1+u)^{n+1}} du \quad (D.11)$$

Comparing the beta function in equation (D.7) to the integrals in equation (D.9), (D.10) and (D.11) gives m and $m + \alpha + 2$ as shown in table D.1, the solution for $m + 1$ and $\alpha + 1$ is also given here.

Expression	Noise Source		
	Series	Flicker	Parallel
m	$\frac{1}{2}$	0	$-\frac{1}{2}$
$m + \alpha + 2$	$n + 1$	$n + 1$	$n + 1$
$m + 1$	$\frac{3}{2}$	1	$\frac{1}{2}$
$\alpha + 1$	$n - \frac{1}{2}$	n	$n + \frac{1}{2}$

Table D.1: α and m values for the beta function in the noise integrals for CR-RCⁿ shaper.

Inserting the values in table D.1 into the beta function for each of the equations (D.9), (D.10) and (D.11), and substituting $f_0 = 1/(2\pi\tau)$ gives equation (4.36), (4.37) and (4.38) as given in section 4.2.2.

$$\langle v_{out}^2 \rangle_{nw} = v_{nw}^2 C_T^2 \frac{1}{4\pi\tau^3} k^2 B \left(\frac{3}{2}, n - \frac{1}{2} \right) \quad (4.36)$$

$$\langle v_{out}^2 \rangle_{n1/f} = A_f C_T^2 k^2 \frac{1}{2\tau^2} \frac{1}{n} \quad (4.37)$$

$$\langle v_{out}^2 \rangle_{ni} = i_n^2 \frac{1}{4\pi\tau} k^2 B \left(\frac{1}{2}, n + \frac{1}{2} \right) \quad (4.38)$$

Later in section 4.2.2 a different transfer function is considered, which gives the square of the absolute value of the transfer function as in equation (4.40).

$$|T(j2\pi f)|^2 = k^2 \frac{\left(\frac{f}{f_0}\right)^2}{\left(1 + \left(\frac{f}{f_0}\right)^2\right)^{n+2}} \quad (4.40)$$

Inserting the spectral densities in equations (4.33), (4.34) and (4.35), and the square of the absolute value of the transfer function in equation (4.40) into equation (4.31). This gives equation (D.12), (D.13) and (D.14).

$$\langle v_{out}^2 \rangle_{nw} = v_{nw}^2 C_T^2 4\pi^2 f_0^2 k^2 \int_0^\infty \frac{\left(\frac{f}{f_0}\right)^4}{\left(1 + \left(\frac{f}{f_0}\right)^2\right)^{n+2}} df \quad (D.12)$$

$$\langle v_{out}^2 \rangle_{n1/f} = A_f C_T^2 4\pi^2 f_0 k^2 \int_0^\infty \frac{\left(\frac{f}{f_0}\right)^3}{\left(1 + \left(\frac{f}{f_0}\right)^2\right)^{n+2}} df \quad (D.13)$$

$$\langle v_{out}^2 \rangle_{ni} = i_n^2 \int_0^\infty k^2 \frac{\left(\frac{f}{f_0}\right)^2}{\left(1 + \left(\frac{f}{f_0}\right)^2\right)^{n+2}} df \quad (D.14)$$

Now using the substitution in equation (D.8) on (D.12), (D.13) and (D.14), gives equation (D.15), (D.16) and (D.17).

$$\langle v_{out}^2 \rangle_{nw} = v_{nw}^2 C_T^2 2\pi^2 f_0^3 k^2 \int_0^\infty \frac{u^{\frac{3}{2}}}{(1+u)^{n+2}} du \quad (D.15)$$

$$\langle v_{out}^2 \rangle_{n1/f} = A_f C_T^2 2\pi^2 f_0^2 k^2 \int_0^\infty \frac{u^1}{(1+u)^{n+2}} du \quad (D.16)$$

$$\langle v_{out}^2 \rangle_{ni} = i_n^2 \frac{f_0}{2} k^2 \int_0^\infty \frac{u^{\frac{1}{2}}}{(1+u)^{n+2}} du \quad (D.17)$$

Comparing the beta function in equation (D.7) to the integrals in equation (D.15), (D.16) and (D.17) gives m and $m + \alpha + 2$ as shown in table D.2, the solution for $m + 1$ and $\alpha + 1$ is also given here.

	Noise Source		
Expression	Series	Flicker	Parallel
m	$\frac{3}{2}$	1	$\frac{1}{2}$
$m + \alpha + 2$	$n + 2$	$n + 2$	$n + 2$
$m + 1$	$\frac{5}{2}$	2	$\frac{3}{2}$
$\alpha + 1$	$n - \frac{1}{2}$	n	$n + \frac{1}{2}$

Table D.2: α and m values for the beta function in the noise integrals for CR²-RCⁿ shaper.

Inserting the values in table D.2 into the beta function for each of the equations (D.15), (D.16) and (D.17), and substituting $f_0 = 1/(2\pi\tau)$ gives equation (4.41), (4.42) and (4.43) as given in section 4.2.2.

$$\langle v_{out}^2 \rangle_{nw} = v_{nw}^2 C_T^2 \frac{1}{4\pi\tau^3} k^2 B\left(\frac{5}{2}, n - \frac{1}{2}\right) \quad (4.41)$$

$$\langle v_{out}^2 \rangle_{n1/f} = A_f C_T^2 \frac{1}{2\tau^2} k^2 B(2, n) \quad (4.42)$$

$$\langle v_{out}^2 \rangle_{ni} = i_n^2 \frac{1}{4\pi\tau} k^2 B\left(\frac{3}{2}, n + \frac{1}{2}\right) \quad (4.43)$$

More Simulation Results

E.1 Simulation of Complete Circuit

This appendix is a supplement to the simulations of the complete circuit in section 4.4. The following figures show the magnitude and phase of the frequency response and the noise spectral density for the outputs for all the different variations shown in table 4.7.

E.1.1 AC-Response of Summing Configuration

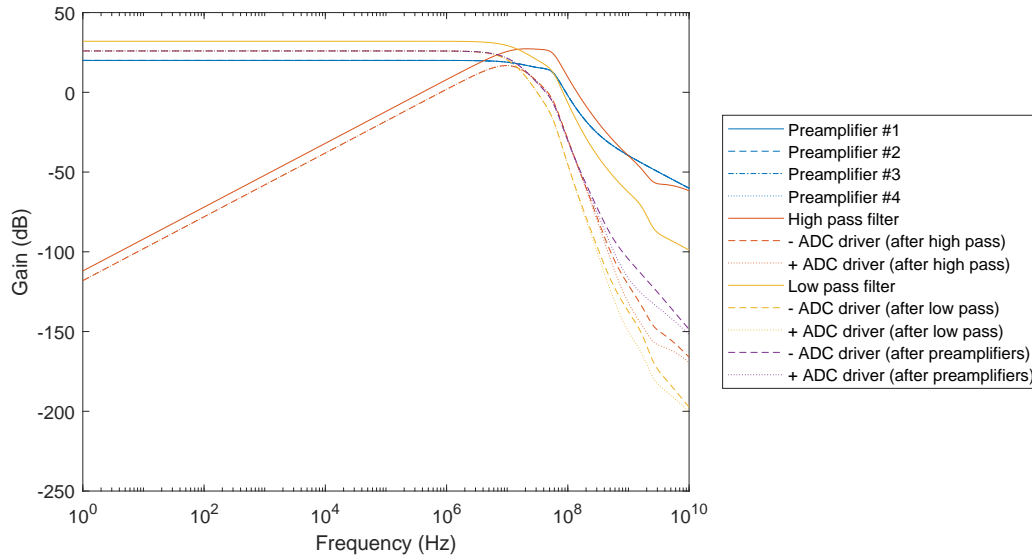


Figure 4.35: Gain of frequency response using time constant $\tau_{shaper} = 10$ ns, feedback resistor in preamplifier $R_f = 10 \Omega$, other resistors around $1 \text{ k}\Omega$, and gain of the summing amplifier equal to 1. (repeated from page 89)

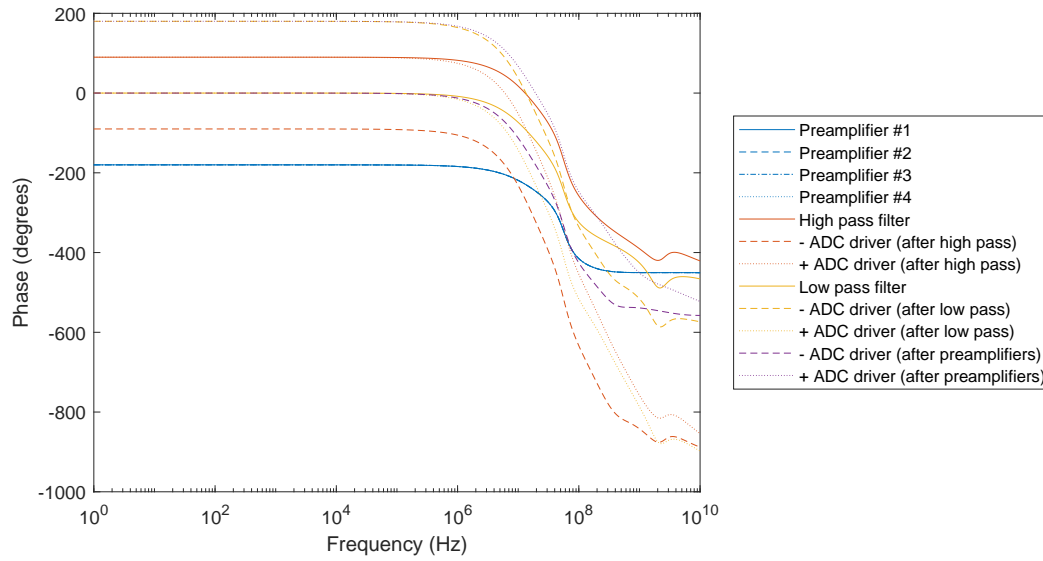


Figure 4.36: Phase of frequency response using time constant $\tau_{shaper} = 10$ ns, feedback resistor in preamplifier $R_f = 10 \Omega$, other resistors around $1 \text{ k}\Omega$, and gain of the summing amplifier equal to 1. (repeated from page 89)

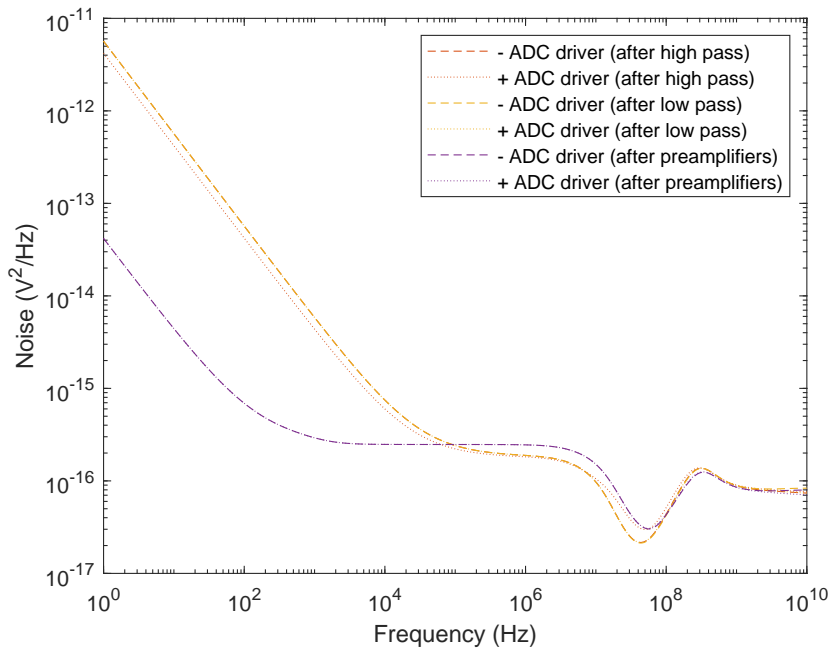


Figure 4.37: Output noise spectral density on the different outputs when using time constant $\tau_{shaper} = 10$ ns, feedback resistor in preamplifier $R_f = 10 \Omega$, other resistors around $1 \text{ k}\Omega$, and gain of the summing amplifier equal to 1. (repeated from page 90)

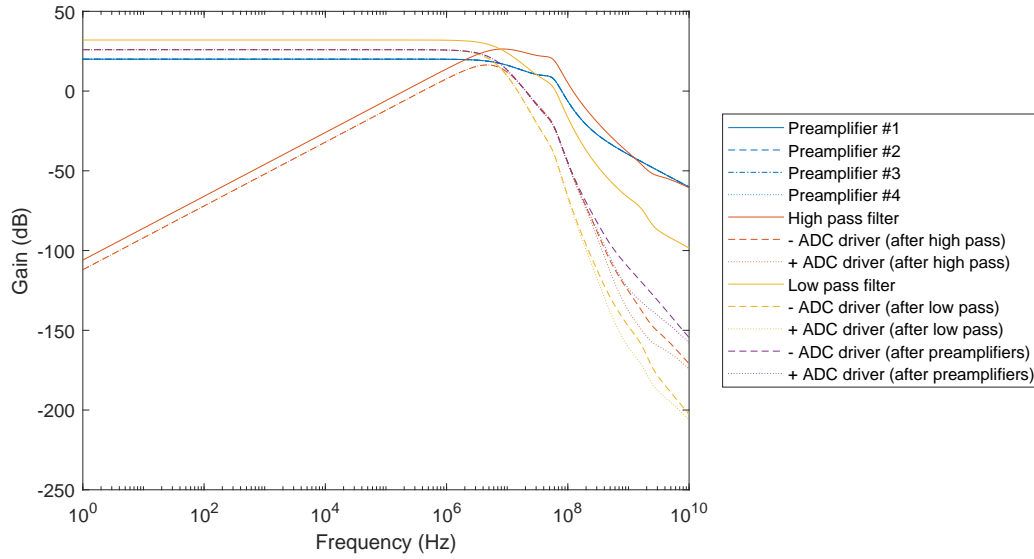


Figure E.1: Gain of frequency response using time constant $\tau_{shaper} = 20$ ns, feedback resistor in preamplifier $R_f = 10 \Omega$, other resistors around $1 \text{ k}\Omega$, and gain of the summing amplifier equal to 1.

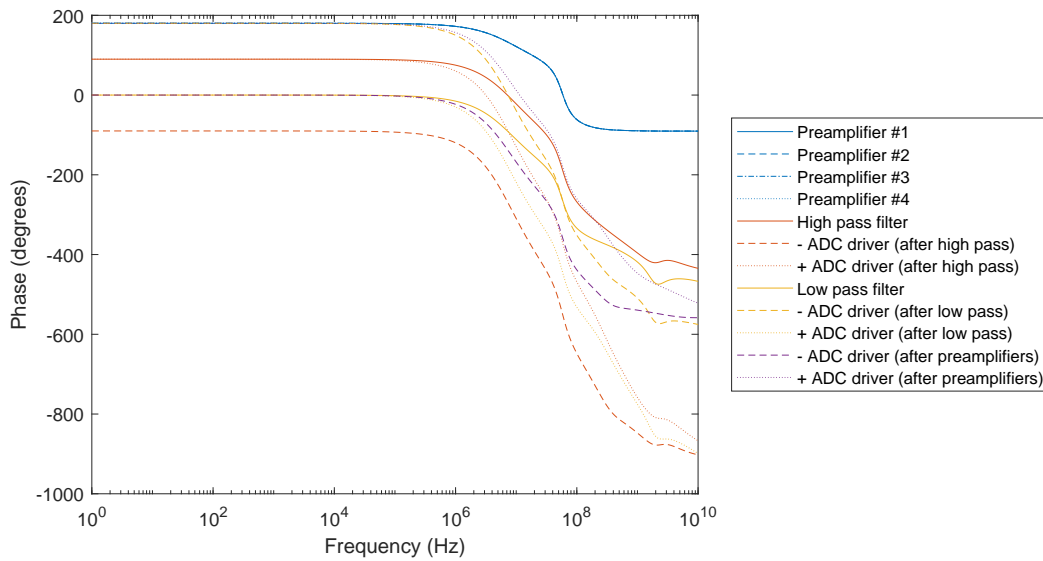


Figure E.2: Phase of frequency response using time constant $\tau_{shaper} = 20$ ns, feedback resistor in preamplifier $R_f = 10 \Omega$, other resistors around $1 \text{ k}\Omega$, and gain of the summing amplifier equal to 1.

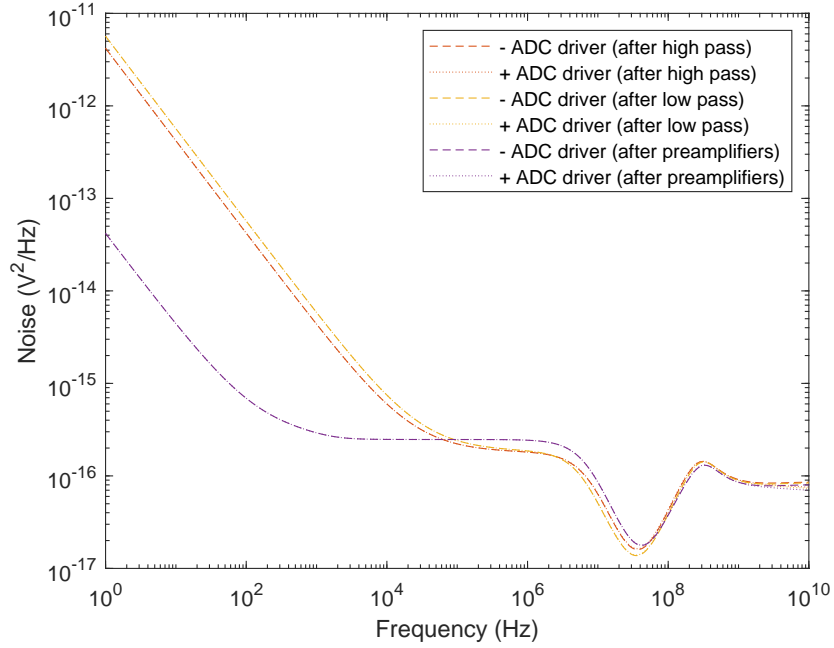


Figure E.3: Output noise spectral density on the different outputs when using time constant $\tau_{shaper} = 20$ ns, feedback resistor in preamplifier $R_f = 10 \Omega$, other resistors around $1 \text{ k}\Omega$, and gain of the summing amplifier equal to 1.

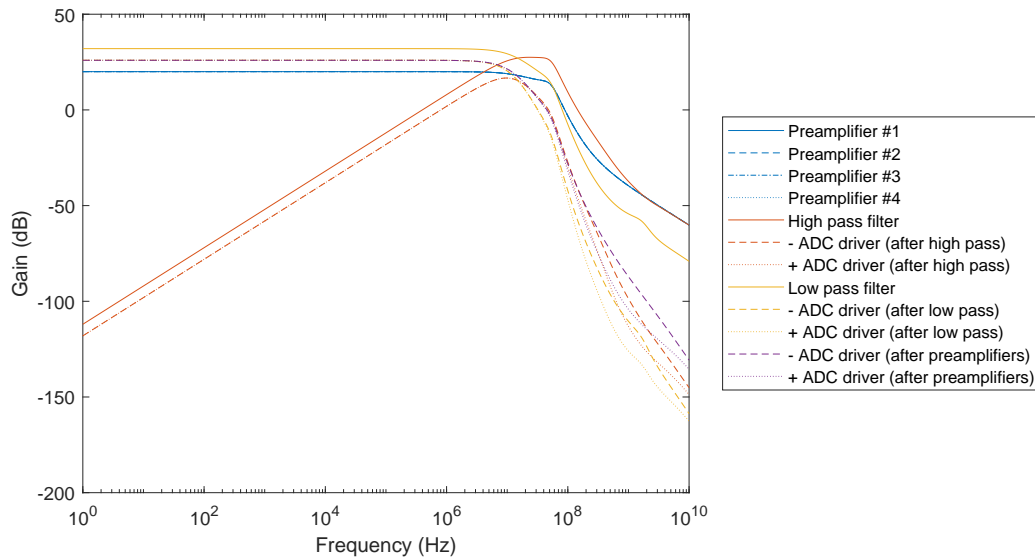


Figure E.4: Gain of frequency response using time constant $\tau_{shaper} = 10$ ns, feedback resistor in preamplifier $R_f = 10 \Omega$, other resistors around 100Ω , and gain of the summing amplifier equal to 1.

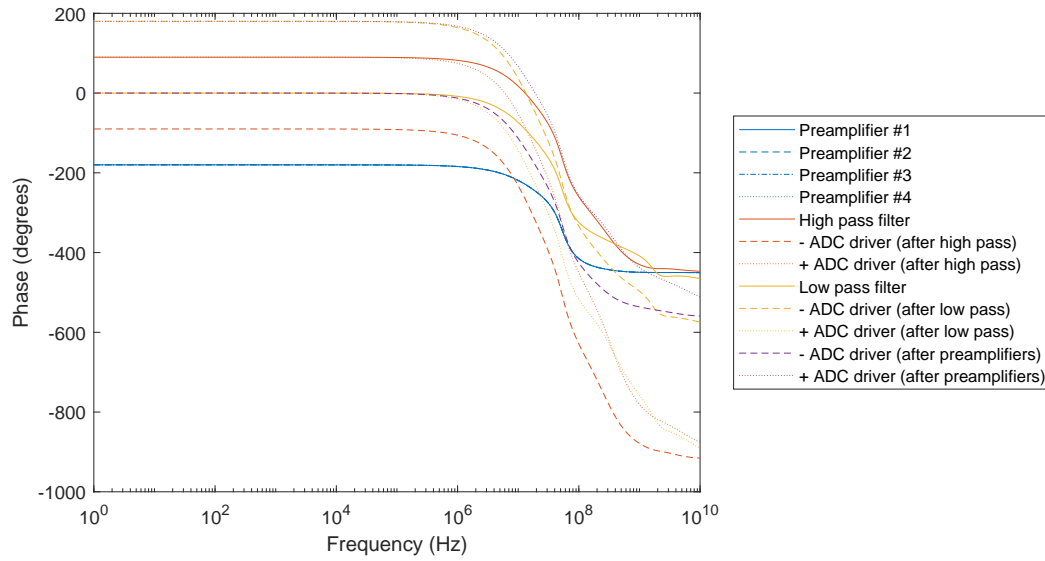


Figure E.5: Phase of frequency response using time constant $\tau_{shaper} = 10$ ns, feedback resistor in preamplifier $R_f = 10 \Omega$, other resistors around 100Ω , and gain of the summing amplifier equal to 1.

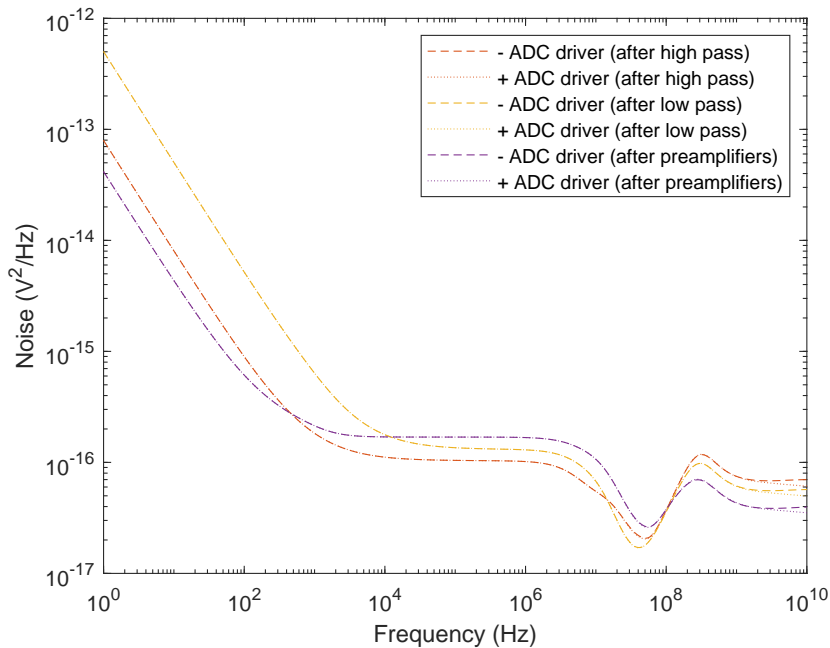


Figure E.6: Output noise spectral density on the different outputs when using time constant $\tau_{shaper} = 10$ ns, feedback resistor in preamplifier $R_f = 10 \Omega$, other resistors around 100Ω , and gain of the summing amplifier equal to 1.

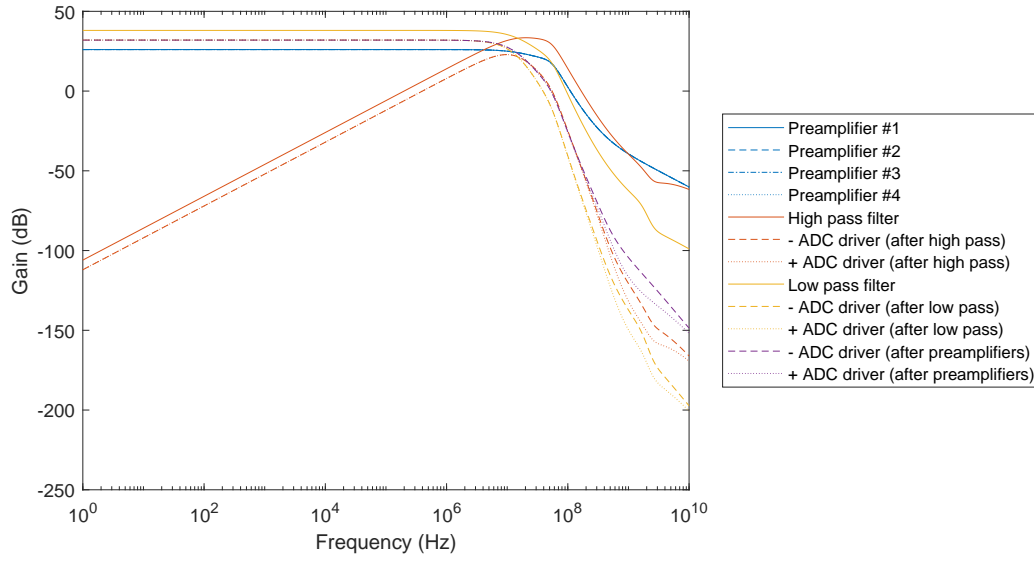


Figure E.7: Gain of frequency response using time constant $\tau_{shaper} = 10$ ns, feedback resistor in preamplifier $R_f = 20 \Omega$, other resistors around $1 \text{ k}\Omega$, and gain of the summing amplifier equal to 1.

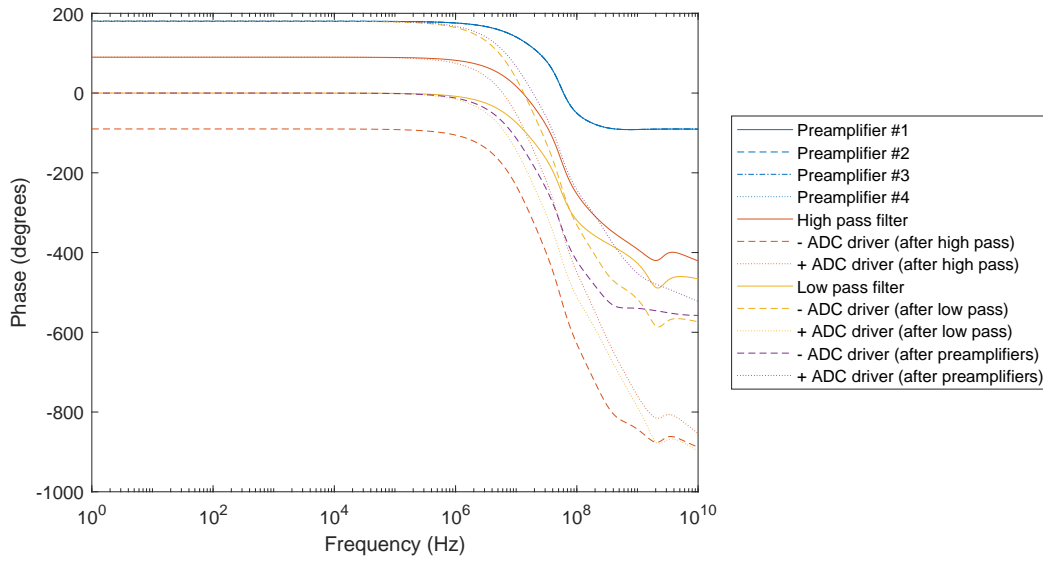


Figure E.8: Phase of frequency response using time constant $\tau_{shaper} = 10$ ns, feedback resistor in preamplifier $R_f = 20 \Omega$, other resistors around $1 \text{ k}\Omega$, and gain of the summing amplifier equal to 1.

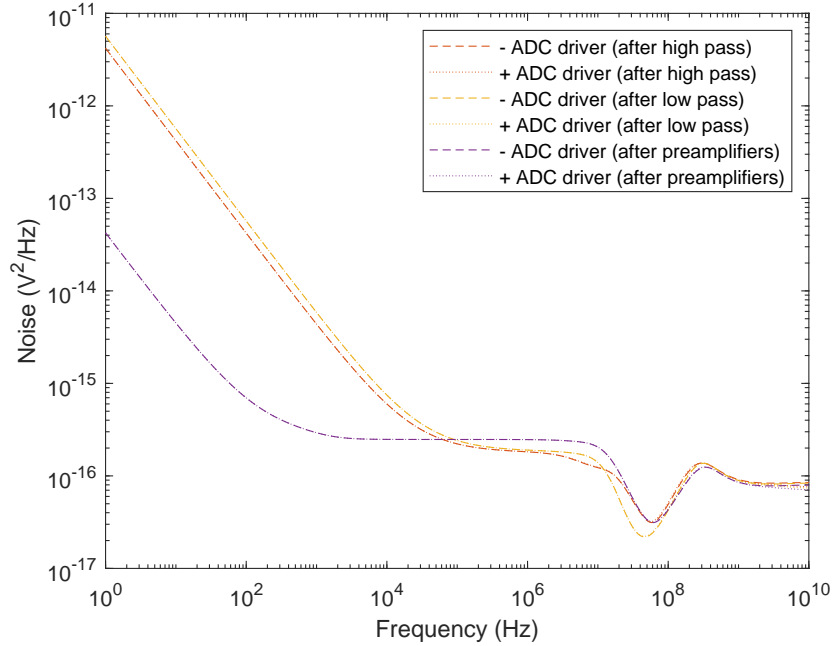


Figure E.9: Output noise spectral density on the different outputs when using time constant $\tau_{shaper} = 10$ ns, feedback resistor in preamplifier $R_f = 20 \Omega$, other resistors around $1 \text{ k}\Omega$, and gain of the summing amplifier equal to 1.

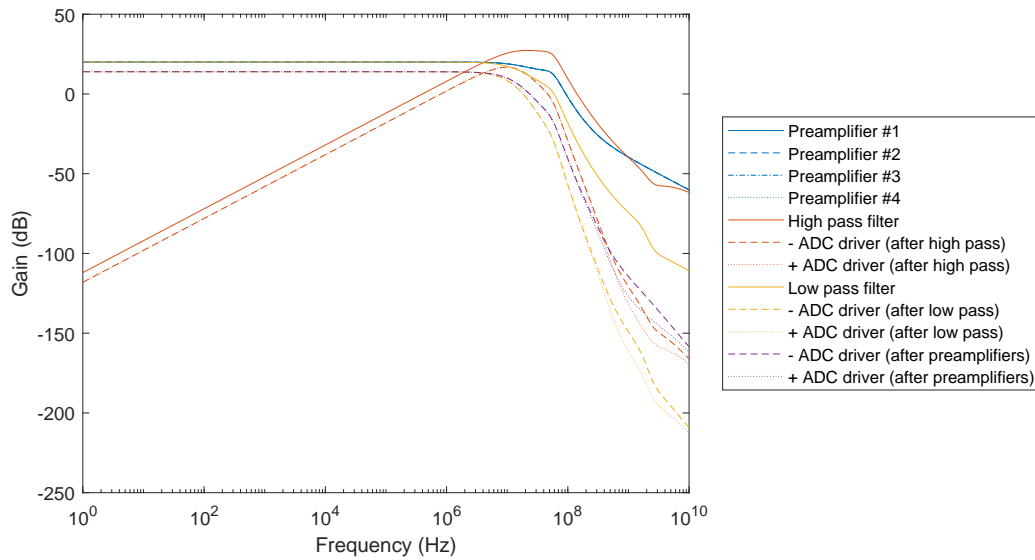


Figure E.10: Gain of frequency response using time constant $\tau_{shaper} = 10$ ns, feedback resistor in preamplifier $R_f = 10 \Omega$, other resistors around $1 \text{ k}\Omega$, and gain of the summing amplifier equal to 0.25.

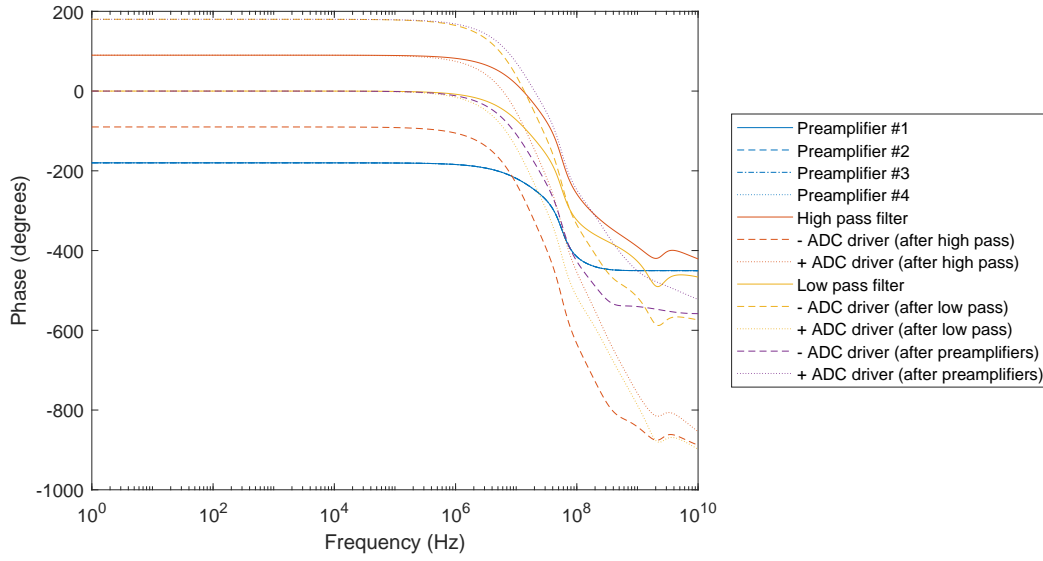


Figure E.11: Phase of frequency response using time constant $\tau_{shaper} = 10$ ns, feedback resistor in preamplifier $R_f = 10 \Omega$, other resistors around $1 \text{ k}\Omega$, and gain of the summing amplifier equal to 0.25.

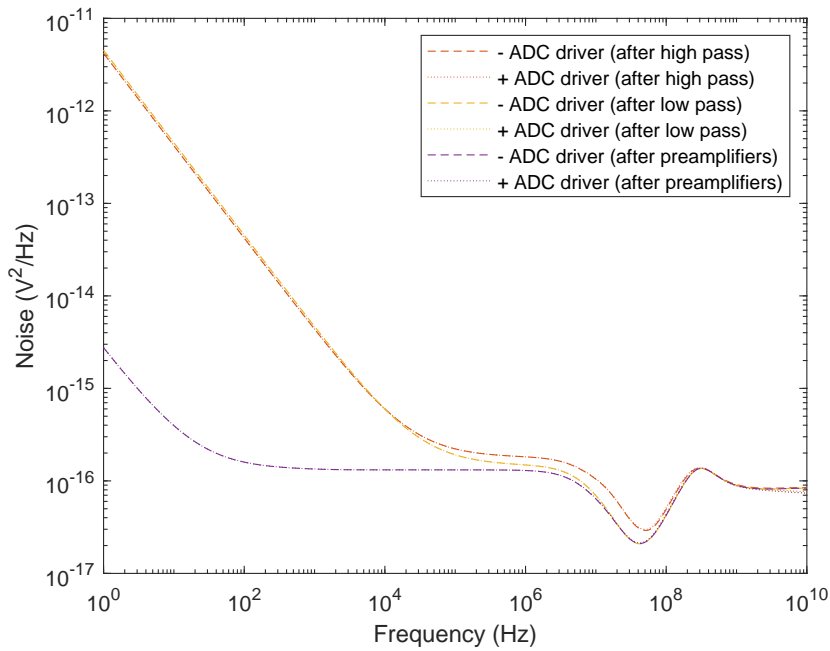


Figure E.12: Output noise spectral density on the different outputs when using time constant $\tau_{shaper} = 10$ ns, feedback resistor in preamplifier $R_f = 10 \Omega$, other resistors around $1 \text{ k}\Omega$, and gain of the summing amplifier equal to 0.25.

Bibliography

- [1] Aleksander Waage and Sindre Jacobsen Færø. “Design a PCB for ALOT”. Bachelor Thesis. Department of Computer science, Electrical engineering and Mathematical sciences at the Western Norway University of Applied Sciences, 2019.
- [2] Aleksander Kårstad Nes. “Evaluation and design of readout electronics for electron and proton detectors”. Master Thesis. Department of Physics and Technology, University of Bergen, June 2017.
- [3] Digilent. *Zybo Z7*. URL: <https://digilent.com/reference/programmable-logic/zybo-z7/start> (visited on 05/12/2022).
- [4] Digilent. *ZedBoard*. URL: <https://digilent.com/reference/programmable-logic/zedboard/start> (visited on 05/12/2022).
- [5] Asbjørn Magnus Midtbø and Harald Træet Læg Reid. “Design of an embedded data storage system using PYNQ”. Bachelor Thesis. Department of Computer science, Electrical engineering and Mathematical sciences at the Western Norway University of Applied Sciences, 2021.
- [6] J. R. Dwyer, D. M. Smith, and S. A. Cummer. “High-Energy Atmospheric Physics: Terrestrial Gamma-Ray Flashes and Related Phenomena”. In: *Space Science Reviews* Volume 173 (2012), pp. 133–196.
- [7] Thomas E. Johnson. *Introduction to Health Physics*. 5th ed. McGraw-Hill Education, 2009.
- [8] The ALOFT Collaboration. “Airborne Lighting Observatory for FEES and TGFs Campaign (ALOFT)”. Internal white paper. 2020.
- [9] Yvonne Gibbs, ed. *NASA Armstrong Fact Sheet: ER-2 High-Altitude Airborne Science Aircraft*. National Aeronautics and Space Administration. Sept. 17, 2014. URL: <https://www.nasa.gov/centers/armstrong/news/FactSheets/FS-046-DFRC.html> (visited on 05/10/2022).
- [10] N. Østgaard et al. “Gamma Ray Glow Observations at 20-km Altitude”. In: *Journal of Geophysical Research-Atmospheres* Volume 124 (2019), pp. 7236–7254.

-
- [11] R. S. Hansen et al. “How simulated fluence of photons from terrestrial gamma ray flashes at aircraft and balloon altitudes depends on initial parameters”. In: *Journal of Geophysical Research-Space Physics* Volume 118 (2013), pp. 2333–2339.
- [12] S. Gundacker and A. Heering. “The silicon photomultiplier: fundamentals and applications of a modern solid-state photon detector”. In: *Physics in Medicine and Biology* Volume 65 (2020).
- [13] Fabio Acerbi and Stefan Gundacker. “Understanding and simulating SiPMs”. In: *Nuclear Instruments and Methods in Physics Research Section A: Accelerators, Spectrometers, Detectors and Associated Equipment* 926 (2019). Silicon Photomultipliers: Technology, Characterisation and Applications, pp. 16–35. ISSN: 0168-9002. DOI: <https://doi.org/10.1016/j.nima.2018.11.118>. URL: <https://www.sciencedirect.com/science/article/pii/S0168900218317704>.
- [14] Glenn F. Knoll. *Radiation Detection and Measurement*. 4th ed. John Wiley & Sons, Inc., 2010.
- [15] *Introduction to the Silicon Photomultiplier (SiPM)*. AND9770/D. Rev. 8. onsemi. July 2021.
- [16] *Biasing and Readout of ON Semiconductor SiPM Sensors*. AND9782/D. Rev. 3. Onsemi. Apr. 2019.
- [17] D. Marano et al. “Silicon Photomultipliers Electrical Model Extensive Analytical Analysis”. In: *IEEE Transactions on Nuclear Science* 61.1, 1 (Feb. 2014), pp. 23–34. ISSN: 0018-9499. DOI: 10.1109/TNS.2013.2283231.
- [18] M. Petasecca et al. “Thermal and electrical characterization of silicon photomultiplier”. In: *IEEE Transactions on Nuclear Science* 55.3, 3 (June 2008). 15th International Workshop on Room-Temperature Semiconductor X- and Gamma-Ray Detectors/ 2006 IEEE Nuclear Science Symposium, San Diego, CA, OCT 29-NOV 04, 2006, 1686–1690. ISSN: 0018-9499. DOI: {10.1109/TNS.2008.922220}.
- [19] F. Corsi et al. “Electrical Characterization of Silicon Photo-Multiplier Detectors for Optimal Front-End Design”. In: *2006 IEEE Nuclear Science Symposium Conference Record*. Vol. 2. 2006, pp. 1276–1280. DOI: 10.1109/NSSMIC.2006.356076.
- [20] F. Corsi et al. “Modelling a silicon photomultiplier (SiPM) as a signal source for optimum front-end design”. In: *Nuclear Instruments and Methods in Physics Research Section A: Accelerators, Spectrometers, Detectors and Associated Equipment* 572.1 (2007). Frontier Detectors for Frontier Physics, pp. 416–418. ISSN: 0168-9002. DOI: <https://doi.org/10.1016/j.nima.2006.10.219>. URL: <https://www.sciencedirect.com/science/article/pii/S0168900206021449>.

- [21] Francesco Licciulli and Cristoforo Marzocca. “Parameter Extraction Method for the Electrical Model of a Silicon Photomultiplier”. In: *IEEE Transactions on Nuclear Science* 63.5 (2016), pp. 2517–2526. DOI: 10.1109/TNS.2016.2594585.
- [22] Robert Klanner. “Characterisation of SiPMs”. In: *Nuclear Instruments and Methods in Physics Research Section A: Accelerators, Spectrometers, Detectors and Associated Equipment* 926 (2019). Silicon Photomultipliers: Technology, Characterisation and Applications, pp. 36–56. ISSN: 0168-9002. DOI: <https://doi.org/10.1016/j.nima.2018.11.083>. URL: <https://www.sciencedirect.com/science/article/pii/S0168900218317091>.
- [23] *Silicon Photomultipliers (SiPM), High PDE and Timing Resolution Sensors in a TSV Package J-Series SiPM Sensors*. MICROJ-SERIES/D. Rev. 7. Onsemi. Aug. 2021.
- [24] S. Seifert et al. “Accurate measurement of the rise and decay times of fast scintillators with solid state photon counters”. In: 7.09 (2012), P09004–P09004. DOI: 10.1088/1748-0221/7/09/p09004. URL: <https://doi.org/10.1088/1748-0221/7/09/p09004>.
- [25] Advatech. *LYSO(Ce) - Lutetium Yttrium Orthosilicate (Ce)*. URL: https://www.advatech-uk.co.uk/lyso_ce.html (visited on 11/10/2021).
- [26] *LYSO Scintillation Material*. Saint-Gobain. June 2018. URL: <https://www.crystals.saint-gobain.com/sites/hps-mac3-cma-crystals/files/2021-08/LYSO-Material-Data-Sheet.pdf> (visited on 05/30/2022).
- [27] H. Alva-Sanchez et al. “Understanding the intrinsic radioactivity energy spectrum from Lu-176 in LYSO/LSO scintillation crystals”. In: *Scientific Reports* 8 (Nov. 2018). ISSN: 2045-2322. DOI: 10.1038/s41598-018-35684-x.
- [28] Evgeny Kuznetsov. “Temperature-compensated silicon photomultiplier”. In: *Nuclear Instruments & Methods in Physics Research Section A-Accelerators Spectrometers Detectors and Associated Equipment* 912.SI (Dec. 2018). 8th International Conference on New Developments in Photodetection (NDIP), Tours, FRANCE, JUL, 2017, pp. 226–230. ISSN: 0168-9002. DOI: 10.1016/j.nima.2017.11.060.
- [29] *Silicon Photomultiplier (SiPM) High Fill-Factor Arrays*. ARRAYJ-SERIES/D. Rev. 7. Onsemi. Sept. 2021.
- [30] Angelo Rivetti. *CMOS Front-End Electronics for Radiation Sensors*. CRC Press, 2015.
- [31] *LMH6629 Ultra-Low Noise, High-Speed Operational Amplifier with Shutdown*. LMH6629. Rev. G. Texas Instruments. Dec. 2014.
- [32] *OPA855 8-GHz Gain Bandwidth Product, Gain of 7-V/V Stable, Bipolar Input Amplifier*. OPA855. Rev. A. Texas Instruments. July 2018.
- [33] Texas Instruments. *Operational amplifiers (op amps) - Products*. URL: <https://www.ti.com/amplifier-circuit/op-amps/products.html> (visited on 01/10/2022).

-
- [34] J. Kaspar et al. “Design and performance of SiPM-based readout of PbF2 crystals for high-rate, precision timing applications”. In: *Journal of Instrumentation* 12 (Jan. 2017). ISSN: 1748-0221. DOI: {10.1088/1748-0221/12/01/P01009}.
- [35] *Octal, 14-Bit, 40/65 MSPS, Serial LVDS, 1.8 V Analog-to-Digital Converter*. AD9257. Rev. A. Analog Devices. Apr. 2013.
- [36] *Dual Channel 12-Bit 500MSPS Analog-to-Digital Converter*. ADS5404. Rev. B. Texas Instruments. Jan. 2014.
- [37] *Wideband Operational Amplifier*. THS4304. Rev. A. Texas Instruments. July 2004.
- [38] *Wideband, Low-Distortion, Fully Differential Amplifiers*. THS4505. Rev. D. Texas Instruments. May 2008.
- [39] *RB751CS40 Schottky barrier diode Product data sheet*. RB751CS40. Rev. 2. Nexperia. Apr. 2021.
- [40] *RB521CS30L 100 mA low V_F MEGA Schottky barrier rectifier Product data sheet*. RB751CS30L. Rev. 1. Nexperia. Jan. 2011.